Electrodeposition of Nickel-Based Non-Noble Transition Metal Compounds for Electrocatalytic Water Splitting

A Dissertation Approved by the Department of Materials and Earth Sciences in Fulfillment of the Requirements for the Degree of Doctor Rerum Naturalium (Dr. rer. nat.)

M. Eng. Shasha Tao from Hu Nan, People's Republic of China

TECHNISCHE UNIVERSITÄT DARMSTADT

Surface Science

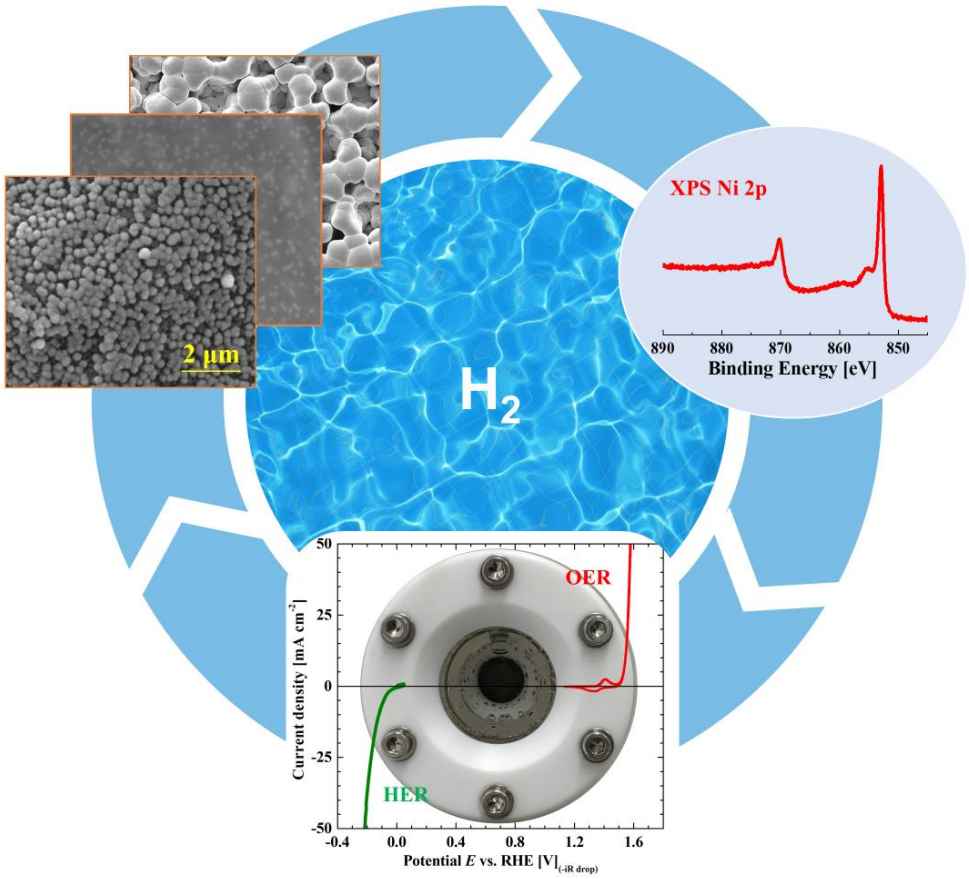

Technische Universität Darmstadt, Germany

A Dissertation Approved by the Department of Materials and Earth Sciences in Fulfillment of the Requirements for the Degree of Doctor Rerum Naturalium (Dr. rer. nat.)

Electrodeposition of Nickel-Based Non-Noble Transition Metal Compounds for Electrocatalytic Water Splitting

M. Eng. Shasha Tao

From Hu Nan, People's Republic of China

TECHNISCHE UNIVERSITÄT DARMSTADT

Referee: PD Dr. Bernhard Kaiser

Co-referee: Prof. Dr. Bastian J. M. Etzold

Fachbereich Material- und Geowissenschaften

Technische Universität Darmstadt

Date of submission: 29.05.2019

Date of oral examination: 12.07.2019

Darmstadt 2019

D 17

Dedicated to my parents (献予我的父母)

Declaration

M. Eng. Shasha Tao

Nieder-Ramstädter Str. 11

64283 Darmstadt

Declaration

This work described in this thesis was carried out at the Department of Materials and Earth Sciences, Technische Universität Darmstadt during the period August 2014 to April 2018. This thesis represents the author's original work, except where otherwise stated, and no part of it has been submitted for a degree at any other university. Prior to the submission of this thesis, some work has been published as described in the relevant chapters herein.

Eidesstattliche Erklärung

Hiermit erkläre ich an Eides statt, dass ich die vorliegende Dissertation selbstständig und nur mit den angegebenen Hilfsmitteln angefertigt habe. Von mir wurde weder an der Technischen Universität Darmstadt noch einer anderen Hochschule ein Promotionsversuch unternommen.

Darmstadt, den 28.05.2019

Shasha Tao (陶沙沙)

Contents

List of Figures

List of Tables

List of abbreviations

ALD	Atomic layer deposition
BE	Binding energy
CE	Counter electrode
CNT	Carbon nanotubes
CV	Cyclic voltammetry
CVD	Chemical vapor deposition
DFT	Density functional theory
ECSA	Electrochemical surface area
ED	Electrodeposition/Electrochemical deposition
EDX/EDS	Energy-dispersive X-ray spectroscopy
EIS	Electrochemical impedance spectroscopy
ESCA	Electron spectroscopy for chemical analysis
FWHM	Full width at half maximum
HER	Hydrogen evolution reaction
ITO	Indium tin oxide
LDH	Layered double hydroxides
LSV	Linear sweep voltammetry
MOFs	Metal organic frameworks
MWCNTs	Multi-walled carbon nanotubes
NPs	Nanoparticles
OCP	Open circuit potential
OER	Oxygen evolution reaction
ORR	Oxygen reduction reaction
PDS	Potential-determining step
PV	Photovoltaic
PVD	Physical vapor deposition
RE	Reference electrode

RDS	Rate-determining step
RHE	Reversible hydrogen electrode
RSF	Relative sensitivity factors
SEI	Secondary electron imaging
SEM	Scanning electron microscopy
SHE	Standard hydrogen electrode
TMs	Transition metals
UHV	Ultra-high vacuum
VB	Valence band
WE	Working electrode
XRD	X-ray diffraction
XPS	X-ray photoelectron spectroscopy

Abstract

Electrochemical water splitting has become increasingly important in energy-related applications. Especially, efficient storage of the electrical energy harvested from the sunlight and from wind in chemical bonds is crucial for a future renewable energy economy. The overpotentials for the hydrogen and the oxygen evolution reactions (HER, OER) are standardly reduced by employing rare and expensive metal-based catalysts. The replacement of these materials by abundant and low-cost alternatives is therefore of utmost technological importance.

In the present work, Ni-based non-noble transition metal compounds such as Ni metal and its hydroxides and oxides as nanoparticles (NPs) and/or thin films as well as highly porous mixed Ni-Mo films were investigated for the electrocatalytic HER, OER and the overall water splitting reaction. They were prepared by employing electrochemical deposition techniques. The surface chemical composition and morphology of the synthesized materials were characterized by X-ray photoelectron spectroscopy (XPS) and scanning electron microscopy (SEM), respectively. These analyses were carried out before and after the electrochemical reactions in order to gain a deeper understanding of the critical parameters for the catalytic activities. For the composite Ni/NiO/$Ni(OH)_2$ NPs, the catalytic activity for the HER increases with an increase in the amount of NiO and reaches a maximum at the right composition of the active sites with approximately 25% Ni metal and $Ni(OH)_2$ each, as well as 50% NiO. For the OER, a pre-treatment of the electrodeposited $Ni(OH)_2$ films by thermal annealing in normal atmosphere is of extreme importance to form a large amount of the catalytically most active NiOOH species during the electrochemical reaction. As bifunctional electrocatalysts for the water splitting reaction, porous Ni-Mo structures were synthesized and investigated. In summary it can be stated, that the here prepared and tested Ni-based catalysts show activities comparable to the Pt for the HER and even better than the commercial RuO_2 for the OER, respectively.

Finally, the stabilities of the newly synthesized catalyst materials were investigated in relation to their activities and chemical compositions. Long-term measurements (up to 30 h) on the Ni composite NPs for the HER show a gradual transformation of the highly active catalyst compound consisting of Ni^0, NiO, and $Ni(OH)_2$ into the almost pure less-active $Ni(OH)_2$ phase, which requires then the double overpotential to keep the current density at -10 mA cm^{-2}. In contrast, the stability test of the annealed $Ni(OH)_2$ films for the OER indicates an activation during the first 2 h with a corresponding decrease in overpotential, which is associated with the formation of the catalytically active NiOOH species. After the activation, the OER catalyst exhibits excellent electrochemical stability during the following 24 h.

Zusammenfassung

Die elektrochemische Wasserspaltung hat im Hinblick auf Energie-bezogene Anwendungen eine zunehmende Bedeutung erfahren. Insbesondere ist die effiziente Speicherung von Elektrizität aus Wind- und Solarstrom für eine zukünftige Ökonomie mit erneuerbarer Energie essentiell. Die bei den Wasserstoff- und Sauerstoffentwicklungsreaktionen (HER, OER) auftretenden Überspannungen werden standardmäßig durch den Einsatz von raren und teuren metallen reduziert. Der Ersatz dieser Materialien durch häufig vorkommende und günstige Alternativen ist daher von sehr großer technologischer Bedeutung.

In der vorliegenden Arbeit wurden unedle Ni basierte Übergangsmetallverbindungen wie Ni Metall und dessen Hydroxide und Oxide als Nanopartikel (NP) und/oder dünnen Schichten sowie hochporöse gemischte Ni-Mo Filme in Bezug auf ihre elektrokatalytische Aktivität für die HER, die OER und für die gesamte Wasserspaltungsreaktion untersucht. Diese wurden durch den Einsatz von elektrochemischen Abscheidemethoden präpariert. Die chemische Oberflächenzusammensetzung und die Morphologie der synthetisierten Materialien wurden mittels Röntgen-Photoelektronen-Spektroskopie (XPS) und Raster-Elektronen-Mikroskopie (SEM) untersucht. Diese Analysen erfolgten jeweils vor und nach der elektrochemischen Untersuchung, um ein vertieftes Verständnis der kritischen Parameter für die katalytische Aktivität während der elektrochemischen Reaktion zu erzielen. Für den Verbundstoff aus Ni/NiO/$Ni(OH)_2$ NP nimmt die katalytische Aktivität bezüglich der HER bei zunehmendem Gehalt von NiO zu und erreicht ihr Maximum durch die richtige Zusammensetzung der aktiven Zentren aus jeweils 25% Ni und $Ni(OH)_2$ sowie 50% NiO. Eine thermische Vorbehandlung der elektrochemisch abgeschiedenen $Ni(OH)_2$ Filme in Luftatmosphäre ist von essentieller Bedeutung für die OER Aktivität, da nur dann unter Reaktionsbedingungen ein hoher Anteil der katalytisch sehr aktiven NiOOH Spezies gebildet wird. Als bifunktionale Elektrokatalysatoren für die Wasserspaltungsreaktion wurden hochporöse Ni-Mo Strukturen synthetisiert und untersucht. Zusammenfassend kann gesagt werden, dass die hier hergestellten und untersuchten Ni-basierten Katalysatoren vergleichbare Aktivitäten wie Pt für die HER und sogar besser als kommerzielles RuO_2 für die OER erzielen.

Abschließend wurden die Stabilitäten der neu synthetisierten Katalysatormaterialien in Bezug auf ihre Zusammensetzung und Aktivität untersucht. Langzeitmessungen (bis zu 30 Stunden) an den Ni Verbundstoffen für die HER zeigen eine graduelle Transformation des hochaktiven Materials aus Ni^0, NiO und $Ni(OH)_2$ hin zu einer fast reinen geringer aktiven $Ni(OH)_2$ Phase, die zum Aufrechterhalten der Stromdichte von -10 mA cm^{-2} die doppelte Überspannung benötigt. Im Gegensatz dazu zeigt der Stabilitätstest der präparierten $Ni(OH)_2$ Filme für die OER eine Aktivierung des Materials und Abnahme der Überspannung während der ersten beiden Stunden, welche mit der vermehrten Bildung der katalytisch aktiven NiOOH Phase einher geht. Nach dieser Aktivierung zeigt der Katalysator eine exzellente elektrochemische Stabilität für die darauffolgenden 24 Stunden.

1. Introduction

This chapter gives a general introductory background on the topic of electrocatalytic water splitting. The importance of energy storing technology, the advantages of hydrogen as an energy carrier and the superiority of hydrogen production by water electrolysis using renewable energies are reviewed. Moreover, the motivation and objective for studying nickel-based non-noble compounds as the electrocatalysts for the water electrolysis, along with why electrochemical deposition as the synthesis strategy, are presented. Finally, the organization of the thesis is outlined.

1.1 Motivation

Since the industrial revolution began in the 18th century, fossil fuels, i.e., coal, oil and natural gas, have powered the technologies and transportation networks that drive society. However, the continuing rise of demand for fossil fuels threatens our energy stocks and puts enormous strain on the environment. In response to the global rise in population and the changes in the standards of living, the world's need for energy is projected to be approximately 30 and 46 TW in 2050 and 2100, respectively.[1-2] Since the fossil fuels are limited, restrictive shortages of oil and natural gas have been projected to occur in our lifetimes.[1] Consequently, a secure energy supply is increasingly difficult to assure. Moreover, the chemical and particulate pollution created by using fossil fuels puts our own health at risk, and carbon dioxide (CO_2) and other greenhouse gas emissions associated with global warming threaten the stability of the Earth's climate. Due to the problems mentioned above, there is a shift towards renewable energy sources, which can provide light, heat and electricity without environmental pollution. Solar radiation (photons), wind, biomass, ocean currents, tides and waves as well as geothermal heat are examples of renewable energy sources.

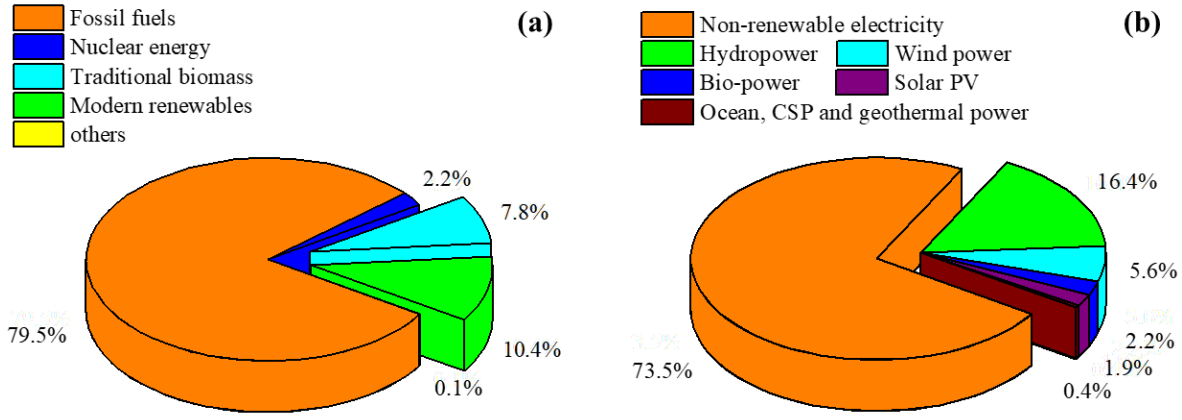

Figure 1.1 (a) Estimated renewable share of total final energy consumption, 2016. (b) Estimated renewable energy share of global electricity production, End-2017. CSP: Concentrating solar thermal power. Based on data from REN21's 2018 report.[3]

Based on REN21's 2018 report,[3] renewable sources (including traditional biomass and modern renewables)

contributed 18.2% to human's global energy consumption and 26.5% to the generation of electricity, respectively (**Figure 1.1**). In addition, the generating capacity of renewable power saw its largest annual increase ever in 2017, with an estimated 178 GW installed worldwide, increasing total capacity by nearly 9% over 2016. Solar photovoltaic (PV) led the way, accounting for almost 55% of newly installed renewable power capacity.[3] The added solar PV capacity in 2017 is even higher than the net additions of fossil fuels and nuclear power combined. Wind and hydropower contributed most of the remaining renewable capacity additions, accounting for more than 29% and nearly 11%, respectively. The total renewable power capacity was more than doubled in the decade 2007-2017, and the non-hydropower renewable capacity was increased more than six-fold (**Figure 1.2**).[3]

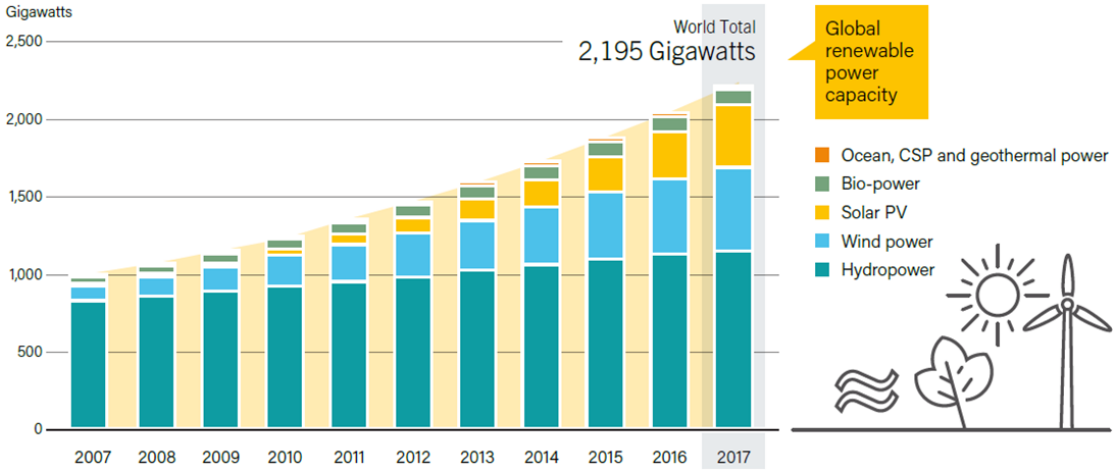

Figure 1.2 Global renewable power capacity, 2007-2017. Based on data from REN21's 2018 report.[3]

A fundamental problem in using renewable energies such as solar and wind is their seasonal and diurnal fluctuations. This is not compatible with our energy-consuming habits unless they will be integrated with efficient storing systems, so that excess energy produced at peak production times can be stored and released at minimum energy production times. There are different technologies available to store renewable energies, and most of them can be categorized into four generalized groups, namely, mechanical energy storage (e.g. pumped hydro, flywheels and compressed air energy storage systems), thermal energy storage (e.g. sensible heat), electrochemical energy storage (e.g. batteries, fuel cells, supercapacitors and electrolytic capacitors), and chemical energy storage (e.g. hydrogen and ammonia).[4-6] **Figure 1.3** displays the discharge duration versus the power delivered for different storage systems. Besides the large-scale storage technologies such as pump hydropower storage or compressed air electricity storage (CAES), new storage systems are emerging with more flexibility and adaptation to the various scales and variability of the renewable energy sources. Flywheels are increasingly being considered as renewable energy systems being able to span a large range of power delivery capabilities and durations.[7] Basically, excess energy is utilized to rotate the flywheel, and on demand, the flywheel slows down and powers a generator. The main advantages of flywheel storage systems are their high charge and discharge rates as well as a robustness of

twenty years, while the main disadvantages are the high costs and relatively high self-discharge rates. Nowadays, batteries as energy storage systems are playing an important role in people's daily lives. The use of batteries in electronics and transportation industries is emerging as advanced Lithium-ion (Li-ion) batteries with high capacities.[6] Many projects are now deployed worldwide. The main research and development efforts are concentrated on Li-ion battery components (electrodes and electrolytes), their packaging, and load-cycle management with the aim of improving both their lifetime and safety. The efforts are also dedicated towards the reduction of weight using new concepts, e.g. Li-polymer and Li-air batteries.[8]

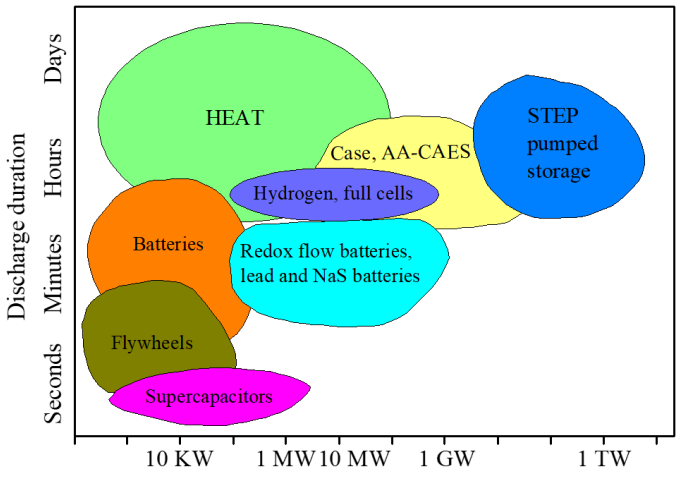

Figure 1.3 Discharge duration versus stored power of various energy storage technologies.[8] AA-CAES: Advanced Adiabatic Compressed Air Electricity Storage.

Storage of energy in chemical bonds is also an emerging approach. In this case renewable energies are used to drive endergonic reactions whose products can be stored and subsequently recombined to release the bond energy in a controlled manner when it is needed. The simplest and maybe the best reaction for this option is conversion to hydrogen by water splitting. Hydrogen has been considered as an ideal energy carrier especially because of its high gravimetric energy density (33.3 kWh kg^{-1}) and small environmental footprint with water being the only product of its oxidation. Within the vision for a sustainable future, several methods have been developed for renewable hydrogen production from water, such as electrolysis, photoelectrolysis, thermochemical, and biophotolysis.[9-11] Among them, water splitting by electrolysis represents the most established technology in industry for the electrochemical synthesis of hydrogen. During water electrolysis, renewable energies can be used as the electricity source to split water into hydrogen and oxygen without emission of greenhouse gases.[12-14] The generated hydrogen can then be either stored and used in chemical industry or used for electricity generation through fuel cells or internal combustion engines with zero post-combustion pollutants.[2, 15] Furthermore, high purity oxygen is a valuable by-product. Its utilization both in medical care and in chemical industry could bring a substantial decrease to the nominal cost of water electrolysis.[2, 16]

Although the electrochemical process involves simple reactants and requires only two electrons to produce

a hydrogen molecule, the overall efficiency is highly hindered by slow kinetics due to the large energy barriers caused by the multiple reaction steps of the cathodic and anodic half-reactions. Therefore, electrocatalysts are indispensable to accelerate the reaction, lower the overpotential, and minimize the energy cost. To date, platinum (Pt) has been recognized as the best-performing electrocatalyst for the hydrogen evolution reaction (HER),[17-18] whereas ruthenium (Ru) and iridium (Ir) oxides are regarded as the most-efficient electrocatalysts for the oxygen evolution reaction (OER).[17, 19] However, their large-scale industrial applications are significantly restricted by the low abundance and high market price. As an economical and efficient replacement of the conventional noble metal (Pt, Pd, Au, Ag, Ir and Ru)-based catalysts, earth-abundant transition metals (Fe, Co, Mo, Ni, V, Cu, etc.) have gained extensive research interest in energy storage/conversion applications, especially in the field of electrocatalysis [HER/OER/Oxygen Reduction Reaction (ORR)]. Among these transition metal materials, Ni has emerged as one of the most promising constituents owing to its interesting electronic properties (multivalent oxidation states), large abundance, low cost, high electrical conductivity and good heat conduction.[15] As schematically shown in **Figure 1.4**, a wide variety of Ni-based electrocatalysts in shape of metal, alloys, oxides, sulfides, carbides, nitrides, phosphides, borides, selenides, etc. have been explored towards HER or/and OER. **Table 2.2** and **Table 2.4** in Chapter 2 summarize the catalytic performance of some representative Ni-based catalysts for the HER and OER, respectively. Many of them exhibit very promising catalytic activity and stability as monofunctional or bifunctional materials.

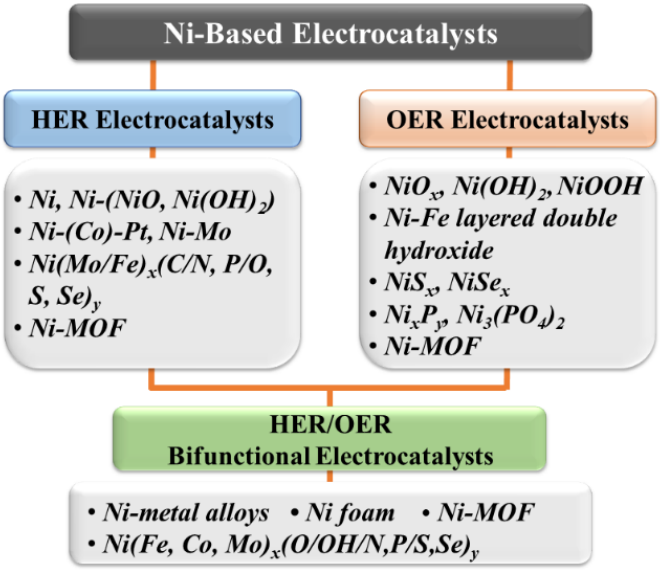

Figure 1.4 Diagrammatic representation of nickel-based electrocatalysts for water splitting.[17, 20-26]

Recently, researchers have invested great efforts dedicated to a thorough understanding of the catalytic mechanism of the Ni-based catalysts and to a further improvement of their catalytic activity through careful electrode design. However, the catalytic activity and stability of the Ni-based catalysts have not been studied well in detail employing X-ray photoelectron spectroscopy (XPS) to identify their chemical composition and electronic structures, yet. Thus, the main objective of the here performed work is to

explore economical and abundant Ni-based transition metal compounds for electrocatalytic water splitting, and to study the involved active sites and the ongoing elementary reaction steps by correlating the electrocatalytic behavior with the chemical composition as well as the electronic and geometric structures obtained by XPS and scanning electron microscopy (SEM).

Several methods can be used for the synthesis of Ni-based electrocatalysts, such as hydrothermal methods, organic synthesis, chemical vapor deposition (CVD), physical vapor deposition (PVD) and atomic layer deposition (ALD). Here, electrodeposition or electrochemical deposition (ED) has been chosen because it is one of the best strategies possessing unique intrinsic advantages:[27-29]

1. Electrodeposition can be performed both in the laboratory and industrially with relatively cost-effective equipment and straightforward procedures.
2. The technique is scalable to large surface areas and is therefore amenable to mass production.[27, 29]
3. The material types that can be prepared by electrodeposition are extensive and include almost all catalysts that have been used for catalytic water splitting (e.g. metals, alloys, oxides, chalcogenides, phosphides, selenides). The diversity is on one side in terms of the choice of deposition solution (also named as 'deposition bath'), and on the other side the choice of synthesis variables including the pH and temperature of the solution, the use of additives, and the concentration of the soluble precursors. The nature of the precursors themselves is a further parameter that can be altered to great advantage. Simple metal salts are the most frequently employed, while some sophisticated metal-ligand complexes are often used as well.
4. The amount of material deposited can be tuned by monitoring the charge flow of the electrochemical reactions. A good control can be achieved by altering the deposition duration, the current or potential at which the deposition is performed (whether steady state or varying according to a pre-defined protocol), or via a combination of these variables.
5. The morphologies (e.g. surface areas, nanostructures, orientations) of the deposited materials can be remarkably affected by easy manipulation of various synthetic variables (e.g. pH, additives, types of solvents, temperature). Besides, deposition potential and current can be applied as additional synthesis variables to finely tune the nucleation and growth processes of desired materials. Uniform doping can be also easily achieved by modifying the composition of the deposition solutions. As a result, an exceptional control of morphology and composition is possible.
6. The oxidation state of the metal(s) in electrodeposited films can be controlled through the applied potential. In trivial terms, this means that more oxidized deposits can be synthesized under more oxidizing potentials (favoring therefore more oxidized phases in the deposited materials). It is also possible to deposit metal oxide films by ramping the potential or by cycling the potential (as we used to deposit Ni composite nanoparticles in Chapter 4). The latter approaches enable a particular polymorph of the material first deposited at a lower potential and then oxidized in situ to give a

more highly oxidized version of the oxide which retains certain morphologies characteristic of the lower oxide.

Through a careful tuning of the parameters for electrodeposition mentioned above, many recent innovations in the development of electrocatalysts for energy-related applications have been achieved.[30-31] In this work, Ni-based electrocatalysts with variable morphology, structure, composition, oxidation state and hence electrochemical property were electrochemically deposited for optimization of the water splitting reaction.

1.2 Scope of the Thesis

With the motivation mentioned above, the further thesis is organized in the following manner:

Chapter 2 presents a general description of the thermodynamic and kinetic aspects of the water splitting reaction by electrolysis and gives an overview of the state of research with regard to the mechanistic understanding of the HER and OER. The electrocatalytic behaviors of some Ni-based materials for the HER and OER are especially discussed.

Chapter 3 gives a description of the different techniques used throughout this thesis.

After setting the base, the actual research results are presented in chapters 4 to 6: Chapter 4 describes a single-step electrochemical deposition of Ni nanoparticles (NPs) with a mixture of Ni^0, NiO and $Ni(OH)_2$ as electrocatalysts for the HER in alkaline media. The employed deposition method is presented in detail. The resulting NPs are characterized by SEM and XPS. The catalytic activity and stability of the Ni NPs are then discussed in correlation with the chemical composition obtained by XPS to identify the right combination of materials providing the active sites for the HER reaction steps.

Chapter 5 presents a simple method to convert the low-activity electrodeposited $Ni(OH)_2$ materials to a much more highly active form of the catalyst by a thermal annealing treatment in air atmosphere. An exploration on the origin of the catalytic enhancement by this simple pre-treatment was performed by XPS along with electrochemical techniques (e.g. cyclic voltammetry, electrochemical impedance spectroscopy). The catalytic activity and stability of the $Ni(OH)_2$ films were studied by relating to the XPS investigations conducted before, during and after the electrocatalytic OER to elucidate the redox states of the active components.

Chapter 6 is dedicated to the electrodeposition and characterization of porous Ni-Mo films as bifunctional electrocatalysts for both the hydrogen- and oxygen-evolution reactions. The variation of the surface chemical composition due to the deposition reaction and the electrochemical reactions were analyzed by XPS and were correlated with their electrocatalytic activity to identify the involved active sites.

Finally, the key points in this thesis have been summarized and addressed in the conclusion, as well as possible future developments based on this doctoral thesis are discussed in the end.

2. Theoretical Background

This chapter presents the theoretical background aiming at providing information that will be used to discuss and explain the observed effects in this thesis. Section 1 gives a general description of the water splitting by electrolysis with regard to the thermodynamic and kinetic description. Some important basic concepts are presented and briefly explained. Section 2 and 3 summarize the current state of understanding of the HER and OER mechanisms. Additionally, an overview of the materials that are being investigated for the HER and OER is presented, before finally a brief discussion of some Ni-based catalysts involved in electrochemical water splitting is given.

2.1 Electrochemistry of water splitting

Electrochemistry is concerned with the interaction between electrical energy and the Gibbs energy for chemical change. At the interface of an electronic conductor (the electrode) and an ionic conductor (the electrolyte), a chemical reaction can be caused by an externally supplied current, as in electrolysis, or an electric current can be produced by a spontaneous chemical reaction, as in a battery. The electrochemical reactions involving electron transfer are called oxidation-reduction or simply redox reactions. Water splitting by electrolysis is an electrochemical process that converts water into its component elemental gases hydrogen and oxygen through the flow of electrons arising from the application of an external voltage.

2.1.1 The electrochemical cell and reactions

A typical electrolysis cell for water splitting is illustrated in **Figure 2.1**. It consists of three parts: a cathode, an anode, and an aqueous electrolyte. By applying a high enough external voltage between the two electrodes, the hydrogen evolution reaction (HER, reduction reaction) and the oxygen evolution reaction (OER, oxidation reaction) occur at the negatively charged cathode and positively charged anode, respectively.[32-34]

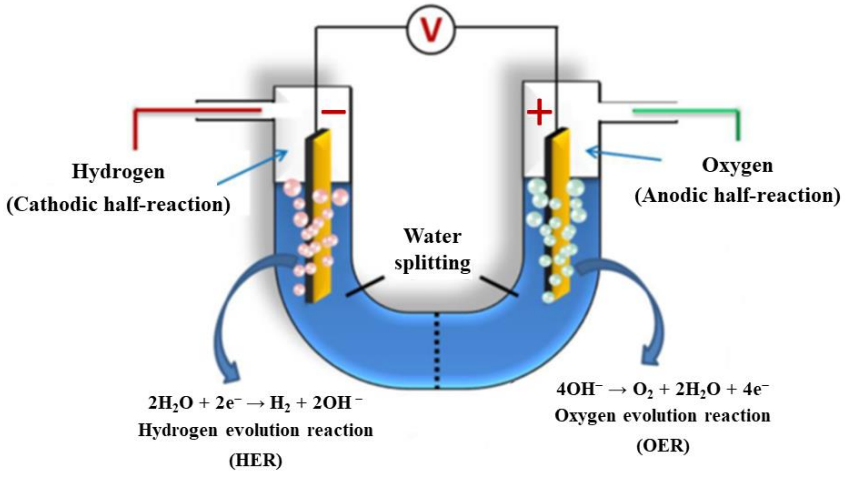

Figure 2.1 Schematic illustration of an alkaline water electrolyzer.[17]

Depending on the pH of the aqueous electrolytes in which water splitting proceeds, the electrochemical half-reactions can be generally expressed by the following equations **(2.1)** to **(2.4)**:[34]

In acidic or neutral solution:

Red.: $2\ H^+ + 2\ e^- \rightarrow H_2$ **(2.1)**

Ox.: $2\ H_2O \rightarrow O_2 + 4\ H^+ + 4\ e^-$ **(2.2)**

In alkaline solution:

Red.: $2\ H_2O + 2\ e^- \rightarrow H_2 + 2\ OH^-$ **(2.3)**

Ox.: $4\ OH^- \rightarrow O_2 + 2\ H_2O + 4\ e^-$ **(2.4)**

Addition of the two half-reaction pairs yields the same overall water splitting reaction **(2.5)**:[12]

$2\ H_2O \rightarrow 2\ H_2 + O_2$ **(2.5)**

2.1.2 Thermodynamic fundamentals

2.1.2.1 Cell potential

For a general cell reaction, the Gibbs free energy change of the reaction ($\Delta_r G$) can be written as

$$\Delta_r G = -nFE \quad \textbf{(2.6)}$$

where n is the number of electrons transferred in the reaction, F is Faraday constant (96 485 C mol^{-1}), E is the maximum potential between two electrodes, also known as the zero-current cell potential. It is the applied bias potential, so that no current is flowing through the cell. A point to note here is that, due to the minus sign in equation **(2.6)**, all spontaneous reactions (i.e. with $\Delta_r G < 0$) will have a positive equilibrium potential ($E > 0$), and vice versa. If there is a current flowing through an electrochemical cell as a result of a chemical process (i.e. the cell is discharging or behaving as a galvanic cell), then the potential difference between the electrodes, or cell voltage $E_{cell}^{galv} < E$, and if the current flows through an electrolysis cell, then the potential required to drive the cell $E_{cell}^{elec} > E$.

If the reactants and products of the cell reaction are in their standard states at the temperature of the transformation, i.e. the gases are at unit atmospheric pressure and the soluble species at unit mean activity, equation **(2.6)** can be written as

$$\Delta_r G^0 = -nFE^0 \quad \textbf{(2.7)}$$

In this case, $\Delta_r G^0$ is the standard free energy, and the potential is known as the standard cell potential (E^0) or the standard potential.

The reaction free energy $\Delta_r G$ varies with the composition of the reaction mixture by

$$\Delta_r G = \Delta_r G^0 + RT \ln Q \quad \textbf{(2.8)}$$

where R is the universal gas constant (8.3145 J mol^{-1} K^{-1}), T is the absolute temperature, and Q is the reaction quotient for the cell reaction which is formulated by writing the activities of the products in the numerator and that of the reactants in the denominator. By combining equations **(2.6)** – **(2.8)**, the obtained mathematical expression describing the cell potential at equilibrium is known as the Nernst equation:

$$E = E^0 - \frac{RT}{nF} \ln Q \qquad \textbf{(2.9)}$$

2.1.2.2 Half-cell potential

Considering the following half-cell reaction:

$$\mathrm{Ox} + n\ \mathrm{e}^- \rightleftharpoons \mathrm{Red} \qquad \textbf{(2.10)}$$

the half-cell electrode potential at equilibrium (ε) can be related to the standard electrode potential (ε^0) by the Nernst equation **(2.11)**:[35-36]

$$\varepsilon = \varepsilon^0 + \frac{RT}{nF} \ln \frac{a_{\mathrm{Ox}}}{a_{\mathrm{Red}}} \qquad \textbf{(2.11)}$$

where n is the number of transferred electrons involved in the half-cell reaction, and a_{Ox}, a_{Red} are the activities of the oxidizing agent and the reducing agent, respectively. The activity a for species i (a_i) is defined by $a_i = \gamma_i c_i$, where γ_i is the activity coefficient, and c_i is the mole fraction. At room temperature (25 °C), the Nernst equation is simplified by subsuming the universal gas constant and the Faraday constant, and is frequently expressed in terms of the base-10 logarithm, in which case it is written by equation **(2.12)**:

$$\varepsilon = \varepsilon^0 + \frac{0.059}{n} \lg \frac{a_{\mathrm{Ox}}}{a_{\mathrm{Red}}} \qquad \textbf{(2.12)}$$

Since the individual potential of a half-cell is not directly measurable, but only the difference of two half cells, the standard hydrogen electrode (SHE) is used as the reference point for all other half-cell reactions. The SHE consists of a platinized platinum electrode immersed in an aqueous solution with unit activity of H^+(aq) in contact with hydrogen gas at a pressure of one atmosphere. The potential of the SHE is defined arbitrary as zero at all temperatures. Each half-cell reaction has a specific standard potential, which is obtained as the standard cell potential versus the SHE. Common standard potentials for different electrodes (e.g. metal-ion, gas or redox) are supplied in tabulated form.[35] Accordingly, the standard electrode potentials for the water splitting half-reactions **(2.1)** to **(2.4)** are calculated to ε^0 (H^+/H_2) = 0 V, ε^0 (O_2/H_2O) = 1.23 V, ε^0 (H_2O/H_2) = - 0.83 V and ε^0 (O_2/OH^-) = 0.40 V. In an electrochemical cell, the potential difference between the two electrodes equals the cell potential:

$$E = \varepsilon_{\mathrm{cathode}} - \varepsilon_{\mathrm{anode}} \qquad \textbf{(2.13)}$$

Thus, the total potential difference provides the minimum bias potential of 1.23 V necessary for the water splitting reaction to take place.

By application of equation **(2.12)** to the HER and OER half-reactions, the electrode potentials at equilibrium (ε) versus the SHE are given by equations **(2.14)** and **(2.15)**:

HER: $\varepsilon = 0 - 0.059$ pH **(2.14)**

OER: $\varepsilon = 1.23 - 0.059$ pH **(2.15)**

It is important to note, that both potentials required to drive the cell reaction shift with the pH on the SHE scale. However, when we evaluate the performance of a catalyst for one of the two half-reactions with a potentiostat, the pH of the electrolyte must be considered. In this case, potential is applied for only one half-reaction, and the value will vary depending on the pH, as indicated by the diagram in **Figure 2.2**. In contrast, equilibrium potentials on the reversible hydrogen electrode (RHE) scale for the HER and OER are always at 0 and 1.23 V, respectively, regardless of the pH. Thus, the measured potentials are often given referenced to the RHE, which allows us to compare directly the position of a redox event of interest with the standard potentials of the HER and OER at any pH level.

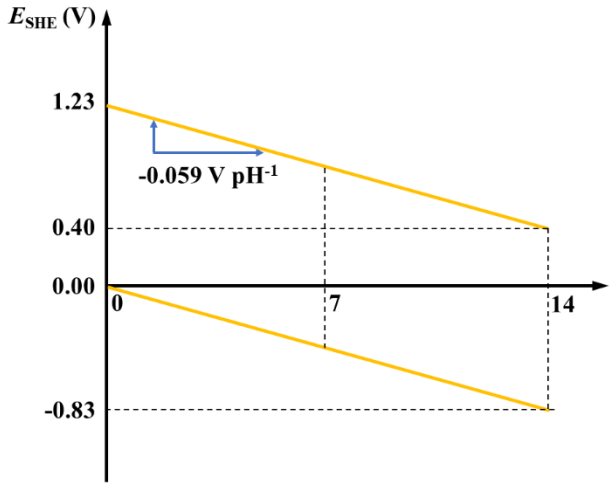

Figure 2.2 The dependence of half-cell electrode potentials (vs. SHE) on the pH of aqueous medium.[37]

2.1.3 Kinetics of electrode reactions

2.1.3.1 Overpotentials

As mentioned above, the minimum voltage required to drive the OER and HER (to split water) is known to be 1.23 V at standard condition. However, additional energy is demanded due to the internal resistance present in the cell system such as solution resistance and contact resistance, as well as the need to overcome the intrinsic activation barriers of electrode reactions. For each electrode, the difference between the experimentally observed electrode potential value (E_i) at a given current (i) and the value at equilibrium (no current, E_{eq}) is called overpotential (η):

$$\eta = E_i - E_{eq} \quad \textbf{(2.16)}$$

For a water splitting system, the overall operative voltage (V_{op}) can be expressed as

$$V_{op} = 1.23 + \Sigma\eta + iR \qquad \textbf{(2.17)}$$

where iR represents the ohmic drop occurring due to the internal resistance of the system, which can be minimized by optimizing the cell design; $\Sigma\eta$ is the sum over all overpotentials at the anode and cathode electrodes. For an electrode reaction, the overpotential can be considered as a sum of different overpotential contributions including the electron transfer overpotential (η_{CT}), the mass transport overpotential (η_{MT}) and the reaction overpotential (η_R), etc.[35]

At low currents, the rate of change of electrode potential with the current is associated with the limitation of electron transfer across the phase boundary between the electronically conducting electrode and the ionically conducting electrolyte, and it is termed the electron transfer overpotential. The electron transfer rate at a given overpotential has been found to depend on the nature of the species participating in the reaction, and also on the properties of the electrolyte and the electrode materials. At higher current densities, the primary electron transfer rate is usually no longer limiting; instead, limitations arise through slow transport of reactants from solution to the electron surface or conversely the slow transport of product away from the electrode (mass transport overpotential), in which the ionic transport governs the reaction process. The mass transfer of the ions may take place as diffusion induced by a concentration gradient, migration caused by the electric field, and convection arising from mechanical stirring or a density gradient in the liquid. In addition to the electron transfer and mass transport limitations on the rate of an electrochemical reaction, the presence of pre- or post-electron transfer chemical equilibria may also restrict the rate, especially in those regions where electron transfer and mass transport are expected to be intrinsically rapid. Examples include adsorption or desorption of species participating in the reaction or the participation of chemical reactions before or after the electron transfer step. This will lead to a reaction overpotential.

2.1.3.2 Electron transfer theory

Among the various factors affecting the reaction rates of an electrode, including electron transfer, mass transport and chemical processes, limitations due to the rate of electron transfer are unavoidable.[35] A classical theory for the reaction rate is based on the model of the activated complex, which describes the charge transfer by formation of a transition state (or an activated complex) with an activation energy of $\Delta G^{\#}$.[38] For a chemical process

$$A + B \xrightarrow{(AB)^{\#}} \text{products} \qquad \textbf{(2.18)}$$

The activated complex theory means that the free energy difference (or the activation energy) $\Delta G^{\#}$ between the reactants A + B and the transition state $(AB)^{\#}$ has to be overcome.[38] The $\Delta G^{\#}$ can be directly related to the reaction rate constant (k) via the Arrhenius equation:[38-39]

$$k = k^0 \exp\left(\frac{-\Delta G^{\#}}{RT}\right) \qquad \textbf{(2.19)}$$

where k^0 is the pre-exponential factor, a constant for each chemical reaction. The overall reaction rate can be expressed as

$$\upsilon = k\, c_A c_B = k^0 c_A c_B \exp\left(\frac{-\Delta G^{\#}}{RT}\right) \qquad \textbf{(2.20)}$$

where c_A and c_B are the concentrations of reactants A and B at the electrode surface. Obviously, any alteration in $\Delta G^{\#}$ will affect the reaction rate; small $\Delta G^{\#}$ will result in a high υ, and vice versa.

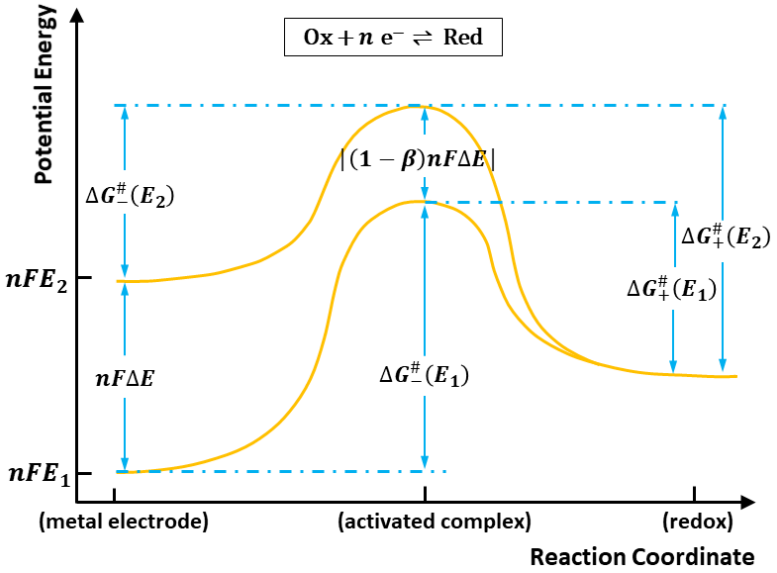

Figure 2.3 Potential energy diagram of an electrochemical reaction Ox + n e^- ⇌ Red. The electron has to be transferred from the inert metal electrode to an activated transition state (complex) before the redox reaction can be completed. $\Delta E = E_1 - E_2$, where the electrode potential E_2 is more negative than E_1.[35]

A similar case can be considered for an electrochemical reaction as shown by equation **(2.10)**. Using a metallic electrode and an electrolyte solution with a high ionic concentration, the change in potential between electrode and electrolyte is essentially limited to within the Helmholtz layer. Assuming that neither Ox nor Red species are adsorbed on the electrode surface, then their potential energy will not be influenced by an applied external potential. **Figure 2.3** demonstrates the potential energy shift between energy level E_1 and E_2 by applying a potential $\Delta E = E_1 - E_2$, where E_2 is more negative than E_1. The applied potential ΔE can alter the electrons' potential energy by a maximum value of $\Delta G = -nF\Delta E$, where F is the Faraday constant (96 485 C mol^{-1}), and n is the number of transferred electrons involved in the reaction. The electron needs to bring up the activation energy, and to form the activated complex before the reaction can proceed. For a process in a single step, there is only a fraction of the total free energy change $(1-\beta)|nF\Delta E|$ actually transferred to the activated complex. The factor β is called the 'asymmetry parameter', which describes the influence of the applied potential on the dynamic equilibrium between the redox reactions, ranging from 0 to 1. Thus, for the cathodic (reduction) reaction with the activation energy written as $\Delta G^{\#}_{-}$ as shown in

Figure 2.3, the activation energy at potential E_2 is:[35]

$$\Delta G_{-}^{\#}(E_2) = \Delta G_{-}^{\#}(E_1) + \beta nF\Delta E \qquad \textbf{(2.21)}$$

and the activation energy for the anodic (oxidation) reaction at potential E_2:[35]

$$\Delta G_{+}^{\#}(E_2) = \Delta G_{+}^{\#}(E_1) \; - \; (1-\beta)nF\Delta E \qquad \textbf{(2.22)}$$

According to equation **(2.20)**, the reaction rate can be determined, which in turn can be identified with the current density, providing the cathodic current density:

$$j^{-}(E_1) = \; - nFc_{\mathrm{Ox}}k_0'^{-} \exp\left[\frac{-\Delta G_{-}^{\#}(E_1)}{RT}\right] \qquad \textbf{(2.23)}$$

and with the potential varied from E_1 to E_2, the cathodic current density turns to:

$$j^{-}(E_2) = \; - nFc_{\mathrm{Ox}}k_0'^{-} \exp\left[-\frac{\Delta G_{-}^{\#}(E_1) + \beta nF\Delta E}{RT}\right] \qquad \textbf{(2.24)}$$

where $k_0'^{-}$ is the cathodic reaction rate constant, and c_{Ox} is the concentration of oxidized species, which is assumed to be constant by rapid transfer of Ox from solution to the surface. If the potential E_1 is defined as the zero point with respect to the reference electrode used in the experiment, then the value of $\exp\left[\frac{-\Delta G_{-}^{\#}(E_1)}{RT}\right]$ can be treated as a constant and incorporated into the reaction rate constant. Using E to replace E_2 and ΔE, the cathodic current density at potential E can be expressed as

$$j^{-}(E) = \; - nFc_{\mathrm{Ox}}k_0^{-} \exp\left(\frac{-\beta nFE}{RT}\right) \qquad \textbf{(2.25)}$$

Similarly, the anodic current density can be described as

$$j^{+}(E) = \; + nFc_{\mathrm{Red}}k_0^{+} \exp\left[\frac{(1-\beta)nFE}{RT}\right] \qquad \textbf{(2.26)}$$

where c_{Red} is the concentration of reduced species, and the values of the electrochemical rate constant k_0^{-} and k_0^{+} are dependent on the choice of the potential zero and hence the reference scale used. At the equilibrium potential (E_{eq}), when the net current is zero, the cathodic and anodic current densities are numerically equal to each other, and both have the magnitude of the so-called exchange current density (j_0), that is

$$j^{-}(E_{\mathrm{eq}}) = \; - j_0 = \; - nFc_{\mathrm{Ox}}k_0^{-} \exp\left(-\frac{\beta nFE_{\mathrm{eq}}}{RT}\right) \qquad \textbf{(2.27)}$$

$$j^{+}(E_{\mathrm{eq}}) = \; + j_0 = \; + nFc_{\mathrm{Red}}k_0^{+} \exp\left[+\frac{(1-\beta)nFE_{\mathrm{eq}}}{RT}\right] \qquad \textbf{(2.28)}$$

Equating these two, E_{eq} can be expressed as

$$E_{\mathrm{eq}} = \frac{RT}{nF}\ln\frac{k_0^{+}}{k_0^{-}} + \frac{RT}{nF}\ln\frac{c_{\mathrm{Ox}}}{c_{\mathrm{Red}}} \qquad \textbf{(2.29)}$$

which is obviously identical to the Nernst equation **(2.11)** for $E_0 = \frac{RT}{nF}\ln\frac{k_0^+}{k_0^-}$. If the actual electrode potential E is written as $(E_{eq} + \eta)$, where η is the overpotential, according to equations **(2.27)** and **(2.28)**,

$$j^-(E) = -nFc_{Ox}k_0^- \exp\left(-\frac{\beta nFE_{eq}}{RT} - \frac{\beta nF\eta}{RT}\right) \qquad \textbf{(2.30)}$$

$$j^+(E) = +nFc_{Red}k_0^+ \exp\left[+\frac{(1-\beta)nFE_{eq}}{RT} + \frac{(1-\beta)nF\eta}{RT}\right] \qquad \textbf{(2.31)}$$

From the definition of the exchange current density and calculated with equations **(2.27)** and **(2.28)**, equations **(2.30)** and **(2.31)** can be arranged as

$$j^-(E) = -j_0 \exp\left(-\frac{\beta nF\eta}{RT}\right) \qquad \textbf{(2.32)}$$

$$j^+(E) = j_0 \exp\left[\frac{(1-\beta)nF\eta}{RT}\right] \qquad \textbf{(2.33)}$$

The net current density for a reversible electrode reaction is

$$j = j^- + j^+ = j_0\left\{\exp\left[\frac{(1-\beta)nF\eta}{RT}\right] - \exp\left(-\frac{\beta nF\eta}{RT}\right)\right\} \qquad \textbf{(2.34)}$$

the famous Butler-Volmer equation,[35] which is at the base of the treatment of electrochemical kinetics.

The resulting current voltage behavior of the redox reaction is displayed in **Figure 2.4a**. In case of $\beta = 0.5$, the half reaction current densities are symmetric to each other. For asymmetric cases, $\beta > 0.5$ means that the slope of the cathodic current density is steeper than the slope of the cathodic curve, and $\beta < 0.5$ describes the opposite case. At large overpotentials $|\eta| >> RT/nF$ (≈ 25.7 / n mV at 25 °C), where the electrode reaction becomes irreversible, equation **(2.34)** can be simplified as[35]

$$\lg|j| = \lg j_0 + \frac{\beta nF}{2.303RT}|\eta| \qquad \textbf{(2.35)}$$

for the cathodic reactions or

$$\lg j = \lg j_0 + \frac{(1-\beta)nF}{2.303RT}\eta \qquad \textbf{(2.36)}$$

for anodic reactions. Equations **(2.35)** and **(2.36)** can be further arranged as

$$\eta = a + b\lg|j| \qquad \textbf{(2.37)}$$

This is so-called Tafel equation, with $a = \left(\frac{2.303RT}{\beta nF}\right)\lg j_0$ or $-\frac{2.303RT}{(1-\beta)nF}\lg j_0$, and $b = -\left(\frac{2.303RT}{\beta nF}\right)$ or $\frac{2.303RT}{(1-\beta)nF}$ for the cathodic and anodic reactions, respectively. A Tafel plot with $\beta = 0.5$ is illustrated in **Figure 2.4b**.

The Tafel plot is often used to evaluate the electrocatalytic performance of a catalyst. The Tafel slope b is a measure of how efficiently the electrode responds to an applied potential to produce current: the smaller the Tafel slope, the better the performance. Besides, Tafel plots allow the linear section extrapolated to $\eta =$

0, i.e., to equilibrium potential, with the intercept giving the exchange current density (j_0). It can be considered as a measure of how vigorously the anodic and cathodic reactions occur during dynamic equilibrium. If j_0 is large enough, the system can provide large current even at very low η, which means the activation of the overall reaction is easy with fast electrode kinetics.

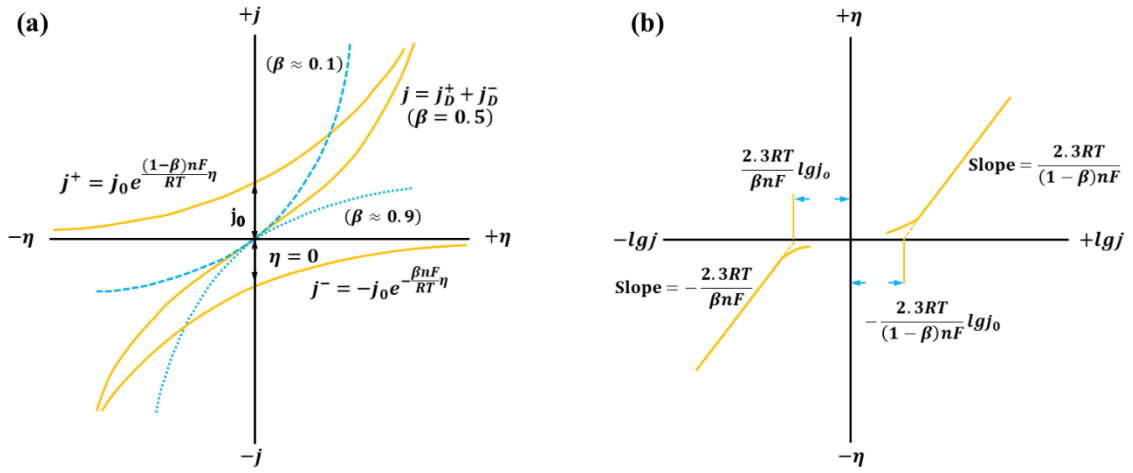

Figure 2.4 (a) Illustration of the Butler-Volmer dependence of the current density j on the overpotential η and (b) the Tafel plot with asymmetry parameter $\beta = 0.5$.[35]

Although the Tafel equation is widely accepted and applied to basically any kind of electrodes, the Butler-Volmer equation was originally developed for metal electrodes and a simple one electron transfer. Therefore, its applicability to electrodes that are not strictly metals and to reactions involving multiple electrons transfer should be considered with care. The electrocatalysts described in the following sections are oxides, hydroxides, oxyhydroxide and many other materials whose behaviors in terms of kinetics will be probably somewhere between that of metals and that of molecular species. It is still important to note, that neither tunneling nor electronic states from intermediate adsorbates are considered. Moreover, the Butler-Volmer equation is often accurate for low current densities, but other factors may come into play at higher current densities or larger overpotentials.

2.1.3.3 Multistep reactions

Most electrochemical reactions involve multiple electrons transfer and a series of consecutive reaction steps with the formation of different intermediates (e.g. the HER and the OER). The set of all intermediate steps is called the reaction pathway, which can be either electron transfer steps or chemical steps such as association or dissociation reactions. On the basis of the validity of equations **(2.34)** and **(2.37)** for all heterogeneous electrocatalysts, the Tafel slope can be used to infer which reaction step is the rate-limiting one, and therefore how is the mechanism of reaction.[40-41] For a multistep reaction, the Tafel slope for the overall reaction is generally described as

$$b = \frac{2.303RT}{\alpha' F} \qquad \textbf{(2.38)}$$

where α' is the charge transfer coefficient for the overall reaction.[42] Deduced from the microkinetics, the apparent α' is a composite value linked to different elementary steps, and it is not only contributed by the charge transfer coefficient (α, $\alpha + \beta = 1$) of the rate-determining step (RDS, an elementary step with the most sluggish kinetics) but also the number of electrons transferred before the RDS.[42-43] Derived by Bockris and Reddy,[44] the transfer coefficient α' for a multiple-electron transfer reaction can be calculated by equation **(2.39)**:

$$\alpha' = \frac{n_f}{v} + n_r\alpha \qquad \textbf{(2.39)}$$

where n_f is the number of electrons that transfer before the RDS, v is the number of occurrences of the RDS in the overall reaction, n_r is the number of electrons that participate in the RDS, and α is typically taken as 0.5 for single-electron transfer steps or 0 for chemical steps without electron transfer. This equation shows the predictive power for predicting the RDS.[42, 45-46] For example, if the first electron transfer reaction is the rate-determining step, the values of n_f is equal to 0 while v, n_r and α are 1, 1 and 0.5, respectively. Then the apparent transfer coefficient α' is 0.5 and the corresponding Tafel slope, at 25 °C (T = 298.15 K), is calculated to be 120 mV dec^{-1} (similar to a single electron transfer reaction) . If the rate-determining step is a chemical reaction without electron transfer and follow after a one-electron transfer step, the values of n_f and v are both equal to 1 while the value of n_r is 0. Consequently, the α' is 1 and the Tafel slope becomes 60 mV dec^{-1}.

Nevertheless, some important facts on Tafel slope have been collected based on the experimentally obtained Tafel kinetics data. First, the values of Tafel slope may not be well consistent with the classical values as predicted. In this case, knowledge on the reaction mechanism of the multistep electrocatalytic reaction under study is required for the further interpretation of the kinetic data. Second, the measured Tafel slope, for some systems, can vary due to different experimental conditions. For example, the reported Tafel slope for the HER on Pt (111) ranges from 30 to 74 mV dec^{-1}, and on Pt (100) it is from 30 to 112 mV dec^{-1}.[47-48] The experimental results reveal a complex nature of electrocatalytic reactions depending on the used electrode. The factors such as the solution environment and the presence of surface defects may also strongly influence the Tafel kinetics. Moreover, the Tafel slope is dependent on the potential and an abrupt change of Tafel slope at a certain potential has been observed in electrocatalytic reactions. For instance, the Tafel slope of the OER on RuO_2 and the ORR on Pt shifts from ≈ 120 mV dec^{-1} at high η to ≈ 60 mV dec^{-1} at low η.[40, 49] The shift is often regarded as an indicator of the change in reaction mechanism (e.g. RDS) due to the variation of reaction conditions such as the intermediate coverage and surface morphology induced by the electrical potential. Thus, it has been recognized the Tafel equation alone is often not sufficient to interpret the mechanism of complex electrochemical reactions.

2.2 The hydrogen evolution reaction (HER)

2.2.1 Reaction mechanism and kinetics

The hydrogen evolution reaction (HER) is the cathodic part of the overall water splitting reaction with the transfer of two electrons for one molecule of hydrogen. It is described to proceed with one catalytic intermediate, H* (where * represents an active site on the electrode surface), and may occur via either the Volmer-Heyrovsky or the Volmer-Tafel mechanism.[13, 17, 50] The mechanism by which the HER proceeds is strongly dependent on the type of electrolyte, the inherent surface chemistry and electronic structure of a catalyst, and it is usually determined by the experimentally obtained Tafel slope value.[51-54] The overall equation and the involved reaction steps of the HER are summarized in **Table 2.1**.

Table 2.1 Overall reaction pathways for the HER in acidic and alkaline solutions.[13, 17]

Overall reaction (Condition)	**Reaction pathway**	
$2\ H^+ + 2\ e^- \rightarrow H_2$	$H^+ + e^- + *^{[a]} \rightarrow H^*$	(Volmer)
(Acidic solution)	$H^+ + e^- + H^* \rightarrow H_2 + *$	(Heyrovsky)
	or $2\ H^* \rightarrow H_2 + 2\ *$	(Tafel)
$2\ H_2O + 2\ e^- \rightarrow H_2 + 2\ OH^-$	$H_2O + e^- + * \rightarrow H^* + OH^-$	(Volmer)
(Alkaline solution)	$H_2O + e^- + H^* \rightarrow H_2 + OH^- + *$	(Heyrovsky)
	or $2\ H^* \rightarrow H_2 + 2\ *$	(Tafel)

[a] * represents a binding site at the electrode surface.

The first step in acidic media is the discharge of protons on the electrode surface to form adsorbed hydrogen atoms (H*) by the combination of a proton transferred from the electrolyte with an electron transferred through the electrode surface (Volmer reaction). The Tafel slope for the Volmer reaction ($b_{1,v}$) can be described as[52]

$$b_{1,V} = \frac{2.303RT}{\alpha F} \qquad \textbf{(2.40)}$$

where R is the ideal gas constant (8.3145 J mol^{-1} K^{-1}), T is the absolute temperature, α is the charge transfer coefficient (typically taken as 0.5), and F is the Faraday constant (96 485 C mol^{-1}). In contrast to the acidic environments where a large number of protons are available to promote the reaction,[55-56] the hydrogen intermediate (H*) in alkaline solutions is formed by an initial water dissociation process in the Volmer reaction.[55] This additional step may bring an extra energy barrier and probably affect the overall reaction rate.[57] Depending on the coverage of adsorbed hydrogen (H*), there are two possible steps for the HER to proceed either by electrochemical H_2 desorption, known as the Heyrovsky step, or by chemical desorption of H_2, known as the Tafel step.[52] If the coverage of H* is low and the electrode surface has sufficient active

sites near the H* sites, the adsorbed H atoms will preferably bind to a nearby proton, which is simultaneously reduced to H, to evolve a hydrogen molecule. This is the so-called Heyrovsky step, and its Tafel slope ($b_{2,H}$) can be given by

$$b_{2,H} = \frac{2.303RT}{(1+\alpha)F} \qquad \textbf{(2.41)}$$

In case of high H* coverage, two adjacent H* will chemically bind together and release one hydrogen molecule. This is the Tafel step, and its Tafel slope can be expressed as

$$b_{2,T} = \frac{2.303RT}{2F} \qquad \textbf{(2.42)}$$

At 25 °C (i.e. T = 298.15 K), values of the Tafel slopes for the Volmer, Heyrovsky, and Tafel reactions have been calculated to be 118 mV dec^{-1}, 39 mV dec^{-1}, and 29 mV dec^{-1}, respectively. Utilizing the Tafel slope values as reference, one can roughly analyze the reaction route and the rate-determining step on a catalyst in a specific electrolyte.[51-55]

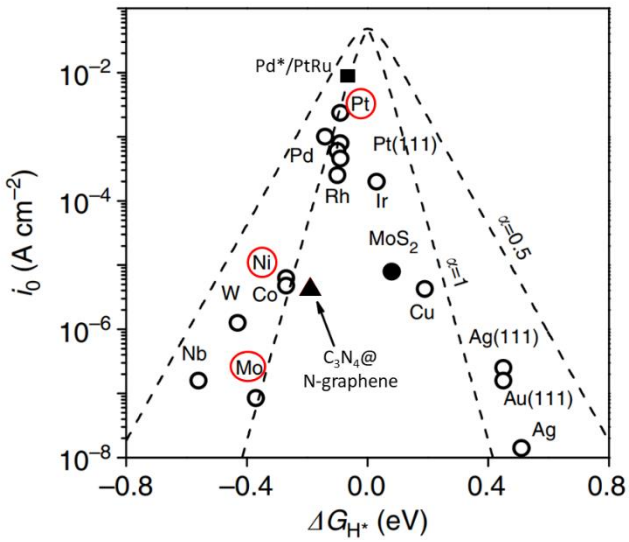

Figure 2.5 Volcano plot of the exchange current density against the DFT-calculated hydrogen adsorption free energy for the surfaces of various metals, alloy compounds, and non-metallic materials in acidic medium.[13, 58-59]

The overall reaction rate for the HER is largely determined by the hydrogen adsorption free energy (ΔG_{H^*}).[14, 60-61] If hydrogen binds to the catalytic surface too weakly, the adsorption (Volmer) step will limit the overall reaction rate; whereas if the binding is too strong, the desorption (Heyrovsky or Tafel) step will limit the rate; moderate adsorption energies permit a compromise between the extremes.[14, 60-61] In recent years, the density functional theory (DFT) calculated ΔG_{H^*}/hydrogen binding energy (ΔE_{H^*}) on the catalytic surface has been widely used as a reasonable descriptor for the catalytic activity of the hydrogen evolution materials.[14, 60-61] Plotting the logarithm of the measured exchange current densities (i_0) versus the calculated ΔG_{H^*} for a wide range of catalyst materials (including many traditional metals, metal composites/metal

alloys, and non-metallic materials) in acidic solutions, a volcano shaped curve is obtained (**Figure 2.5**). It is a quantitative illustration of the so-called Sabatier principle, which states that the optimal catalytic activity can be achieved by a catalyst surface with an appropriate binding energy for the reactive intermediate.[61-64] The volcano plot has been used as a guiding principle to design HER catalysts, predicting that materials with an optimal adsorption energy (neither too strong nor too weak) will show the highest activity as well as be at the top of volcano such as the platinum.[55]

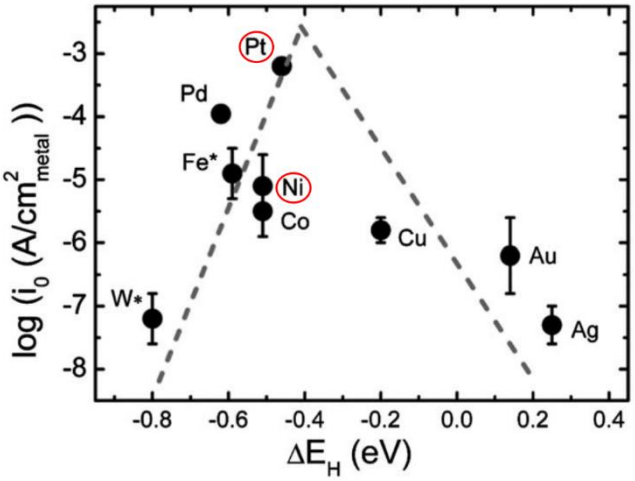

Figure 2.6 Logarithm of exchange current densities as a function of the calculated hydrogen binding energy on monometallic surfaces in alkaline solution. The i_0 values for non-Pt metals were obtained by extrapolation of the Tafel plots between -1 and -5 mA $cm^{-2}_{geometric}$ to the reversible potential of the HER and then normalization by the electrochemical surface areas (ECSA) of these metal surfaces.[65]

An important consideration when the surface-dependent HER is analyzed is the pH of the solution at which the reaction proceeds. To investigate the behavior of the HER activity in alkaline solution, Sheng et al. studied the HER activities on a series of monometallic surfaces under such conditions, demonstrating that the exchange current density of the HER can be also related to the calculated hydrogen binding energies values of the metallic surfaces via a Volcano type of relationship (**Figure 2.5**).[65] Similar to the case in acidic medium, Pt is still at the summit of the Volcano plot. W, Fe, Ni, Co and Pd are located on the left-branch for their too strong hydrogen adsorption energies, while the opposite is true for Cu, Ag and Au. The HER activity of a metal in alkaline media decreases by several orders of magnitude as its hydrogen binding energy deviates from that of Pt, thus strongly suggesting that the hydrogen binding energy on the catalytic surface can be also a useful descriptor for identifying the HER reaction rate in alkaline environments.[14, 60-61] However, the reliability of the volcano plots as the descriptor for the HER is controversial because of the uncertain surface properties of some metals used to catalyze the HER.[66] For instance, the surfaces of metals such as Ni and W can be easily covered with in situ formed oxide films, which will obscure the real activities of the metals towards the HER.[67] Moreover, the OH^- in the solution phase from the alkaline media is

observed to largely influence the hydrogen binding energy via adsorption on the active sites and conversely affecting the HER activity.[68] Therefore, a direct relationship between the hydrogen binding energy on the catalytic surface and HER activity is occasionally misleading.

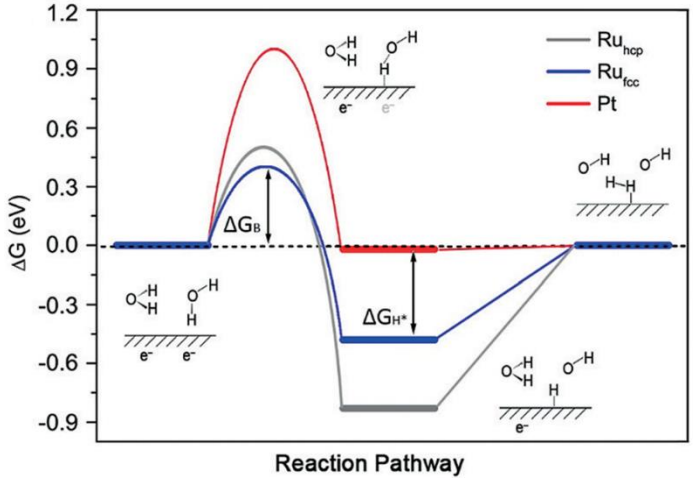

Figure 2.7 Gibbs free energy (ΔG) diagram of alkaline HER on the surfaces of hexagonal close-packed (hcp) Ru (0001), face-centered cubic (fcc) Ru (111) and fcc Pt (111) including reactant initial state, intermediate state, final state, and an additional transition state representing water dissociation. ΔG_{H^*} denotes hydrogen adsorption free energy, and ΔG_B indicates the free energy barrier for water dissociation.[69]

To further explore the HER mechanism under alkaline conditions, Zheng et al. recently performed DFT calculations associated with the thermodynamics and kinetics of alkaline HER on different metal surfaces.[69] The calculated ΔG diagram (**Figure 2.7**) indicates that aside from the thermodynamic ΔG_{H^*}, the kinetic barrier to water dissociation may also control the overall reaction rate of HER in alkaline solutions.[69] Taking the most well-studied Pt (111) and Ru (0001) surfaces as example, under pH 13 condition, the Pt (111) surface possesses an optimal ΔG_{H^*} close to zero, but its high barrier to water dissociation limits the apparent HER activity. On the contrary, Ru_{hcp} has a low barrier to water dissociation, but its relatively strong hydrogen adsorption energy (negative ΔG_{H^*}) inhibits the desorption of products.[57, 69] This behavior can be described by the Brønsted-Evans-Polanyi (BEP) relationship, showing that the activation energy of a process is linearly dependent on the enthalpy of the reaction.[57] Correspondingly, the BEP relationship is embodied in the water dissociation process, which generates H* and OH*.[70] Obviously, a low water dissociation barrier demands strong enough H/OH adsorption on the surface. Thus, from a microscopic point of view, three major factors are identified to govern the apparent HER activity under alkaline conditions: appropriate (not too weak nor too strong) H-binding and/or OH-binding energies, and low barrier to water dissociation. Quantitative analysis on the contribution of each factor to the overall reaction rate has not been reached, yet. As a result, the descriptor of the HER activity in alkaline solution is still being debated: Is it the free energy of hydrogen adsorption, the water dissociation barrier, or both of them

to play a role in the determination of the overall rate. A thorough understanding of the HER catalysis is highly desirable that can guide us to design and tailor non-noble materials along with their hetero-nanostructures as highly efficient electrocatalysts for the HER.

2.2.2 HER on Ni-based electrocatalysts

Among the various non-precious catalyst materials, metallic Ni showing a small ΔG_{H^*} value and a high HER exchange current density (see **Figure 2.5**) has been considered as a promising candidate for the HER electrocatalysis.[62] Therefore, a lot of Ni-based HER electrocatalysts has been explored in recent decades. The electrocatalytic activities of some representative catalysts are summarized in **Table 2.2**.

.

Table 2.2 Summary of the electrocatalytic activity of representative Ni-based HER catalysts, with values for Pt/C provided for comparison.

Electrocatalyst	Substrate	Loading mass [mg cm^{-2}]	Electrolyte	Current density [mA cm^{-2}]	Overpotential [mV]	Tafel slope [mV dec^{-1}]	Ref.
Ni nanoparticles	glassy carbon	0.35	1 M NaOH	10	180	111	71
3DOM/m Ni	glassy carbon	≈0.25	1 M NaOH	10	171	52	72
Ni dendrites	glassy carbon	0.0043	6 M KOH	10	≈300	102.7	73
Ni-Mo nanopowder	Ti foil	1.0	2 M KOH	20	70	-	74
Ni-Mo nanopowder	Ti foil	3.0	0.5 M H_2SO_4	20	80	-	74
$MoNi_4/MoO_2$	Ni foam	≈43.4	1 M KOH	10	≈15	30	75
NiFe LDH-NS@DG[a]	glassy carbon	0.28	1 M KOH	10	300	110	76
NiFe LDH-NS@DG[a]	Ni foam	2	1 M KOH	20	115	-	76
SL $Ni(OH)_2$-Pt/C	GC-RDE	-	0.1 M KOH	5	157	-	77
SL $Ni(OH)_2$-Pt/C	GC-RDE	-	0.1 M LiOH	5	121	-	77
$Ni(OH)_2$-PtO_2	Ti mesh	1.48	0.1 M KOH	4	31.4	89	78
Ni-Mn_3O_4	Ni foam	-	1 M KOH	10	91	110	79
Ni/NiO	Ni foam	0.30	1 M KOH	5	110	43	80
NiO/Ni-CNT	Ni foam	0.28	1 M KOH	10	80	82	81
Ni@NiO-Cr_2O_3	Ni foam	24	1 M KOH	100	115	-	82
A-Ni–C	glassy carbon	≈0.283	0.5 M H_2SO_4	10	34	41	83
Ni_3N	Ni foam	1.9	1 M KOH	10	121	109	84
Ni_3N	Ni foam	1.9	1 M PBS[b]	10	234	230	84
Ni_3N	Ni foam	1.9	0.5 M H_2SO_4	10	145	94	84
$NiMoN_x/C$	glassy carbon	0.25	0.1 M $HClO_4$	3.5	200	35.9	85
MoS_2@Ni	carbon cloth	7.8	1 M KOH	10	91	89	86
Ni_5P_4/Ni	Ni foil	3.475	1 M KOH	10	150	≈53	87
Ni_5P_4/Ni	Ni foil	3.475	0.5 M H_2SO_4	10	140	≈40	87
NiS microsphere	Ni foam	43	1 M KOH	10	≈125	83	24
NiSe nanowire	Ni foam	2.8	1 M KOH	10	96	120	88
$NiSe_2$/Ni	Ni foam	119	0.5 M H_2SO_4	10	143	49	23
Pt/C	glassy carbon	0.28	0.5 M H_2SO_4	20	≈50	30	89
Pt/C	glassy carbon	0.283	1 M KOH	10	≈75	64	76

[a] DG: defective graphene; [b] PBS: phosphate buffer solution.

Many of the electrocatalysts are reported to exhibit excellent HER catalytic activity in acidic media. However, the lack of non-noble electrocatalysts for the oxygen evolution reaction has limited the development of cost-effective water splitting devices in acidic conditions,[90] while the presence of highly active oxygen evolution electrocatalysts that can be used in alkaline solutions has stimulated the development of novel structures based on non-noble metal for the HER catalysis in alkaline medium.[91] Moreover, alkaline electrolytes due to their lower vapor pressure evaporate less gases even under high temperature conditions, which favors the production of pure hydrogen gas.[55, 79] Last but not least, non-noble transition metals possess a better stability in alkaline solutions with less corrosion and dissolution. Hence, the use of alkaline solutions is much more attractive than working under acidic conditions.[55, 92]

Herein, the Ni-based HER electrocatalysts for the HER in alkaline solutions will be systematically discussed, including nanostructured metallic Ni, Ni-based alloys as well as Ni oxide/hydroxide-based heterostructures. The information concerning other Ni-based catalytic systems, such as chalcogenides, carbides, borides and nitrides can be found in the review articles[2, 17, 20, 55] and will not be discussed here.

(i) Nanostructured nickel metal

The emergence and rapid development of nanotechnology has provided us with a variety of synthetic methods to build nanostructures with a uniform size and morphological distribution.[93-95] For electrocatalysis the current density at a given overpotential can be dramatically improved by the significantly higher surface area afforded by the nanostructures due to the increased number of accessible active sites for the reactants. Therefore, considerable efforts have been made in recent years to enhance the catalytic performance of metallic Ni toward the HER by nanostructuring and surface engineering to maximize the number of catalytical active sites and facilitate a larger mass transport. For instance, various nano-sized metallic Ni materials, such as 3D-ordered macro/mesoporous Ni,[72] Ni dendrites,[73] and urchin-like Ni nanoparticles,[71] have been synthesized for efficient HER. However, the various Ni nanostructures exhibit a very similar electrochemical behavior owing to their identical chemical nature. The current density increases almost linearly with the increase in their surface areas.

(ii) Nickel-based alloys

Ni structures with higher active surface areas can be expected to show better HER activities, but it would still be restricted by metallic Ni's intrinsic catalytic activity. Therefore, to further improve the catalytic activity, researchers have started to tune the chemical environment of Ni besides taking advantage of Ni-based nanostructures with high surface areas. An effective method for tuning the chemical properties as well as the HER catalytic activity of metallic Ni is to introduce additional metal elements to form Ni-based alloys. An adjacent hetero-atom can alter the surface adsorption/desorption energy on the nearby Ni atom, and it may also provide adsorption/desorption sites for certain intermediates to accelerate the catalytic process of the HER. Brown et al. first studied a series of alloys as HER catalyst candidates.[96] Thereafter, for the same purpose, Aruraj et al. investigated Ni-based binary and ternary alloy co-deposits prepared by

electrodeposition methods. It was shown that their electrocatalytic effects for the HER rank in the order of Ni-Mo > Ni-Zn (after leaching Zn) > Ni-Co > Ni-W > Ni-Fe > Ni-Cr > Ni plated steel,[97] while the corresponding rank of Ni-Mo-based ternary alloys followed the trend Ni-Mo-Fe > Ni-Mo-Cu > Ni-Mo-Zn > Ni-Mo-Co ~ Ni-Mo-W > Ni-Mo-Cr.[98] From then on, other controlled electrodeposition methods of Ni-based alloys have been developed for the HER catalysis.[99-101]

With the optimum d-orbital overlap in the intermetallic phase, Ni-Mo-based alloy electrocatalysts (Ni_xMo_y) have achieved noble-metal-like catalytic activity for the HER.[13, 102-103] They are considered as promising candidates to effectively accelerate the sluggish HER kinetics under alkaline conditions. For example, very recently, Zhang et al. reported a $MoNi_4$ electrocatalyst supported by MoO_2 cuboids on Ni foam exhibiting a Pt-like catalytic activity.[75] The superior HER catalytic activity was achieved by a large reduction of the energy barrier of the Volmer step for the $MoNi_4$ nanoparticles, a high catalyst loading and a three-dimensional substrate structure. Even so, the detailed explanation of the improved HER catalytic activity reached by surface alloying with hetero-atoms remains unclear and needs to be further investigated. Elucidating the oxidation states of Ni and other hetero-atoms, along with the surface adsorption behavior of the reactants and intermediates, could help to clarify the role of surface alloying and assist the further optimization of HER catalysts through chemical design (e. g. doping, alloying, variation of chemical composition).[14, 20]

(iii) Nickel oxide/hydroxide-based heterostructures

As mentioned above, one intrinsic disadvantage of alkaline HER is the requirement for an additional step of water dissociation for the Volmer reaction. This is usually revealed by catalytic activities of about two or three orders of magnitudes lower than that in acidic solution. Recently, researchers have experimentally proved that the alkaline HER activity can be improved by developing composite materials to facilitate different steps of the overall HER process in alkaline environments: an oxide to provide the active sites for dissociation of water, and a metal to facilitate adsorption of the produced atomic hydrogen and its subsequent recombination to form H_2 from these intermediates.[66, 104-105] As an example, the Markovic group developed a $Ni(OH)_2$-decorated Pt catalyst, which increases the HER activity of pure Pt by a factor of ~8 at an overpotential of -0.1 V (**Figure 2.8a**). The catalytic process is schematically shown in **Figure 2.8b:** Water dissociation occurs at the edges of $Ni(OH)_2$ clusters to form hydrogen intermediates; Subsequently, the produced hydrogen intermediates adsorb on the neighboring Pt active sites and recombine to yield hydrogen molecules, which are then released. From a theoretical perspective, Zeng et al. recently verified this synergistic catalysis process by simulating water dissociation and hydrogen adsorption processes at the three-phase boundary of $Ni(OH)_2$/Pt(111)/H_2O.[106]

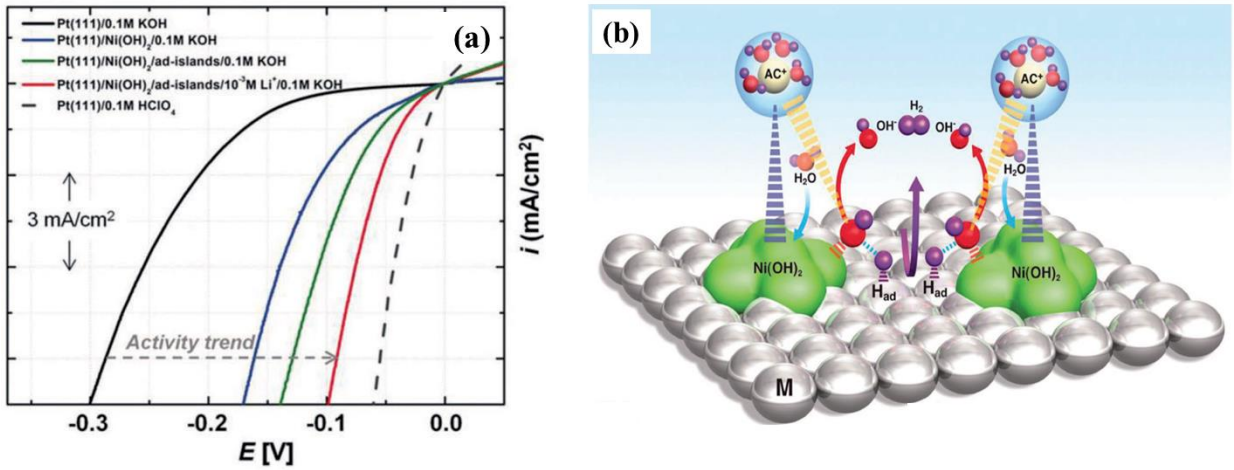

Figure 2.8 (a) Comparison of HER activities with Pt (111) as the substrate. The activity for the unmodified Pt(111) surface in 0.1 M $HClO_4$ is shown for reference.[104] (b) Schematic representation of water dissociation and hydrogen evolution on a $Ni(OH)_2$ decorated Pt catalyst surface.[104]

The improvement in catalytic activity achieved by incorporation of $Ni(OH)_2$ was also employed for other surfaces, such as Pt(110) and nano-Pt, indicating that the $Ni(OH)_2$/M interfaces could function as a general system to optimize the HER activity under alkaline conditions.[104] Following this strategy, the group further developed various $Ni(OH)_2$/M (M = Cu, Ag, Au, Ru, Ir, Pt, Ni, V and Ti) surfaces by constructing $Ni(OH)_2$ nanoclusters on different metal sites and observed an enhancement of the HER activity over the pure metal sites, matching the HER activity trend of pure metals established in acidic media (see **Figure 2.5**).[66] Specifically, the activity of $Ni(OH)_2$/Ni structure is enhanced by about four times compared to that of $Ni(OH)_2$ free-Ni metal surface.[66] Moreover, Gong et al. created nanoscale nickel oxide-nickel (NiO/Ni) heterostructures on carbon nanotubes (CNT), which showed a high catalytic activity for the HER similar to that of platinum.[81] By comparing the HER activity with those of pure Ni/CNT and NiO/CNT, the NiO/Ni nano-interfaces displayed significant advantages: They achieved a current density of 10 mA cm^{-2} at an overpotential of less than 100 mV under a loading of about 0.28 mg cm^{-2} on glassy carbon, and 100 mA cm^{-2} at an overpotential of less than 100 mV under a loading of about 8 mg cm^{-2} in Ni foam. With regard to the possible mechanism it was suggested, that the OH^- anions generated by the Volmer step preferentially attach to the NiO sites at the NiO/Ni interface, and the H atoms move to adjacent Ni metal sites for recombination to produce hydrogen molecules. Pure NiO surfaces are not good at catalyzing the HER because of its incapability to stabilize the H atoms, while pure Ni surfaces will eventually be occupied by the generated OH^- anions, therefore blocking the active sites.

Therefore, although bulk Ni oxide and hydroxide have been generally considered as inactive HER materials because of their unsuitable hydrogen atom adsorption energy (excessively strong adsorption of H on O, but extremely weak adsorption of H on Ni), the electronic structures of the Ni-based oxides can be adjusted in a way to form appropriate surfaces for efficient HER catalysis.[91] The usage of $Ni(OH)_2$/M and NiO/M interfaces provides opportunities for an enhancement of the electrocatalytic activity by employing an

appropriate combination between the metal oxide/hydroxide and metal content.

In summary, with the aim of replacing precious-metal materials, researchers have invested extensive efforts in development of efficient HER electrocatalysts through nanostructuring and surface engineering to maximize the catalytically active sites; modifying electronic properties by fabricating alloys and by tailoring oxide/hydroxide-metal interfaces; and by doping C/N/P/S/Se into metal lattices to achieve Pt-like HER catalytic properties.

In addition to the catalytic activity, long-term stability is another important concern for the electrocatalysts.[107-109] Generally, three important sources for degradation of catalyst performance over time have been identified:

1) Corrosion, a concern for any material, often taking its effect on electrode activity over a long time period.
2) Poisoning by solution impurities, which can significantly deactivate a catalyst even with very small amounts of deleterious material present.
3) Changing in chemical composition or surface morphology, by which the catalyst activity can be diminished.

These degradation effects can take place over short- or long-time scales, e.g. hydrogen absorption on Ni, which begins instantly and progresses as the electrode is continually being used, leading to a remarkable increase of the Tafel slope with a corresponding decline of efficiency.[110] The degradation mechanisms depend to a great extent on the exact conditions under which the electrode is operated, including the composition and pH of the electrolyte, the cell housing, the temperature, the potential, and the current density of the specific operating conditions. General approaches can be used to avoid the rapid catalyst deterioration, but well-defined procedures must be developed individually for each set of material system and operating conditions to fully minimize these deleterious effects.[12]

2.3 The oxygen evolution reaction (OER)

2.3.1 Reaction mechanism and kinetics

The anodic-half cell reaction, oxygen evolution reaction (OER), is a far more complex process, which involves either four-electron ($4e^-$) or two-step two-electron ($2e^-$) transfer. Many research groups have proposed possible reaction mechanisms for oxygen evolution under either acid or alkaline conditions. The generally accepted overall reaction equations for the OER are listed in **Table 2.3**.[13, 43, 111-113] The proposed reaction mechanisms of the OER proceed through the initial elementary steps of water or hydroxide ion adsorption in acidic or alkaline solution on the catalytically active site (*). In the second step, the adsorbed hydroxide ions (*OH) form oxygen moieties (*O). For the following steps there are two different approaches to form O_2(g) from the *O intermediates: Either the direct combination of two adjacent *O

intermediates to produce O_2(g), or the formation of a peroxide (*OOH) intermediate (3rd electron transfer), which subsequently decomposes after the fourth electron transfer process to release O_2(g).[43, 111-112]

Table 2.3 Proposed reaction mechanisms for the OER in acidic and alkaline solutions.[13, 43, 111-112]

Overall reaction (Condition)	**Reaction pathway**
$2\ H_2O \rightarrow O_2 + 4\ H^+ + 4\ e^-$ (Acidic solution)	$H_2O + *^{[a]} \rightarrow *OH + H^+ + e^-$ $*OH \rightarrow *O + H^+ + e^-$ $2\ *O \rightarrow 2* + O_2$ or $*O + H_2O \rightarrow *OOH + H^+ + e^-$ $*OOH \rightarrow *O_2 + H^+ + e^-$ $*O_2 \rightarrow O_2 + *$
$4\ OH^- \rightarrow O_2 + 2\ H_2O + 4\ e^-$ (Alkaline solution)	$OH^- + * \rightarrow *OH + e^-$ $*OH + OH^- \rightarrow H_2O + *O + e^-$ $2\ *O \rightarrow 2* + O_2$ or $*O + OH^- \rightarrow *OOH + e^-$ $*OOH + OH^- \rightarrow *O_2 + H_2O + e^-$ $*O_2 \rightarrow O_2 + *$

[a] * represents a binding site at the electrode surface.

The kinetic barriers related to each elementary step contribute to the overall required activation overpotential. Generally, overpotential (η), exchange current density (j_0), and Tafel slope (b) are the parameters used to evaluate the reaction kinetics of an OER electrocatalyst, and are critical for obtaining insightful information on the OER mechanism.[13, 114] Since the OER involves the transfer of four electrons/protons and the possible formation of a range of adsorbed intermediates (e.g. *O, *OH, *OOH), it may give rise to many possible pathways with different rate-determining reaction steps.[42] Moreover, the rate-determining steps for different mechanisms may have similar Tafel slopes.[42, 113] These are the reasons why there is no Tafel slope classification in the literature, which can be used to analyze the reaction route and the rate-determining step for the OER as it has been proposed for the HER.[42] But, it does not mean that the Tafel slope evaluation is completely useless: In addition to giving us a measure of how efficient the catalyst is, it can help us to confirm or rule out a proposed mechanism, which is based on complementary data (e.g. spectroscopic or DFT calculations). Some of the most typical Tafel slope values for the OER based on metal-oxide catalysts are reported to be 120 mV dec^{-1} and 60 mV dec^{-1}.[46, 115]

Figure 2.9 presents the four-step reaction mechanism for the OER in acidic and alkaline solutions proposed by Rossmeisl et al.,[116] where $\Delta G_{1\text{-}4}$ denotes the Gibbs energy change of individual reactions. For many years the rate-determining step, i.e. the step with the highest kinetic activation energy, has been the central topic of investigation. Recently, also the potential-determining step (PDS), which emphasizes the thermochemical aspects of the OER overpotential, has received considerable attention.[112, 117-118] The PDS

indicates the step with the maximum change of Gibbs free chemisorption energy (ΔG_{max}) of two consecutive adsorbed intermediates. The theoretical OER overpotential (η^{OER}) related to the PDS can be calculated under standard conditions at an electrode potential $E = 0$ V vs. SHE as:[118]

$$\eta^{OER} = \left(\frac{\Delta G_{max}}{e}\right) - 1.23\ \text{V} \qquad \textbf{(2.43)}$$

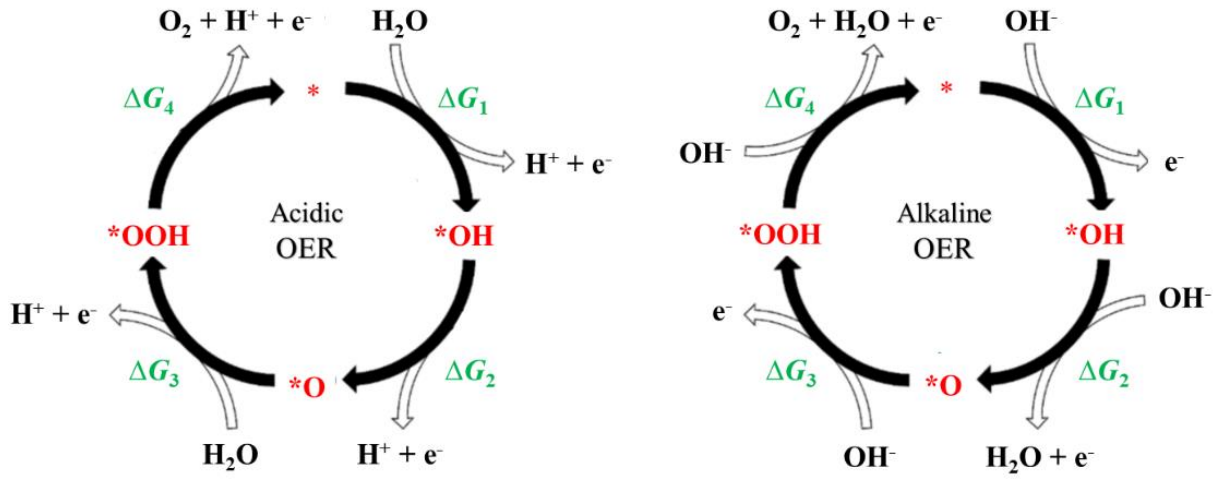

Figure 2.9 A four-step reaction mechanism for the OER under acidic (left) and alkaline (right) conditions proposed by Rossmeisl et al.[116] $\Delta G_{1\text{-}4}$ represents the Gibbs free energy change of individual reactions.

Based on the mechanistic assumption, the energetics of an ideal and a real (RuO_2) OER catalyst are compared (**Figure 2.10**).[113] RuO_2, shown as an example for the case of real catalyst, is known as a highly active catalyst for the OER.[119] Although the results only discuss the case of an acidic solution, Rossmeisl et al. point out, that the analysis can be easily extended to the case of an alkaline environment because the OER in both conditions is proposed to have the same intermediates *OH, *O, and *OOH.[116] For an ideal catalyst without any overpotential losses, the Gibbs reaction energies associated with each elementary step are equal to 1.23 V, i.e. $\Delta G_1 = \Delta G_2 = \Delta G_3 = \Delta G_4 = 1.23$ V at pH = 0 under standard conditions with an electrode potential of $E_1 = 0$ V vs. SHE. Setting liquid water as the zero point in the energy scale, the Gibbs energies for the adsorption of the ideal intermediates would be 1.23 eV, 2.46 eV, and 3.69 eV for *OH, *O, and *OOH, respectively. In this ideal case, there will be no overpotential resulting from the thermodynamic hindrance, and the kinetic barriers raised from the charge transfer reaction as well as from solvent reconstruction are not considered. In contrast to an ideal catalyst with the $\Delta G_{1\text{-}4}$ related to each elementary reaction step being equal to 1.23 eV, DFT calculations show that for the RuO_2 catalyst the ΔG of the elementary steps decreases in the order of $\Delta G_3 > \Delta G_2 > \Delta G_1 > \Delta G_4$ (this might be different for other real catalysts, e.g. TiO_2).[119] ΔG_3 for the formation of *OOH is the largest, indicating that the formation of the *OOH intermediate is the thermochemically least favorable step for the OER on the RuO_2 catalyst.

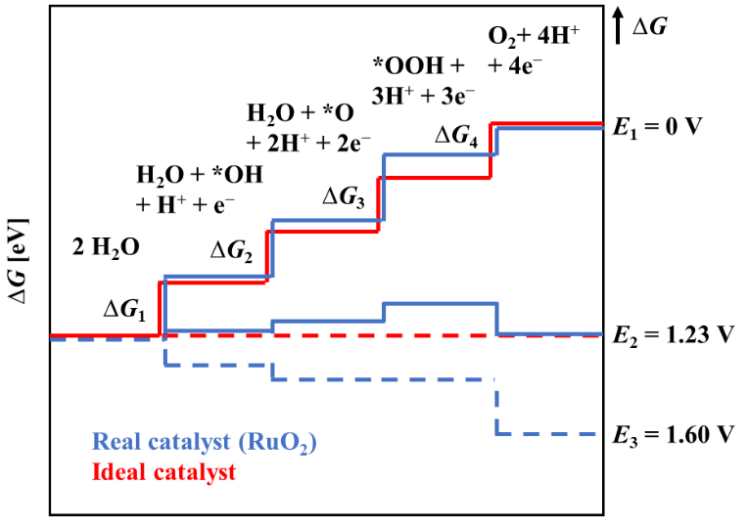

Figure 2.10 Gibbs free energies of reactive species and intermediates vs. the reaction coordinate of the OER on an ideal (red) and a real (a rutile type RuO_2, blue) catalyst surface.[113]

At an applied electrode potential E_1 = 0 V, all steps are energetically uphill for both ideal and real catalysts, and consequently the OER cannot proceed. At E_2 = 1.23 V, the energetic behavior of the ideal and the RuO_2 catalysts are distinctly different. The ideal catalyst presents no more uphill energetics and possesses therefore no overpotential, provided that kinetic limitations are negligible. For the RuO_2 catalyst, ΔG_4 is negative, but ΔG_1, ΔG_2 as well as ΔG_3 remain positive, hindering the OER.[119] A minimum electrode potential of E_3 = 1.60 V is required to make all steps downhill for the RuO_2 catalyst, at which the OER can proceed at a prescribed rate. Simple graphical inspection of **Figure 2.10** suggests that an improved catalytic activity towards the OER using a real OER catalyst could be achieved by reducing the ΔG_x associated with the potential-determining step to smaller values until equal $\Delta G_{1\text{-}4}$ are obtained (red, ideal catalyst).[112, 117] However, Rossmeisl et al. demonstrated that the independent tuning of a single chemisorption energy to achieve optimum relative adsorption energetics is not feasible,[112, 116, 119-120] because the chemisorption energies of the three individual surface intermediates on solid surfaces are strongly correlated.[129, 132-133] That means if the energy associated with one reaction step is changed, the others will do too. As an example, a universal scaling relation between *OH and *OOH was found for a large number of rutile, perovskite, spinel, rock salt, and bixbyite oxides materials, with the difference between the adsorption energies of *OH and *OOH always approximately 3.2 eV, regardless of the binding energy of O* (**Figure 2.11a**).[118] An interesting result derived from the universal scaling relationship is that there is a lower limit value for the OER overpotential.[118] Since the *OH and *OOH intermediates are separated by two proton and two electron transfer steps, the perfect separation in terms of energy should be 2.46 eV, as illustrated in **Figure 2.10**. The difference in the energetics of these two steps between actual catalysts and an ideal one (3.2-2.46 eV)/2 e gives a minimal theoretically overpotential required to drive the OER. To avoid the activity limitation imposed by the scaling relationship, the challenge is to find a way to modify oxide surfaces or the electrochemical interface, such that the relative stability of HOO* and HO* changes.[118]

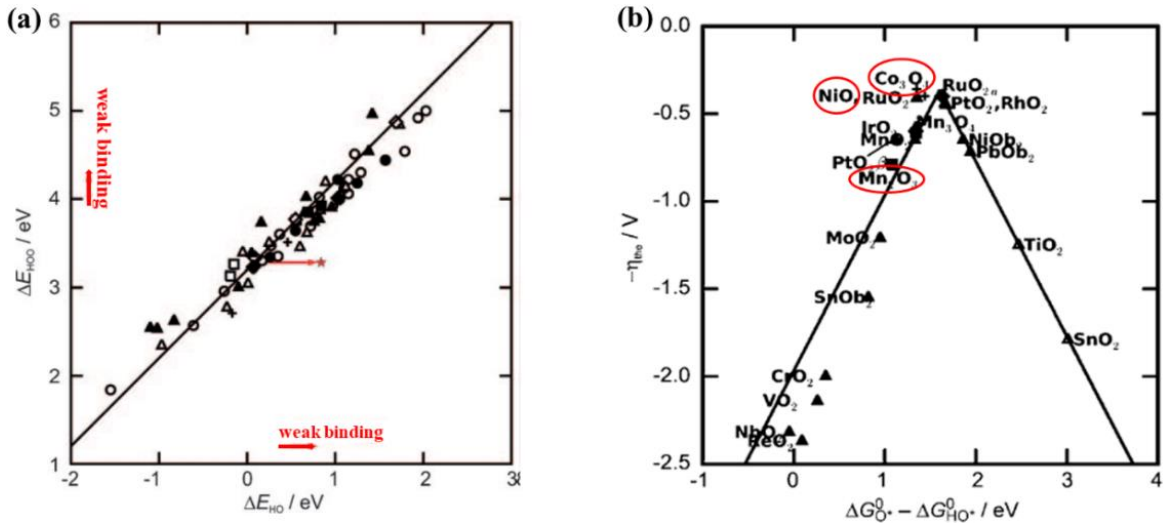

Figure 2.11 (a) The universal scaling relation between adsorption energies of *OH and *OOH on perovskites, rutiles, anatase, NiO, Co_3O_4, and Mn_xO_y oxides.[118] (b) Volcano plot of the calculated activities against the descriptor of $\Delta G_{*O} - \Delta G_{*OH}$ for rutile, anatase, NiO, Co_3O_4 and Mn_xO_y oxides.[118]

Based on the linear scaling relations between the intermediate bonding strengths, the OER activity can be described by using the adsorption energy of a single intermediate, e.g. the *-OH bond strength ΔE_{HO}.[112] From this analysis the energy of the reaction step ($\Delta G_{*O} - \Delta G_{*OH}$) has been proposed as a universal descriptor for the catalytic activity.[118, 121] This theoretical analysis leads to an ordering of catalytic activities for the following perovskites: $SrCoO_3$ > $LaNiO_3$ > $SrNiO_3$ > $SrFeO_3$ > $LaCoO_3$ > $LaFeO_3$ > $LaMnO_3$.[118] This trend is well consistent with experimental findings by Bockris et al.[122] and Y. Matsumoto et al.[123] under alkaline conditions. For the other oxides such as rutile, anatase, NiO, Co_3O_4 and Mn_xO_y, the activity order given by the theoretical calculations reveals a volcano-type relationship (**Figure 2.11b**).[118] A similarly good agreement between the theoretical and experimental values of overpotentials on oxides is also reported by Y. Matsumoto et al.[123] The descriptor approach can be applied to accelerate the screening of new catalysts, but understanding of the activity trends and elucidation of the reaction mechanism on the catalysts is still required to correlate the surface chemical properties with the results from experimental approaches.

2.3.2 OER on Ni-based electrocatalysts

The earth-abundant transition metals and their compounds are excellent candidates for the OER attributed to their multivalent oxidation states, as it was proved that the $M^{+2/+3/+4}$ states are the active sites for the catalytic OER.[124-126 105, 127] Ni-based materials have been investigated strongly in the past decade as electrocatalysts for the OER in alkaline solutions due to their earth-abundant nature, their theoretically high catalytic activity, and stability.[128] In general, such kind of catalysts mainly include Ni-based oxides, Ni-based hydroxides/oxyhydroxide, and Ni-based phosphides, borides, selenides, and nitrides.[128] **Table 2.4** lists the electrocatalytic activity of some representative Ni-based catalysts for the OER. The catalytic

activities of these materials appear to be highly dependent on their surface morphology, chemical composition, oxidation state and electrical conductivity.[129] In the following paragraphs, the recent progress will be summarized, and the catalytic mechanism of Ni-based oxides and hydroxides/oxyhydroxides towards the OER will be discussed. Other OER catalytic systems can be found in the review articles[13, 17, 43, 117, 129] and will not be discussed here.

Table 2.4 Summary of the electrocatalytic activity of representative Ni-based OER catalysts. Values for the IrO_2 and RuO_2 are provided for comparison.

Electrocatalysts	Substrate	Loading mass [mg cm^{-2}]	Electrolyte	Current density [mA m^{-2}]	Overpotential [mV]	Tafel slope [mV dec^{-1}]	Ref.
NiO nanoparticles	Au	~ 0.02	0.5 M KOH	10	320	40	130
NiO stabilized by TiO_2	glassy carbon	~ 0.34	1 M KOH	10	320	52	131
FeNi oxides nanosheets	glassy carbon	0.254	1 M KOH	10	213	32	132
$Ni_{0.69}Fe_{.031}O_x/C$	glassy carbon	2.0	1.0 M KOH	10	280	30	133
$NiCo_2O_4$ nanosheet	glassy carbon	0.4	1.0 M KOH	10	360	50~60	134
Ni-Co oxide	Au	-	1 M NaOH	10	325	39	135
α-$Ni(OH)_2$ nanocrystals	glassy carbon	~ 0.2	0.1 M NaOH	10	331	42	136
2D α-$Ni(OH)_2$-NP	glassy carbon	0.2	1 M KOH	10	260	78.6	137
β-$Ni(OH)_2$/MCNTs[a]	ITO[b]	0.28	0.1 M KOH	10	474	87	138
$Ni(OH)_2$ nanosheets	Carbon paper	1.0 ~ 5.5	1.0 M KOH	20	338	102	139
α-NiOOH Nanosheet	Ni foam	0.2	1.0 M KOH	10	266	76.3	140
NiFe hydroxides	Ni foam	-	1.0 M KOH	10	215	28	28
NiFe hydroxides	glassy carbon	-	1.0 M KOH	10	240	38.9	141
FeNi hydroxides	Au	-	0.1 M KOH	20	280	40	142
NiCo LDH[c]	glassy carbon	1	1 M KOH	10	335	41	143
$Ni_{0.75}V_{0.25}$ LDH	glassy carbon	0.143	1 M KOH	57	350	50	144
Co-doped NiFe LDH	Ni foam	0.25	1 M KOH	10	220	42	145
Ni^{II}-Se nanosheet	glassy carbon	0.143	1 M KOH	10	330	80	146
Ni_3N nanosheets	glassy carbon	0.285	1 M KOH	52.3	350	45	147
Ni_2P nanoparticels	glassy carbon	0.14	1 M KOH	10	290	59	148
Ni_xB nanosheet	glassy carbon	0.21	1.0 M KOH	10	380	89	149
$Ni_{0.13}Co_{0.87}S_{1.097}$	RDE	0.128	1.0 M KOH	10	316	54.7	150
Ni/N/C paper	glassy carbon	0.4	0.1 M KOH	390	10	44	151
IrO_2	glassy carbon	0.21	1 M KOH	10	338	47	143
IrO_2	glassy carbon	0.05	0.1 M KOH	1	320	55	152
IrO_2	glassy carbon	0.05	0.1M $HClO_3$	1	290	45	152
RuO_2	glassy carbon	0.05	0.1 M KOH	1	320	80	152
RuO_2	glassy carbon	0.05	0.1 M $HClO_3$	1	280	50	152

[a] MWCNTs: multi-walled carbon nanotubes; [b] ITO: indium tin oxide; [c] LDH: layered double hydroxides.

(i) Ni-based oxides

Nickel oxides have been widely used in the field of electrocatalysis. In order to improve their activity for catalyzing the OER, great efforts have been devoted to tuning the morphology, surface microstructure and electronic structure.[153] For example, Fominykh et al. fabricated ultrasmall crystalline NiO NPs via a solvothermal reaction using tert-butanol as solvent.[130] It was observed that the decrease in particle size resulted in the formation of a Ni^{3+} state on the surface of the NiO NPs, which is commonly directly associated with the electrocatalytic activity of the nickel-based compounds. Moreover, the surface area can be increased with the decrease of the particle dimensions, which is beneficial for improving the OER activity. The surface energy is also a crucial factor for the electrochemical reactivity, and generally the surface chemical reactivity increases with surface energy.[131, 154] The order of surface energy for NiO facets is (110) ≈ (101) > (113) > (100).[131, 155] Thus, (110) or (101) facets are very desirable for good OER activity. Zhao et al. prepared ultrafine NiO nanosheets with (110) facets (platelet size: ≈ 4.0 nm; thickness: ≈ 1.1 nm) stabilized by TiO_2, and observed excellent OER activity in alkaline solution.[131] The high OER activity was suggested being due to the large proportion of reactive NiO (110) facets containing Ni^{3+} active sites, an abundant number of interfaces, as well as Ti^{3+} sites, which improve the charge-transfer/transport efficiencies at the catalyst/electrolyte interfaces.[131] Furthermore, nanostructured conductive supports, such as carbon nanotubes and graphene, have been reported to significantly enhance the electrocatalytic activity of Ni-based catalysts.[156-158] The synergetic effect between the high activity of the nickel oxides, the high electronic conductivity, and the structural stability of the electrodes led to a good OER activity and stability.

The introduction of other metals (such as Fe and Co) into nickel oxides enhanced their electrochemical performance.[127, 134, 159] Boettcher's group investigated a series of metal oxides towards the OER, including NiO_x, CoO_x, FeO_x, $Ni_yCo_{1-y}O_x$, $Ni_{0.9}Fe_{0.1}O_x$, MnO_x and IrO_x.[127] The results revealed that $Ni_{0.9}Fe_{0.1}O_x$ was the most active OER catalyst, which was attributed to the in-situ formation of layered $Ni_{0.9}Fe_{0.1}OOH$ oxyhydroxide species with nearly every Ni atom being electrochemically active.

(ii) Ni-based hydroxides/oxyhydroxides

Hydroxides and oxyhydroxides of the Ni metal [131, 136, 160-162]are also active for electrocatalytic water oxidation.[131, 136, 162, 231-232141, 163-165] Subbaraman et al. compared the OER activities in 3d transition metals hydr(oxy)oxide with defined morphologies and stoichiometries ratios, and observed the following activity trend of Mn < Fe < Co < Ni, which is governed by the strength of the OH_{ad}-$M^{2+\delta}$ ($0 \leq \delta \leq 1.5$) bond (i.e. Ni < Co < Fe < Mn).[105] Obviously, Ni hydr(oxy)oxides with moderate OH_{ad}-$Ni^{2+\delta}$ bond strength, show a maximum OER activity. For the Ni-based OER electrocatalysts, there are four nickel oxide phases known to be present before oxygen evolution occurs, that is, α-$Ni(OH)_2$, β-$Ni(OH)_2$, γ-NiOOH, and β-NiOOH.[166] According to Bode's model (**Figure 2.12**),[167] upon oxidation α-$Ni(OH)_2$ is usually converted to γ-NiOOH, whereas β-$Ni(OH)_2$ is usually converted to β-NiOOH, and β-NiOOH will be converted to γ-NiOOH upon further oxidation.[167] Bediako et al. observed the formation of Ni hydroxides in electrodeposited Ni-borate thin films,[161] and using in situ X-ray absorption spectroscopy revealed that the γ-NiOOH was the

electrochemical active material for catalyzing the OER.[168] Moreover, Gao et al. synthesized α-Ni(OH)$_2$ and β-Ni(OH)$_2$ nanocrystals by a solvothermal method, and found that α-Ni(OH)$_2$ exhibits a higher OER activity and stability than β-Ni(OH)$_2$ in an alkaline electrolyte.[136] The higher electrochemical performance was mainly contributed to the easier conversion between α-Ni(OH)$_2$ and γ-NiOOH.

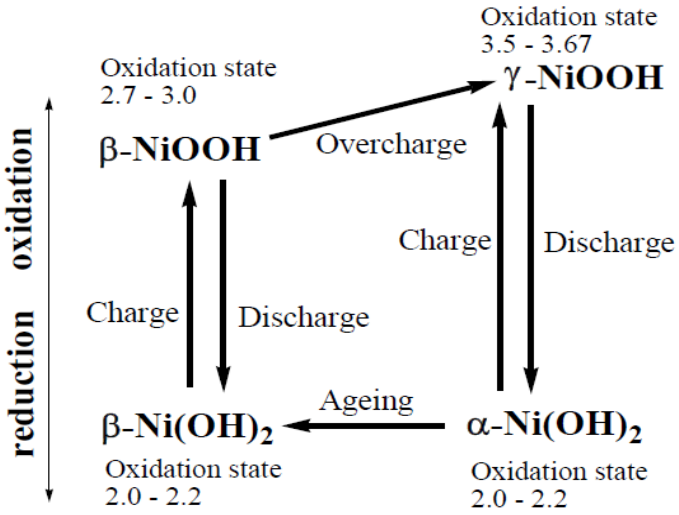

Figure 2.12 A Bode scheme of the Ni(OH)$_2$/NiOOH redox transformation.[167]

After the first observation of the poisoning effect of Fe impurities on the Ni(OH)$_2$ electrodes in alkaline batteries by Edison and Junger,[169-170] systematic studies were undertaken to investigate the role of Fe contamination. These demonstrated that an increase of the Fe contamination leads to a decreasing capacity and cycle life of the alkaline batteries by the lowering of the OER overpotential.[170-172] Motivated by this observation and with the rising interest in water splitting in the 1980s, Corrigan et al. were the first to study the oxygen evolution behavior of nickel oxide electrodes with Fe impurities, and they observed, that the incidental Fe incorporation improved the OER activity of the Ni(OH)$_2$/NiOOH system.[173] Recently, Trotochaud et al. further investigated the doping effects of Fe in bimetallic (oxy)hydroxides [Ni$_{1-x}$Fe$_x$(OH)$_2$/Ni$_{1-x}$Fe$_x$OOH] on the OER activity.[127] The results indicate that the incorporation of Fe impurities led to a disorder of the γ-NiOOH crystal structure and a highly enhanced (> 30-fold) film conductivity. Both effects were favorable for the OER. Meanwhile, Louie et al. also carried out a detailed investigation of the structure and the OER activity of the electrodeposited Ni-Fe films in alkaline solutions.[142] They observed, that the Ni-Fe films with a composition of 40% Fe showed a higher OER activity than that of freshly deposited pure Ni and Fe films. In addition, layered double hydroxides (LDHs) containing cationic brucite like layers separated by exchangeable charge-balancing interlayer anions show relatively open structures (see **Figure 2.13**), which allows the rapid diffusion of reactants and products along with fast proton-coupled electron transfer.[129, 143, 174] Therefore, the catalytic active sites are easily accessible and induce a good electrocatalytic performance.[114, 129, 143, 175] Despite the progress that has been made in the development of novel Ni- or NiFe-based materials with better OER activity and stability, the detailed catalytic mechanism remains unclear, and it should be a focus of future studies. *In situ* spectroscopy and

theoretical calculations with an applied potential might be the possible approaches.

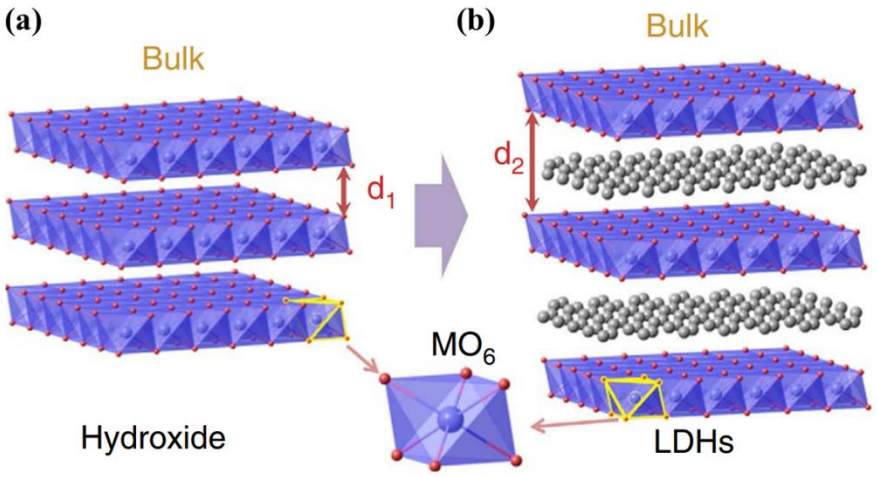

Figure 2.13 (a) Layered hydroxides. d_1 is the inter-layer distance. (b) LDHs with inter-layer anions and water molecules. d_2 is the inter-layer distance, $d_2 > d_1$.[143] Each single layer is composed of edge-sharing octahedral MO_6 moieties (M denotes a metal element). The purple and red spheres represent the metal and oxygen atoms, respectively. The grey spheres illustrate the inter-layer anions and water molecules. Hydrogen atoms are omitted.

In summary, in order to replace the noble metal materials, researchers have provided extensive efforts in the development of alternative HER and OER electrocatalysts, especially Ni-based catalysts, to achieve high HER and OER catalytic properties and stability. In this work, the structural and electronic parameters of the electrodeposited Ni-based materials and their correlation with the catalytic properties are systematically studied with the aid of surface characterization and electrochemistry techniques, thereby gaining a deeper insight into the elementary reaction steps and to identify the involved active phases for both half reactions.

3. Experimental Section

This chapter briefly explains the main experimental methods frequently used in this work in order to give a methodological background prior to their application in the results section. This will make it clear why they were chosen in each case and how they complement each other for different applications. For more extended and fundamental explanations, some suitable literature references are provided.

3.1 Electrodeposition

The word electrodeposition or electrochemical deposition (ED) basically includes the principle electrolysis process in which solids are deposited onto an electrode in different forms and shapes. A historical application of this process is the so-called electroplating technique, where mostly metal or alloy coatings are produced for decorative or protective applications. Nowadays, this technique covers the deposition of a diverse range of solid materials ranging from metals, alloys to semiconductors and polymers in a wide spectrum of size and dimensions. In this work, nano-scale and meso-scale up to macro-sized Ni-based compounds with various chemical properties are electrodeposited as catalysts for the hydrogen evolution reaction or oxygen evolution reaction. This section will briefly describe the electrodeposition cell setup, the use of reference electrodes, the selection of working electrodes (i.e. substrates) as well as the application of electrochemical techniques to deposit the Ni-based electrocatalysts studied in this Ph.D. work. Further detailed information about electrochemical processes in general can be found in ref.[35].

3.1.1 Cell setup

All presented electrochemical depositions were performed at room temperature in a standard three-electrode PECC-2 cell system with a volume of 7.2 mL and were controlled by a ZENNIUM potentiostat (Zahner-Elektrik GmbH & Co. KG). **Figure 3.1a** presents a picture of the PECC-2 cell operated in the three-electrode configuration with a working electrode (WE), a reference electrode (RE), and a Pt coil counter electrode (CE). The WE is mounted between a homemade insulating Teflon holder and an Au-covered metal plate. The active area of the WE exposed to the electrolyte is determined by the diameter of O-ring, which seals the connection to the Teflon plate. The distance between the WE and the RE is 1.1 cm and about 2.3 cm between the WE and the CE. The corresponding cell connections are shown in **Figure 3.1b**.

A schematic illustration of the circuit diagram of the three-electrode arrangement is given in **Figure 3.1c**, where the current flow is measured between the WE and the Pt wire CE, while the potential is measured between WE and the RE. In this setup the potential of the WE is controlled relative to a fixed RE and it provides the possibility to investigate only the half-cell reaction at the WE, without having to consider the electrochemical reactions at the CE. It is also possible to work in a two-electrode configuration without the RE. In this case a potential difference is applied or measured between the WE and CE. This setup is used

to analyze the performance of the whole electrochemical cell rather than just one of the half-cell reactions.

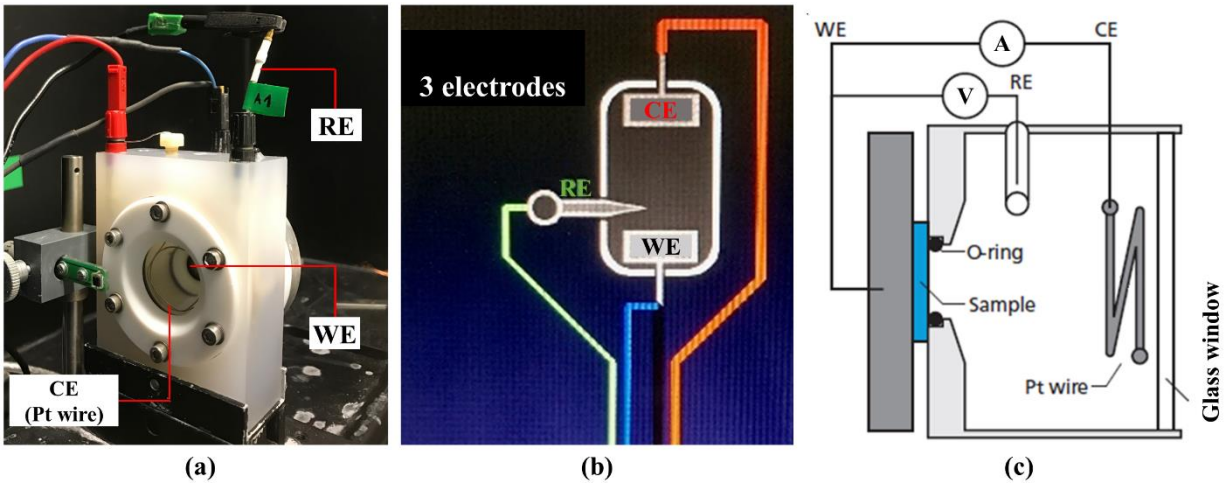

Figure 3.1 (a) Photograph of a PECC-2 cell in three-electrode configuration with a working electrode (WE), a reference electrode (RE) and a Pt wire counter electrode (CE). (b) Screenshot while checking the cell connections by the Zennium software. (c) Schematic picture the circuit diagram in the three-electrode mode.[176]

3.1.2 Reference electrodes

The potential of an electrode that is passing a current (the WE), in general, cannot be determined by measurement with respect to the other current-carrying electrode in the cell (the CE), since the measured cell voltage will include contributions from the potential drop due to the electrolyte resistance and the overpotentials of both the WE and CE.[35] Thus, an important step in the control and measurement of electrode potentials is that of introducing a third electrode into the cell (i.e. the reference electrode). The RE has a stable and known electrode potential and serves as an experimental potential reference point in the electrochemical cell. The high stability of the reference electrode potential is usually achieved by employing a redox system with constant (buffered or saturated) concentrations of each participant involved in the redox reaction. Furthermore, it should be easy to handle. To avoid any overpotential contribution from the RE, the current flowing through the RE is ideally kept to zero, which can be achieved with a high impedance voltmeter as shown in **Figure 3.1c**. Corrections for the uncompensated solution resistance will be discussed further in section 3.4.2.

There are several options for the reference electrode. The Ag/AgCl reference electrode is probably the most common one, which consists of a silver wire immersed in an aqueous AgCl solution, with a standard potential value depending on the concentration of the silver ions in the solution. There are also the Hg/HgO, the Hg/Hg_2SO_4 and the calomel (Hg/Hg_2Cl_2) reference electrodes, which are all based on mercury. A summary of common reference electrodes and their potentials with respect to the standard hydrogen electrode (SHE) at 25 °C can be found in **Table 3.1**. The selection of the type of reference electrode depends on each particular case, especially on the electrolyte pH and on whether or not chlorides can be an

interference for the investigated reaction. In the present work, the Ag/AgCl reference electrode with a 3.0 M KCl solution was employed for the electrodeposition of Ni-based electrocatalysts.

Table 3.1 Common reference electrodes and their potentials with respect to the SHE at 25 °C.[35, 45]

Reference electrode	**Condition**	**Half-cell reaction**	**Potential, V**
Standard hydrogen electrode (SHE)	$a_{H^+} = 1$	$2H^+ + 2e^- \rightleftharpoons H_2$	0.0
Normal hydrogen electrode (NHE)	$c_{H^+} = 1.0$ M	$2H^+ + 2e^- \rightleftharpoons H_2$	≈ 0.0
Reversible hydrogen electrode (RHE)	actual electrolyte	$2H^+ + 2e^- \rightleftharpoons H_2$	0 − 0.0591 pH
Silver/silver chloride electrode	$a_{Cl^-} = 1$	$AgCl + e^- \rightleftharpoons Ag + Cl^-$	+ 0.224
(Ag/AgCl)	saturated KCl		+ 0.1976
	KCl (c = 3.0 M)		+ 0.209
Calomel electrode	$a_{Cl^-} = 1$	$Hg_2Cl_2 + 2e^- \rightleftharpoons 2Hg + 2Cl^-$	+ 0.2682
(Hg/Hg_2Cl_2)	saturated KCl		+ 0.2415
	KCl (c = 1.0 M)		+ 0.2807
Mercury/mercurous sulfate electrode	$a_{SO_4^{2-}} = 1$	$Hg_2SO_4 + 2e^- \rightleftharpoons 2Hg + SO_4^{2-}$	+ 0.6158
(Hg/Hg_2SO_4)	saturated K_2SO_4		+ 0.650
	H_2SO_4 (c = 0.5 M)		+ 0.682
Mercury/mercury oxide electrode	$a_{OH^-} = 1$	$HgO + H_2O + 2e^- \rightleftharpoons Hg + 2OH^-$	+ 0.097
(Hg/HgO)	NaOH (c = 1.0 M)		+ 0.140
	NaOH (c = 0.1 M)		+ 0.165
Copper/copper sulfate electrode	saturated SO_4^{2-}	$Cu^{2+} + 2e^- \rightleftharpoons Cu$	+ 0.314
($Cu/CuSO_4$)			

Each reference electrode was calibrated prior to initial use and tested periodically for drift by using a commercial reversible hydrogen electrode (RHE, company of the SHE). The experimentally determined potentials in this work, i.e. potentials measured against the reference electrode ($E_{\text{vs. ref.}}$), are converted into the potentials versus the RHE ($E_{\text{vs. RHE}}$) according to equation **(3.1),** if not mentioned otherwise:

$$E_{\text{vs. RHE}} = E_{\text{vs. ref.}} + E^0_{\text{ref.}} + 0.0591 \text{ pH} \qquad \textbf{(3.1)}$$

where $E^0_{\text{ref.}}$ is the potential of the reference electrode versus the standard hydrogen electrode (SHE).

3.1.3 Working electrodes

The working electrode acts as the substrate, which supports the heterogeneous electrocatalysts. In this work, Titanium (Ti) foil with a thin native TiO_2 layer was used after special chemical treatments (as detailed below) as the working electrode with the catalyst to be electrodeposited on top of it. There are several reasons for this selection: First, the surface is passivated by the TiO_2 layer, so no further degradation takes place in the alkaline regime. Second, the TiO_2 foil does not show any catalytic activity for the HER and OER by itself, which would be, for example, the case for Ni/NiO_x substrates. Third, the conductivity of a

thin TiO_2 layer should be sufficient, so that it does not influence the measurement of the electrocatalytic activity. Fourth, it is quite often used as adaption and passivation layer in PV-EC cells, also for the work in our group on buried-junction PV-EC cells, were thin TiO_2 layers produced by Atomic Layer Deposition (ALD) are employed. Thus, this substrate resembles then the setup for a complete water splitting device quite well. Prior to the electrodeposition, the Ti foil substrates (10 mm × 10 mm × 0.89 mm, 99.7%, Alfa Aesar) were carefully prepared by etching in 5% HF or 6 N HCl (see details in experimental sections in chapter 4 to 6). Immediately after each pretreatment, the Ti substrate was sealed by a home-made Teflon™ holder with a geometrical area of 0.5 cm^2 (8 mm O-ring diameter) and fixed on top of an Au covered metal plate as shown above in **Figure 3.1**.

3.1.4 Electrodeposition techniques

As an electrolytic electrochemical process, the method of electrodeposition is only feasible under application of an external electromotive force. Thus, the electrodeposition can be either controlled by an applied potential or an applied current, as well as by the parameters (e.g. time, temperature, stirring) recorded during the process. In the first category the potential is controlled with respect to the reference electrode either in potentiostatic, cyclic and linear voltammetric or pulsed modes. Cyclic voltammetry can be used to deposit metal oxides and/or (oxy)hydroxides onto conductive substrates from metal-salt solutions, the number of cycles determine the mass loading, and the morphology of the catalyst depends on the scan rate and the range of applied potentials. Under the second category fall the controlled-current techniques, which are often known as galvanostatic methods. In this category a controlled-current passing through the cell is applied in constant or pulsed modes.

The electrodeposition parameters and conditions, including the working electrodes (substrates), electrolytes, reference electrodes as well as the electrodeposition modes, used to deposit the Ni-based electrocatalysts in this work are detailed in the experimental sections in the chapters 4 to 6.

3.2 X-ray photoelectron spectroscopy (XPS)

The elemental composition and the oxidation state of the involved elements are of critical importance in the understanding of catalytic processes. Metal-based catalysts are often used for redox reactions. Careful control of the metal oxidation state is strongly required to ensure successful operation of the catalyst. Heterogeneous catalytic processes take generally place at the interface of at least two interacting phases, i.e. in electrochemistry at the surface of a solid electrode. Thus, a characterization technique with a very high surface sensitivity must be employed for measuring the chemical and physical properties of the catalyst under investigation. Here, X-ray photoelectron spectroscopy (XPS), also known as electron spectroscopy for chemical analysis (ESCA), is one of the most widely used and powerful experimental techniques for providing this type of information.[177-178] Surface modifications during the analysis are kept to a minimum because samples are analyzed under ultra-high vacuum with relative low radiation dose.

Spectral results are obtained from within the top 10 nm of the surface depending on the kinetic energy of the emitted electrons, which allows XPS to obtain information directly from the crucial surface area. Finally, XPS can do both qualitative and quantitative analysis of the elements detected.

In this study, XPS investigations were conducted on the nickel-based samples before, between and after the electrocatalytic hydrogen or oxygen evolution reactions to elucidate the detailed compositional changes induced by the different performed electrochemical reactions. This is necessary in order to obtain a complete understanding of the ongoing elementary reaction steps and the involved active sites.

3.2.1 Operating principle

The main operation principle of XPS is based on the external photoelectric effect, where electrons bound in the inner shells of the atoms are emitted from the sample upon illumination with photons with sufficient energy. The phenomenon of photoemission was discovered by Hertz in 1887, and explained as the photoelectric effect by Einstein in 1905 (Nobel Prize in Physics 1921).[179-180] Siegbahn and coworkers in Sweden were the pioneers to develop significant improvements in the early stages of this technique,[181] which was then also rewarded with the Nobel prize in physics in 1981.

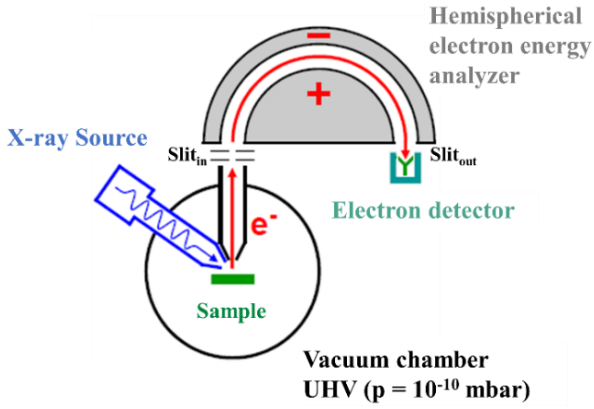

Figure 3.2 Schematics of the basic setup of an X-ray photoelectron spectroscopy instrument.

The basic setup of an XPS instrument is schematically shown in **Figure 3.2**: X-ray photons with a specific energy of *hv* illuminate a small area of a sample causing electrons to be ejected. In XPS instruments, X-rays are generated by striking a metallic anode with high-energy electrons. The energy of the emitted X-rays depends on the anode material, and the beam intensity depends on the electron current bombarding the anode and its energy. Among various materials available to produce different X-ray energies and line widths, Mg or Al anodes are typically utilized, providing photons of 1253.6 eV and 1486.6 eV with energy widths of 0.7 eV and 0.85 eV, respectively.[177] The ejected electrons with remaining kinetic energies (E_{kin}^{S}) escape into the vacuum and are focused onto the entrance slit of a hemispherical electron energy analyzer for the determination of their kinetic energies. Electrostatic fields within the hemispherical analyzer allow only the electrons of a given energy (the so-called Pass Energy) to be collected by a channeltron detector for intensity count.

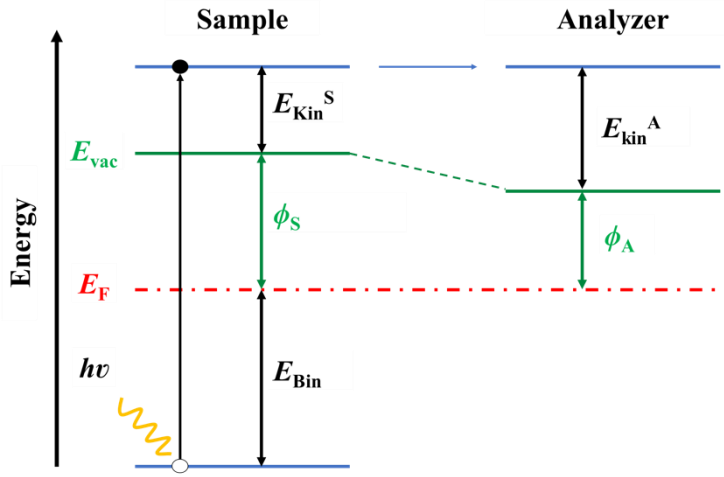

Figure 3.3 Schematic energy diagram of the photoemission process.

The schematic energy diagram of the photoemission process is displayed in **Figure 3.3**. The E_{kin}^{S} of the electron is given by equation **(3.2)**:

$$E_{kin}^{S} = h\upsilon - E_{bin} - \phi_S \qquad \textbf{(3.2)}$$

where $h\upsilon$ is the energy of the X-ray photons being used, E_{bin} is the binding energy of the electron referenced to the Fermi energy of the sample (E_F), and ϕ_S is the work function of the sample.

With the establishment of the electrical contact between the analyzed sample and the spectrometer, the Fermi energy of the sample is aligned with that of the spectrometer. Due to the conservation of energy the electron binding energy (E_{bin}) can therefore be calculated by equation **(3.3)**:

$$E_{bin} = h\upsilon - E_{kin}^{A} - \phi_A \qquad \textbf{(3.3)}$$

where $h\upsilon$ is the energy of the X-ray photons being used, E_{kin}^{A} is the kinetic energy of the electron as measured by the spectrometer, and ϕ_A is the work function of the analyzer. ϕ_A is an instrumental parameter, which is adjusted by setting the Fermi edge emission of a clean metallic sample such as Au or Ag to zero binding energy.

3.2.2 Element identification

The first issue involved in a XPS analysis is to identify the elements present at the surface of a sample by scanning a survey spectrum over a maximum possible energy range defined by the excitation source. As an example, **Figure 3.4** displays a typical XPS survey spectrum recorded from a Ni nanoparticle catalyst prepared by electrodeposition on a Ti/TiO_2 surface. Since every element has a unique electronic structure, the experimentally determined binding energies (BEs) are characteristic for a specific element. By comparing the measured spectrum to reference data,[182] the emissions from all core levels can be assigned to particular electronic states of the elements, as marked in **Figure 3.4**.

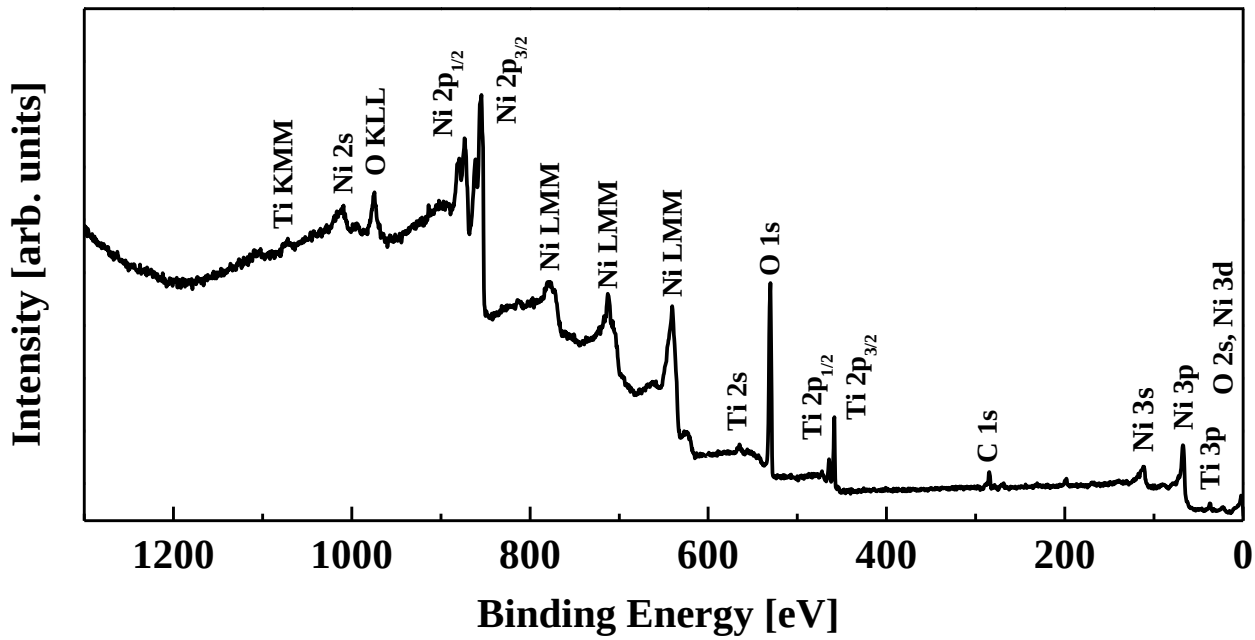

Figure 3.4 XPS survey spectrum of electrodeposited Ni NPs on Ti/TiO_2 surface.

Photoelectron peaks are labeled according to the quantum numbers of the level from which the electron originates. An electron with orbital momentum l (0, 1, 2, 3, … indicated as s, p, d, f, ...) and spin momentum s has a total momentum ($j = l + s$). As the spin may be either up ($s = +1/2$) or down ($s = -1/2$), each level with $l \geq 1$ has two sublevels, with an energy difference called the spin-orbit splitting. Upon photoemission, the spin-orbit coupling is one of the most important interactions. Take the Ni 2p orbital as an example (refer again to **Figure 3.4)**: When an electron is emitted from Ni 2p, an unpaired electron is left behind with spin $s = 1/2$. Since the Ni 2p orbital carries an angular momentum $l = 1$, the spin of the unpaired electron can be either parallel or antiparallel to l resulting in two different final states: one with total angular momentum j ($j = l + s$) of 1/2 and the other with j of 3/2. The intensity ratio of the two peaks of a spin-orbit doublet is determined by the multiplicity of the corresponding levels, equal to $2j + 1$. Hence, the intensity ratio of $j = 1/2$ and $j = 3/2$ components of the Ni 2p doublet is 1:2. Photoelectron peaks from core levels come in pairs (doublets) except for s levels, which give a single peak. **Table 3.2** lists the parameters of spin orbit splitting.

Table 3.2 Summary of the parameters of spin-orbit splitting.

Orbital	l	s	$j = l \pm s$	Intensity ratio
s	0	1/2	1/2	-
p	1	1/2	1/2, 3/2	1:2
d	2	1/2	3/2, 5/2	2:3
f	3	1/2	5/2, 7/2	3:4

In addition to the direct core level emissions, Auger electrons are also emitted because of the relaxation process of the excited ionized atoms, so-called “Auger decay”. The Ti KMM, Ni LMM and O KLL Auger

emission lines are also indicated in the survey spectrum in **Figure 3.4**. In the Auger process, an outer electron falls into the inner orbital core hole created by the original photoemission process, and a second electron is simultaneously emitted carrying off the excess energy. Take LMM lines for example, the peaks represent the energy of the electrons ejected from the atoms due to the filling of the L shell by an electron from the M shell coupled with the ejection of an electron from an M shell. In contrast with the photoelectric peaks, the kinetic energy of the Auger lines does not depend on the photon energy of the X-ray source. Thus, an overlap between XPS and Auger peaks can sometimes be avoided by varying the X-ray energy.

3.2.3 Oxidation state analysis

Binding energies are not only element-specific but contain also chemical information, because the energetic position of the core levels depend on the oxidation state of the atom. Therefore, high-resolution core level spectra of the electronic states are measured to obtain more detailed information about these small energy differences. **Figure 3.5** shows Ni 2p spectra at high resolution with nickel in different oxidation states. The binding energy increases with the oxidation state of the nickel. The reason for this is that the 25 electrons in the Ni^{3+} ion feel a higher attractive force from the nucleus with 28 protons, than the 26 electrons in Ni^{2+} or the 28 in the neutral Ni atom. In other words, the binding energy increases with increasing positive charge on an atom. The chemical shifts in general can be attributed and directly correlated to changes in the initial state ($E_{bin} = E_{initial}$). In addition, the binding energy of a specific atom is also related to the electronegativity of its neighbors. However, these rules do not always strictly hold. The chemical shift cannot always be attributed to a change in the initial state only. The final state can also have an impact in the binding energy. Take cobalt as an example, the binding energy of the electron in Co^{3+} (779.6 eV) is lower than the binding energy of the electron in Co^{2+} (780.5 eV). [183]

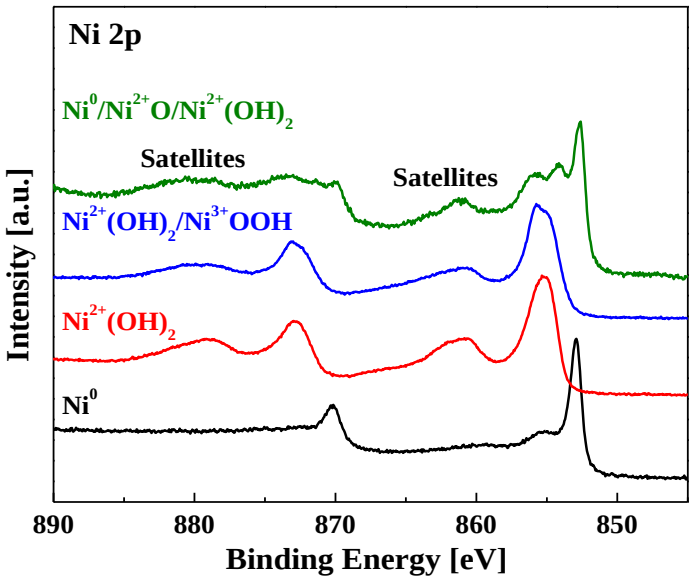

Figure 3.5 High resolution Ni 2p core level spectra of nickel metal (black), nickel hydroxide (red), mixed nickel hydroxide/oxyhydroxide (blue), and mixed nickel metal/oxide/hydroxide (green).

Shake-up and shake-off satellites are another spectral feature arising by final state effects, which appear when the emitted photoelectron imparts energy to another electron of the atom. Ultimately, this electron will be excited to a higher unoccupied state (shake-up, above the Fermi-level) or in an unbound state (shake-off, above the vacuum level). As a result, the photoelectron loses kinetic energy and appears at a higher binding energy in the spectrum. Such losses can have diagnostic value as the precise loss structure depends on the environment of the atom. The oxidation states of a metal, like nickel and molybdenum studied in this work, can be distinguished by a chemical shift in the main line and by its satellites.

An experimental problem in XPS, which needs to be noticed is that charging may take place on electrically insulating samples, e.g. nickel hydroxide films electrodeposited in this work. As photoelectrons are lost during the photoemission process, a significant net positive charge (varying typically from several volts to several tens of volts) accumulates at the surface in the absence of charge compensation. When this occurs, the kinetic energy of all of the emitted photoelectrons will decrease leading to a shift to apparently higher binding energies of the observed peaks in the spectrum.[184-185] To obtain nevertheless useful information on the surface chemical states of the sample affected by charging, XPS charge calibration is necessary. Since adventitious carbon is visible as pollutant on many surfaces, this is usually achieved by shifting the complete spectrum until the carbon C1s peak agrees with its catalogued value of 284.8 eV(C-C, C-H).

3.2.4 Stoichiometry determination

XPS is one of the most important techniques for the qualitative and quantitative analysis of the elemental and chemical composition of surfaces. The underlying assumption when quantifying XPS spectra is, that the intensity (I) of a photoelectron line of a specific atom depends on the average atomic density of atoms (N) in a given state. However, other factors need to be considered as well, including the photon flux density (F), the spectrometer efficiency for detecting the electron with kinetic energy E_{kin} [also called transmission factor, $T(E_{kin})$], the ionization cross-section for the absorption of photons with energy $h\nu$ and electrons with E_{kin} [$\sigma(h\nu, E_{kin})$], the inelastic mean free path of the photoelectrons with E_{kin} [$\lambda(E_{kin})$], the angle between the emission and the surface (θ), and for single crystalline samples also the orientation of the sample with respect to the detector and the polarization plane of the photons.[177] The general expression for the intensity of an emission line, normally given as counts per seconds (CPS), is:[186-187]

$$I(E_{kin}) = F(h\nu) * T(E_{kin}) * \sigma(h\nu, E_{kin}) * N * \lambda(E_{kin}) * \cos\theta \qquad \textbf{(3.4)}$$

A simplified analysis of sample composition is based on tabulated sensitivity factors (S), also known as relative sensitivity factors (RSF) for individual photoelectron lines. The intensity of the line is then given by using the general equation **(3.5)**:

$$I = N*S \qquad \textbf{(3.5)}$$

and the atomic fraction C_x of element x in a sample by equation **(3.6)**:

$$C_x = (I_x/S_x) / (\sum I_i/S_i) \qquad \textbf{(3.6)}$$

The sensitivity factors can be estimated from theory or derived empirically from the analysis of standard samples. A set of RSF are necessary for transitions within an element and for all elements. Quantification requires the selection of one transition per element.

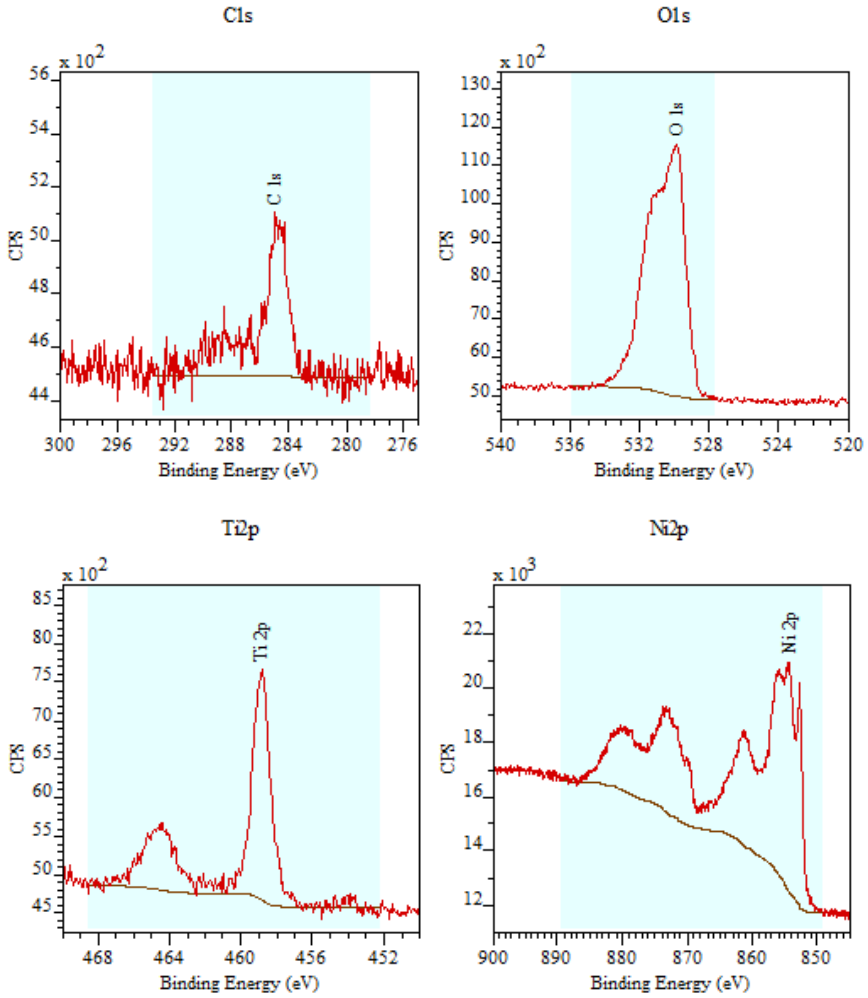

Name	Position	FWHM	Area / (T*MFP)	Area/(RSF*T*MFP)	% Mass Conc	%At Conc
C 1s	284.90	1.483	1715.4	1715.45	4.174	11.631
O 1s	529.85	2.566	19408.1	6623.94	21.467	44.913
Ti 2p	458.85	1.124	6574.1	841.757	8.163	5.707
Ni 2p	854.35	5.284	123591.2	5567.17	66.196	37.748

Figure 3.6 XPS quantification regions (light blue, top) and the quantification table (bottom) based upon values computed from the spectral peak regions using CasaXPS software.[188] FWHM: full width at half maximum; T: transmission factor; MFP: mean free path; RSF: atomic sensitivity factor.

For the evaluation of the XPS spectra, the CasaXPS software Version: 2.3.16Dev52 was used.[188] **Figure 3.6** illustrates the areas targeted by the regions defined for the C 1s, O1s, Ti 2p and Ni 2p transitions, leading to the quantification table displayed below the spectra. The first step in the analysis of a surface composition is the definition of the peak areas of interest for the evaluation, which have to be corrected by subtraction of an appropriate background. This background originates from the inelastic scattering of the photoexcited electrons. Generally, three types of backgrounds are used: the linear background, the Shirley background

and the Tougaard background. Herein, the Shirley background, where the background intensity at any given binding energy is proportional to the intensity of the total peak area above the background in the lower binding energy peak range,[189] was generally adopted because it is a good compromise between the physically unrealistic linear background and the physically realistic Tougaard background, but the latter is not easy to apply in many practical situations.[190] After correcting the peak areas for the atomic sensitivity factor (RSF), the transmission factor (T) and the mean free path (MFP), the information on the mass ratios and the atomic ratios of the identified elements can be obtained (see Table in **Figure 3.6**).

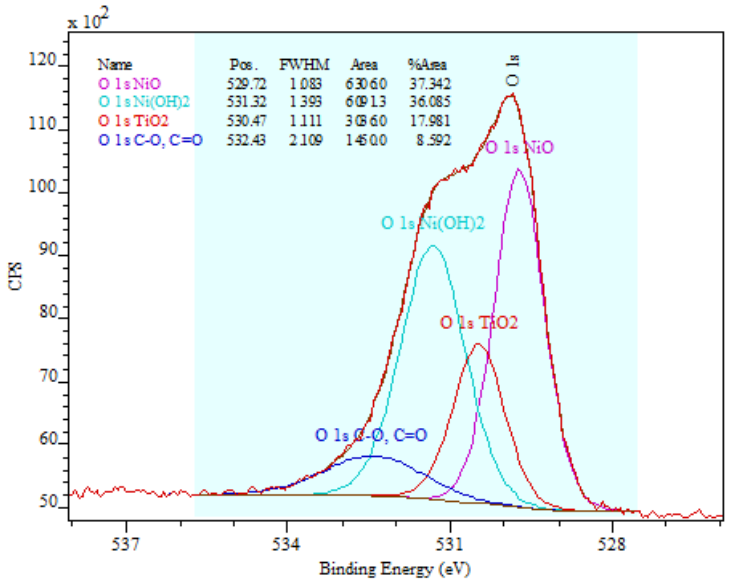

Figure 3.7 Quantitative fitting of the O 1s spectrum of electrodeposited Ni NPs on Ti/TiO_2 surface using CasaXPS software.[188]

Curve fitting can be required if intensities of different chemical species of an element are to be evaluated. A model is typically constructed from a set of Gaussian/Lorentzian line-shapes. An effective fitting result is based on a careful model construction involving additional parameter constraints, including the binding energy differences, full width at half maximum (FWHM) and areas. An example of the quantitative fitting of the O 1s spectrum measured for the electrodeposited Ni NPs on Ti/TiO_2 surface using CasaXPS software is shown in **Figure 3.7**. For the accurate determination of nickel-based oxides, the contributions of carbon-oxygen and titanium-oxygen compounds to the O 1s area must be considered. These were obtained from the C 1s and Ti 2p detail spectra and used to constrain the areas of the fitted O 1s lines representing carbon-oxygen and Ti-O species. From the deconvolution and fitting of the O 1s spectrum, characteristic emission lines associated with the O^{2-} in NiO and TiO_2, OH^- in $Ni(OH)_2$, as well as oxygen in carbon-oxygen species like C-O and C=O can be identified. The information about their peak position, FWHM, peak area and percentage of area can be obtained from the quantification table in **Figure 3.7**.

3.2.5 Instrumentation

The XPS measurements were performed in the Darmstadt's Integrated System for Fundamental Research

(DAISY-FUN). The system combining a wide variety of surface preparation and surface analysis facilities operates under ultrahigh vacuum (UHV) at a base pressure of 10^{-10} mbar to avoid any contamination of the specimen during different processing steps. The XPS system was purchased from SPECS Surface Nano Analysis GmbH. The X-ray source was a monochromatic Al K_α (XR 50 M, Focus 500) tube with an excitation energy of 1486.74 eV. The XPS spectrometer was calibrated by correcting the relative binding energy difference of the measured 3d core level emission lines and the Fermi edges of sputter-cleaned Ag, Au and Cu to their literature values.

3.3 Scanning electron microscopy (SEM) and energy dispersive X-ray spectroscopy (EDX)

Scanning electron microscopy (SEM) yields information about topography, morphology and composition of the probed samples by scanning the surface with a focused beam of electrons. The interaction between the incident primary electron beam and the sample within a teardrop-shaped volume leads to various signals, which can be detected by specialized detectors, as shown in **Figure 3.8**. The most used SEM mode in this study is the detection of secondary electrons emitted by atoms excited by the electron beam. In secondary electron imaging (SEI), these are ejected very close to the specimen surface. Consequently, by scanning the sample and collecting the secondary electrons emitted, very high-resolution images displaying the topography of the surface can be produced.

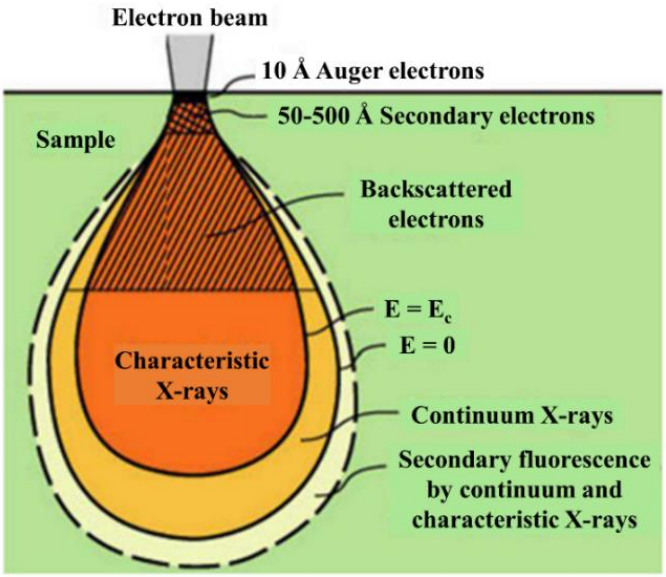

Figure 3.8 Schematic representation of the interaction between the primary electron beam and the sample within the interaction volume.[191]

As indicated in **Figure 3.8,** characteristic X-rays are among the byproducts of electron microscopy, which forms the basis of an analytic technique referred to the energy-dispersive X-ray spectroscopy (EDX). When a high-energy incident beam is focused into the sample being studied, an electron in an inner shell may be excited and ejected from the shell with an electron hole created. Then, an electron from an outer and higher-

energy shell fills the hole, and the energy difference between the higher-energy and the lower-energy shells may be released in the form of an X-ray. The number and energy of the emitted X-rays can be measured by an energy-dispersive spectrometer. As the energies of the X-rays are characteristic of the difference in energy between the two shells and therefore are directly linked to the atomic structure of the emitting element, EDX allows the determination of the elemental composition of the specimen under investigation.

In this study, the specimens were characterized using a Philips XL30 FEG high-resolution scanning electron microscope (FEI Company, Hillsboro, Oregon, USA) coupled with energy dispersive X-ray spectroscopy (EDX, EDAX, Mahwah, USA).

3.4 Electrochemical measurements

3.4.1 Electrochemical cell

Similar to the electrodeposition setup (see **Figure 3.1**), the electrochemical measurements were carried out at room temperature in a standard PEC-cell of 7.2 mL volume (PECC-2, Zahner) using a Zahner potentiostat (Zennium, Zahner) or a GAMRY Interface 1000E potentiostat operating in standard three-electrode mode. The catalyst decorated Ti substrate and a Pt coil served as the working electrode and the counter electrode, respectively. An Ag/AgCl (3 M KCl) reference electrode was used for the measurements in 0.1 M KOH (Carl Roth GmbH + Co. KG, volumetric standard solution 0.1 M ± 0.2%) and 0.5 M H_2SO_4 (Carl Roth GmbH + Co. KG, volumetric standard solution 0.5 M ± 0.2%). A Hg/HgO (1 M NaOH) reference electrode was used for the measurements in 1 M KOH (Carl Roth GmbH + Co. KG, volumetric standard solution 1 M ± 0.1 %).

3.4.2 Electrochemical impedance spectroscopy (EIS)

Impedance spectroscopy represents a powerful method for investigating the electrical properties of materials and interfaces of conducting electrodes. In this study, electrochemical impedance spectroscopy (EIS) measurements were performed to correct the electrochemical data for the electrolyte resistance and to evaluate the catalytic reaction kinetics in different electrode/electrolyte systems.

3.4.2.1 Basics of EIS

For measurements on an electrochemical system, an AC (alternating current) potential is applied and the resulting alternating current response is measured. Generally, electrochemical cells do not behave like linear systems, where the output signals are simply the superposition of the responses to each input signal. Due to the non-linearities, low-amplitude perturbation signals are necessary. With the small perturbation of the electrode state, a pseudo linear response can be described analog to the impedance of linear systems. In most cases, electrochemical systems are linear at signal amplitudes of 10 mV or less. The applied alternating potential to an electrode is expressed as a sinusoidal function in equation **(3.7)**:

$$E_t = E_0 \sin(\omega t) \quad \textbf{(3.7)}$$

where E_t is the potential at time t, E_0 is the amplitude of the sinusoidal potential, and $\omega = 2\pi f$ is the angular frequency. The resulting current response can be described by equation **(3.8)**:

$$I_t = I_0 \sin(\omega t - \phi) \quad \textbf{(3.8)}$$

where I_t is the current at time t, I_0 is the amplitude of the sinusoidal current, and ϕ the phase difference between the potential and the current. The impedance (Z) is generally defined as equation **(3.9)**:

$$Z(\omega) = E_t / I_t = Z_0 e^{j\phi} = Z_0 (\cos\phi + j \sin\phi) \quad \textbf{(3.9)}$$

$$j = (-1)^{1/2} \quad \textbf{(3.10)}$$

The variation of the electrochemical impedance with frequency is often of interest and can be represented graphically in different ways. In a Nyquist plot, the real part of Z (Z_{Im}) is plotted against the imaginary part (Z_{Re}) for different values of ω. An alternative representation, a Bode plot, displays both log $|Z|$ and ϕ versus log ω. Exemplary impedance plots are illustrated in **Figure 3.9**.

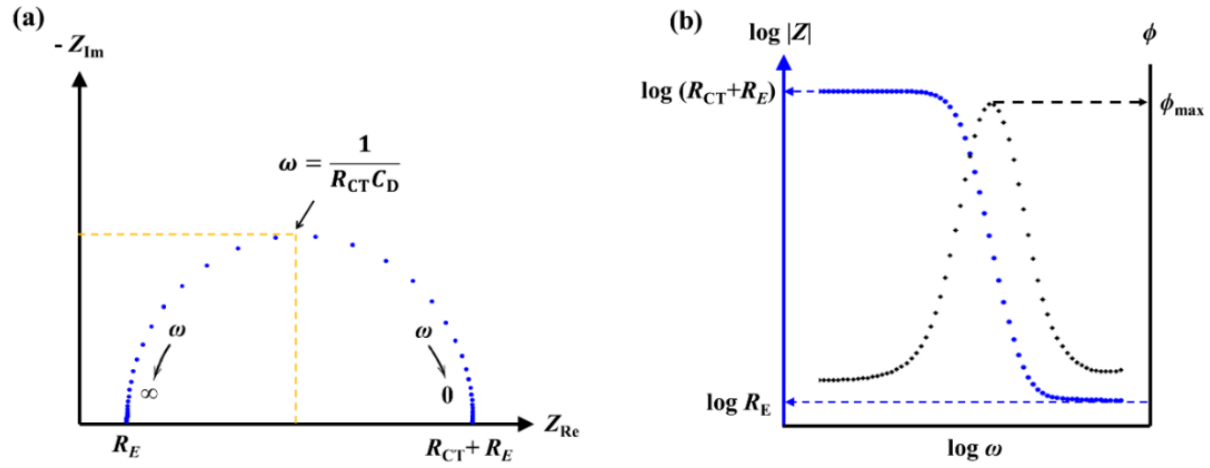

Figure 3.9 (a) Nyquist plot and (b) Bode plot.[35]

In general, an electrochemical half-cell can be considered simply as an impedance for a small sinusoidal excitation; hence its performance can be represented in terms of an equivalent electrical circuit that consists of resistances, capacitances or inductances. **Figure 3.10** presents a simple equivalent circuit corresponding to the spectra shown in **Figure 3.9**, considering the electrolyte resistance R_E, the charge transfer resistance R_{CT} and the double layer capacitance C_D. The parallel components are introduced because the total current through the working interface is the sum of distinct contributions from the faradaic process, i_f, and double-layer charging, i_c. All the current, of course, must pass through the solution resistance; therefore, R_E is inserted as a series component to represent this effect in the equivalent circuit. At high frequencies the capacitance allows the total current to flow and the current is just limited by R_E. At low frequencies the current has to flow via R_{CT}, thus in this case the current is defined by the sum of R_E and R_{CT}. It has to be kept in mind that the equivalent circuit discussed here is based on the simplest electrode process. Many

others may have to be considered in order to investigate more complex situations, such as those involving electro-reactants adsorption, multistep charge transfer, or homogeneous chemistry.

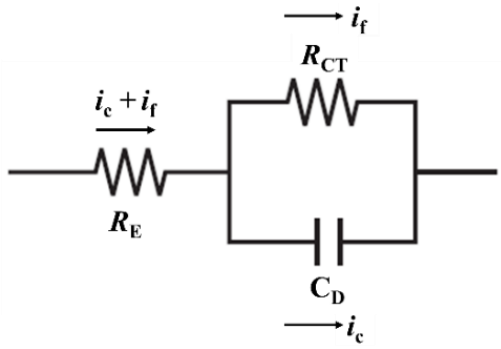

Figure 3.10 Equivalent circuit (Randell circuit) of an electrochemical half-cell for the impedance plots shown in **Figure 3.9**.

3.4.2.2 Correcting for uncompensated series resistance

The electronic and ionic current flow requires an electrostatic potential drop in the electrochemical cell. Most of the potential drop is compensated by using a reference electrode (RE), typically placed close to the working electrode (WE). The potential drop resulting from the ionic current flow through the electrolyte in between the RE and the WE is uncompensated, which will cause extra overpotential for an electrode to achieve a specific current density.[35] Thus, it must be corrected. For a simple planar electrode with a uniform current density the uncompensated resistance (R_u) is given by equation **(3.11)**:[35]

$$R_u = x/(kA) \qquad \textbf{(3.11)}$$

where x is the distance between the WE and the tip of RE (1.1 cm for the PECC-2 cell), A is the area of the WE, and k is the solution conductivity.[192] The uncompensated potential is thus given by equation **(3.12)**:

$$E_{uncompensated} = i * R_u \qquad \textbf{(3.12)}$$

where E is the potential, and i is the current (not current density) flowing through the electrode. In addition to the above three parameters, the conductivity of WE and any resistive components in series with the solution (e.g. bubbles on electrode surface) can also affect the R_u.[192]

To estimate R_u, we equate it to the cell impedance (i.e. R_E in **Figure 3.9**) at high frequency where the phase angle is closest to 0°, showing purely resistive circuit behavior. For every electrode introduced into an electrochemical cell, the R_u is measured prior to our standard series of electrochemical characterization experiments. In this work, the uncompensated resistance was determined to be 45 ~ 50 Ω in 0.1 M KOH, 5.3 ~ 5.6 Ω in 1.0 M KOH and 5.5 ~ 6 Ω in 0.5 M H_2SO_4 with Ti foil as substrates. Once R_u is measured, it can be used to correct the experimental polarization data after collection by following relationship:

$$E_{compensated} = E_{measured} - i * R_u \qquad \textbf{(3.13)}$$

According to the equations, the correction has a slight influence on the onset overpotential for that the

current is very small at that point. However, both the $E_{uncompensated}$ and the shift of the polarization curve will get larger and larger with the increasing of the current. Thus, the iR_E compensation is a useful method to eliminate the uncompensated potential drop, and to get more accurate activity evaluation of electrocatalysts.

3.4.3 Current/potential curves

Current/potential curves present the current flow between the working (WE) and the counter electrode (CE), with a linearly increasing potential relative to reference electrode (RE). The electrical current flow is correlated to the reaction rate, this is called 'Faraday's law'. The shape of the current/potential curve is very useful in providing information on which electrode reactions occur. For a simple one-electron-transfer reaction, only considering the kinetic limitation (e.g. temperature, concentrations of the redox species, activation energy), the current/potential behavior is described by the Butler-Volmer equation **(2.34)**. Special current/potential curves used in this study include open circuit potential (OCP) measurement, cyclic voltammetry (CV), linear sweep voltammetry (LSV), chronopotentiometry (i.e. galvanostatic scan) and chronoamperometry (i.e. potentiostatic scan) measurements:

- OCP measurements give the potential behavior over time for zero current flow.
- CV and LSV are voltammetry techniques, where a linear potential scan is applied to the electrode with the aid of the potentiostat. Since the current is measured as a function of time and the potential also varies with time, the results are usually shown as the potential dependent current, hence named as voltammetry.
- For a chronopotentiometry measurement, a certain current is applied to the electrode by the potentiostat, and the variation of potential is recorded as a function of time. The opposite is called a chronoamperometry measurement.

3.4.4 Test procedures

The electrocatalytic properties of the prepared samples for the HER or OER were investigated according to specified test procedures, which generally include the measurement of the open circuit potential (OCP), the electrochemical impedance spectroscopy (EIS) in a specified frequency range with a modulated signal amplitude of 10 mV near the OCP, a cyclic voltammogram (CV), a linear sweep voltammetry (LSV) and a chronopotentiometry scan. Polarization conditioning at starting potentials of CV and LSV measurements was implemented before each of the CV and LSV tests. The general electrochemical test procedures are summarized in **Table 3.3**.

Table 3.3 General electrochemical test procedures.

Step	Experimental	Conditions		Determined value or performance
		HER test	OER test	
1	OCP scan	15 min	15 min	Open circuit potential
2	EIS	1 Hz to 100 KHz	1 Hz to 200 KHz	Electrolyte resistance
3	Polarization	at 0 V vs. RHE	at 1.23 V vs. RHE	Polarize to start value of step 4
4	CV	50 mV s^{-1}, 3 scans, 0.05 V ~ -0.6 V	10 mV s^{-1}, 3 ~ 6 scans, 1.13 V ~ 1.83 V	Overpotential η at current density j
5	Polarization	at 0 V vs. RHE	at 1.23 V vs. RHE	Polarize to start value of step 6
6	LSV	1 mV s^{-1}, 1 scan, 0.05 V to -0.6 V	2 mV s^{-1}, 1 scan, 1.23 V to 1.83 V	Overpotential η at current density j, onset potential, Tafel slop and exchange current density
7	Chronopotentiometry	at -10 mA cm^{-2}	at +10 mA cm^{-2}	Stability

Potentials measured against the reference electrode were converted to the potentials versus the reversible hydrogen electrode and corrected for the electrolyte resistance based on the electrochemical impedance spectroscopy data. To compare the catalytic activity of the various catalysts with each other, the overpotentials at a current density of 10 mA cm^{-2}, obtained from the cyclic voltammogram or linear sweep voltammetry, are used as an indicator for the activity. The current density of 10 mA cm^{-2} was selected because it represents the approximate value expected for a photovoltaic device with 12.3% solar-to-hydrogen efficiency.[193] In addition, Tafel plot derived from the linear sweep voltammogram gives the information about the intrinsic activity in terms of Tafel slope and exchange current density. To evaluate the stability of the catalysts, chronopotentiometry curves were examined under a constant current density of -10 mA cm^{-2} for the HER or +10 mA cm^{-2} for the OER.

4. Electrodeposition of Nickel Nanoparticles for the HER

4.1 Introduction

Practical design of the HER electrocatalyst in acidic media has often been based on the well-known volcano relation, which generally describes the relationship between the catalytic activity of the metal electrocatalyst and the strength of the interaction between the metal surface and the adsorbed hydrogen (M-H_{ads}).[12, 66, 194] The high catalytic activity, which is shown by Platinum and other noble metals, is understood to be correlated to the intermediate M-H_{ads} bond strength.[12, 195] However, the low abundance and the high cost of these noble metals strongly limit their widespread application for water electrolysis. Among the non-noble metal electrocatalysts, Nickel has been calculated having an appropriate M-H_{ads} adsorption energy close to Platinum and it was identified as a promising alternative to Pt-based catalysts because of its low cost and relatively high electrocatalytic activity.[12, 73, 195] Nevertheless, Nickel metal on its own did not show a high catalytic activity in alkaline solutions.[66, 196] As pointed out in previous studies [66, 104, 197], the catalytic efficiency of the HER at high pH values can be simultaneously controlled by the M-H_{ads} bond strength as well as by the energy required to dissociate water into H and OH^- (the Volmer step: $H_2O + e^- \leftrightarrow H_{ads} + OH^-$). This implies that for Nickel metal with an appropriate M-H_{ads} energy, the water dissociation is an important step for catalyzing the HER under alkaline conditions. Thus, the HER process can be promoted by improving the water dissociation step.[66]

It was reported that the alkaline HER activity is enhanced through a bifunctional mode of the $Ni(OH)_2$/metal system, as the edges of $Ni(OH)_2$ clusters promote the water dissociation by weakening the O-H bond of the absorbed water.[66, 193, 197] The generated H is then "collected" and recombines on the nearby metal sites at a rate similar to that found in acidic.[66, 197] In particularly, N. Danilovic *et al.* have shown that the catalytic activity of the Ni metal surface modified by $Ni(OH)_2$ is improved by a factor of four versus the $Ni(OH)_2$-free Ni surface.[66] The synergistic effect on the HER was also accomplished using other metal/metal oxide electrocatalyst combinations showing a strong activity for the HER similar to Pt. These materials were e.g. nanoscale NiO/Ni heterostructures,[198] Ni/NiO/$CoSe_2$ nanocomposites[199], composite Ni/NiO-Cr_2O_3[200] and three-dimensional core/shell Co/Co_3O_4 nanosheets.[201] These results suggest solutions to improve the catalytic activity of Ni metal for the HER in alkaline media by the synergetic effects of different phases. Moreover, the oxidized Ni species [e.g. NiO, $Ni(OH)_2$ and NiOOH] were also reported to be highly efficient non-noble electrocatalysts for OER in alkaline solutions.[130, 140, 202]

Despite these previous achievements, it is still highly desirable to develop simple strategies to fabricate the Ni-based electrocatalysts and thereby advance their application in practice. The electrochemical deposition method has been considered as one of the best choices, because direct formation of Ni metal/oxides mixtures can be realized and controlled easily.[203-205] It is also an effective method to prepare thin film- and particle-type catalysts with high surface areas.[73, 206] However, the catalytic activity and stability of the electrodeposited Ni metal/oxides has not been investigated in detail employing XPS to identify the chemical

composition and the electronic structure, yet.

In this study, Ni NPs with the composition of Ni^0, NiO, and $Ni(OH)_2$ were electrodeposited onto Ti substrates by using cyclic voltammetry (CV). The surface morphology and the chemical properties of the NPs could be tuned over a wide range by varying the deposition conditions. The catalytic activity and stability of the NPs for the alkaline HER are discussed in correlation to the obtained XPS data.

4.2 Experimental section

4.2.1 Chemicals and electrodeposition

An aqueous solution of 10 mM nickel (II) chloride hexahydrate ($NiCl_2 \cdot 6H_2O$, 99.95%, Alfa Aesar) in 1 mM H_2SO_4 was used as the electrolyte for the electrodeposition of Ni NPs on Ti foil substrates (10 mm × 10 mm × 0.89 mm, 99.7%, Alfa Aesar) at room temperature. The electrodeposition setup is as described in Chapter 3.

Prior to deposition, the Ti substrates were consecutively cleaned (for 5 min) by ultrasonication in acetone, 2-propanol, and Millipore water (Merck Millipore, Milli-Q Reagent-Grade Water System, 18.2 MΩ cm^{-1}). Subsequently, the cleaned Ti substrates were etched for 3 min in 5% HF solution (VWR International GmbH) to remove the native oxides (TiO_x) and to homogenize the surface. Finally, the Ti substrates were thoroughly rinsed with Millipore water and were then dried in nitrogen gas flow. **Figure 4.1** shows the SEM images of cleaned and 5% HF etched Ti surfaces.

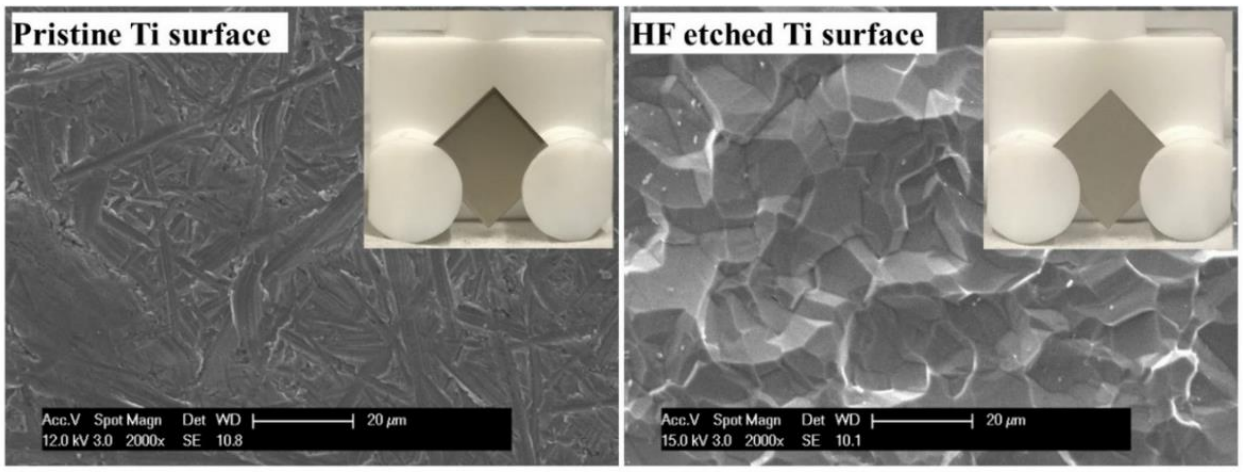

Figure 4.1 SEM images of pristine (cleaned) and 5% HF etched Ti surfaces. The insets show the photographs of the Ti foils inserted into the Teflon holder.

After each electrodeposition, the prepared Ti substrate decorated with Ni deposits (denoted as Ni/Ti) was removed from the electrolyte, ultrasonicated in Millipore water for 3 min, and dried under nitrogen gas flow prior to further characterization.

Table 4.1 Conditions for the electrodeposition of Ni NPs on Ti substrates by using cyclic voltammetry.

Set	Electrode	Potential range [V vs. RHE]	Scan rate [mV s^{-1}]
I	Ni/Ti-1	-1.8 to +0.2	50
	Ni/Ti-2	-1.8 to +0.7	50
	Ni/Ti-3	-1.8 to +1.2	50
	Ni/Ti-4	-1.8 to +1.7	50
	Ni/Ti-5	-1.8 to +2.2	50
II	Ni/Ti-6	-1.8 to +1.2	5
	Ni/Ti-7	-1.8 to +1.2	10
	Ni/Ti-8	-1.8 to +1.2	100

In this work, cyclic voltammetry was employed to prepare the Ni/Ti electrodes. To understand the influence of the deposition parameters on the surface morphology and the chemical composition of the Ni NPs (which will highly affect the HER catalytic activity), several sets of experiments were performed (see **Table 4.5**), but only two were selected here as being representative for all measurements (see **Table 4.1**). For each set of experiments, the potential range and the scan rate were changed. The Ni/Ti samples are annotated as Ni/Ti-*n*. Ni/Ti-1, Ni/Ti-2, Ni/Ti-3, Ni/Ti-4, and Ni/Ti-5 were prepared with different potential ranges (set I); Ni/Ti-3, Ni/Ti-6, Ni/Ti-7, and Ni/Ti-8 were prepared at different scan rates (set II). Each deposition was performed for one cycle, as shown in **Figure 4.10**. Also, the influence of varying the number of cycles for the deposition from one to three was investigated, but it showed only showed a very minor effect (see **Figure 4.2**). Therefore, these measurements are not included here.

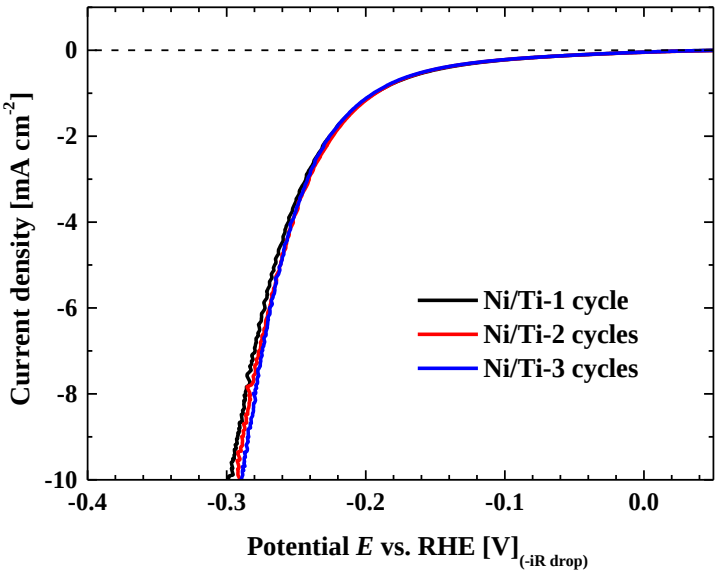

Figure 4.2 LSV curves recorded in 0.1 M KOH (pH = 12.9) of the Ni/Ti electrodes prepared with different number of cycles.

4.2.2 Characterization

After the electrodeposition and the electrochemical measurements, the Ni/Ti electrodes were characterized by SEM and XPS. The average projected particle size of the deposits was obtained by statistical analysis (randomly) on 100 particles in the SEM images with high magnification (≥ 20000V) by using the software package "Nano Measurer 1.2".[207] Further information on the characterization setups and parameters has been given in chapter 3.

4.2.3 Electrochemical measurements

The electrochemical measurements were performed at room temperature by using the setup as described in Chapter 3. The Ni-decorated Ti substrate and a Pt coil served as the working electrode and the counter electrode, respectively. An Ag/AgCl (3 M KCl, 0.209 V vs. SHE) reference electrode was used for the measurements in 0.1 M KOH, and a Hg/HgO (1 M NaOH, 0.11 V vs. SHE) reference electrode was used for the measurements in 1 M KOH. EIS measurements were performed in the frequency range of 1 Hz to 100 KHz with a modulated signal amplitude of 10 mV near the OCP to obtain the resistance of the electrolyte. The catalytic activity for the HER was determined by LSV in the potential range of 0.05 to -0.6 V versus RHE at a scan rate of 1 mV s^{-1}. Stability measurements were performed under a constant current density of -10 mA cm^{-2} for up to 30 h in 0.1 M KOH. Potentials $E_{vs.\ ref.}$, measured against the reference electrodes, were converted to the potentials versus the RHE ($E_{vs.\ RHE}$) according to equation **(3.1)**. The values were corrected for electrolyte resistance on the basis of the EIS data. Furthermore, the current density values were normalized with respect to the geometrical surface area of 0.5 cm^2.

4.3 Results and Discussion

4.3.1 Tuning Ni NPs upon deposition potential range

4.3.1.1 Surface morphology

The surface morphologies of the Ni/Ti electrodes were characterized by SEM. Herein, **Figure 4.3a-e** display the SEM images of the Ni/Ti electrodes prepared with different potential ranges (Ni/Ti-1 to Ni/Ti-5). As can be seen from the images, the Ti substrates are uniformly covered with Ni NPs after CV deposition, which is an indication that the chosen technique can be successfully applied for the formation of Ni NPs. Moreover, one can observe that a nearly mono-dispersed coverage of Ni NPs on the Ti substrates is achieved (see insets in **Figure 4.3a-e**), indicating that a high amount of active sites might be available.[208] **Figure 4.3f** shows a plot of the average projected particle size of the electrodeposited Ni NPs versus the applied potential range. It is obvious, that the average particle size (~100 nm) does not depend on the chosen deposition conditions.

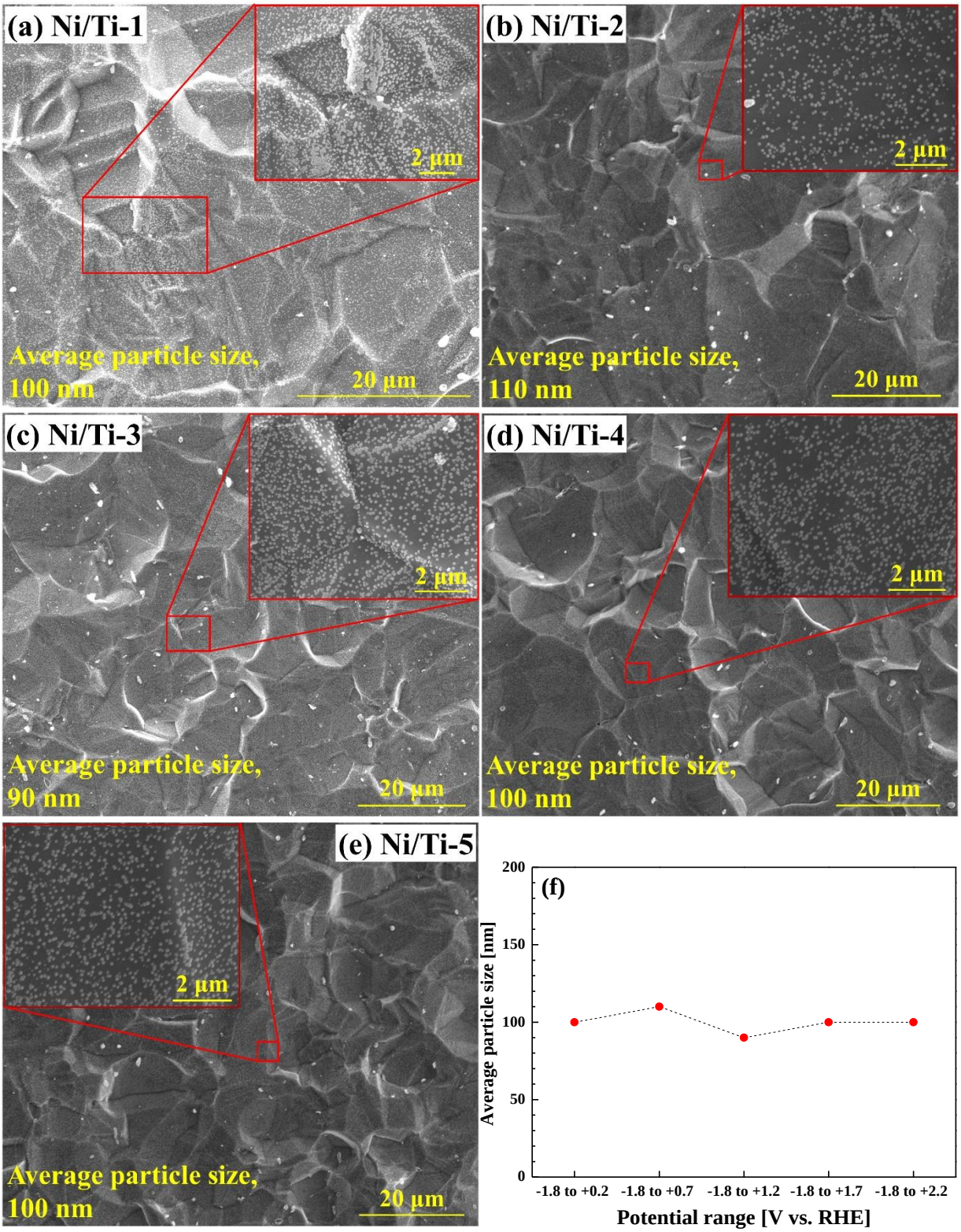

Figure 4.3 (a-e) SEM images of the Ni/Ti electrodes prepared with different potential ranges (see **Table 4.1**). The large structures with sizes between 10 and 20 µm are from the Ti/TiO_2 substrate. The insets show enlarged SEM images of the corresponding marked areas with the bright spots being due to the Ni NPs. (f) Shown is the average particle size of the Ni NPs as a function of the employed potential range.

4.3.1.2 XPS characterization

XPS measurements were conducted to figure out the chemical environment of the electrodeposited Ni NPs on Ti substrates. **Figure 4.4** shows the XP spectra of the Ti substrate after etching in 5% HF solution and the Ni/Ti electrodes (Ni/Ti-1 to Ni/Ti-5) prepared by cyclic voltammetry (one cycle) at different potential ranges with the scan rate of 50 mV s^{-1}. **Figure 4.4a** displays the survey spectra. As expected, no peaks corresponding to the Ni element are observable in case of the bare Ti substrate. However, in case of the Ni/Ti electrodes, Ni signals do appear. The survey spectra of the Ni/Ti electrodes also reveal peaks, which are assigned to the elements of Ti, C and O. No other metal impurities have been detected. An insight into the chemical states and the chemical composition of the Ni NPs can be evaluated by the examination of the Ni 2p, Ti 2p and O 1s detail XP spectra.

The Ni 2p spectra (**Figure 4.4b**) exhibit typical peaks located at binding energies (BEs) of 852.7 eV and 869.9 eV, which are attributed to Ni $2p_{3/2}$ and Ni $2p_{1/2}$ for Ni metal (Ni^0), respectively.[182, 209] A significant split of the spin-orbit components is found to be about 17.2 eV, which is in good agreement with the literature (Δ_{Ni° = 17.3 eV).[182, 209] One can observe that the intensities of both peaks are gradually reduced from Ni/Ti-1 to Ni/Ti-5. The continuous decrease in these peak intensities indicates that the amount of Ni^0 is reduced when the deposition potential range is increased to higher anodic values from 0.2 to 2.2 V. Further significant peaks at 856.2 eV and 873.9 eV are assigned to Ni $2p_{3/2}$ and Ni $2p_{1/2}$ for $Ni(OH)_2$, respectively. The characteristic spin-orbit distance for the $Ni(OH)_2$ phase is measured to be around 17.7 eV, which is well consistent with data reported previously.[210-212] Additional peaks with small intensities are observed at 854.2 eV and 871.7 eV for Ni $2p_{3/2}$ and Ni $2p_{1/2}$ in case of the Ni/Ti-3, Ni/Ti-4 and Ni/Ti-5 electrodes. The appearance of these two peaks with the spin-orbit distance of 17.5 eV suggests the presence of NiO for those samples.[182, 209] The satellite features present on the spectra at BEs of 859.9 eV, 860.9 eV and 861.5 eV are attributed to Ni $2p_{3/2}$ for Ni^0, NiO and $Ni(OH)_2$, respectively.[209]

The Ti 2p spectra (**Figure 4.4c**) show peaks located at 459.0 eV (Ti $2p_{3/2}$) and 464.8 eV (Ti $2p_{1/2}$) with a spin orbit splitting of 5.8 eV corresponding to TiO_2.[213] The presence of a small peak at 453.8 eV in the spectra of the bare Ti substrate and the Ni/Ti-1 to Ni/Ti-3 electrodes is attributed to the pure Ti metal substrate.[209, 213]

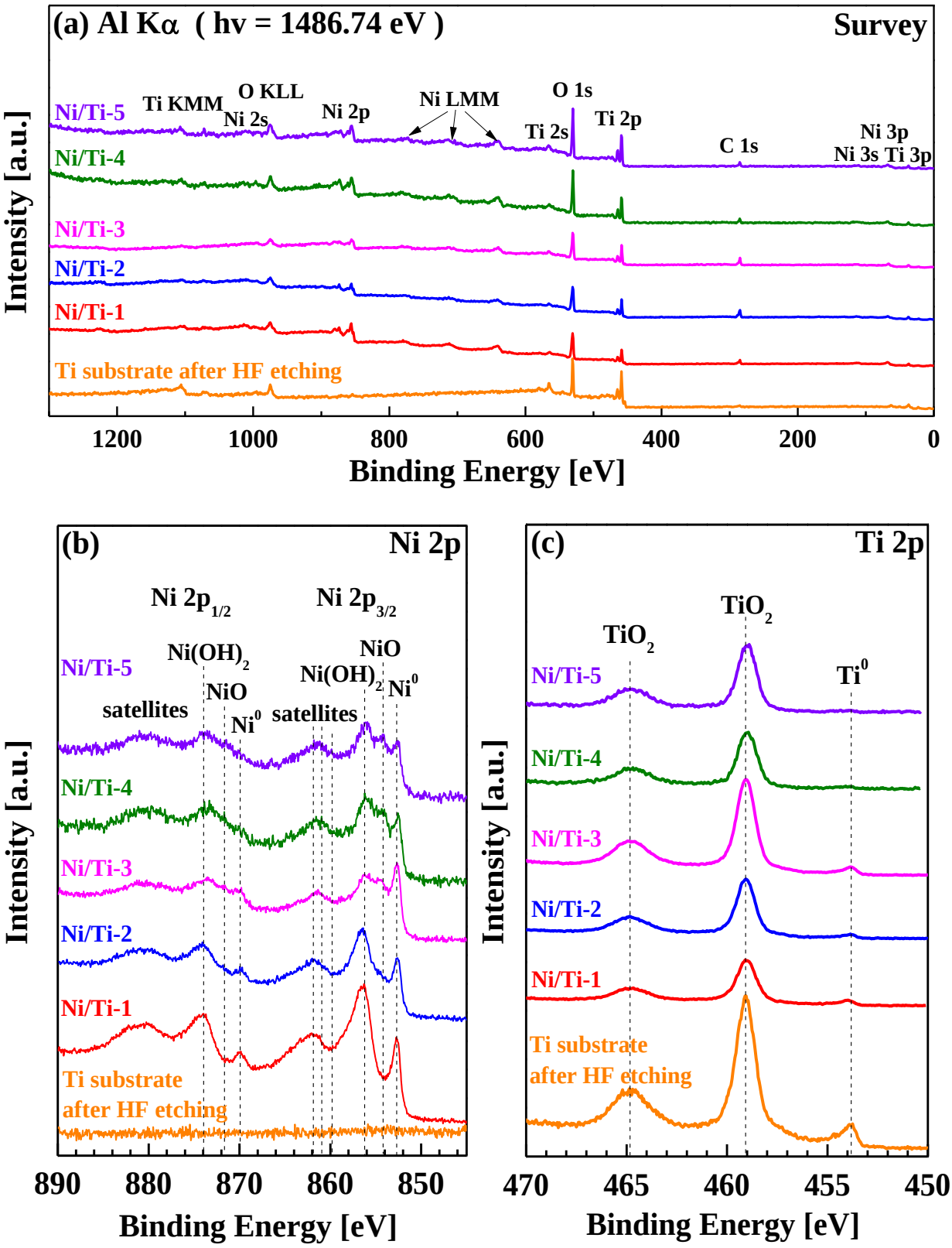

Figure 4.4 X-ray photoelectron spectra of the electrodeposited Ni NPs on Ti substrates (Ni/Ti) using different potential ranges for deposition (see **Table 4.1**): (a) survey, (b) Ni 2p region and (c) Ti 2p region. The Ti substrate after etching in 5% HF is added for comparison.

Additional information about the chemical states of the Ni NPs is obtained from an investigation of the O 1s spectra (**Figure 4.5**). From the deconvolution and fitting of these spectra (Ni/Ti-1 to Ni/Ti-5), several characteristic emission lines can be identified. The peaks located at ≈529.6 eV and ≈531.5 eV are associated with the O^{2-} in the NiO lattice and OH^- in $Ni(OH)_2$, respectively.[209, 212, 214] For comparison, the O 1s spectrum of the etched Ti substrate is also added and reveals two features. The main peak situated at ≈530.4 eV is assigned to lattice O^{2-} in TiO_2, while the shoulder located at a higher BE of ≈531.3 eV is related to the adsorbed water on the TiO_2 surface.[215] The peak associated with the lattice O^{2-} in TiO_2 is visible for all samples. In addition to the previous assigned emissions for Ni/Ti-1 to Ni/Ti-5, features at ≈532.5 eV and ≈533.5 eV are attributed to carbon-oxygen species (e.g. C-O, C=O) and adsorbed H_2O on the surface, respectively.[190, 216] In general, the chemical composition determined from the O 1s spectra is in good agreement with the data obtained from the Ni 2p spectra (see **Figure 4.4b**).

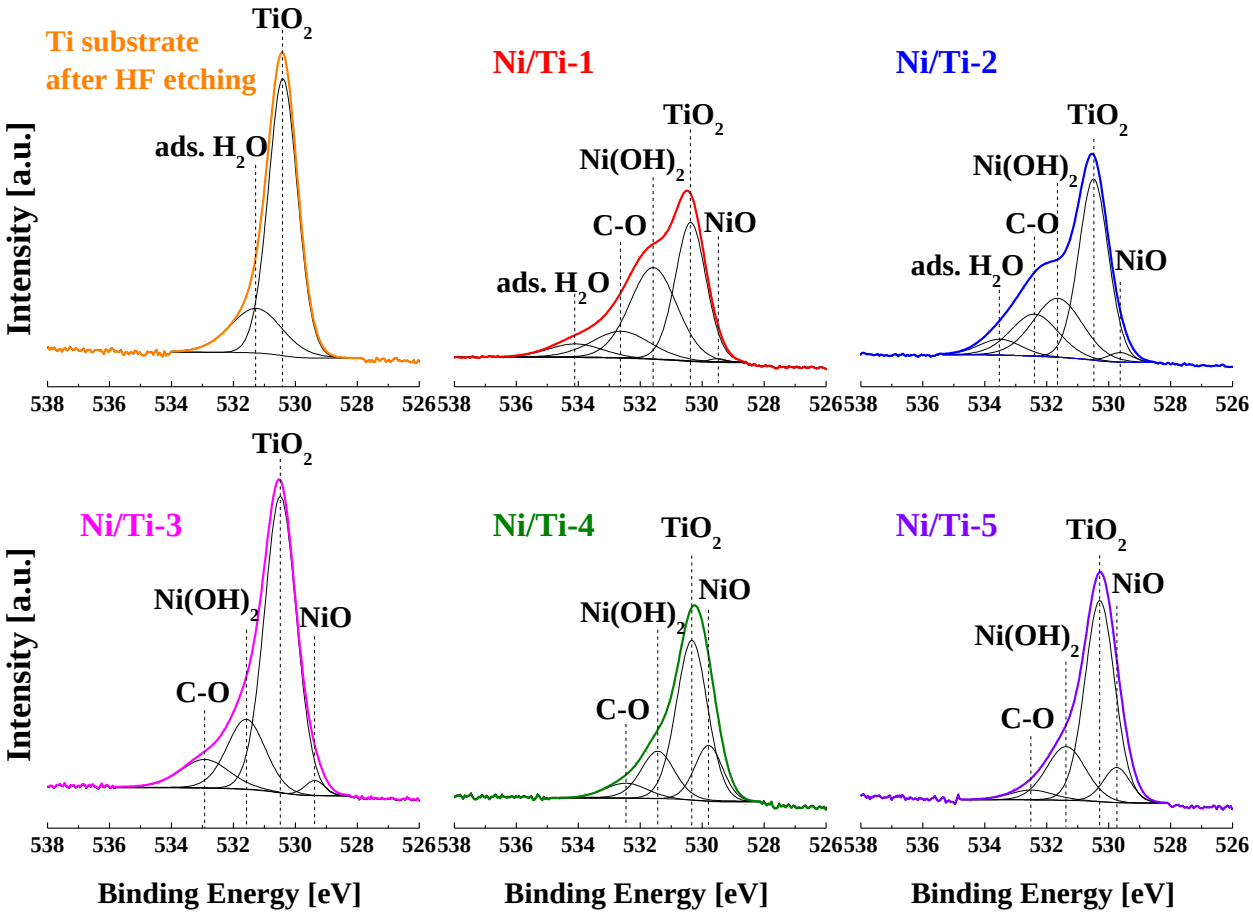

Figure 4.5 Fitted O 1s X-ray photoelectron spectra of the electrodeposited Ni NPs on Ti substrates (Ni/Ti) prepared by varying potential ranges (see **Table 4.1**). The Ti substrate after etching in 5% HF is added for comparison.

The C 1s detail XP spectra of all the Ni/Ti electrodes (**Figure 4.6**) reveal the presence of a C-C component (C-C, 285.0 eV), epoxy/hydroxyls (C-O, ≈286.7 eV) and carbonyl groups (C=O, ≈288.7 eV). There are three main sources of carbon: (1) from the electrolyte solutions and the used equipment, (2) from dissolved

CO_2, and (3) by the adsorption of CO_x compounds during transport of the sample through air from the electrochemical deposition to the XPS machine. With regarded to (1) the same equipment and the highly pure electrolytes with Millipore water as the solvent were always used for the experiments; to point (2): the amount of dissolved CO_2 should be very small under the working condition with the pH value of electrolyte lower than 3. Point (3) cannot be avoided at moment, but we have recently setup a special electrochemical cell, which is directly connected to the surface science apparatus, where experiments can be done under rare gas atmosphere to study the influence on the reaction products from different kind of atmospheric gases. For the determination of NiO and $Ni(OH)_2$ content, the contributions of Carbon-Oxygen compounds to the O 1s area have to be considered. These were obtained from the C 1s detail spectra and used to constrain the area of the fitted O 1s lines representing C-O species. The same procedure was done on the contribution of Ti-O species to the O 1s area.

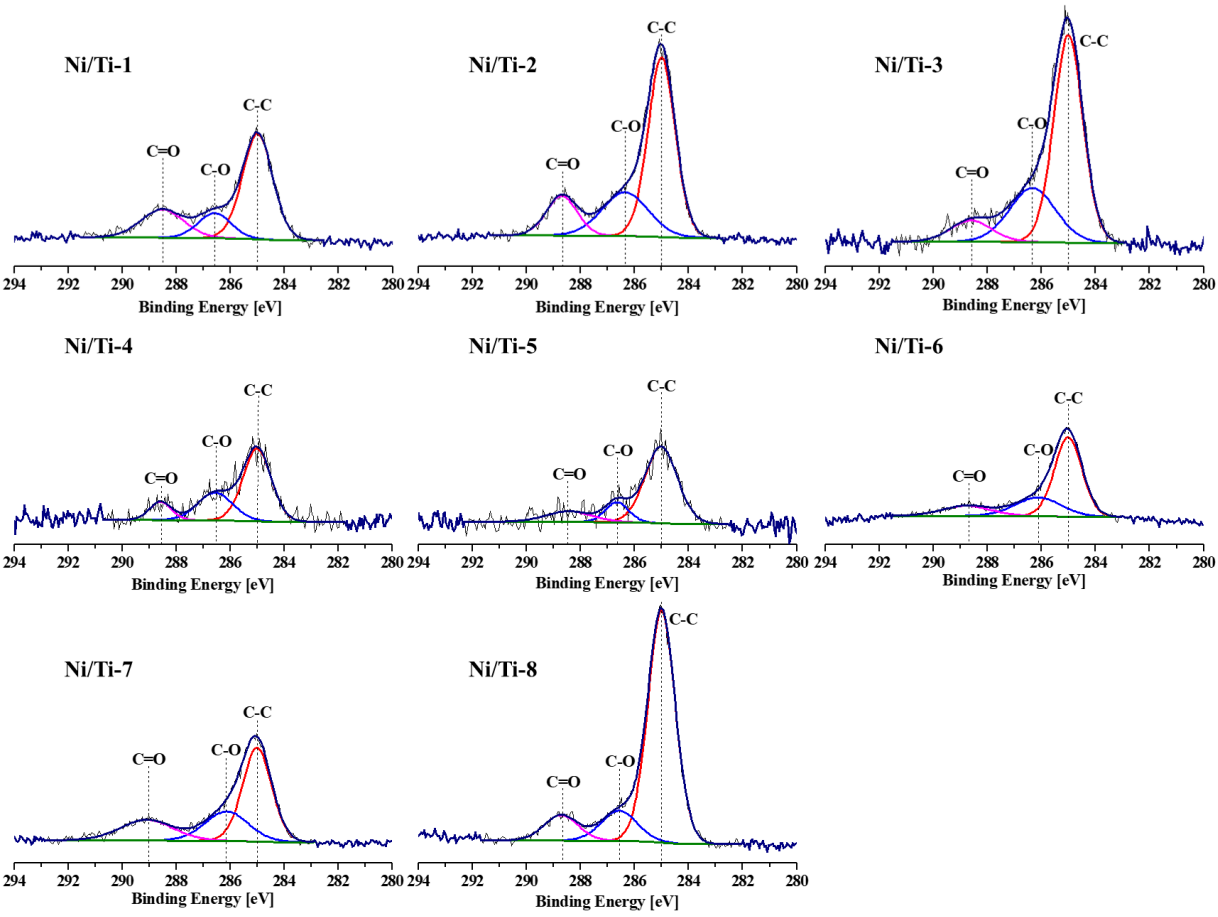

Figure 4.6 C 1s detail X-ray photoelectron spectra of the Ni/Ti electrodes (see **Table 4.1**).

From the quantitative XPS analysis the atomic concentrations of Ni, Ti, C, and O of the differently prepared Ni/Ti electrodes can be obtained, which are summarized in **Table 4.2**. The amount of O is separated into contributions from NiO, $Ni(OH)_2$ and other species including Ti-O, C-O and adsorbed water. Based on these values the chemical composition of the electrodeposited Ni NPs has been calculated, which is also summarized in the table. The results indicate that the concentration of Ni^0 decreases at higher anodic

potentials, where oxidation is taking place during the forward voltammetry sweep. At the same instance the percentage of NiO increases to 55.2 % at an anodic scan potential of 1.7 V. To understand the reduction-oxidation behavior of the Ni species on the Ti substrate under variation of the applied voltage, a typical cyclic voltammogram was recorded between -1.8 and +2.2 V vs. RHE (see **Figure 4.10** and the corresponding text). At deposition voltages above 1.7 V we additionally observe a strong increase in the OER. Therefore, we assume that by using such a high anodic potential part of the initially formed $Ni^{2+}O$ is oxidized to $Ni^{3+}OOH$, which can explain the decrease in the NiO intensity for Ni/Ti-5 compared to the Ni/Ti-4 compound. The formed NiOOH cannot be easily discriminated in XPS from $Ni(OH)_2$.[212]

Table 4.2 Atomic concentrations of Ni, Ti, C, and O of the Ni/Ti electrodes prepared with different potential ranges (see **Table 4.1**) as well as the chemical composition of the deposited Ni NPs.

Electrodes	Potential range (V vs. RHE)	Ni (%)	Ti (%)	C (%)	O (%)			chemical composition of the Ni NPs (%)		
					O in NiO	O in $Ni(OH)_2$	Other [a]	Ni^0 [b]	NiO	$Ni(OH)_2$
Ni/Ti-1	-1.8 to +0.2	19.7	9.0	17.5	0.3	21.3	32.2	44.4	1.5	54.1
Ni/Ti-2	-1.8 to +0.7	12.7	10.6	24.6	1.1	13.5	37.5	38.2	8.7	53.1
Ni/Ti-3	-1.8 to +1.2	10.3	13.9	24.1	1.2	9.9	40.6	40.2	11.7	48.1
Ni/Ti-4	-1.8 to +1.7	17.4	14.1	14.6	9.6	9.5	34.8	17.5	55.2	27.3
Ni/Ti-5	-1.8 to +2.2	14.0	15.8	15.2	5.5	12.2	37.3	17.1	39.3	43.6

[a] includes the O in Ti-O, adsorbed water and carbon-oxygen species; [b] was calculated by first calculating the concentrations of NiO and $Ni(OH)_2$ from the O 1s data. Ni^0 is the remaining concentration.

In summary, the XPS results indicate that the electrodeposition of Ni leads to NPs with a mixed chemical composition of $Ni/NiO/Ni(OH)_2$. The relative contribution of the different compounds can be controlled by the variation of the potential range employed for the electrodeposition process.

4.3.2 Tuning Ni NPs upon scan rate

4.3.2.1 Surface morphology

Figure 4.7a-d show the SEM images of the Ni/Ti-6, Ni/Ti-7, Ni/Ti-3 and Ni/Ti-8 electrodes prepared with scan rates of 5, 10, 50 and 100 mV s^{-1}, respectively. A nearly mono-disperse coverage of Ni NPs is again observed on the Ti substrates (see **the insets in Figure 4.7a-d)**. Moreover, an increase in the scan rate from 5 to 100 mV s^{-1} results in a decline of the Ni NPs average size from 160 to 60 nm, as shown in **Figure 4.7e.**

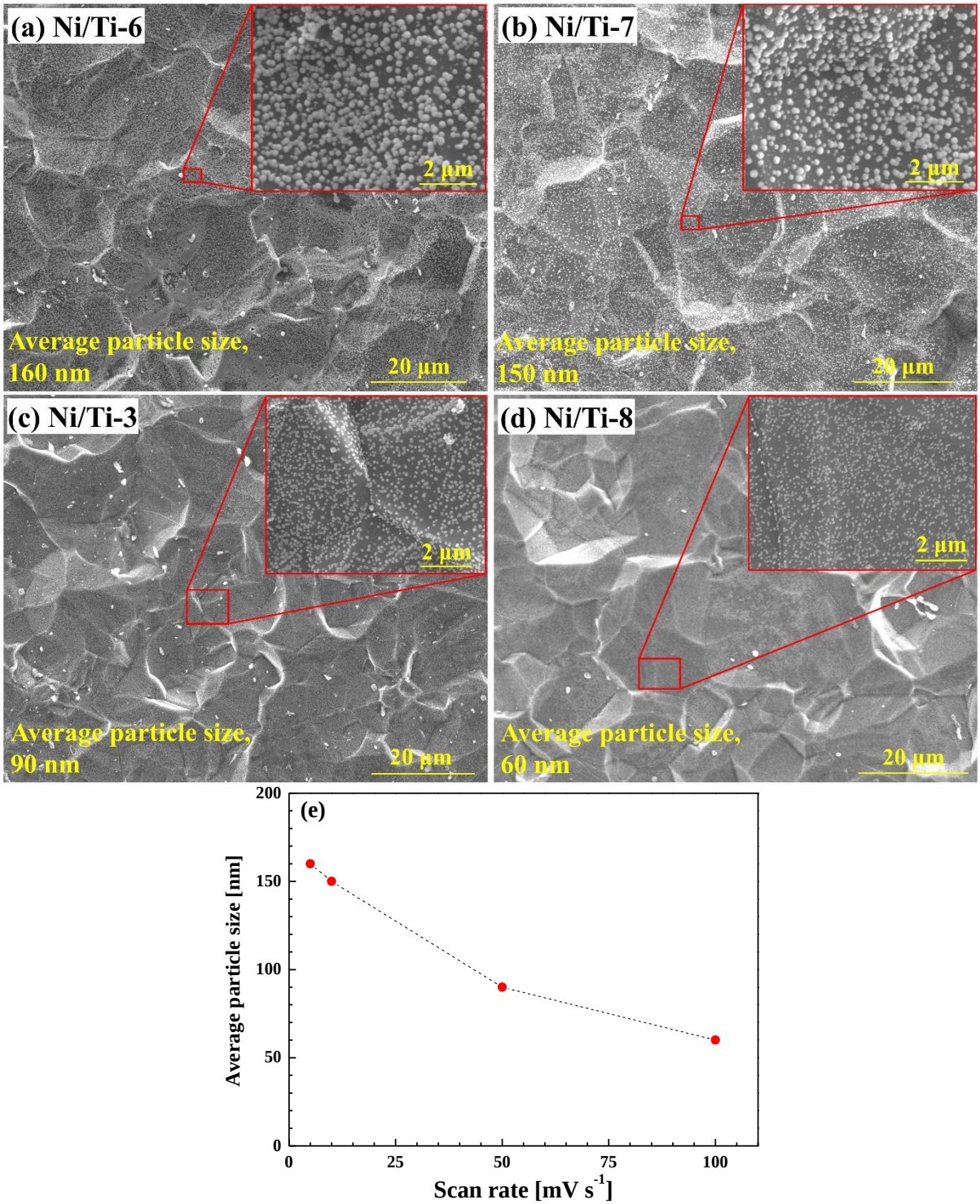

Figure 4.7 (a-d) SEM images of the Ni/Ti electrodes prepared with different scan rates (see **Table 4.1**). The insets show the enlarged SEM images of the corresponding marked areas. (e) Shown is the average particle size of the electrodeposited Ni NPs as a function of the scan rate.

4.3.2.2 XPS characterization

To figure out the influence of the scan rate, XPS measurements were conducted on the electrodes of Set II, including Ni/Ti-6 (5 mV s^{-1}), Ni/Ti-7 (10 mV s^{-1}), Ni/Ti-3 (50 mV s^{-1}) and Ni/Ti-8 (100 mV s^{-1}).

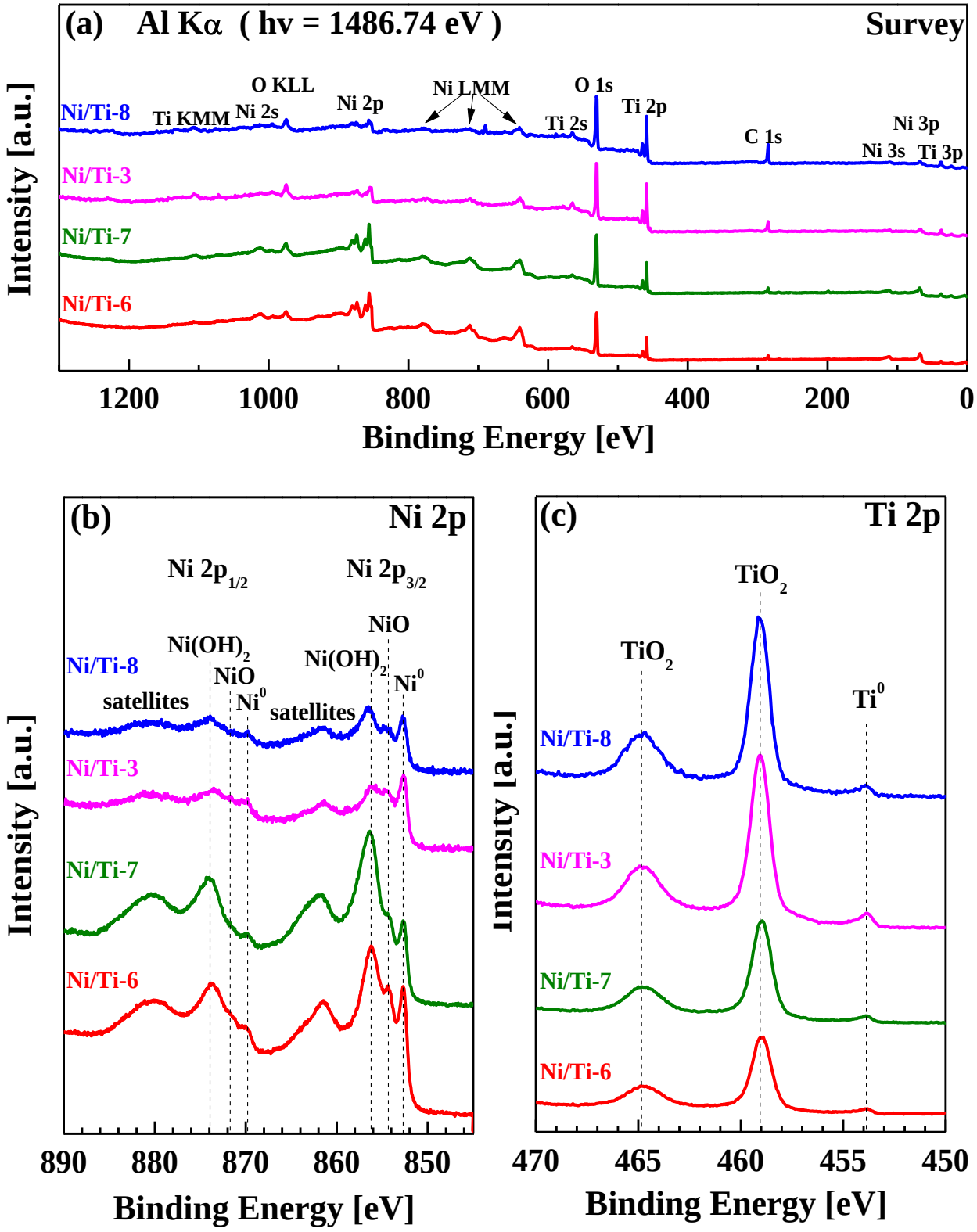

Figure 4.8 X-ray photoelectron spectra of the electrodeposited Ni NPs on Ti substrates (Ni/Ti) obtained with different scan rates: (a) survey, (b) Ni 2p region and (c) Ti 2p region. The Ni/Ti samples are listed in **Table 4.1**.

Figure 4.8a shows the survey spectra of those Ni/Ti samples. The survey spectra point out that increasing the scan rate leads to less intensity of the Ni 2p signals and at the same time to a higher intensity of the Ti 2p signals. These observations are in good accordance with the SEM images recorded for those samples, indicating that a larger amount of Ni is deposited on the substrate at a lower scan rate. **Figure 4.8b** shows the Ni 2p core level spectra. Similar to the Ni 2p spectrum of Ni/Ti-3 electrode, the spectra of Ni/Ti-6 to Ni/Ti-8 electrodes also exhibit the characteristic peaks of Ni $2p_{3/2}$ and Ni $2p_{1/2}$ ascribed to Ni^0 (852.7 eV and 869.8 eV), NiO (854.3 eV and 871.7 eV) and $Ni(OH)_2$ (856.2 eV and 873.9 eV), respectively. **Figure 4.8c** shows the Ti 2p core level spectra. The intensities of the peaks attributed to TiO_2 (459.0 eV and 464.8 eV) and Ti metal (453.8 eV) are reduced with decreasing the scan rate, further indicating that a lower scan rate leads to a higher coverage of the Ni NPs.

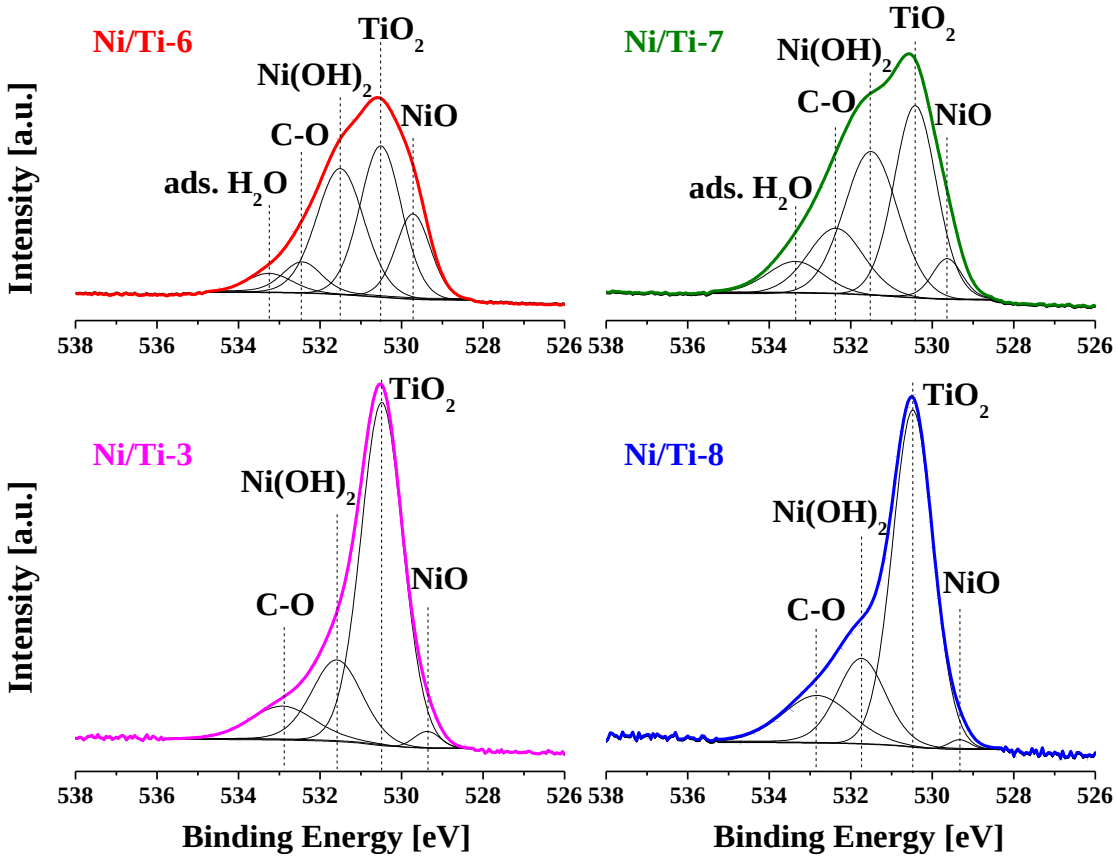

Figure 4.9 Fitted O 1s X-ray photoelectron spectra of the electrodeposited Ni NPs on Ti substrates (Ni/Ti) obtained with different scan rates. The Ni/Ti samples are listed in **Table 4.1**.

The deconvolution analysis of the O 1s spectra presents features at BEs of ≈529.5 eV and ≈531.6 eV, which are attributed to NiO and $Ni(OH)_2$ species, respectively (**Figure 4.9**).[190, 214] Three other peaks can be also observed at 530.5 eV, ≈532.6 eV and 533.3 eV, which are assigned to O^{2-} lattice in TiO_2, carbon-oxygen species and adsorbed water, respectively. These observations suggest that Ni/NiO/$Ni(OH)_2$ composite NPs are deposited on all these four electrodes. Moreover, the intensity of the peak corresponding to NiO is increased with decreasing the scan rate, indicating that a higher amount of NiO can be deposited at lower

scan rate. **Table 4.3** summarizes the atomic concentrations of Ni, Ti, C and O of the Ni/Ti electrodes prepared with different scan rates as well as the calculated chemical composition for the obtained Ni NPs. With the decrease of the scan rate from 100 mV s^{-1} to 5 mV s^{-1}, the percentage of NiO in the Ni NPs increases from 7.1% to 34.3%.

Table 4.3 Atomic concentrations of Ni, Ti, C, and O of the Ni/Ti electrodes prepared with different scan rates (see **Table 4.1**) and the chemical composition of the obtained Ni NPs.

Electrode	Scan rate (mV s^{-1})	Ni (%)	Ti (%)	C (%)	O (%)			chemical composition of the Ni NPs (%)		
					O in NiO	O in $Ni(OH)_2$	other [a]	Ni^0 [b]	NiO	$Ni(OH)_2$
Ni/Ti-6	5	27.1	8.2	10.4	9.3	18.9	26.1	30.8	34.3	34.9
Ni/Ti-7	10	25.6	8.1	11.8	4.4	20.3	29.8	43.2	17.2	39.6
Ni/Ti-3	50	10.3	13.9	24.1	1.2	9.9	40.6	40.2	11.7	48.1
Ni/Ti-8	100	7.0	12.6	34.2	0.5	8.8	36.9	30	7.1	62.9

[a] includes the O in Ti-O, adsorbed water and carbon-oxygen species; [b] was calculated by difference.

4.3.3 Deposition behavior by cyclic voltammetry

4.3.3.1 Reduction-oxidation of the nickel species in voltammetric electrodeposition

To understand the reduction-oxidation behavior of the Ni species on the Ti substrate under variation of the applied voltage, a typical cyclic voltammogram was recorded between -1.8 and +2.2 V vs. RHE at a scan rate of 50 mV s^{-1} (see **Figure 4.10a**). The arrows show the scan directions.

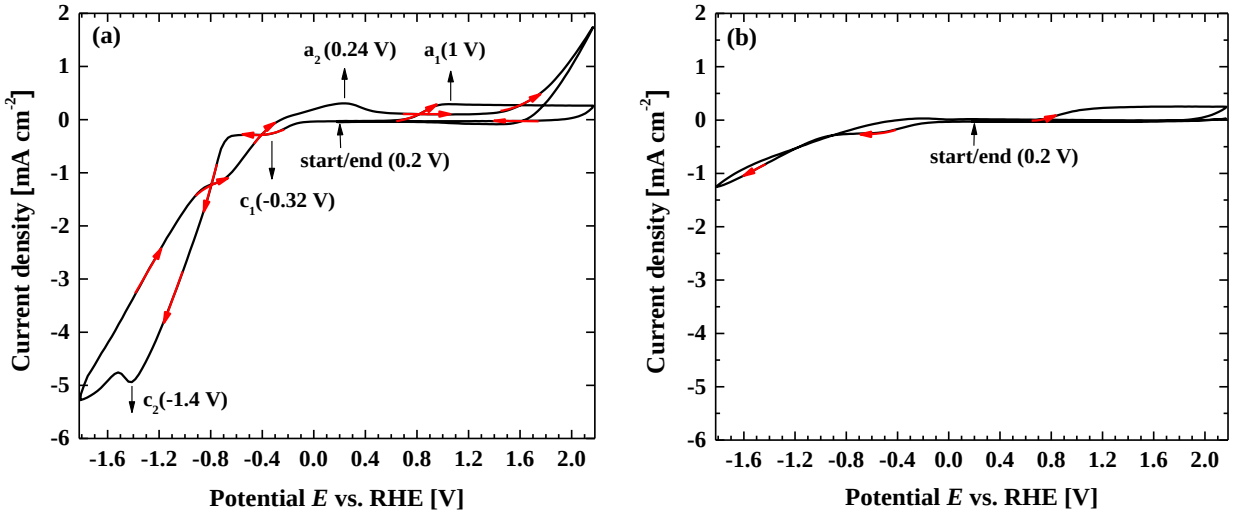

Figure 4.10 (a) CV curve of Ni electrodeposition onto Ti substrate in the deposition electrolyte of 10 mM $NiCl_2$ in 1 mM H_2SO_4; (b) CV curve of the Ti substrate in 1 mM H_2SO_4 without $NiCl_2$. Scan rate: 50 mV s^{-1}.

The scan was initiated at +0.2 V, then sequentially reversed at +2.2 V, -1.8 V and +2.2 V, and terminated at +0.2 V. The CV curve can be clearly observed including two anodic peaks (a_1 and a_2) and two cathodic peaks (c_1 and c_2). The anodic peak a_1 during the scan from +0.2 V to +2.2 V is due to the oxidation of the Ti substrate (see **Figure 4.10b**). The cathodic peak c_1 appears at -0.32 V, which is attributed to the electro-reduction of Ni^{2+} ions into Ni metal:[73, 203, 205, 217]

$$Ni^{2+}(aq) + 2\ e^- \rightarrow Ni^0\downarrow\ (E° = -0.26\ V). \qquad \textbf{(4.1)}$$

At more negative potentials, an exponential increase in current density was observed beyond -0.64 V, which is related both to Ni^{2+} reduction on the substrate and hydrogen evolution on the deposited Ni surface.[73, 205, 218] There exist a large number of publications on the electroplating of Ni and Ni-oxides/hydroxides on different type of substrates, which in general agree that the formation of the Ni-hydroxide as an important intermediate or as a competing process is the crucial reaction step for the Ni deposition.[30, 73, 204-205, 208, 218-219] The reduction of H^+ at the cathode causes a local increase of the pH, which then leads to the competing reaction **(4.2)**:

$$Ni^{2+}(aq) + 2\ H_2O \rightarrow Ni(OH)_2\ (ads) + 2\ H^+ \qquad \textbf{(4.2)}$$

$$Ni(OH)_2\ (ads) + 2\ e^- + 2\ H^+\ (aq) \rightarrow Ni\ (s) + 2\ H_2O \qquad \textbf{(4.3)}$$

The formed Nickel hydroxide is then partially reduced to metallic Ni according to reaction **(4.3)**, which shows a maximum peak c_2 at -1.4 V. The exact position of this peak depends strongly on the scan rate and it can also depend on the type of anion and the general pH of the solution. The reduction process can also be described involving a singly hydroxylated Nickel species adsorbed on the surface. A very good discussion of the different involved steps for Nickel electroplating is given in ref.[219].

From the XPS data we obtain an almost 1:1 concentration relation of Ni^0 and $Ni(OH)_2$ on our electrode for the deposition reaching only up to 0.2 V into the anodic regime, which suggests a comparable contribution of reactions **(4.2)** and **(4.3)** to the overall composition.

The anodic peak a_2 at +0.24 V on the CV curve indicates the oxidation of Ni^0 to nickel oxides species. The XPS results imply that the growth of NiO could be also realized by the transformation of hydroxide, since both the Ni^0 as well as the $Ni(OH)_2$ concentration decrease with the increase of the NiO:[203, 205]

$$Ni(OH)_2\ (ads) \rightarrow NiO\ (ads) + H_2O \qquad \textbf{(4.4)}$$

4.3.3.2 Determination of Ni NPs loadings

Figure 4.11 shows the deposition current as a function of the time for the electrodeposition for five different samples from **Table 4.3** and **Table 4.6**. From the areas of the I-t curves related to the reduction and oxidation of the Ni species the corresponding electric quantities and the total Ni amount are calculated and summarized in the following **Table 4.4**. The Ni amount is calculated by assuming that all electrons are used to reduce the Ni^{2+}. However, due to the hydrogen evolution in the cathodic regime, the calculated values could be overestimated.

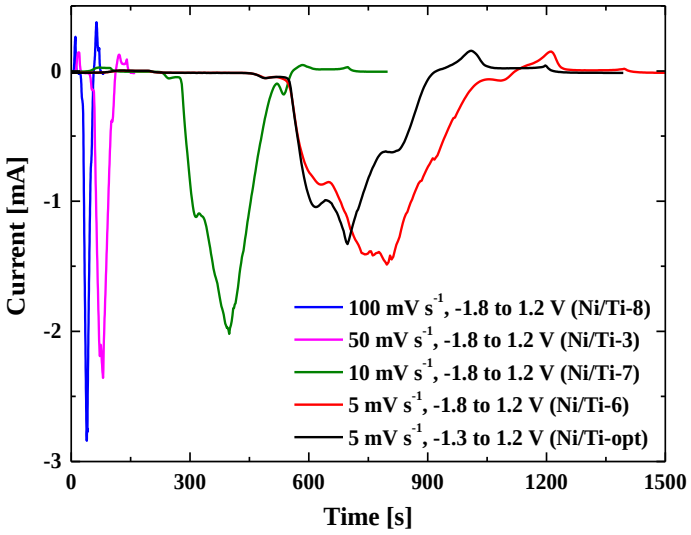

Figure 4.11 Current-time curves of the Ni NPs electrodeposition.

Table 4.4 Calculation of the amount of deposited Ni from **Figure 4.11**.

Sample			Area (mA s)	Electric charge (C)	Calculated Ni amount [a] (mg)
Number	Deposition condition				
Ni/Ti-6	-1.8 to 1.2 V vs. RHE	5 mV s^{-1}	-414.4	-0.4144	0.126
Ni/Ti-7	-1.8 to 1.2 V vs. RHE	10 mV s^{-1}	-267.6	-0.2676	0.082
Ni/Ti-3	-1.8 to 1.2 V vs. RHE	50 mV s^{-1}	-65.5	-0.0655	0.020
Ni/Ti-8	-1.8 to 1.2 V vs. RHE	100 mV s^{-1}	-35.3	-0.0353	0.011
Ni/Ti-opt	-1.3 to 1.2 V vs. RHE	5 mV s^{-1}	-257.1	-0.2571	0.078

[a] is calculated by assuming that all electrons are used to reduce the Ni^{2+}.

4.3.4 HER catalytic activity of the electrodeposited Ni NPs

4.3.4.1 Influence of the potential range

The catalytic properties of the as-prepared Ni/Ti electrodes on the HER were measured in 0.1 M KOH alkaline solution. **Figure 4.12** shows the linear sweep voltammetry (LSV) curves of the electrodes prepared with different potential ranges. The Ti foil and Pt foil electrodes data are also shown for comparison. As expected, the Pt foil exhibits the highest HER catalytic activity, while the Ti foil exhibits no activity at all. Addition of Ni to the Ti electrodes enables electrocatalytic H_2 evolution under negative bias. To achieve a cathodic current density (j) of 10 mA cm^{-2}, the Ni/Ti-4 electrode requires an overpotential (η_{10}) of 275 mV, which is the best performance obtained as compared to the other Ni/Ti electrodes of this series. The Ni/Ti-1, Ni/Ti-2, Ni/Ti-3 and Ni/Ti-5 electrodes exhibit lower catalytic activities than the Ni/Ti-4 electrode with η_{10} of 340, 330, 297 and 285 mV, respectively. Interestingly, these results can be correlated with the amount of the NiO contained in the Ni NPs (**see Table 4.2**). The greater the percentage of the NiO compound, the

lower the resulting overpotential. This indicates that NiO seems to be the active species for catalyzing the HER. As Gong et al.[198] have proposed, the HER process can involve the adsorption of a H_2O molecule on the Ni/NiO particle, which then dissociates into OH^- adsorbed on a NiO site, and a reduced proton adsorbed on a nearby Ni metal site. The latter is being the intermediate for H_2 generation. This interpretation is also supported by previous work on Ni-(hydr)oxide clusters.[66, 104, 199-200] The model implies that a mixture of Ni/NiO_x particles is necessary for a high catalytic performance, since the metallic Ni facilitates the H adsorption, whereas the OH^- is adsorbed on the NiO_x.

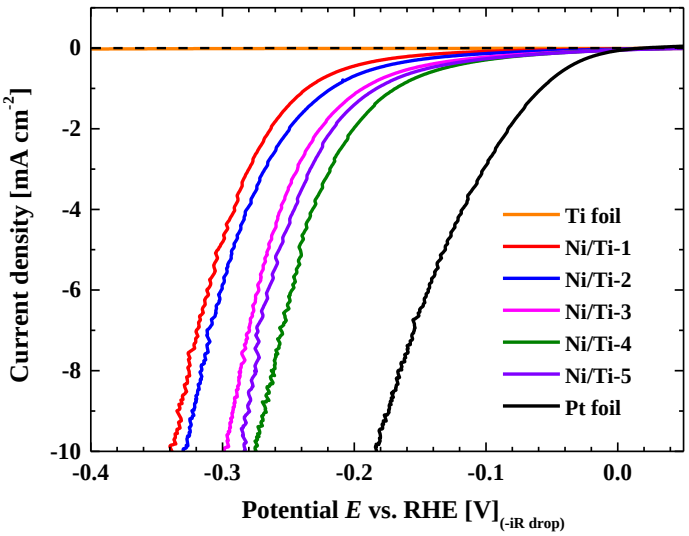

Figure 4.12 LSV curves of the Ni/Ti electrodes prepared with different potential ranges (see **Table 4.1**) in 0.1 M KOH (pH = 12.9). Ti foil and Pt foil electrodes data are added for comparison.

4.3.4.2 Influence of the scan rate

Figure 4.13 shows the LSV curves of the Ni/Ti electrodes obtained after electrodeposition of the Ni NPs by the change in the scan rate. The Ni/Ti-6, Ni/Ti-7, Ni/Ti-3 and Ni/Ti-8 electrodes exhibit η_{10} of 250, 275, 297 and 308 mV, respectively. These results indicate that a higher catalytic performance can be achieved by decreasing the deposition scan rate. This might be due to the higher amount of the total Ni composite deposited at the lower scan rate (see **Table 4.4**). But more importantly, the catalytic activity clearly correlates with the amount of NiO in the NPs (see **Table 4.3**): Increasing the percentage of the NiO in the as-deposited Ni NPs, decreases the required overpotential for the HER. This observation is well consistent with the results of Set I electrodes.

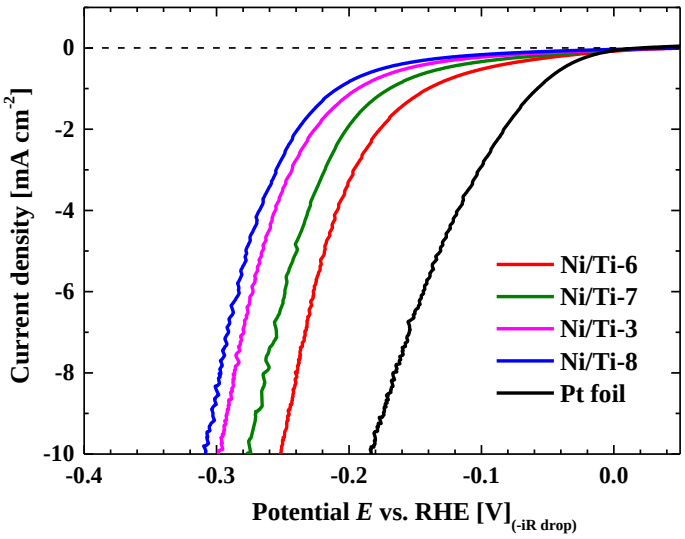

Figure 4.13 LSV curves of the Ni/Ti electrodes prepared with different scan rates (see **Table 4.1**) in 0.1 M KOH (pH = 12.9). Pt foil electrode data are added for comparison.

4.3.5 Optimized Ni NPs

From the above exemplary results, the Ni/Ti-6 electrode shows the highest HER catalytic activity. However, the catalytic activity could be further improved by testing many more parameter combinations, all of which are shown in **Table 4.5**. From that data collection an optimized Ni/Ti electrode (denoted as Ni/Ti-opt) has been prepared at 5 mV s^{-1} with a narrow deposition potential range from -1.3 to +1.2 V (1 cycle).

Table 4.5 Overpotentials at -10 mA cm^{-2} (η_{10}, mV) in 0.1 M KOH of the Ni composite NPs deposited at different potential ranges with variation of scan rate. The η_{10} values with grey background are recorded on the optimal Ni/Ti electrodes in these three series of samples.

Scan rate [mV s^{-1}]	Potential range		to potential [V vs. RHE]				
			0.2	0.7	1.2	1.7	2.2
50	from potential [V vs. RHE]	-2.0	347	345	310	295	310
		-1.8	340	330	297	275	285
		-1.5	382	370	365	356	363

Scan rate [mV s^{-1}]	Potential range		to potential (V vs. RHE)				
			0.2	0.7	1.2	1.7	2.2
10	from potential (V vs. RHE)	-1.8	307	284	275	261	282
		-1.5	287	264	223	247	255
		-1.3	286	258	244	309	276
		-1	347	375	409	422	467

Scan rate [mV s^{-1}]	Potential range		to potential (V vs. RHE)				
			0.2	0.7	1.2	1.7	2.2
5	from potential (V vs. RHE)	-1.8	283	256	250	259	265
		-1.5	272	238	225	246	248
		-1.3	271	223	210	248	261
		-1	313	335	362	376	435

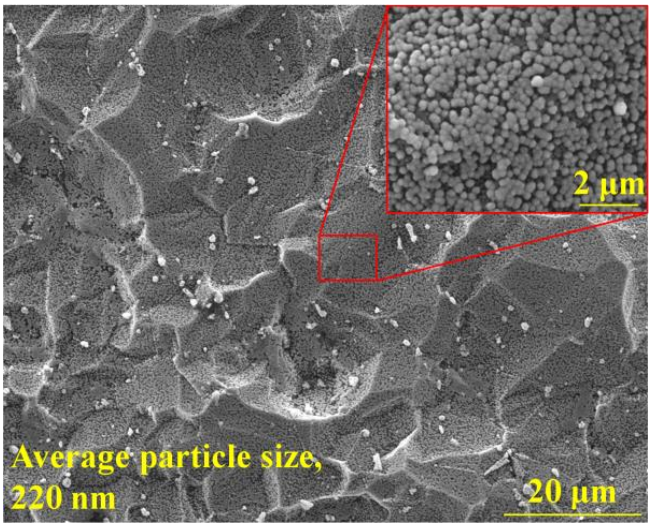

Figure 4.14 SEM image of the optimized Ni/Ti electrode obtained after one cycle between -1.3 and 1.2 V with a scan rate of 5 mV s^{-1}. The inset shows a magnification image of the marked area.

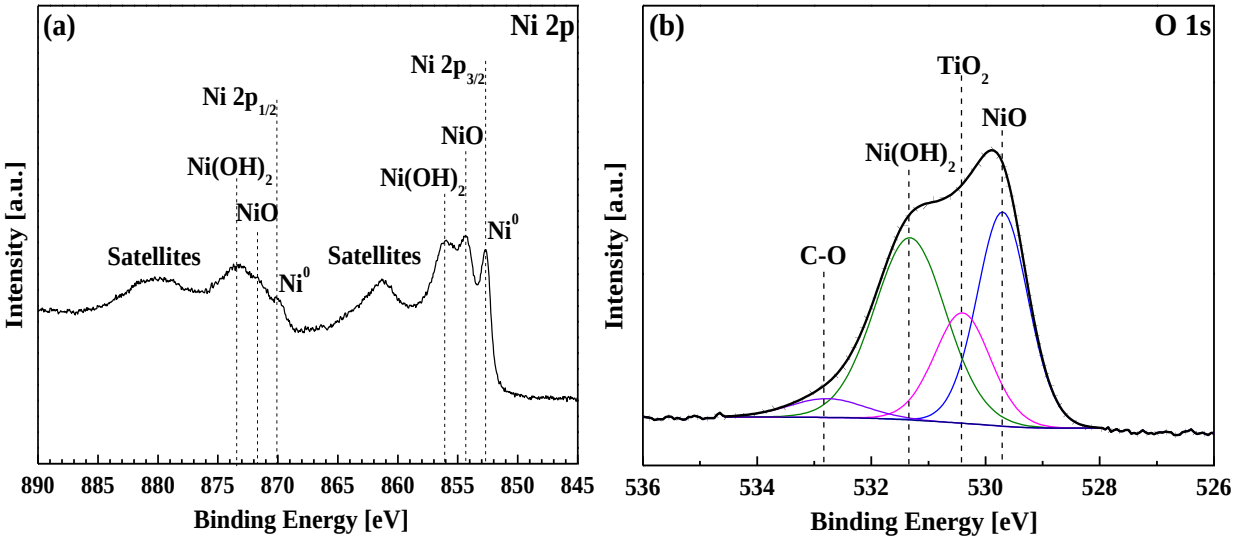

Figure 4.15 (a) Ni 2p and (b) fitted O 1s X-ray photoelectron spectra of the optimized Ni/Ti electrode obtained after one cycle between -1.3 and 1.2 V with a scan rate of 5 mV s^{-1}.

Table 4.6 Atomic concentrations of Ni, Ti, C, and O of the optimized Ni/Ti electrode and the chemical composition of the obtained Ni NPs.

Electrodes	Potential range (V vs. RHE)	Scan rate (mV s^{-1})	Ni (%)	Ti (%)	C (%)	O (%)			chemical composition of the Ni NPs		
						O in NiO (%)	O in $Ni(OH)_2$ (%)	other[a] (%)	Ni^{0} [b] (%)	NiO (%)	$Ni(OH)_2$ (%)
Ni/Ti-opt	-1.3 to +1.2	5	34.6	5.4	11.9	16.7	19.8	11.6	23.1	48.3	28.6

[a] includes the O in Ti-O, adsorbed water and carbon-oxygen species; [b] was calculated by difference.

Figure 4.14 and inset show the SEM images of the Ni/Ti-opt electrode. The inset higher magnification image of this electrode displays that a dense, but still clearly separated NP layer has been formed on the substrate with an average particle size of 220 nm. **Figure 4.15** depicts the Ni 2p and O 1s core level spectra of the Ni/Ti-opt electrode. The Ni 2p spectrum indicates the presence of multiple peaks. The peaks at 852.7 eV, 854.3 eV and 856 eV are attributed to Ni^0, NiO and $Ni(OH)_2$, respectively. As expected, another group of emission lines corresponding to Ni $2p_{1/2}$ are also present at BEs of approximately +17 eV from the Ni $2p_{3/2}$ peaks. The deconvolution of the O 1s core level spectrum indicates two features with high intensities at 529.7 eV and 531.3 eV, which are assigned to NiO and $Ni(OH)_2$, respectively. Here again, the contribution of the smaller peak intensities at 530.4 eV and 532.8 eV assigned to TiO_2 and C-O species are also observable. From the detailed XPS analysis we find that the Ni NPs are composed of 23.1% Ni^0, 48.3% NiO and 28.6% $Ni(OH)_2$ (see **Table 4.6**), presenting an even higher amount of NiO compared to the Ni NPs on the Ni/Ti-6 electrode.

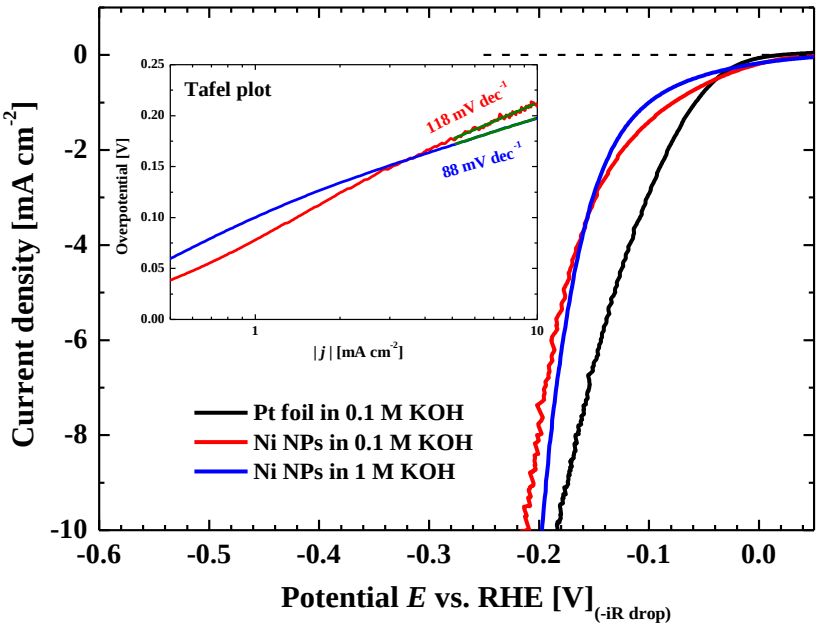

Figure 4.16 LSV curve of the optimized Ni/Ti electrode for the HER in 0.1 M KOH (pH = 12.9) and 1 M KOH (pH = 14). Pt foil electrode data are added for comparison. The inset shows the Tafel plot derived from the LSV curves.

The catalytic behavior of the Ni/Ti-opt electrode obtained after CV from -1.3 to 1.2 V with a scan rate of 5 mV s^{-1} was investigated in 0.1 M and 1 M KOH solutions (see **Figure 4.16**). The Ni composite NPs exhibit a remarkably high activity with an onset potential of ~ 0 V. The overpotentials required to produce a cathodic current density of 10 mA cm^{-2} in 0.1 M and 1 M KOH are 210 mV and 197 mV, respectively. A decrease of the η_{10} by 40 mV is reached for this sample as compared to the Ni/Ti-6 electrode. The better catalytic performance is expected with the greater amount of NiO in the NPs.

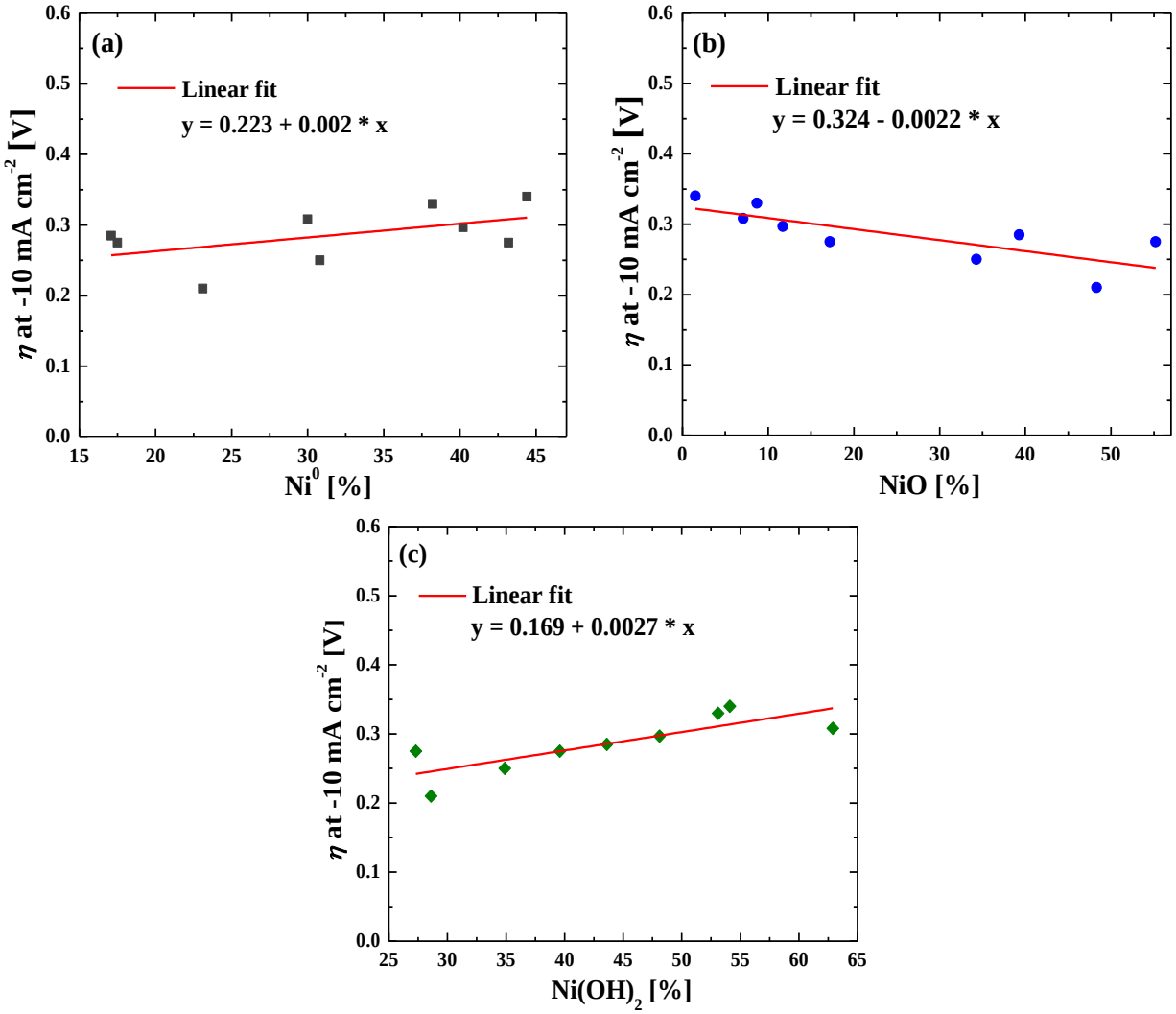

Figure 4.17 Plots of the overpotential at -10 mA cm^{-2} versus the content of Ni^0 (a), NiO (b) and $Ni(OH)_2$ (c) for different Ni NPs.

The dependence of the η_{10}-values on the content of the different species for all of the above presented samples is summarized in **Figure 4.17**. From this compilation it is clear that the activity increases with the NiO content in the particles, and it decreases with an increasing proportion of Ni^0 or $Ni(OH)_2$. Moreover, the η_{10} for the optimized electrode is comparable to the value, which we have obtained for the Pt foil, and lower than most reported nanostructured Ni-based electrocatalysts in alkaline solutions, including electrodeposited Ni dendrites (>300 mV),[73] crystalline Ni_3S_2 NPs (335 mV),[220] Ni_3Se_2 nanoforest grown on Ni foam (203 mV),[221] Ni_2P NPs (220 mV)[148] and NiCu nanoalloys (229 mV).[222] The observations made so far seem to suggest, that the highest activity could be achieved with a pure NiO catalyst, but the opposite is actually found (see **Figure 4.18**). Therefore, it must be concluded that in order to achieve the highest activity the right combination of active sites on particles with a different composition for the different reaction steps of the HER are required.

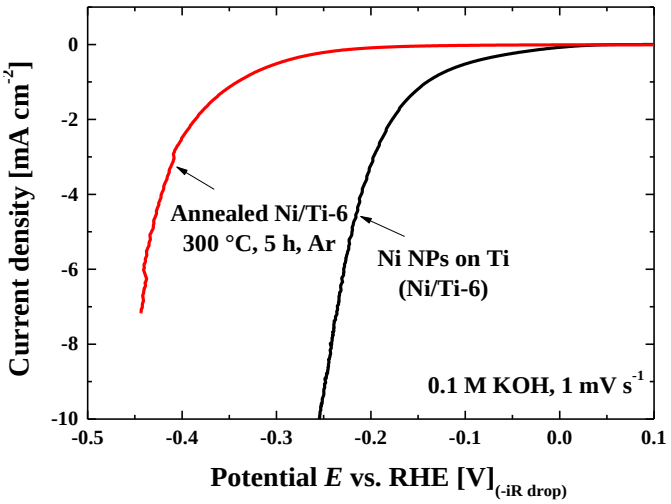

Figure 4.18 Activity of the Ni composite catalysts after annealing at 300 °C for 5 h in Ar atmosphere compared to the unannealed sample. (This is just a single measurement. To really study this effect a whole new series of measurements would be necessary.)

The linear regions of the Tafel plot (**inset in Figure 4.16**), derived from the LSV curves, have been fitted using the Tafel equation **(4.5)**:

$$\eta = a + b \log |j| \qquad \textbf{(4.5)}$$

where a is the intercept related to the exchange current density (j_0), and b is the Tafel slope. In the current density region from -5 to -10 mA cm^{-2} (η ~ 170-210 mV), Tafel analysis indicates Tafel slopes of 118 and 88 mV dec^{-1} in 0.1 M and 1 M KOH, respectively. In alkaline media, the HER in the water electrolysis process generally proceeds by an initial formation of hydrogen intermediates (denoted as H_{ads}). The H_{ads} is formed by an electron-transfer step through the discharge of water

Volmer step: ($H_2O + e^- \leftrightarrow H_{ads} + OH^-$). **(4.6)**

This is then followed either by a second electron transfer through the

Heyrovsky step: ($H_{ads} + H_2O + e^- \leftrightarrow H_2 + OH^-$), **(4.7)**

or by the

Tafel step: ($H_{ads} + H_{ads} \leftrightarrow H_2$). **(4.8)**

Tafel slopes of about 120, 40, or 30 mV dec^{-1} correlate with the Volmer, Heyrovsky or Tafel steps as the rate-determining step of the HER process, respectively.[198-199, 223] The observed Tafel slope of 118 mV dec^{-1} in 0.1 M KOH indicates the Volmer step to be the rate-determining reaction. The Tafel slope of 88 mV dec^{-1} in 1 M KOH does not match the expected Tafel slopes related with different rate-determining steps. This value is comparable to that of most reported HER electrocatalysts in the same solution, including NiO/Ni-CNT (82 mV dec^{-1}),[198] Ni_3S_2 NPs (97 mV dec^{-1}),[220] CoP nanowires on carbon cloth (129 mV dec^{-1}),[224] NiCu nanoalloys (116 mV dec^{-1})[222] and Ni-Mo/Cu nanowires (107 mV dec^{-1}).[225] Additionally, the exchange

current density (j_0) is considered to be a reasonable measure of the catalytic efficiency for the HER. The j_0 of 1.6×10^{-1} mA cm^{-2} for the HER in 0.1 M KOH are within the same order of magnitude as that of the commercial Pt/C catalyst,[199] indicating the good catalytic performance of those Ni composite NPs. Although the j_0 of 5.7×10^{-2} mA cm^{-2} in 1 M KOH is still lower than that of the commercial Pt/C catalyst, it is a satisfactory value for a non-noble catalyst for the HER at the current state of the art.[199] It is difficult here to compare our data with all the data obtained by other groups so far, because of the different conditions and substrates, which have been employed. But, all groups agree, that Ni-based catalysts can reach high efficiencies in alkaline solution, which are comparable to standard Pt-based catalysts. Furthermore, the synthesis of a bifunctional Ni/NiO catalyst with an optimum composition is necessary for obtaining the highest efficiencies as shown clearly by our results. Surface sensitive XPS measurements deliver here important information about the system under investigation.

4.3.6 Stability test

Figure 4.19 shows a chronopotentiometry measurement of the optimized electrode for total periods of 12 and 30 h, respectively. It can be clearly observed, that there is a linear increase in voltage to maintain a current density of -10 mA cm^{-2} for up to 12 h. Afterwards the required voltage stays almost constant at the double value of the starting voltage.

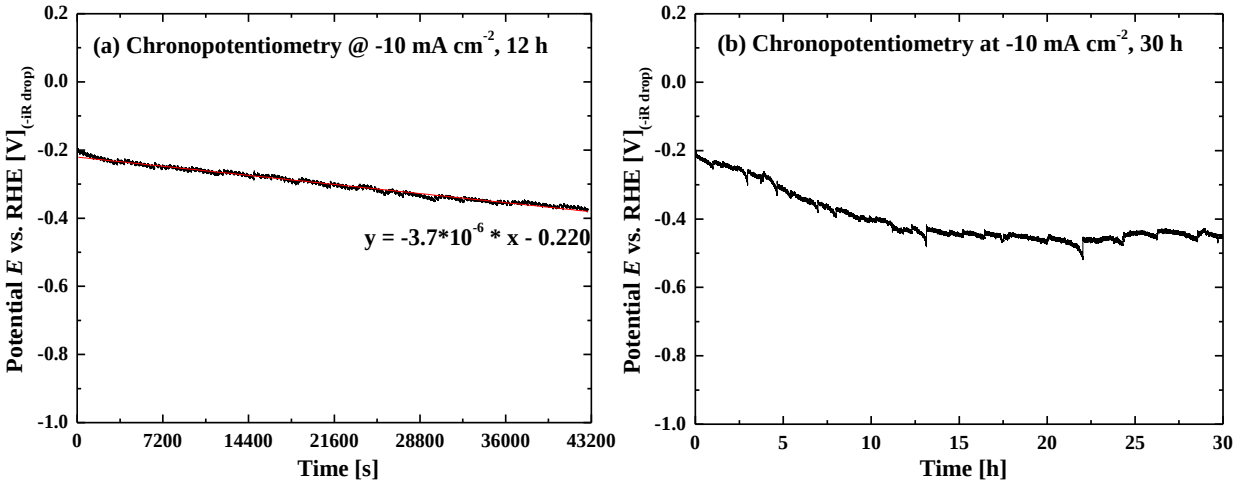

Figure 4.19 Chronopotentiometry measurement of the Ni/Ti-opt electrode under a constant current density of -10 mA cm^{-2} for 12 and 30 h in 0.1 M KOH.

From the SEM investigations the morphology doesn't change during the electrochemical long-time test (see **Figure 4.20**). But, the XPS data clearly show (see **Figure 4.21a-b**) that there is an almost complete loss of the peak intensities corresponding to Ni^0 and NiO after 12 h of long-time testing. It appears, that there is no loss of material, but a complete transformation of the Ni^0 and NiO to the less active $Ni(OH)_2$, which is also supported by the change in the substrate signal (see **Figure 4.21c**). This also coincides well with the observation that the activity stays almost constant after 12 h. Additionally, this observation confirms the necessity of a mixed Nickel/Nickel oxide heterostructure as the highly active site for the HER as proposed

by Gong et al.[198] The shift in the TiO_2 peaks to lower positions indicates the reduction of Ti^{4+} to lower oxidation states, e.g. Ti^{3+}, under the long-time HER condition.[226]

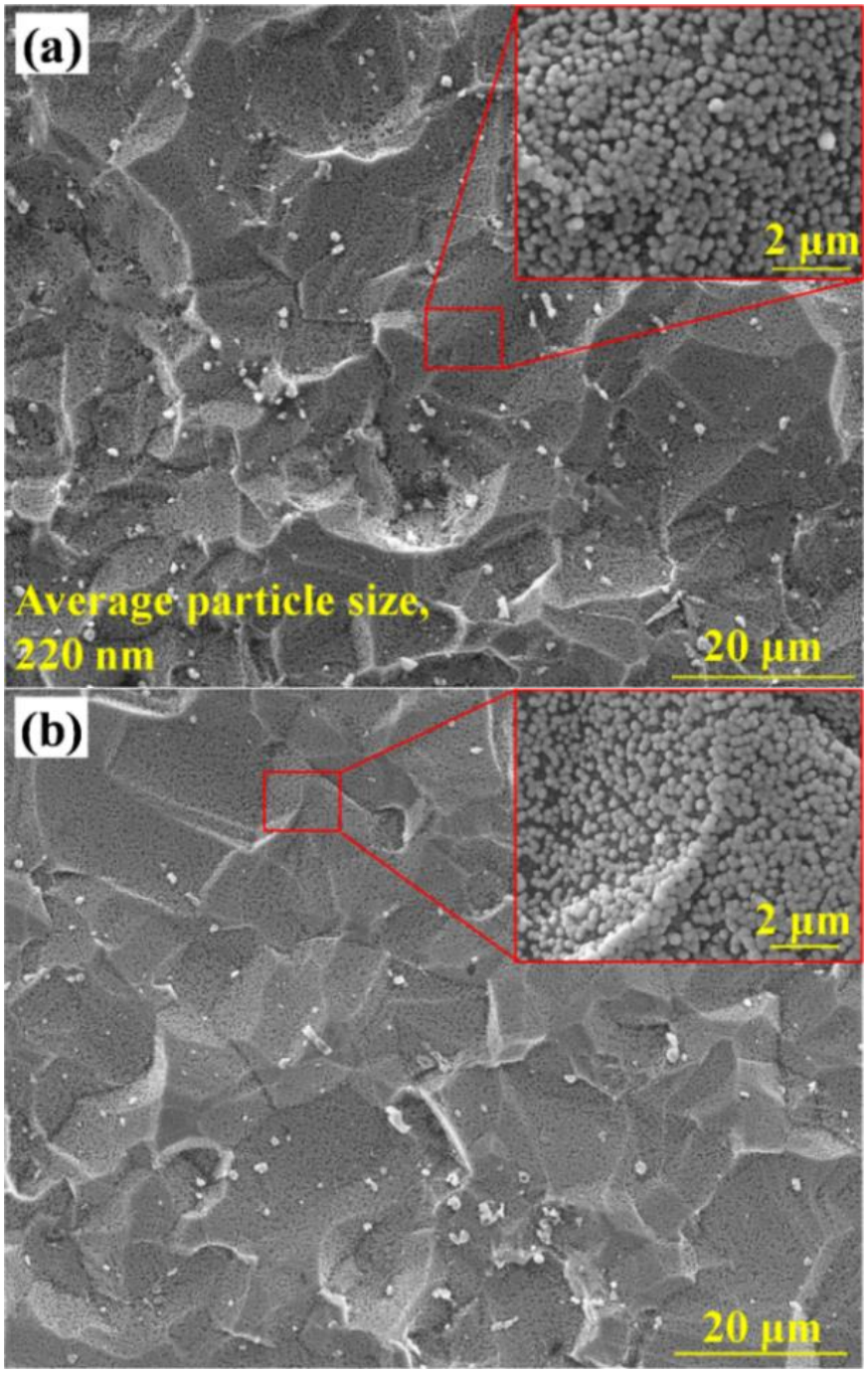

Figure 4.20 SEM images of the Ni/Ti-opt electrode before (a) and after (b) 30 h stability measurement. The insets show enlarged images of the marked areas.

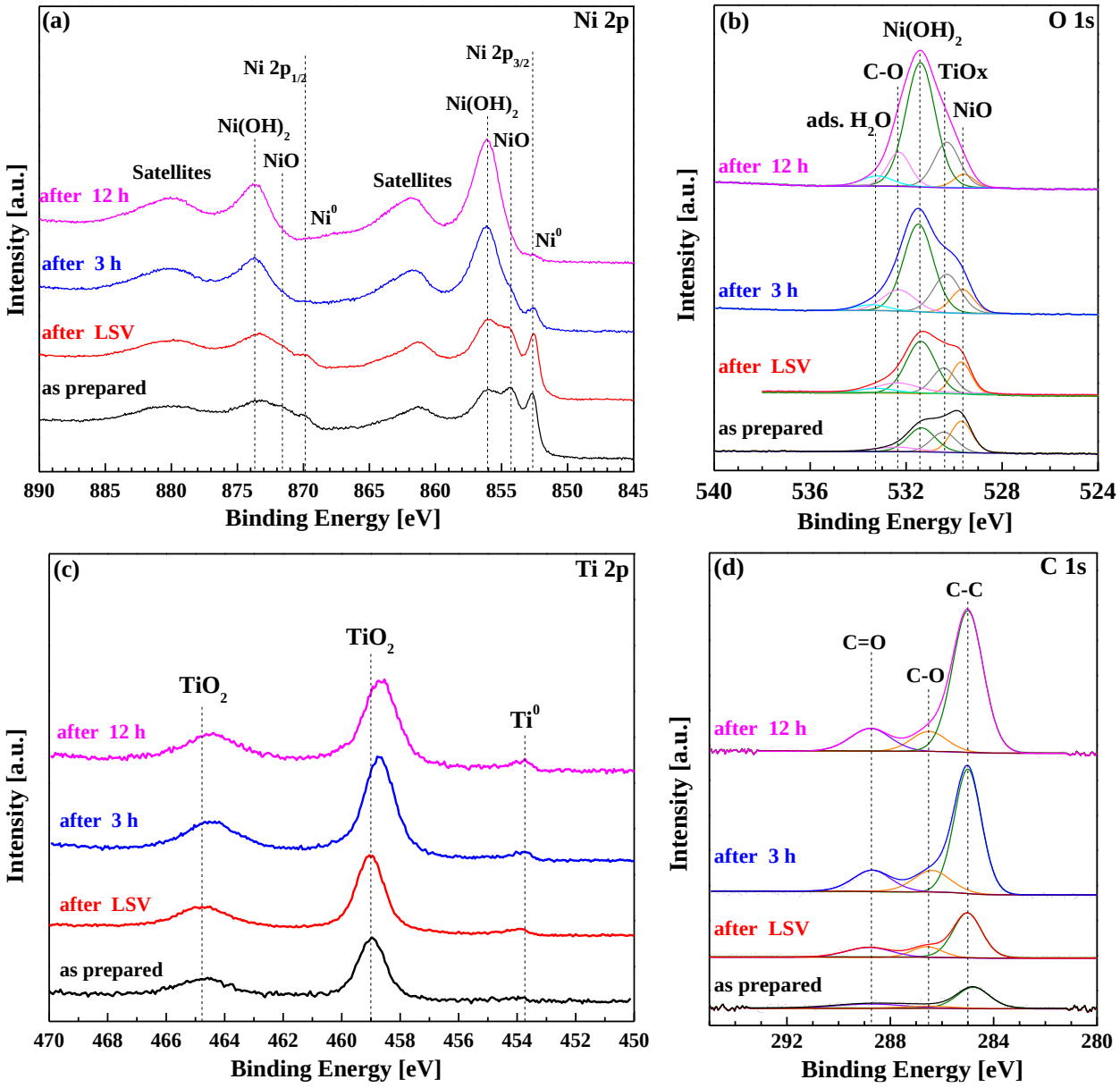

Figure 4.21 (a) Ni 2p, (b) fitted O 1s, (c) Ti 2p and (d) C 1s X-ray photoelectron spectra of the as-prepared Ni/Ti-opt electrode and the Ni/Ti-opt electrode after LSV measurement, 3 h and 12 h chronopotentiometry at -10 mA cm^{-2}.

4.4 Summary

We have demonstrated that Ni NPs with the mixture of Ni^0, NiO and $Ni(OH)_2$ can be directly electrodeposited onto Ti substrates using cyclic voltammetry. The amount of Ni^0, NiO and $Ni(OH)_2$ in the composite NPs could be tuned by varying the deposition parameters like potential range and scan rate. The electrocatalytic activity on the HER was evaluated for each prepared catalyst in alkaline solution. The higher activity of the Ni/NiO/$Ni(OH)_2$ composite NPs is strongly correlated with the higher amount of NiO, but the pure NiO on its own shows only a reduced activity. The same has been observed for the pure Ni^0 and the pure $Ni(OH)_2$ NPs. Therefore, the right combination of materials providing the active sites for the reaction steps of the HER gives the highest activity. Our optimized catalyst achieves an onset potential of ~ 0 V and a HER current density of 10 mA cm^{-2} at an overpotential of 197 mV in 1 M KOH. Furthermore, it shows a small Tafel slope of 88 mV dec^{-1} and a high exchange current density of 5.7×10^{-2} mA cm^{-2}. Stability measurements for up to 30 h show the slow conversion of the Ni/NiO/$Ni(OH)_2$ NPs to $Ni(OH)_2$, which requires then the double potential to keep the current density at -10 mA cm^{-2}. The conversion is finished after a period of about 12 h, from where on the potential and the surface composition stay constant. Nevertheless, the deposition of Ni composite NPs by the here presented one-step method seems to be most promising for the formation of a highly active electrocatalyst for the hydrogen evolution reaction from water.

Further experiments are needed to improve the stability of the Ni composite catalyst using an optimized substrate or to try to recover the catalyst to the original condition with a higher activity. In-situ techniques will be necessary to gain an even deeper understanding of the ongoing processes at the active sites.

5. Electrodeposition of Nickel Hydroxide Films for the OER

5.1 Introduction

In electrochemical water splitting, the OER is more complex than the HER and endures sluggish kinetics, because the production of one oxygen molecule involves transfer of 4 e^- and removal of 4 H^+ from water, which results in a high overpotential for the whole water splitting reaction.[17, 212] The high OER overpotential significantly impedes the whole efficiency of the water splitting process, hence hindering the production of hydrogen at the industrial level.[17] Oxides, hydroxides, and oxyhydroxides of the first-row transition metals (Mn,[227-229] Fe,[230-231] Co,[232-234] Ni,[131, 136, 160-162] and Cu[235-236]), containing either single or multiple metal elements, are active for electrocatalytic water oxidation.[141, 163-165]

In order to improve the activity of transition metal-based materials for catalyzing the OER, great efforts have been devoted to tuning the morphology, surface microstructure, chemical composition and electronic structure.[153] For example, Fominykh et al. fabricated ultrasmall crystalline NiO NPs via a solvothermal reaction using tert-butanol as solvent.[130] It was observed that the decrease in particle size resulted in the formation of a Ni^{3+} state on the surface of the NiO NPs, which is commonly associated with the high electrocatalytic activity of the nickel-based compounds. Corrigan et al. observed that the incorporation of Fe can improve the OER activity of the $Ni(OH)_2$ system considerably, resulting in remarkably reduced OER overpotential.[173] In addition, the OER activity of the $Ni(OH)_2$ system can be improved via electrochemical pre-conditioning, i.e., the α-$Ni(OH)_2$ and β-$Ni(OH)_2$ can be initially oxidized into γ-NiOOH and β-NiOOH, respectively, before the OER.[166] This is because the NiOOH phase is the electrochemical active material for catalyzing the OER.[161, 168]

Very recently, Gao et al. found that the α-$Ni(OH)_2$ exhibits a higher OER catalytic activity and stability than that of the β-$Ni(OH)_2$ in an alkaline electrolyte due to the easier conversion between α-$Ni(OH)_2$ and γ-NiOOH.[136] This study demonstrates the possibility for replacing the expensive commercial OER electrocatalysts such as RuO_2 or IrO_2 by using the cheap and easily prepared α-$Ni(OH)_2$ (e.g. by electrochemical deposition). However, as the α-$Ni(OH)_2$ phase is an insulator with rather low electrical conductivity ($\approx 10^{-13}$ to 10^{-17} S cm^{-1}),[237] the electrochemical activation of the α-$Ni(OH)_2$ is quite slow.[136] This phenomenon has also been observed in the present study, where a transparent α-$Ni(OH)_2$ film has been electrodeposited onto the Ti surface. The as-deposited α-$Ni(OH)_2$ film exhibits poor OER activity even after electrochemical pre-conditioning. Surprisingly, it was found that a simple thermal treatment of the α-$Ni(OH)_2$ film in air atmosphere can completely overcome this problem. The results show that after annealing at a moderate temperature, the α-$Ni(OH)_2$ film can be immediately activated in the first CV cycle and exhibits remarkably improved OER activity. This result indicates that a significant change of the initial status of the α-$Ni(OH)_2$ film must occur during annealing, which plays a critical role in the enhancement of the OER catalytic activity of the α-$Ni(OH)_2$ film. In order to deep understand the reason, the OER catalytic activity of the $Ni(OH)_2$ films annealed at different temperatures and times were evaluated by

electrochemical techniques such as cyclic voltammetry (CV), polarization Tafel analysis and electrochemical impedance spectroscopy (EIS). XPS characterization was performed on the as-deposited and annealed $Ni(OH)_2$ specimens to extract chemical and structural information associated with the annealing treatment. Furthermore, the catalytic activity and stability of the $Ni(OH)_2$ samples were studied by relating to the XPS investigations conducted before, during and after the electrocatalytic OER to elucidate the redox states of the active components.

5.2 Experimental section

5.2.1 Catalyst preparation

Preparation of $Ni(OH)_2$ films

An aqueous solution of 10 mM $NiCl_2 \cdot 6H_2O$ [nickel (II) chloride hexahydrate, 99.95%, Alfa Aesar)] in 1 mM H_2SO_4 was prepared for electrodeposition of $Ni(OH)_2$ films. Millipore water (Merck Millipore, Milli-Q Reagent-Grade Water System, 18.2 MΩ cm^{-1}) was used as the solvent in the deposition solution. The electrodeposition setup and the substrates (5% HF etched Ti foils) as well as their preparation procedure are as described in chapter 3 and chapter 4.

Three differently treated samples were prepared: For the first sample (S1) $Ni(OH)_2$ films were synthesized by a two-step strategy: In the first step, Ni deposits were electrodeposited onto the Ti substrate after 2 cycles between -1.8 and 1.2 V vs. RHE with a scan rate of 50 mV s^{-1}; then, the Ni decorated Ti electrode was ultrasonicated in Millipore water for 3 minutes before drying. For the second (S2) and third samples (S3) $Ni(OH)_2$ films were electrodeposited after 2 and 3 cycles between -1.8 and 1.2 V vs. RHE with a scan rate of 50 mV s^{-1}, respectively.

After deposition, the $Ni(OH)_2$ films decorated Ti substrates were carefully withdrawn from the electrolyte and rinsed in Millipore water without ultrasonication. Prior to further treatments and characterizations, the as-prepared $Ni(OH)_2$ films were dried under a nitrogen gas flow.

Preparation of the RuO_2/Ti electrode

As a standard reference catalyst RuO_2 deposited onto Ti was purchased from Metakem with a load of 15 g m^2. According to the testimony of Metakem, the electrodes were prepared in a special ink procedure with TiO_2 as a binder. The electrodes were cleaned prior to use by dipping into acetone solution for 5 min followed by rinsing with Millipore water.

5.2.2 Annealing treatment

The as-deposited $Ni(OH)_2$ samples were treated by thermal annealing in air atmosphere. To investigate the effect of annealing treatment and to obtain the optimal parameters, $Ni(OH)_2$ films (S3) were heated at different temperatures with variation of annealing time, and then cooled to room temperature. According

to the result of the optimization (see **Figure 5.18**), $Ni(OH)_2$ films annealed at 150 °C with 1 h holding time showed the best OER electrocatalytic activity. Hence, all the other $Ni(OH)_2$ catalysts discussed in the main text were pre-treated at this optimal condition before further characterizations.

5.2.3 Characterization

After each preparation step as electrodeposition, annealing and the electrochemical measurements, the catalysts were characterized by SEM/EDX and XPS. Further information on the characterization setups and parameters has been given in chapter 3.

5.2.4 Electrochemical measurements

Electrochemical measurements were carried out in a standard PEC-cell of 7.2 mL volume (PECC-2, Zahner) using a Zahner potentiostat (Zennium, Zahner) operated in standard three-electrode mode. All measurements were conducted in 1.0 M KOH electrolyte solution. A platinum coil was used as the counter electrode and the Hg/HgO (1 M NaOH) electrode was used as a reference. Potentials measured against the reference electrode ($E_{vs.\ ref.}$) were converted to the potentials versus the reversible hydrogen electrode ($E_{vs.\ RHE}$) and corrected for the electrolyte resistance (R_E) based on the electrochemical impedance spectroscopy (EIS) data. R_E was determined to be 5.3 to 5.6 Ω in 1.0 M KOH with the Ti substrate. The overpotential η was calculated using Equation **(5.1)**:

$$\eta = E_{vs.\ RHE} - iR_E - 1.23\ V \qquad \textbf{(5.1)}$$

where i is the current. Catalysts were investigated according to a specified test procedure in 1.0 M KOH , which includes the measurements of the open circuit potential (OCP) for 5 min, the electrochemical impedance spectroscopy (EIS) in the frequency range from 1 Hz to 200 KHz with a modulated signal amplitude of 10 mV near the OCP, cyclic voltammograms (CVs) recorded with a scan rate of 10 mV s^{-1}, a linear sweep voltammetry (LSV) recorded with a scan rate of 2 mV s^{-1}, a galvanostatic conditioning performed at 10 mA cm^{-2} for 15 min, and repeated CVs and LSVs measurements after the galvanostatic scans. Polarization at 1.23 V for 3 min was implemented before each CV and LSV. Stability measurements were performed by chronopotentiometry using a GAMRY Interface 1000E potentiostat under a constant current density of 10 mA cm^{-2}.

5.3 Results and Discussion

5.3.1 Characterization of as-prepared materials

5.3.1.1 Surface morphology

Figure 5.1 shows the top-view SEM images of the bare Ti substrate and the $Ni(OH)_2$ films deposited on the Ti substrates. The large structures in the low-magnification images with sizes between 10 and 20 µm are from the Ti/TiO_2 substrate. **Figure 5.1b** shows the SEM images for S1. The bright spots in the high-

magnification image with an average projected particle size of 150 nm are being due to the Ni particles. After 2 cycles of deposition (S2, **Figure 5.1c**), the Ti substrate still maintains its surface morphology, indicating the thin characteristic of Ni films. The high-magnification image (insert in **Figure 5.1c**) shows translucent and milky Ni films with particles below the film structures, which have been deposited onto the Ti surface. As discussed in chapter 4 (see **Figure 4.3c**), the particles below the film structures were formed during the first CV scan. Ni films on top of the Ni particles and the Ti substrate were grown during the second CV scan. After 3 cycles of deposition (S3, **Figure 5.1d**), some obvious cracks can be observed on the boundaries of the substrate structures. Moreover, the Ni particles under the films become vague. It reveals that Ni films with increasing thickness are deposited after 3 cycles of CV scans. The corresponding EDX analyses (insets in **Figure 5.1b, c and d**) validates the presence of the elements Ni, O, and Ti.

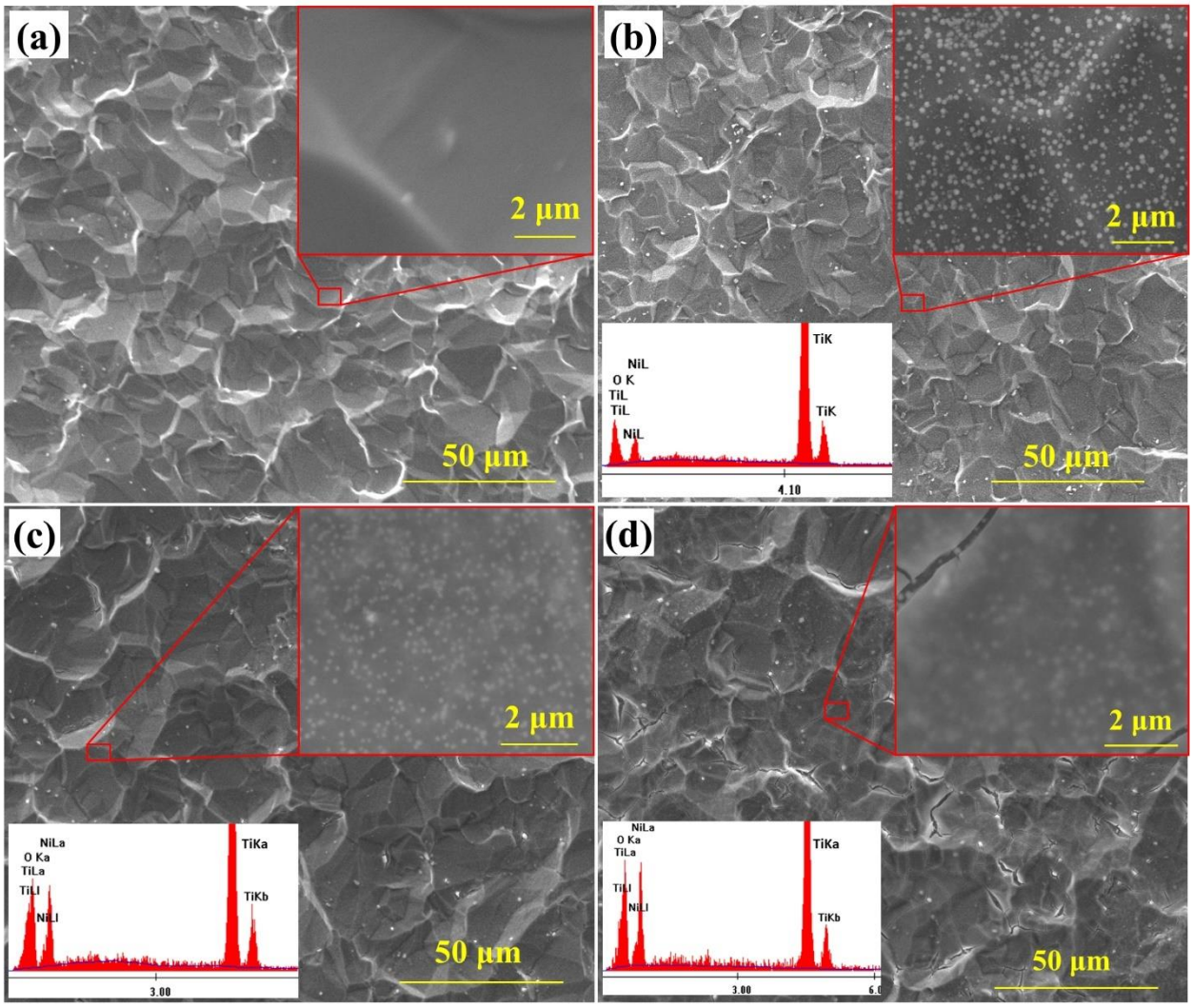

Figure 5.1 SEM images of (a) bare Ti substrate, (b) S1, (c) S2, and (d) S3. Insets show the high-resolution images enlarged from the marked areas and the EDX spectra.

5.3.1.2 XPS characterization

XPS studies were carried out to analyze the elemental and chemical surface composition of the film

catalysts deposited on the Ti substrates. **Figure 5.2** shows the survey spectra. As expected, no peaks corresponding to the Ni element are observable in case of the Ti substrate after 5% HF etching. In case of the as-prepared Ni films on the Ti substrates, Ni signals do appear. In addition, the survey spectra reveal the presence of the elements O, C, Cl and S. Signals attributed to the Ti element are absent on the film-decorated electrodes, indicating a film thickness larger than 10 nm. No other metal impurities have been detected.

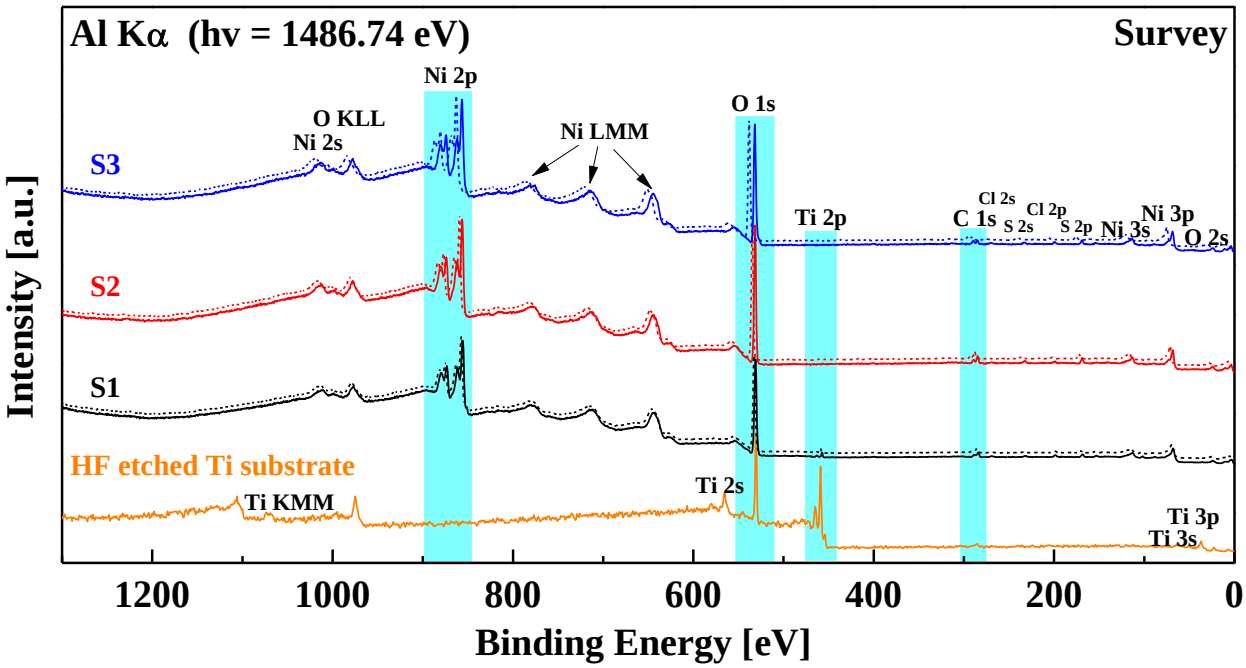

Figure 5.2 XPS survey spectra of the as-prepared Ni films on Ti substrates (dashed lines: measured; solid lines: corrected). The measured lines are corrected by assigning a binding energy of 284.8 eV to the C 1s peak of adventitious carbon species (C-C, C-H).

It is worth noting that the measured survey spectra are shifted to higher binding energies (BEs) compared to that of the HF etched Ti substrate. Apparent shifts can be easily observed on the measured high-resolution C 1s, Ni 2p and O 1s core level spectra (see **Figure 5.3a, b and d**). This could be expected, that the low conductivity of the $Ni(OH)_2$ leads to a charging of the samples.[184-185, 238] For a conductive sample, the positive charge generated from the photoionization can be immediately neutralized by an electron flux. However, in case of a semiconductor or an insulator, neutralization is only partial and a significant net positive charge (varying typically from several volts to several tens of volts) will accumulate at the surface. As this occurs, the kinetic energy of the emitted photoelectrons decrease leading to a shift to higher BEs of the observed peaks in the spectrum.[184-185] Different shifts are observed on these three samples. Typically, larger shifts can be detected on the thicker films, indicating their higher resistivities.[185]

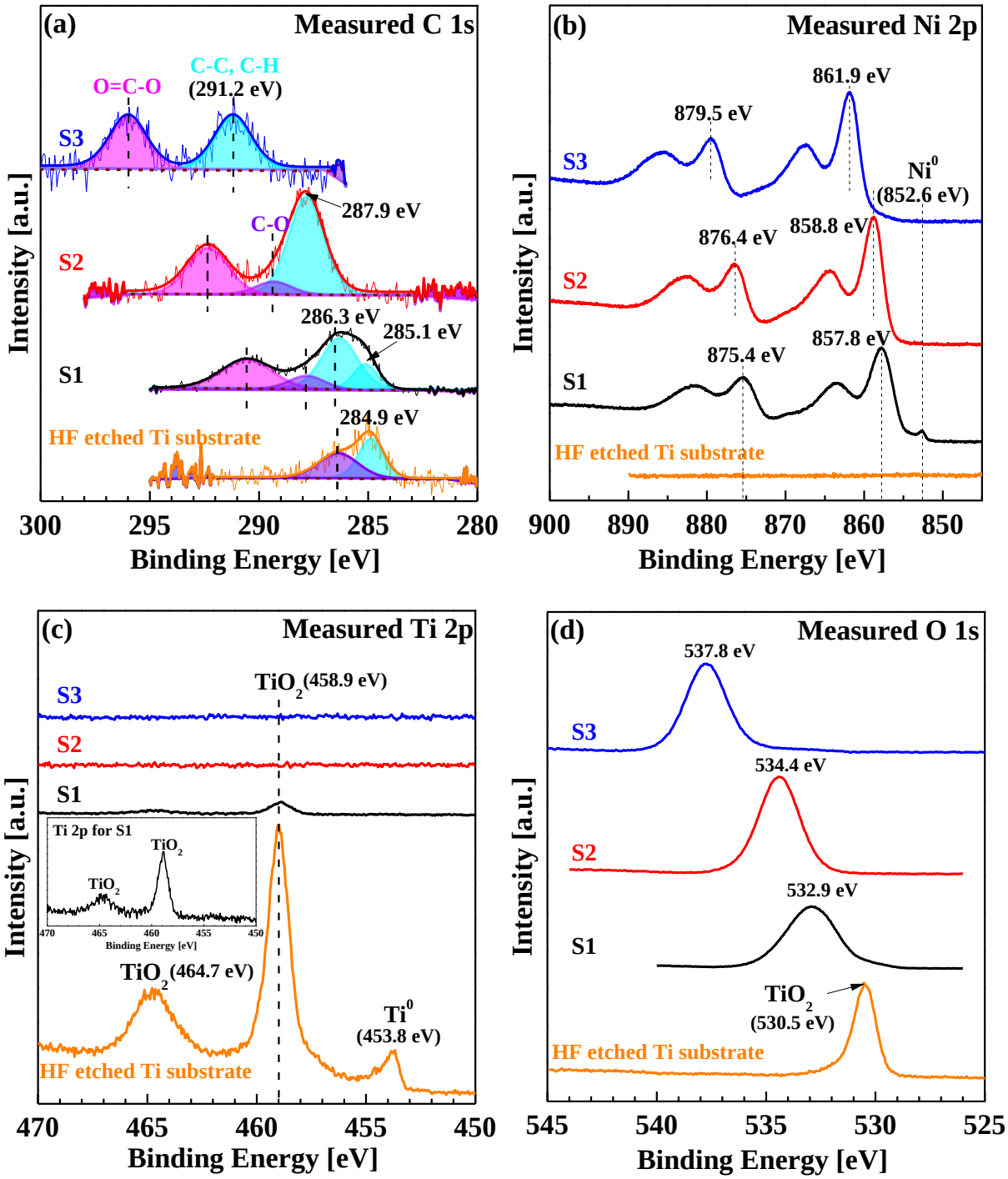

Figure 5.3 Measured XPS detail spectra of the as-prepared Ni films on Ti substrates: (a) fitted C 1s, (b) Ni 2p, (c) Ti 2p, and (d) O 1s. Insert in (c) is the magnified Ti 2p spectrum of S1.

Interestingly, the measured Ni 2p spectrum of S1 in **Figure 5.3b** exhibits a small feature located at a BE of 852.6 eV, which can be attributed to Ni $2p_{3/2}$ for Ni metal (Ni^0).[182, 209] In addition, the measured Ti 2p spectrum of the S1 (see inserted spectrum in **Figure 5.3c**) presents peaks located at 458.9 eV (Ti $2p_{3/2}$) and 464.7 eV (Ti $2p_{1/2}$) with a spin orbit splitting of 5.8 eV corresponding to TiO_2.[213] It is found for S1, that the peak positions associated with Ni metal and TiO_2 from the substrate are not or slightly shifted compared to literature values. However, the main peak associated with the $Ni(OH)_2$ on the Ni 2p spectrum is located at

the BE of 857.8 eV. This value is higher than the data reported previously (855.4 ~ 856.1 eV).[21, 190, 239] This unexpected result leads us to consider the presence of differential charging during the spectral acquisition.[238] As described,[238, 240-241] differential charging in XPS can be observed when a heterogeneous material containing at least two components with differing electrical properties are exposed to sufficient X-rays to experience a net electron flux. Less conductive components will develop a positive bias, i.e. stronger charge effect, while more conductive components will result in photoelectrons emitted at a kinetic energy more closely associated with their originating orbitals.[238, 240-241] In all, the data observed here indicate the differential charging effect was occurred on the Ni/Ni(OH)$_2$/TiO$_2$ surface during the XPS measurements. This might be the reason why there are two peaks attributed to adventitious C 1s spectral component (C-C, C-H) observed on the S1 (see **Figure 5.3a**). No peaks corresponding to Ni metal and Ti species can be observed on S2 and S3.

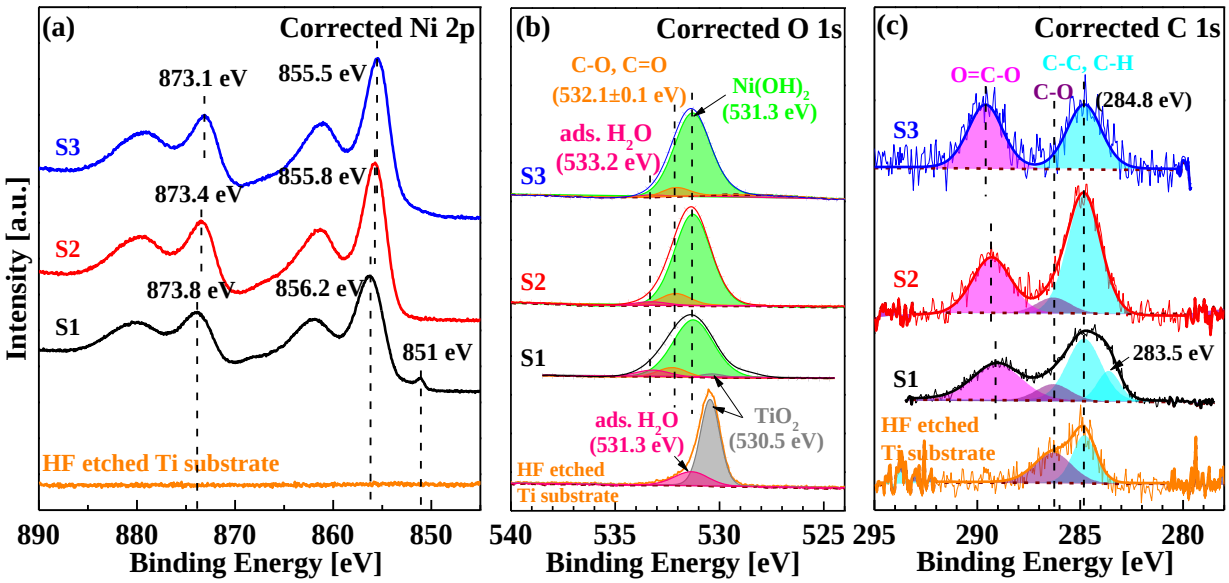

Figure 5.4 Corrected XPS detail spectra of the as-prepared Ni films on Ti substrates: (a) Ni 2p, (b) fitted O 1s and (c) fitted C 1s. The corrected lines are obtained by assigning a binding energy of 284.8 eV to the C 1s peak of the adventitious carbon species (C-C, C-H).

To obtain useful information on the surface chemical states of the as-prepared Ni films, XPS charge correction is necessary. Adventitious carbon at 284.8 eV is extensively used for this purpose.[184-185, 190] As shown in **Figure 5.3a**, the C 1s spectra for adventitious carbon are fitted by defining a peak constrained to be 1.5 eV above the main peak, of equal full width at half maximum (FWHM) to the main peak (C-C, C-H). This higher BE peak is ascribed to alcohol and/or ester functionality (C-OH, C-O-C). Further high BE components of C=O and O=C-O are centered at approximately 3 eV and 4 ~ 4.5 eV above the main peak, respectively. The measured spectra are then charge corrected by shifting all peaks so that the adventitious C 1s spectral component (C-C, C-H) BE is set to 284.8 eV (see corrected survey scan, Ni 2p, O 1s and C 1s spectra in **Figure 5.2** and **Figure 5.4**). From this procedure, positive shifts approximating 1.5 V, 3.1 V and 6.4 V are observed at the surfaces of S1, S2 and S3, respectively.

Figure 5.4a shows the corrected Ni 2p spectra. In case of S1, the significant peak at higher BE is now observed at 856.2 eV (after charge correction from 857.8 eV). In case of S2 and S3, the compensated Ni 2p lines show significant peaks located at BE of 855.8 eV for S2 (corrected from 858.8 eV) and 855.5 eV for S3 (corrected from 861.9 eV). Emission lines corresponding to Ni $2p_{1/2}$ are present at BEs of approximately +17.6 eV from the Ni $2p_{3/2}$ peaks for these three samples, which is well consistent with data reported for $Ni(OH)_2$ previously.[210-212] In addition, considering the symmetric shape of the main peaks, the Ni 2p spectral features can still be associated with $Ni(OH)_2$.[212] The slight variation of the peak position can result from the charge correction process and/or due to the chemical composition of the prepared samples. Moreover, the assignment of the $Ni(OH)_2$ species can be further supported by the O 1s component at 531.3 eV (see **Figure 5.4b**).[212, 242] From deconvolution and fitting of the O 1s spectra, several characteristic emission lines can be obtained. The main peaks situated at BE of 531.3 eV are associated with the OH^- in $Ni(OH)_2$. The small peaks located at higher BEs of around 532.1 eV and 533.2 eV are related to carbon-oxygen species like C-O and C=O and adsorbed H_2O, respectively.[190, 212, 242] The surface chemical composition of S1, determined from the fitted O 1s and Ni 2p spectra, includes ≈ 13% Ni metal and ≈ 87% $Ni(OH)_2$. Pure $Ni(OH)_2$ were prepared on the surface of S2 and S3.

5.3.2 Annealing treatment: XPS analysis

XPS analysis was undertaken on the as-deposited and annealed $Ni(OH)_2$ specimens electrodeposited with 3 cycles (S3) to extract chemical and structural information related to the annealing treatment.

5.3.2.1 Influence of annealing temperature

Figure 5.5a, b and **c** present the measured Ni 2p, O 1s and C 1s detail spectra of the $Ni(OH)_2$ films electrodeposited with 3 cycles (S3) annealed at different temperatures for 1 h: 100, 150, and 200 °C. The as-deposited sample is shown for comparison. It can be observed, that the peak features on the Ni 2p, O 1s and C 1s lines are shifted to lower BEs after annealing. This observation indicates a minimized charging effect, which occurred on the annealed $Ni(OH)_2$ specimen during the XP spectral acquisition. This also reveals an enhanced electrical conductivity,[179-180, 236] probably caused by the loss of the weakly adsorbed/bonded water molecules.[243-244] However, the charge effect does not decrease in accordance with the increase of the annealing temperature. Taking Ni 2p in **Figure 5.6a** for example, the peak positions are shifted by 2.6 eV to lower BEs after annealing at 100 °C. Stronger shifts are not observed for the samples annealed at 150 °C and 200 °C. Both samples show a shift of the Ni 2p spectral features of only 1.9 eV to lower BEs. It seems that there was a drastic increase in conductivity of the electrodeposited $Ni(OH)_2$ after annealing at 100 °C, and the conductivity slightly decreased and remained constant after annealing at 150 °C and 200 °C. The charge effect was still present after annealing. The measured C 1s and O 1s (**Figure 5.5b and c**) show a similar trend compared to that of Ni 2p.

After fitting and deconvolution of the measured C 1s and assigning a binding energy of 284.8 eV to the C 1s peak of the adventitious carbon species (C-C, C-H), the corrected Ni 2p, O 1s and C 1s detail spectra are

obtained as given in **Figure 5.6a, b** and **c**. The corrected Ni 2p spectra (**Figure 5.6a**) show that the as-deposited and annealed samples demonstrate similar spectral features assigned to $Ni(OH)_2$ with a Ni $2p_{1/2}$ – Ni $2p_{3/2}$ binding energy separation of around 17.6 eV and a symmetric shape of the main peak.[210-212] The assignment can be verified by the fitted O 1s spectra with a main peak at 531.1 eV corresponding to $Ni(OH)_2$ (see **Figure 5.6b**).[212, 242] In addition, **Figure 5.6b** presents a small peak located at BE of 529.4 eV indicating the formation of NiO on the sample annealed at a temperature of 200 °C.

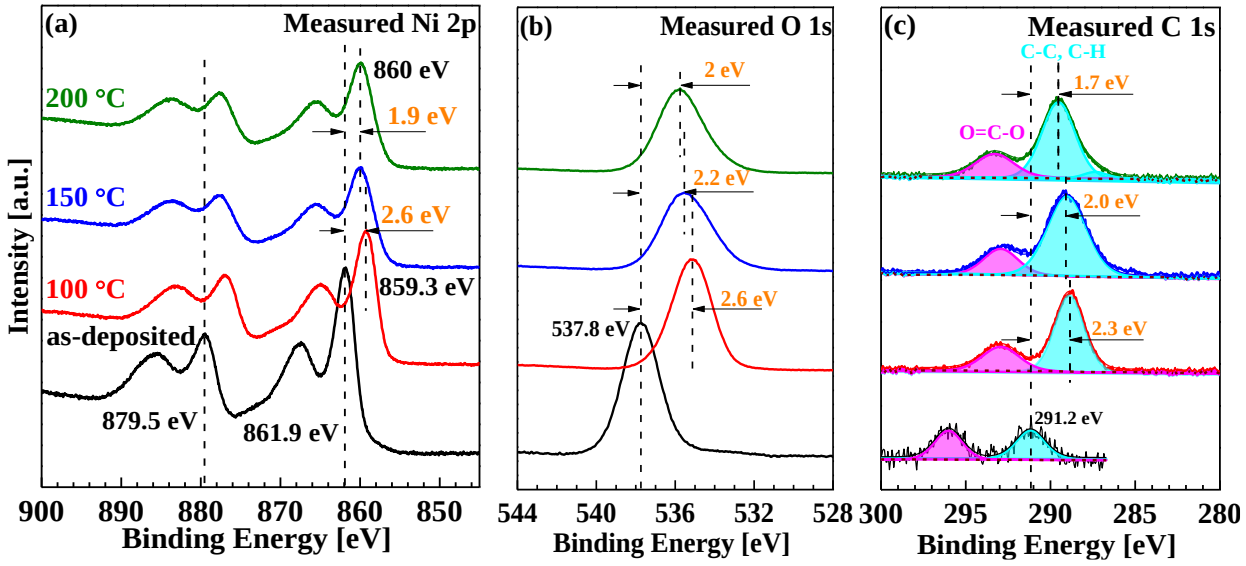

Figure 5.5 Measured Ni 2p, O 1s and C 1s XPS detail spectra of the electrodeposited $Ni(OH)_2$ films (S3) annealed at various temperatures for 1 h: as-deposited, 100 °C, 150 °C, and 200 °C.

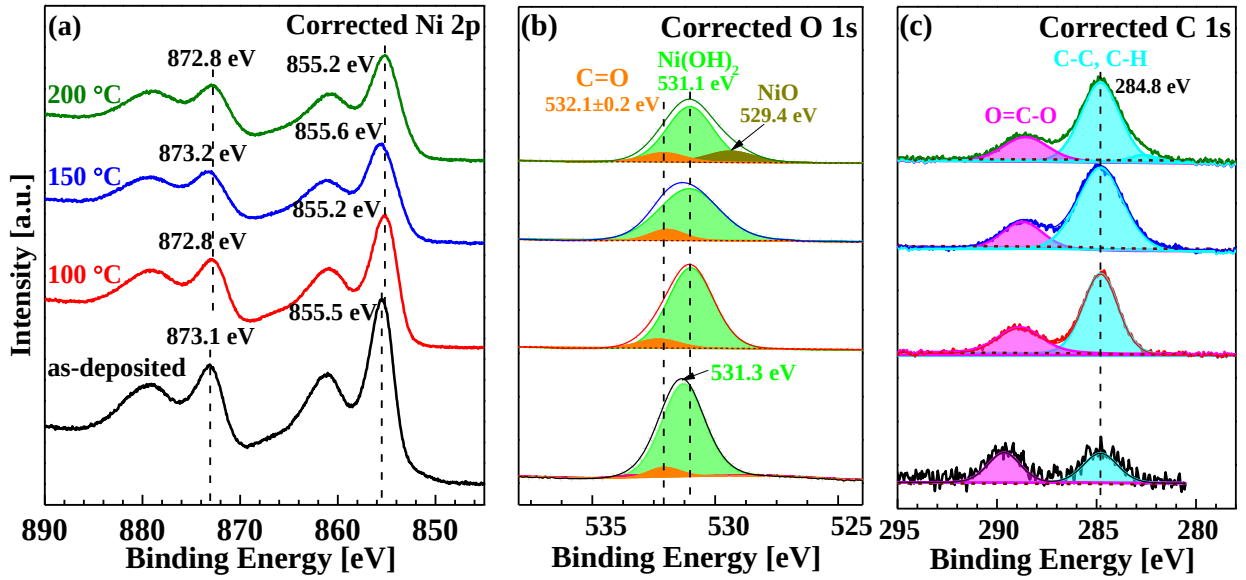

Figure 5.6 Corrected Ni 2p, O 1s and C 1s XPS detail spectra of the electrodeposited $Ni(OH)_2$ films (S3) annealed at various temperatures for 1 h: as-deposited, 100 °C, 150 °C, and 200 °C. The corrected spectra are obtained by assigning a binding energy of 284.8 eV to the C 1s peak of adventitious carbon species (C-C, C-H).

Previous investigations reported, that water can be either adsorbed or structurally bonded in between the $Ni(OH)_2$ lattice.[245-246] Thermogravimetric analyses on the nickel hydroxide hydrates in air and nitrogen atmosphere showed, that there are three reactions taking place during the dehydration process on the α-nickel hydroxide hydrate:[245]

1. Removal of absorbed/adsorbed water at lower temperatures (≈ 50 − 90 °C);
2. Removal of structurally bonded/intercalated water at higher temperatures (≈ 90 − 180 °C);
3. Decomposition of $Ni(OH)_2$ to NiO at temperatures higher than 180 °C.

and two reactions for the β-nickel hydroxide hydrate:

1. Removal of absorbed/adsorbed water at temperatures of ≈ 50 − 150 °C;
2. Decomposition of $Ni(OH)_2$ to NiO at temperatures higher than 180 °C.

Thus, the observation of NiO on the sample annealed at 200 °C is due to the thermal decomposition of $Ni(OH)_2$.

5.3.2.2 Influence of annealing time

To probe the influence of the annealing time, XPS studies are conducted on the electrodeposited $Ni(OH)_2$ (S3) annealed at the optimal temperature (towards OER) of 150 °C with different time: 30 min, 1 h, and 3 h. The as-deposited sample is shown for comparison. **Figure 5.7a, b** and **c** present the measured Ni 2p, O 1s and C 1s detail spectra. As discussed above, emission lines of the annealed samples show shifts to lower BEs of the peaks compared to those of the as-deposited sample, but the difference is, that in this case an increasing shift of the emission lines to lower BEs can be observed with an increase of the annealing time. This observation demonstrates, that a longer annealing time at the constant temperature of 150 °C can lead to a more enhanced sample conductivity, thereby reducing the charging effect, which occurred during the XPS spectral acquisition.[179-180, 236] The measured Ni 2p spectra display a right shift of the peak positions by 1.7 eV to 2.0 eV with an increase of the annealing time from 30 min to 3 h (see **Figure 5.7a**).

Figure 5.8a, b and **c** show the corrected Ni 2p, O 1s and C 1s detail spectra obtained by assigning a BE of 284.8 eV to the C 1s peak of the adventitious carbon species (C-C, C-H). The corrected Ni 2p spectra (**Figure 5.8a**) show, that the as-deposited and annealed samples demonstrate spectral features, which can be assigned to $Ni(OH)_2$ with a Ni $2p_{1/2}$ − Ni $2p_{3/2}$ binding energy separation of around 17.6 eV and a symmetric shape of the main peak.[210-212] This assignment can be verified by the O 1s spectra with a main peak at 531.1 eV corresponding to $Ni(OH)_2$.[207, 240] The main peaks in the Ni 2p and O 1s spectra corresponding to $Ni(OH)_2$ show a similar FWHM.

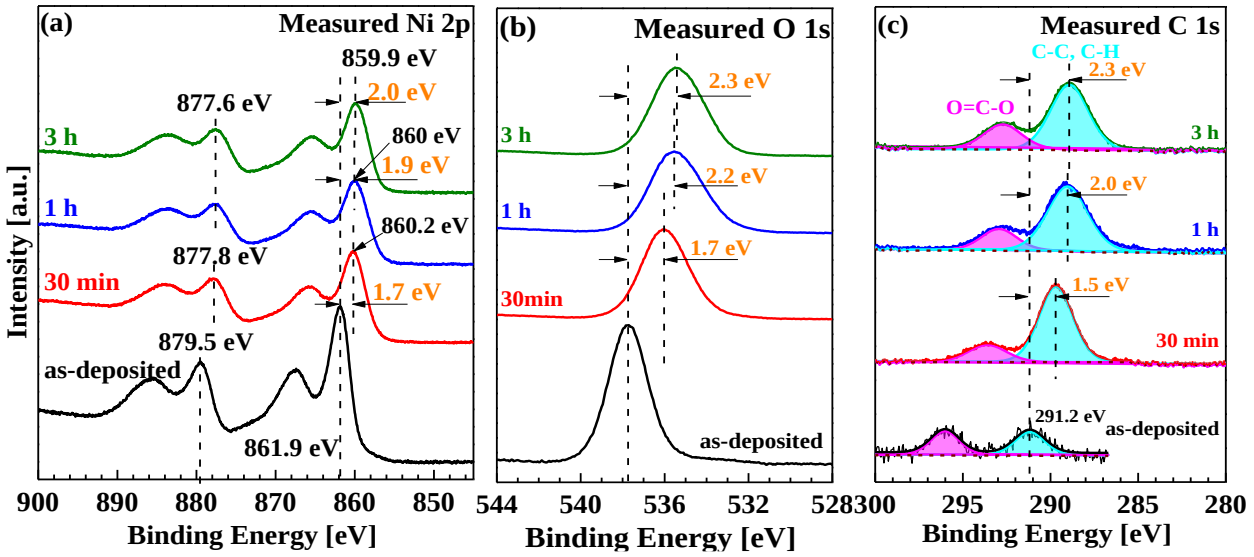

Figure 5.7 Measured Ni 2p, O 1s and C 1s XPS detail spectra of the electrodeposited $Ni(OH)_2$ catalyst (S3) annealed at 150 °C with different holding time: as-deposited, 30 min, 1 h, and 3 h.

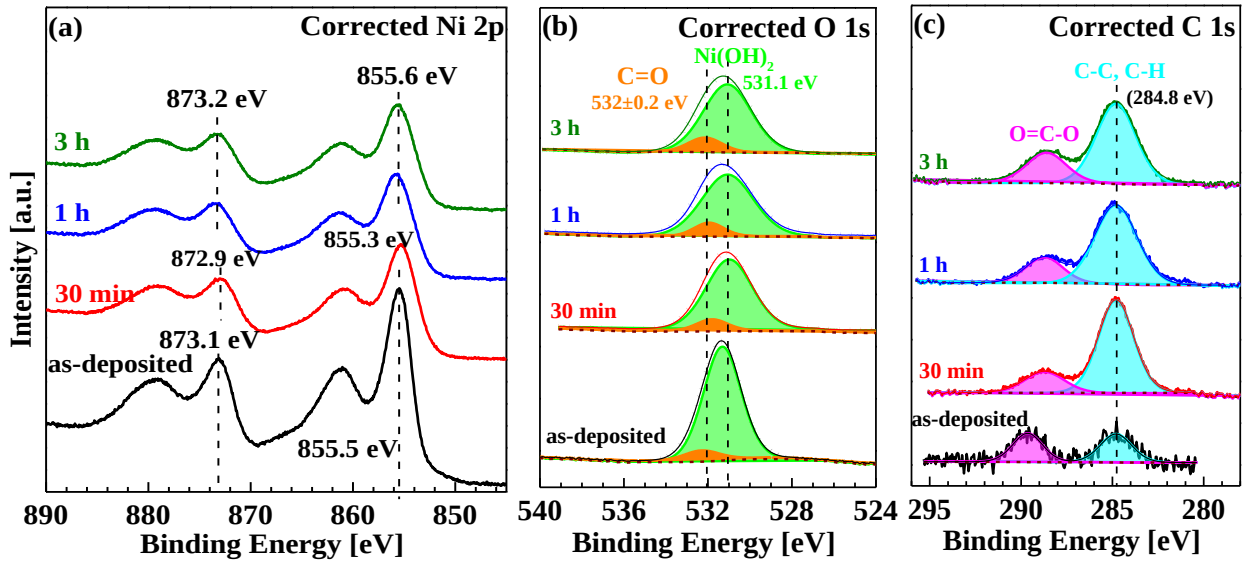

Figure 5.8 Corrected Ni 2p, O 1s and C 1s XPS detail spectra of the electrodeposited $Ni(OH)_2$ catalyst (S3) annealed at 150 °C with different holding time: as-deposited, 30 min, 1 h, and 3 h. The corrected spectra are obtained by assigning a binding energy of 284.8 eV to the C 1s peak of adventitious carbon species (C-C, C-H).

The XPS spectra of S1 and S2, respectively, before and after annealing at 150 °C for 1 h have also been obtained for comparison. **Figure 5.9a** shows the measured Ni 2p spectra for the as-deposited and annealed $Ni/Ni(OH)_2$ NPs. A right shift of 0.8 eV for the main spectral feature attributed to $Ni(OH)_2$ can be observed due to the annealing, while there is no shift for the small peak related to Ni metal located at BE of 852.6 eV. After correction (**Figure 5.9b**), the spectral features indicate the presence of Ni metal and $Ni(OH)_2$. **Figure 5.9c** displays the measured Ni 2p spectra for the as-deposited and annealed $Ni(OH)_2$

electrodeposited with 2 cycles (S2), illustrating a right shift of 1.9 eV after annealing at 150 °C for 1 h, which coincides with the value for the $Ni(OH)_2$ electrodeposited with 3 cycles (S3) annealed under identical conditions. The corrected spectra in **Figure 5.9d** still reveal pure $Ni(OH)_2$ on the surface.

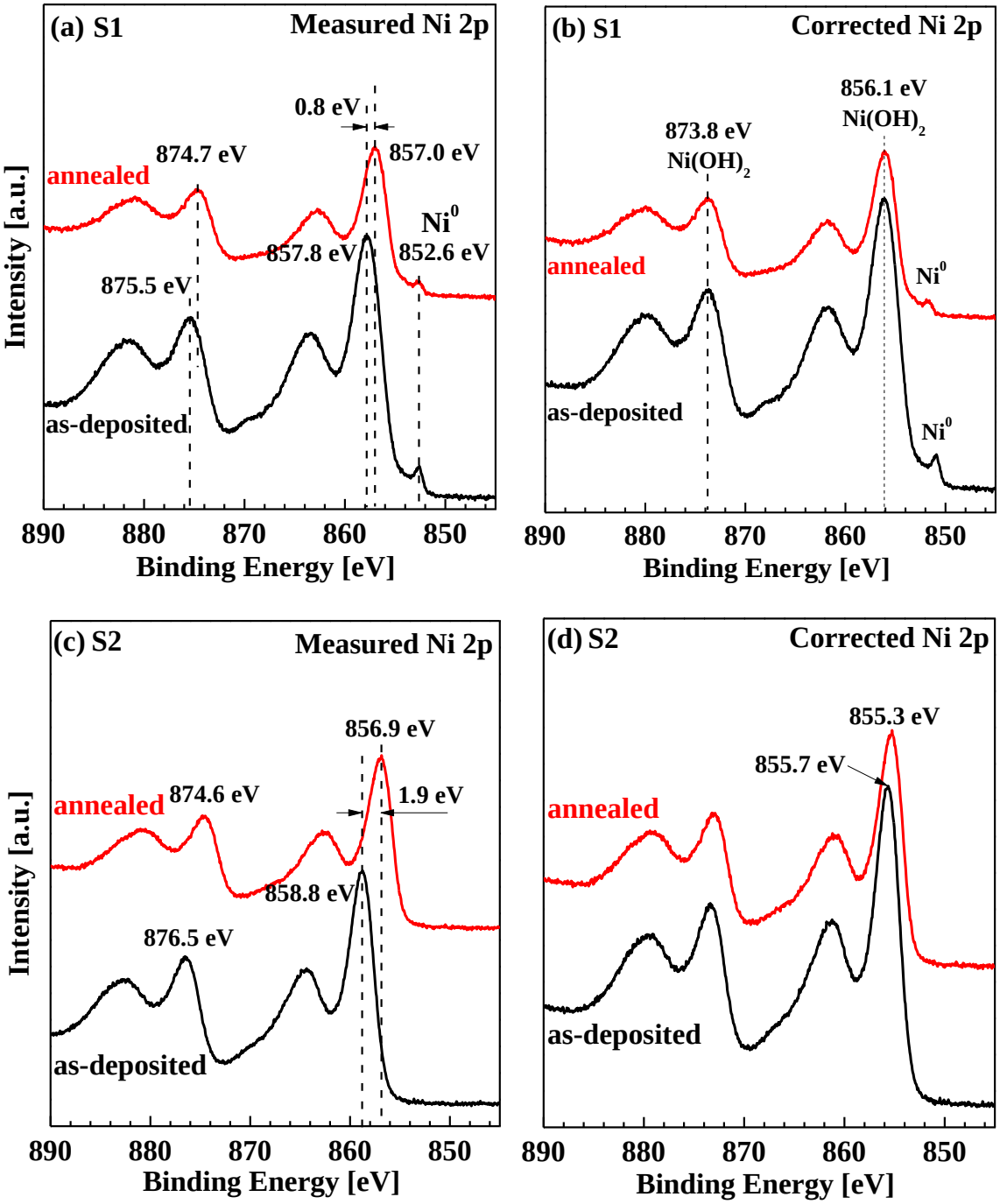

Figure 5.9 Measured and corrected Ni 2p XP spectra of as-deposited and annealed (150 °C, 1 h) S1 (a, b) and S2 (c, d).

Figure 5.10 shows the SEM images of the as-deposited and annealed (150 °C, 1 h) $Ni(OH)_2$ films electrodeposited for 3 cycles (S3). It can be seen that the surface morphologies of the $Ni(OH)_2$ films do not significantly change as a result of the annealing treatment.

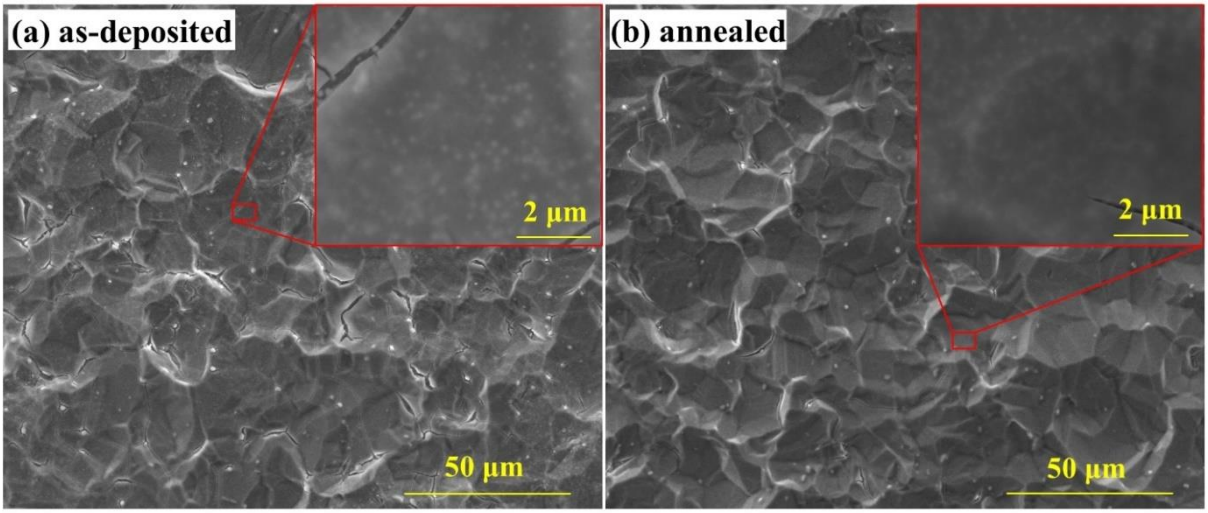

Figure 5.10 SEM images of (a) as-deposited and (b) annealed (150 °C, 1 h) $Ni(OH)_2$ films electrodeposited for 3 cycles (S3). Insets in right-upper corners show the high-resolution images of the marked areas.

5.3.3 Electrochemical behavior after annealing

The electrochemical behavior of the as-deposited and annealed $Ni(OH)_2$ catalysts towards the OER were investigated through detailed electrochemical studies in alkaline solution (1.0 M KOH). Fundamental electrochemical techniques such as CV, polarization Tafel analysis and EIS are used to discuss the influence of the annealing treatment and to form the basis of a comprehensive kinetic study of the OER.

5.3.3.1 Cyclic voltammetry

Effect of annealing temperature

Figure 5.11 shows the *iR* corrected CVs recorded on the as-deposited and annealed (100 °C, 150 °C and 200 °C) $Ni(OH)_2$ films (S3) in 1.0 M KOH at scan rates of 10 mV s^{-1}. The Ti electrode data are shown for comparison. As observed, the blank Ti substrate has no catalytic activity towards OER. Various redox characteristics can be observed on the $Ni(OH)_2$ catalysts. A very small anodic peak at high voltage around 1.55 V is observed for the as-deposited sample, while a strong and broad anodic peak corresponding to the $Ni(OH)_2$/NiOOH transition can be noted at lower potential of 1.46 V for the sample annealed at 100 °C. This correlates well with the XPS analysis shown in the previous chapters, where the improvement after annealing is attributed to the dehydration induced enhancement of the electric conductivity. Interestingly, two anodic peaks at potentials of 1.39 V and 1.43 V, respectively, can be clearly observed on the CV curve for the sample annealed at 150 °C, indicating there are two states of $Ni(OH)_2$ existing on this sample. XPS cannot easily differentiate the two states. Moreover, the anodic peak at 1.45 V decreases considerably for the films annealed at 200 °C. This is attributed to a progressive ordering of the $Ni(OH)_2$ crystals with a decrease of the "*c*" spacing of the unit cell due to water removal from planes perpendicular to the *c*-axis.[245, 247] Furthermore, **Figure 5.11** shows, that the annealing treatment can highly affect the OER electrocatalytic

properties of the electrodeposited $Ni(OH)_2$. They show a significant improvement in the OER activity after annealing. The highest current density at a fixed OER potential is observed for the $Ni(OH)_2$ films annealed at 150 °C, indicating a better OER activity in comparison to that of the films annealed at 100 °C or 200 °C.

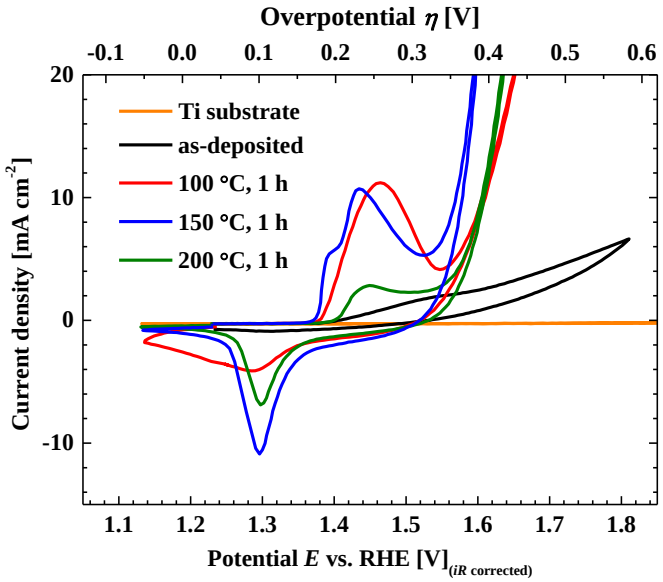

Figure 5.11 CVs (first scan) recorded on the as-deposited and annealed (100 °C, 150 °C and 200 °C) $Ni(OH)_2$ films (S3) in 1.0 M KOH at a scan rate of 10 mV s^{-1}.

The electrochemical pre-conditioning step was reported previously to play an important role for the OER activity of transition metal based electrocatalysts.[127, 202, 248-249] **Figure 5.12a** shows the CV curves obtained after five CV scans, where they reached a stable state. After annealing treatments, the electrodeposited $Ni(OH)_2$ films show a significant enhancement in the catalysis of the OER. The activity is considerably improved with an increase of the annealing temperature from 100 to 150 °C. However, a further increase of the temperature to 200 °C results in a decline of the catalytic activity, but it is still better than that of the films annealed at 100 °C. **Figure 5.12b** shows the CV curves obtained after a subsequent 15 min galvanostatic conditioning step at 10 mA cm^{-2}. All the annealed $Ni(OH)_2$ samples show an improved OER catalytic activity after the conditioning, while no apparent improvement is observed for the as-deposited one.

Moreover, it is observed, that the redox wave characteristics related to the original surface state (**Figure 5.11**) also show considerable changes: (1) the anodic peaks corresponding to the oxidation of $Ni(OH)_2$ to NiOOH [249-250] are shifted to lower potentials; (2) the two oxidation peaks on the sample annealed at 150 °C have been transformed to one strong peak located at approximately 1.36 V; (3) the redox wave of the sample annealed at 200 °C is highly increased in intensity and features a pair of anodic and cathodic peaks almost identical to the sample annealed at 150 °C. Even though the original redox characteristics disappeared, the annealed $Ni(OH)_2$ films still show a highly enhanced OER catalytic activity and the optimum temperature is found to be 150 °C. As proposed by previous literatures,[127, 250-251] the number of electrochemically

accessible Ni atoms can be determined from the charge corresponding to the Ni^{2+} redox reaction according to the equation: $Ni(OH)_2 + OH^- \leftrightarrow NiOOH + H_2O + e^-$. Thus, XPS and voltammetry analysis reveal, that the annealing (mainly a dehydration process) causes an improvement of the electric conductivity and an increase in the active site of the electrodeposited $Ni(OH)_2$, which are essential for the highly enhanced OER activity.

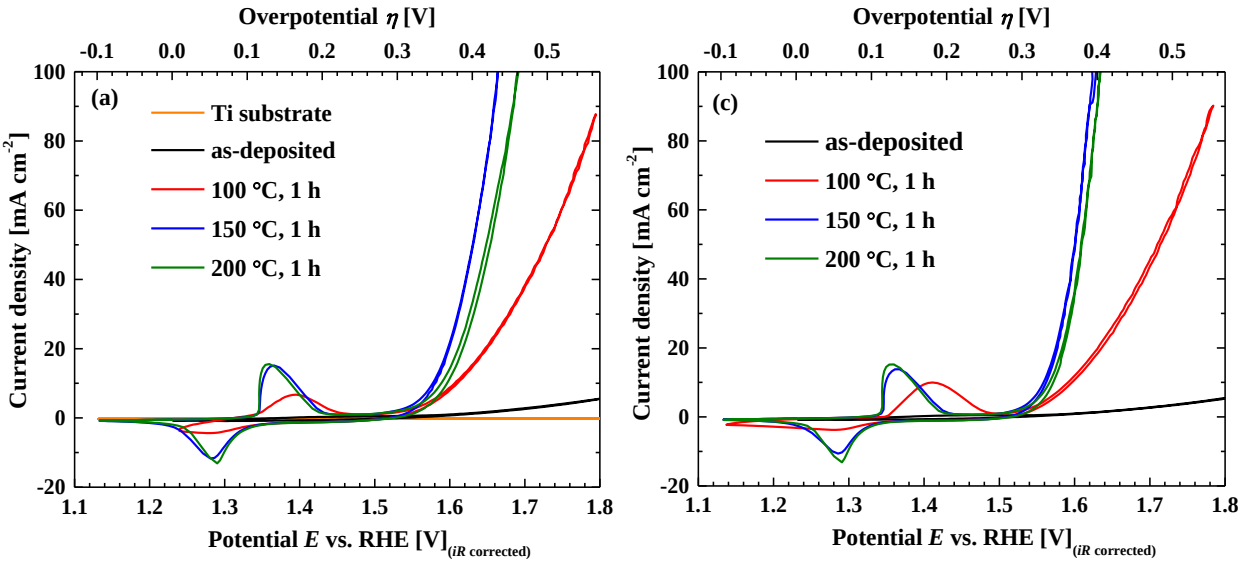

Figure 5.12 CVs of the electrodeposited $Ni(OH)_2$ films (S3) annealed at different temperatures for 1 h collected in 1.0 M KOH at a scan rate of 10 mV s^{-1}: (a) CVs recorded after electrochemical pre-conditioning by CV scans (5 cycles); (b) CVs recorded after subsequent 15 min galvanostatic conditioning at 10 mA cm^{-2}.

Effect of annealing time

Figure 5.13 exhibits the initial CVs recorded on the as-deposited $Ni(OH)_2$ films (S3) and the freshly annealed $Ni(OH)_2$ films at 150 °C with different holding time (30 min, 1 h and 3 h) collected in 1.0 M KOH at a scan rate of 10 mV s^{-1}. The Ti electrode data are shown for comparison. As can be seen, the two anodic peaks are reproducible on these three samples annealed at 150 °C, further identifying the presence of different $Ni(OH)_2$ phases. Moreover, one can observe that the ratio of the anodic peak intensities changes with the variation of the annealing time, indicating a tunable composition of the $Ni(OH)_2$ phases. The OER electrocatalytic properties of the annealed $Ni(OH)_2$ films can be slightly influenced by varying the annealing time, which is consistent with the XPS spectra in **Figure 5.8**. The higher activity is exhibited by the sample annealed for 1 h.

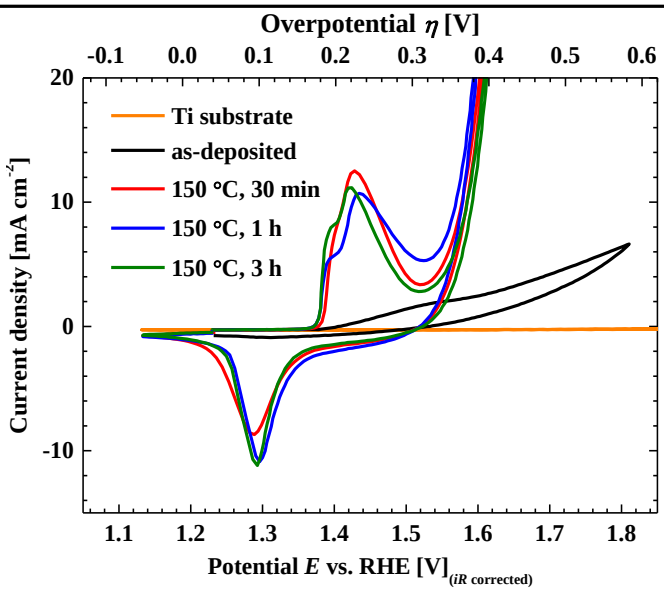

Figure 5.13 CVs (first scan) recorded on the $Ni(OH)_2$ films (S3) as-deposited and annealed at 150 °C with different holding time (30 min, 1 h and 3 h) in 1.0 M KOH at a scan rate of 10 mV s^{-1}.

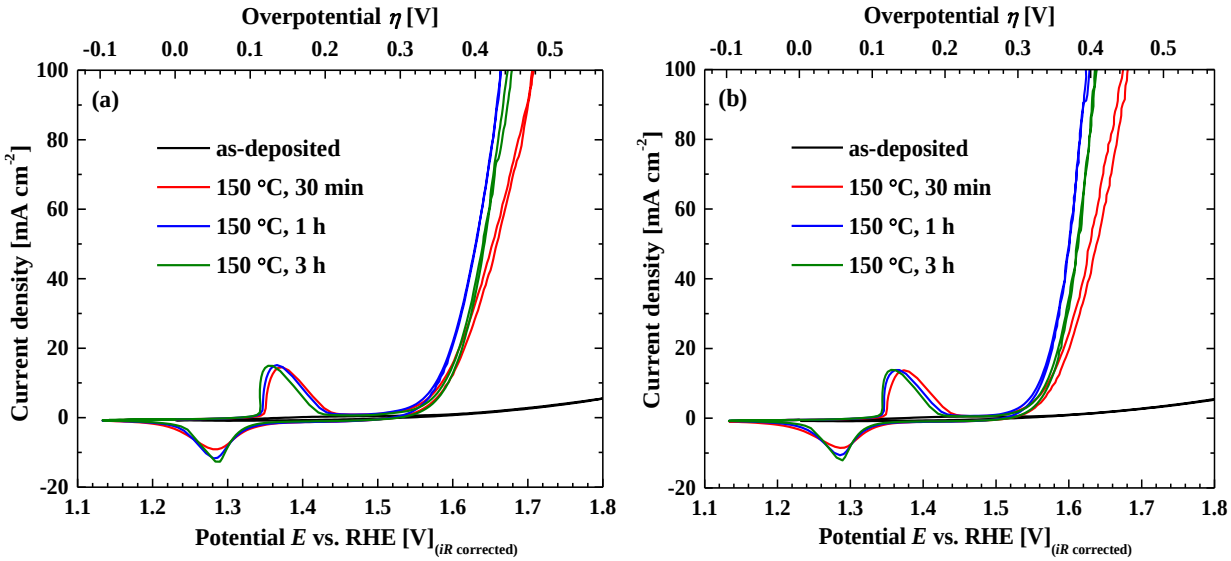

Figure 5.14 CVs of the $Ni(OH)_2$ films (S3) annealed at 150 °C with different time collected in 1.0 M KOH at a scan rate of 10 mV s^{-1}: (a) CVs recorded after electrochemical pre-conditioning by CV scans (5 cycles); (b) CVs recorded after subsequent 15 min galvanostatic conditioning at 10 mA cm^{-2}.

Figure 5.14 shows the CV curves obtained after five CV scans and after an additional subsequent 15 min galvanostatic conditioning at 10 mA cm^{-2} of the electrodeposited $Ni(OH)_2$ films annealed at 150 °C with different holding time. The OER catalytic activity improves with increasing annealing time from 30 min to 1 h. A further increase of the annealing time to 3 h leads to a reduced catalytic activity, but it is still better than that of the films annealed for 30 min. All the annealed $Ni(OH)_2$ samples show an enhanced OER activity after 15 min galvanostatic conditioning, while no apparent improvement is observed for the as-

deposited one. Higher catalytic activity is still observed for the $Ni(OH)_2$ films annealed for 1 h. The overpotentials required to drive a current density of 10 mA cm^{-2} for all the annealed samples are summarized in **Figure 5.18a**.

5.3.3.2 Tafel slope

The Tafel slope is another important parameter, that provides critical insights into the OER reaction kinetics. **Figure 5.15** shows the Tafel plots derived from the LSV curves of the as-deposited and annealed $Ni(OH)_2$ films (150 °C, 1 h) collected at a scan rate of 2 mV s^{-1} in 1.0 M KOH solution. A linear dependency of the overpotential on the decadic logarithm of the current density is observed, and the different corresponding slopes are displayed. The Tafel slope of the as-deposited $Ni(OH)_2$ is 265 mV dec^{-1}, while it decreases remarkably to 64 mV dec^{-1} after annealing, suggesting that charge transport is much better for the annealed sample. After activation by 15 min galvanostatic conditioning at 10 mA cm^{-2}, Tafel slopes of the as-deposited and annealed samples are both decreased to 245 and 53 mV dec^{-1}, respectively. It is worth noting, that the annealed films still show a much lower Tafel slope than the as-deposited sample. The Tafel slope values for all the annealed samples are summarized in **Figure 5.18b**.

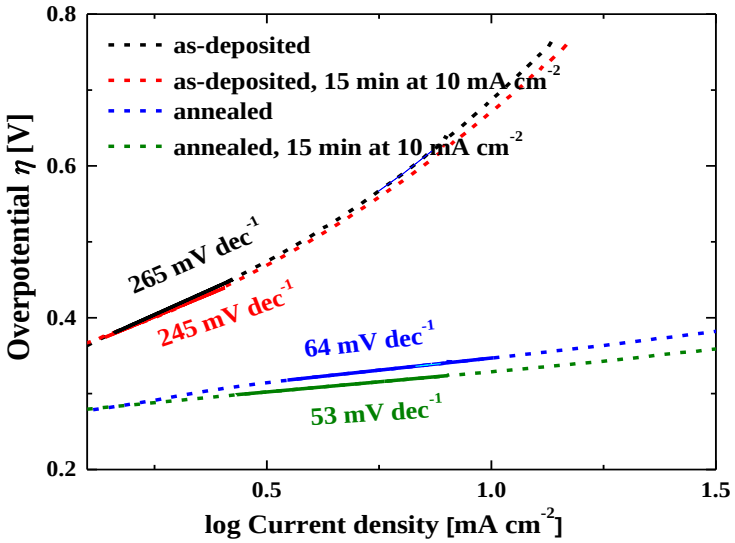

Figure 5.15 Tafel plots derived from the LSV curves of the as-deposited and annealed (150 °C, 1 h) $Ni(OH)_2$ films (S3) collected in 1.0 M KOH at a scan rate of 2 mV s^{-1}.

5.3.3.3 Electrochemical impedance spectroscopy

To further evaluate and compare the electrocatalytic kinetic characteristics of the as-deposited and annealed $Ni(OH)_2$ films, electrochemical impedance spectroscopy (EIS) was conducted. **Figure 5.16** shows the electrochemical impedance spectra in the Nyquist presentation for the as-deposited and annealed (150 °C, 1 h) $Ni(OH)_2$ films (S3) taken in the potential range from OCP (i.e. 0.59 V for the as-deposited sample and 0.75 V for the annealed one) to 1.83 V vs. RHE (without *iR* correction) in 1.0 M KOH. The frequency range used for the EIS measurement was 1 Hz to 200 kHz with an amplitude of 10 mV. In the high frequency

region, the impedance is independent of frequency. It represents the series resistance of the cell (the electrolyte, the intrinsic resistance in the substrate material and contact resistances in the circuit.[243, 252] This type of resistance does not change with potential, and the as-deposited and annealed $Ni(OH)_2$ films show similar values at ≈ 5.5 Ω, which are mainly due to the geometry of the test cell and the electrolyte resistance. In lower frequency region, semi-arcs are evidently observed with applied potential higher than 1.43 V. The semi-arc is generated because of the OER occurring at the electrode/electrolyte interface and the diameter of the arc is a measure of the charge transfer resistance involved. With an increase of the applied potential, the diameters decrease for both the as-deposited and annealed samples. Rapid charge transfer at the electrode/electrolyte interface is required for fast OERs. Smaller semi-arc means smaller charge transfer resistance. With this, it is apparent that the annealed sample exhibits much smaller semi-arc and is more efficient catalyst for the OER. In addition, the observation of the Warburg impedance and the 2nd semi-circle at higher potentials (**Figure 5.16a**) indicates, that the reaction rate of the OER on the as-deposited $Ni(OH)_2$ films was also affected by the mass diffusion.[35]

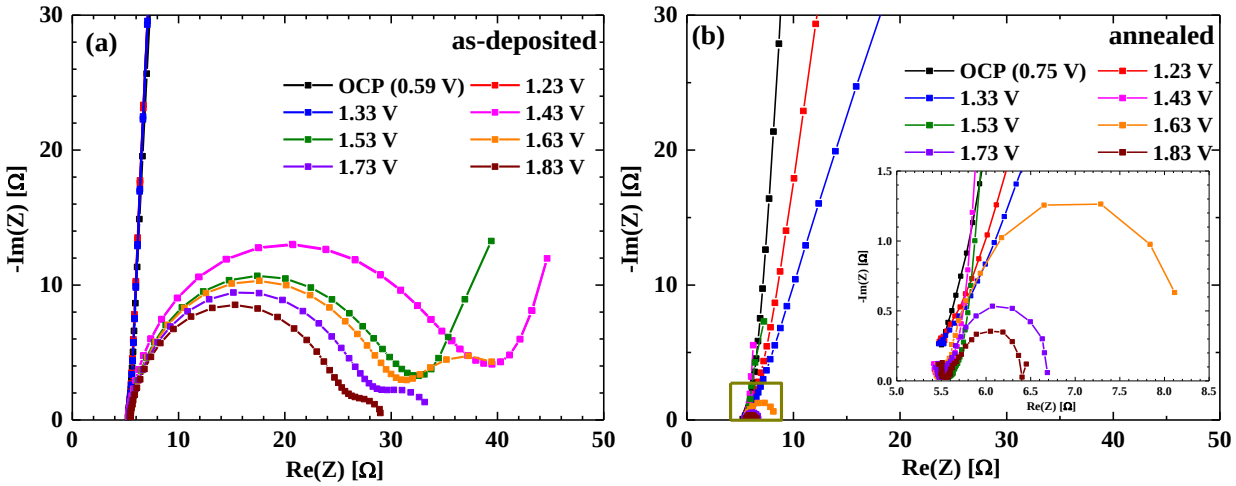

Figure 5.16 Nyquist plots recorded in 1.0 M KOH at a series of potentials (vs. RHE, without *iR* correction) for (a) as-deposited and (b) annealed (150 °C, 1 h) $Ni(OH)_2$ films. The experimental data are represented by discrete points and the fitted impedance response is given by a continuous line. Inset in (b) is enlarged from the dark yellow square. Nyquist plots of as-deposited and annealed (150 °C, 1 h) $Ni(OH)_2$ films with bias of 400 mV overpotential. Inset in (d) is enlarged from the red square.

The impedance parameters related to the electrochemical activity can be obtained through fitting of the EIS data using EC Lab software (Bio-Logic Science Instruments)[253] with a simple equivalent circuit (Randall, inset in **Figure 5.17a**), where R_E is the resistance of the electrolyte, R_{CT} is the charge transfer resistance across the interface of electrode/electrolyte, and C_D is the capacitance for double layer. The results are consistent with the CV curves. The as-deposited sample show very low and almost constant C_D values in the potential range (see **Figure 5.17a**). For the annealed films, the C_D values depend on the potential and

show a dramatic increase at the anodic peak (about 1.4 V), while it decreases again at higher potentials in the OER region. As suggested,[254] the reduction of the C_D is due to the presence of oxygen bubbles which block the surface in contact with the electrolyte. Moreover, the potential dependence of R_{CT} (see **Figure 5.17b**) displays a remarkable decrease also at the anodic peak for both the as-deposited and the annealed samples. The R_{CT} values continue to decrease at higher potentials in the OER region. The annealed sample shows a greater decrease in R_{CT}, indicating a more efficient catalyst for the water oxidation.

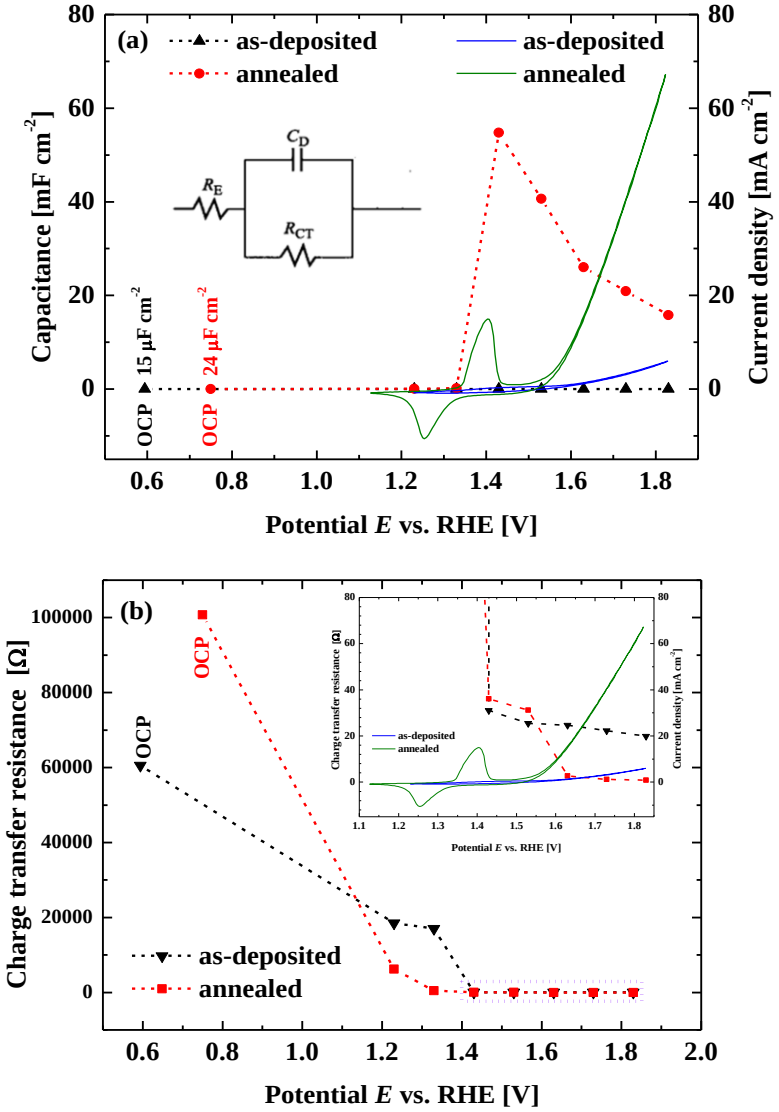

Figure 5.17 (a) CVs and the double-layer capacitance (C_D) values determined via EIS as a function of potential (without *iR* correction) for the as-deposited and annealed (150 °C, 1 h) $Ni(OH)_2$ films (S3). Inset in (a) shows the equivalent circuit (Randall) used to model the AC impedance of the electrochemical cell, with parameters including the resistance of the electrolyte (R_E), the charge transfer resistance (R_{CT}) and the C_D. (b) The R_{CT} values determined via EIS as a function of potential (without *iR* correction) for the as-deposited and annealed (150 °C, 1 h) $Ni(OH)_2$ films. Inset in (b) shows CVs and the R_{CT} values (magnified from the purple square).

5.3.3.4 Optimization of the annealing treatment

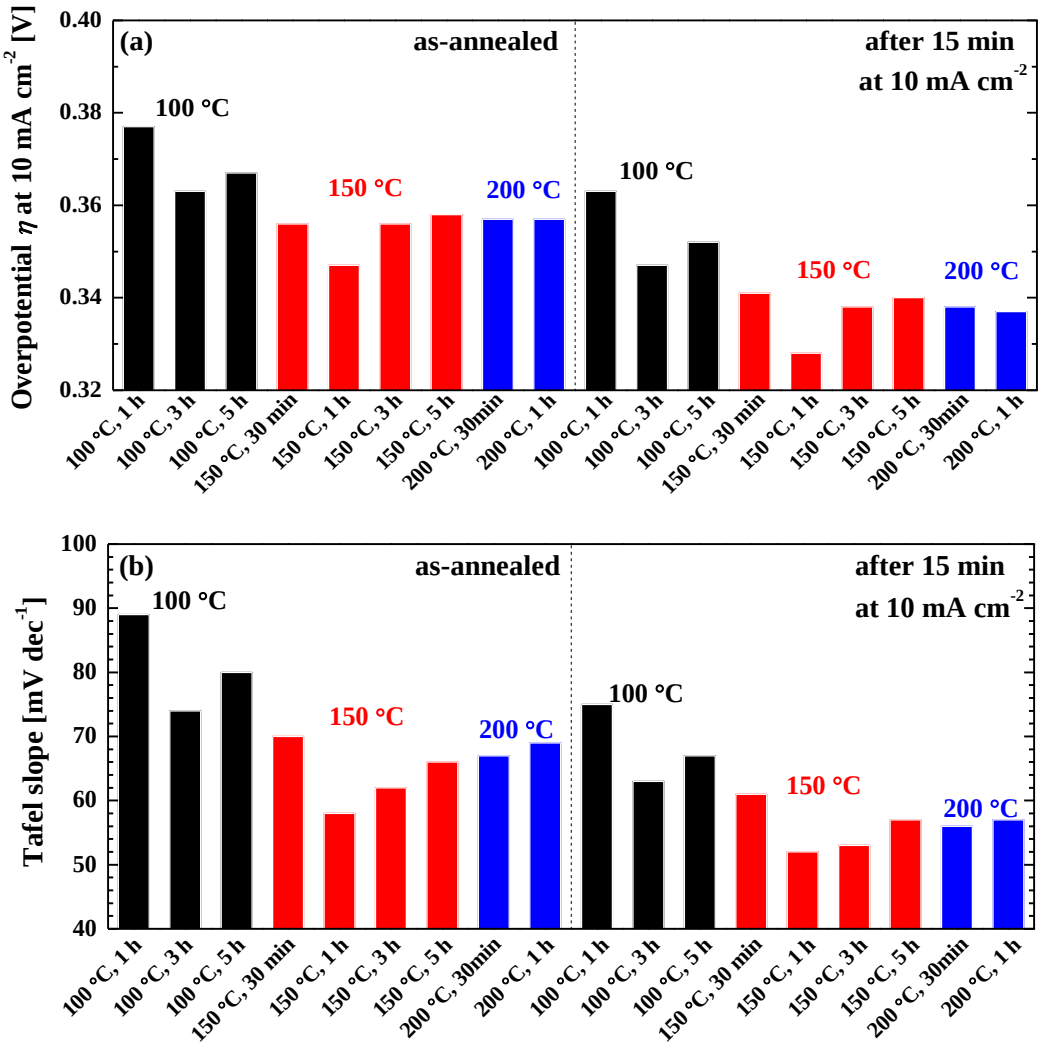

Figure 5.18 (a) Overpotentials at 10 mA cm^{-2} (η_{10}, V) and (b) Tafel slopes of the $Ni(OH)_2$ films (S3) after different annealing treatments and after further activation by a 15 min galvanostatic scan at 10 mA cm^{-2} in 1.0 M KOH.

To obtain the optimum annealing treatment towards catalytic OER, electrodeposited $Ni(OH)_2$ films (S3) annealed with different temperature & time combinations were evaluated before and after 15 min galvanostatic conditioning at 10 mA cm^{-1} in 1.0 M KOH. Two parameters were used to compare the OER catalytic activity: the overpotential at 10 mA cm^{-2} (η_{10}) and the Tafel slope. The current density of 10 mA cm^{-2} was selected because it represents the approximate value expected for a photovoltaic device with 12.3% solar-to-hydrogen efficiency.[193] A lower Tafel slope indicates a more rapid increase in current density with an increase in overpotential. **Figure 5.18** shows the results obtained from the differently annealed $Ni(OH)_2$ samples and the samples after activation by 15 min galvanostatic conditioning at 10 mA cm^{-2}. Even though the annealed $Ni(OH)_2$ are not completely activated after 15 min of electrochemical conditioning (see section 5.3.4), the comparison can still be used as a reference to obtain the optimum annealing treatment. From the

data collection it is obvious, that the electrodeposited $Ni(OH)_2$ films annealed at 150 °C for 1 h show the highest OER catalytic activity before and after the 15 min electrochemical conditioning with the lowest η_{10} and the smallest Tafel slopes.

5.3.4 Effect of electrochemical conditioning

Figure 5.19a, c and **e** show several series of CVs collected from the as-deposited and annealed (150 °C, 1 h) $Ni(OH)_2$ films (S1, S2 and S3, respectively) during several times of galvanostatic conditioning at an anodic current density of 10 mA cm^{-2} for 15 min in 1.0 M KOH at a scan rate of 10 mV s^{-1}. The CVs of the annealed samples feature a pair of anodic and cathodic peaks appearing at around 1.36 V vs. RHE corresponding to the reversible $Ni(OH)_2$/NiOOH redox reaction.[249-250] No apparent anodic and cathodic peaks can be observed on the as-deposited samples.

Following the Ni^{2+} oxidation wave, a sharp increase in current density due to the OER occurs above 1.5 V. To achieve a current density (j) of 10 mA cm^{-2}, the annealed S1 requires an overpotential (η_{10}) of 374 mV. After 15 min conditioning at 10 mA cm^{-2}, the CV curve does not change and shows a similar η_{10}, indicating a fast activation process of the thin-film catalyst material. The annealed S2 shows an initial OER activity with η_{10} = 355 mV. After 15 min conditioning at 10 mA cm^{-2}, the overpotential decreases to η_{10} = 342 mV. CV scans taken after further 15 min conditioning steps show that the OER activity increases, and the current density reaches 10 mA cm^{-2} already at η_{10} = 331 mV after three times of conditioning. To achieve a current density (j) of 10 mA cm^{-2}, the annealed S3 requires an overpotential (η_{10}) of 345 mV. After 15 min conditioning at 10 mA cm^{-2}, the overpotential has decreased to η_{10} = 325 mV. CV scans taken after each 15 min conditioning display an increased OER activity, and the current density reaches 10 mA cm^{-2} at η_{10} = 310 mV after five times conditioning. No large changes are observed in subsequent CV scans with additional conditioning. However, for the as-deposited $Ni(OH)_2$ films without annealing, very low current density was measured even at large potentials, and no enhancement in the OER activity can be observed after electrochemical conditioning (see **Figure 5.19a** and **e**).

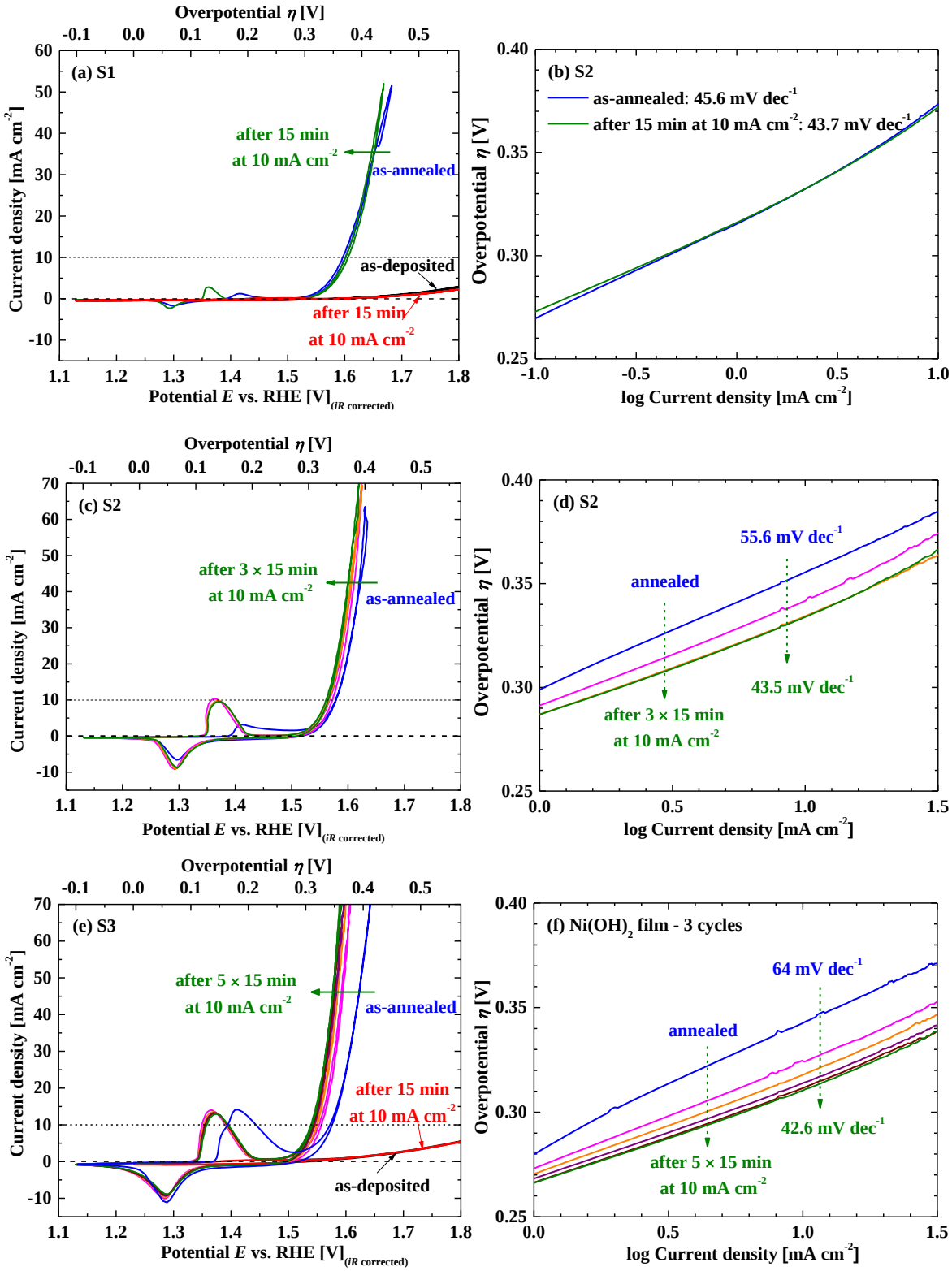

Figure 5.19 (a, c and e) CVs of the as-deposited and as-annealed (150 °C, 1 h) $Ni(OH)_2$ films (S1, S2 and S3, respectively) collected in 1.0 M KOH at a scan rate of 10 mV s^{-1}. After collection of the initial scan, subsequent scans were taken after repeated 15 min anodic galvanostatic conditioning steps at 10 mA cm^{-2}. (b, d and f) Tafel plots derived from the LSV curves of the annealed $Ni(OH)_2$ films collected in 1.0 M KOH at a scan rate of 2 mV s^{-1}.

Tafel measurements for the annealed $Ni(OH)_2$ films after each conditioning are shown in **Figure 5.19b, d** and **f**. In the overpotential region from 280 to 330 mV, Tafel plots of the annealed $Ni(OH)_2$ catalysts show good linearity. The Tafel slope of the annealed S1, S2 and S3 decreases from 45.6 to 43.7 mV dec^{-1}, from 55.6 to 43.5 mV dec^{-1} and from 64 to 42.6 mV dec^{-1} after conditioning, respectively, validating the improvement of the OER catalytic activity. The low Tafel slope values suggest very efficient kinetics for the water oxidation and demonstrate the outstanding performance of the annealed $Ni(OH)_2$ films.

The CV curve for the well-known OER catalyst RuO_2 electrode collected under identical conditions is shown for comparison in **Figure 5.20**, where the overpotential at 10 mA cm^{-2} is η_{10} = 356 mV with a Tafel slope of 84 mV dec^{-1}. Apparently, the annealed $Ni(OH)_2$ films catalysts exhibit a better OER activity than that of the commercial RuO_2 material.

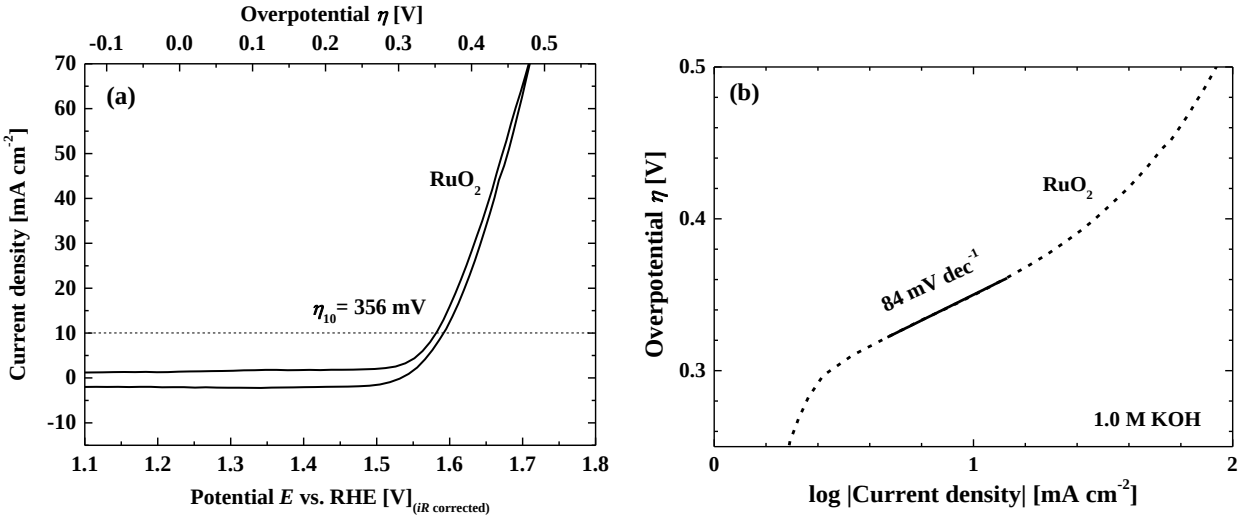

Figure 5.20 (a) CV of the commercial RuO_2 collected in 1.0 M KOH at a scan rate of 10 mV s^{-1}, and (b) corresponding Tafel plot.

Table 5.1 summarizes the η_{10}, the Tafel slopes as well as the electrochemically accessible Ni atoms obtained by integration of the total charge contained in the reduction wave of the annealed $Ni(OH)_2$ films samples before and after conditioning. As the charge obtained from the anodic peak of the Ni^{2+} redox process may contain some contribution from the OER process, the cathodic peak is more reasonably used to determine the amount of the catalytically active Ni atoms.[251] The OER catalytic activity can be increased by galvanostatic conditioning, while the number of electrochemically accessible Ni atoms is almost constant after conditioning on these three samples. Moreover, the $Ni(OH)_2$ films after conditioning present that, lower η_{10} is associated with the sample with higher accessible Ni atoms, while similar Tafel slopes around 43 mV dec^{-1} are observed on the operando obtained active nickel (oxy)hydroxide [denoted as $NiO_x(OH)_y$].

Table 5.1 Electrochemical parameters of the $Ni(OH)_2$ catalysts as-annealed and after galvanostatic conditioning measured in 1.0 M KOH. RuO_2 data are added for comparison.

	Sample	η @ 10 mA cm^{-2} (mV)	Tafel slope (mV dec^{-1})	Electrochemically accessible Ni atoms (mC cm^{-2})
S1	as-annealed	374	45.6	8
S1	after conditioning	371	43.7	8
S2	as-annealed	355	55.6	45
S2	after conditioning	331	43.5	47
S3	as-annealed	345	64	81
S3	after conditioning	310	42.6	78
S3	after stability (26 h)	318	46.8	82
RuO_2	--	356	84	--

5.3.5 Chemical composition correlated catalytic activity

XPS investigations were performed to elucidate the detailed compositional structures and redox states of the active components before, during and after the electrochemical reaction to gain a full understanding of the ongoing elementary reaction steps at the active sites involved. No charge effect was observed for the samples after the electrochemical measurements. This is because the electrically insulating Ni^{2+} in $Ni(OH)_2$ can be oxidized to the nominally 3+ oxidation state under OER conditions, which is electronically a quite good conductor.[237, 248]

Annealed $Ni(OH)_2$ films

Figure 5.21 presents the high-resolution Ni $2p_{3/2}$ and O 1s XPS spectra of the freshly annealed $Ni(OH)_2$ films (S3) and the annealed S3 after 15 min and 5×15 min electrochemical conditionings. The Ni $2p_{3/2}$ spectrum of the as-prepared annealed $Ni(OH)_2$ sample (**Figure 5.21a**) shows one predominant symmetric peak at a BE of 855.6 eV with a FWHM of 3.2 eV. The O 1s spectrum of the as-annealed $Ni(OH)_2$ films (**Figure 5.21b**) displays a major peak at a BE of 531.1 eV associated with OH^- in $Ni(OH)_2$ and a small peak located at a BE of 532 eV assigned to carbon-oxygen species.[255-256] **Figure 5.21d** and **g** show the Ni $2p_{3/2}$ lines of the annealed $Ni(OH)_2$ catalyst after 15 min and 5×15 min electrochemical conditioning, respectively. Asymmetric shapes of the Ni $2p_{3/2}$ lines are observed. Especially for the sample with 5×15 min electrochemical conditioning (**Figure 5.21g**), the Ni $2p_{3/2}$ spectrum reveals a shape with mixed Ni^{2+} and Ni^{3+} contributions.[255-256] The Ni $2p_{3/2}$ spectral features point to a transformation from $Ni(OH)_2$ to NiOOH.

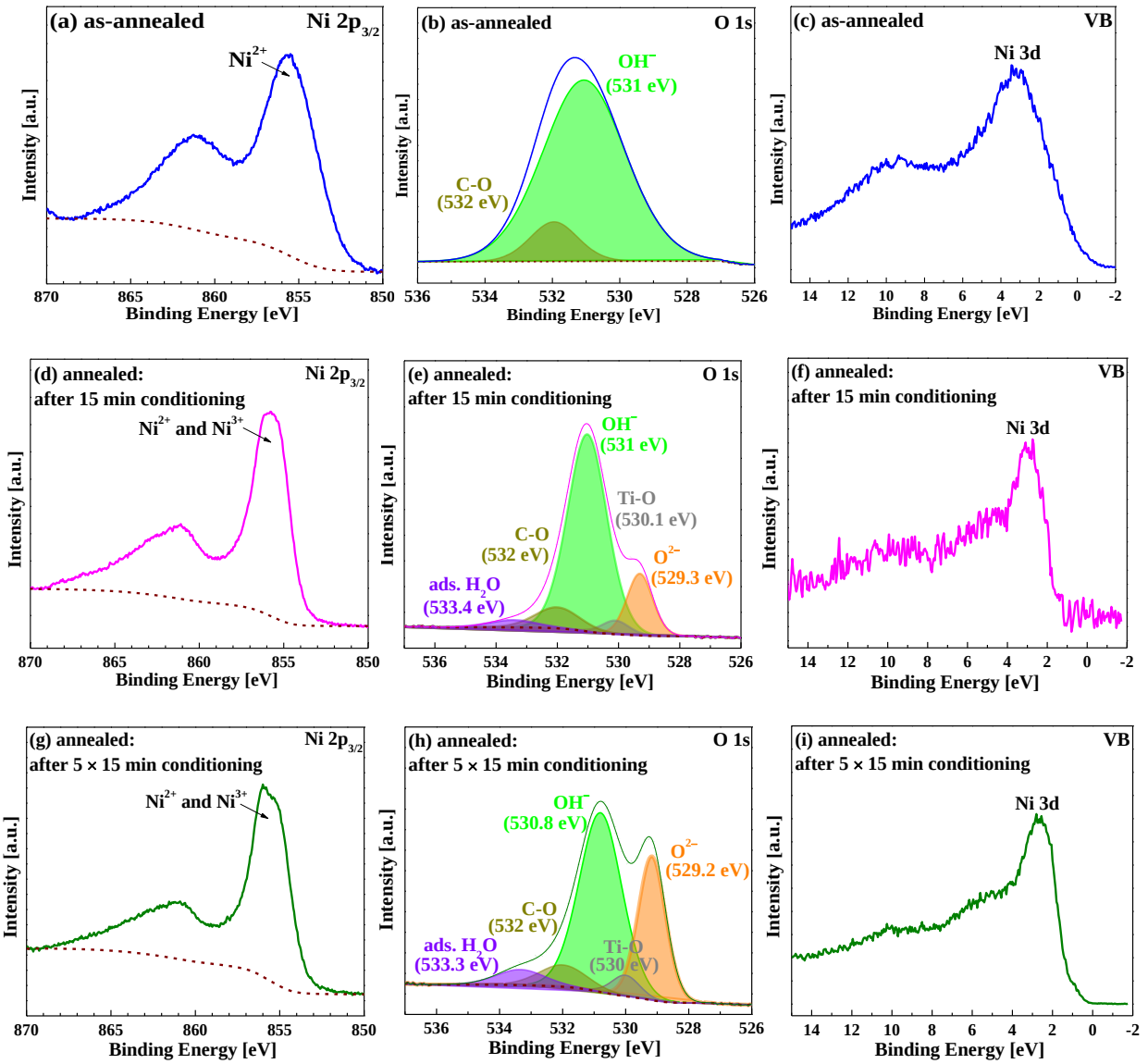

Figure 5.21 XPS Ni $2p_{3/2}$, O 1s and valence band (VB) detail spectra of the annealed $Ni(OH)_2$ films (S3), and the annealed films after 15 min and 5×15 min electrochemical conditionings.

The change in the bonding environment can be also observed in the O 1s XPS region. Fitting and deconvolution of the O1s spectrum obtained from the sample conditioned for 15 min (**Figure 5.21e**) exhibits a main peak located at a BE of 531 eV with a FWHM of 1.51 eV assigned to OH^- in Ni-OH species [$Ni(OH)_2$ or NiOOH]. Except for that, a shoulder feature at lower BE of 529.3 eV with a FWHM of 0.99 eV can be clearly observed, and it is ascribed to metal bonded oxygen within a regular oxide crystal (O^{2-}).[212, 255] Both peaks are also present in the O1s spectrum of the sample conditioned after 5×15 min with FWHMs of 1.55 eV and 1.03 eV, respectively (see **Figure 5.21h**). Moreover, the feature associated with O^{2-} in Ni-O clearly increases with electrochemical conditioning. The O 1s envelopes are also fitted with three additional peaks at ≈ 530 eV, ≈ 532 eV and ≈ 533.3 eV associated with O^{2-} lattice in Ti-O, carbon-oxygen species and adsorbed water, respectively. Both the Ni $2p_{3/2}$ spectrum and the O 1s spectrum show similar line shapes as observed by Payne et al. on NiOOH samples.[255-256] The O 1s peaks located at lower BEs can be assigned to

the O^{2-} in NiOOH.[255-256] It can be observed, that the OER catalytic activity correlates well with the amount of O^{2-} at the surface: the higher the presence of O^{2-}, the lower are the required overpotential and the Tafel slope for the OER, hence indicating that NiOOH is a more active intermediate for the OER.

Table 5.2 Surface elemental and chemical composition of the as-deposited, annealed and electrochemically conditioned samples as well as the comparison of the OER catalytic activity.

Sample	Elemental composition [%]						O/Ni[c]	Chemical composition [$NiO_x(OH)_y$]	OER catalytic activity	
	Ni	Ti	C	O					η @ 10 mA cm^{-2} [mV]	Tafel slope [mV dec^{-1}]
				O^{2-}	OH^-	Other[b]				
as-deposited	20.7	0	25.4	0	47.9	6.0	2.3	$Ni(OH)_{2.3}$	685	265
as-deposited, 15 min GC[a]	20.5	0.4	26.8	2.2	40.0	10.1	2.0	$NiO_{0.1}(OH)_{1.9}$	670	245
as-annealed	21.1	0	25.3	0	47.2	6.4	2.2	$Ni(OH)_{2.2}$	345	64
annealed, 15 min GC	25.1	1.1	18.2	8.0	39.3	8.3	1.9	$NiO_{0.3}(OH)_{1.6}$	325	50
annealed, 5 ×15 min GC	21.1	1.1	32.1	13.2	23.7	8.8	1.7	$NiO_{0.6}(OH)_{1.1}$	310	42.6
annealed, stability (26 h)	21.8	1.8	25.4	14.1	25.6	11.3	1.8	$NiO_{0.6}(OH)_{1.2}$	318	46.8

[a] GC represents galvanostatically conditioning at 10 mA cm^{-2}; [b] includes oxygen in Ti-O, adsorbed water and carbon-oxygen species; [c] The O/Ni ratio was calculated using the combined atomic concentrations of the O^{2-} and OH^- species.

Table 5.2 summarizes the elemental and chemical composition of the as-prepared and electrochemically conditioned samples, where the amount of oxygen is separated into contributions from O^{2-}, OH^- and other species in Ti-O, C-O and adsorbed water. The appearance of the substrate signal (Ti) in the XPS spectra after the electrochemical characterization is due to the cracking of the films (see **Figure 5.24**). The substrate signal does not increase even after 26 h stability test, indicating still a good adhesion of the electrodeposited films on the Ti substrate. The O/Ni ratios are calculated, and the value decrease from 2.2 to 1.7 with increasing conditioning time to 5 ×15 min. It has been proposed, that this observation may represent a structure undergoing degradation through loss of OH^-.[256] We refer to these $Ni(OH)_2$/NiOOH phases as (oxy)hydroxides and denote them with the general formula of $NiO_x(OH)_y$. The XPS characterization reveals, that the redox active Ni hydroxide/oxyhydroxide phases can be the active catalyst for the OER, which is well consistent with previous studies.[127]

As-deposited $Ni(OH)_2$ films

XPS measurements were also carried out on the as-deposited sample (without annealing) before and after electrochemical characterization to figure out the remarkable difference in the OER catalytic activity between the annealed and not annealed $Ni(OH)_2$ films. The surface elemental and chemical composition of the as-deposited and electrochemically conditioned samples are listed in **Table 5.2**. The signal assigned to O^{2-} in NiOOH is also collected from the conditioned as-deposited $Ni(OH)_2$ films. However, the intensity is much less than that of the annealed sample conditioned for the same duration. This might be one reason

why the OER catalytic activity of the not-annealed films is significantly lower than that of the annealed ones. On the other hand, the voltammetry of the not-annealed films shows a very weak redox wave, indicating a low amount of electrochemically accessible Ni atoms. Moreover, the OER activity of the not-annealed films is still strongly restricted by the low electrical conductivity. Thus, for the OER the pre-treatment of the electrodeposited $Ni(OH)_2$-based materials by thermal annealing is of extreme importance to form a large amount of the catalytically active NiOOH species on the surface during the electrochemical reaction.

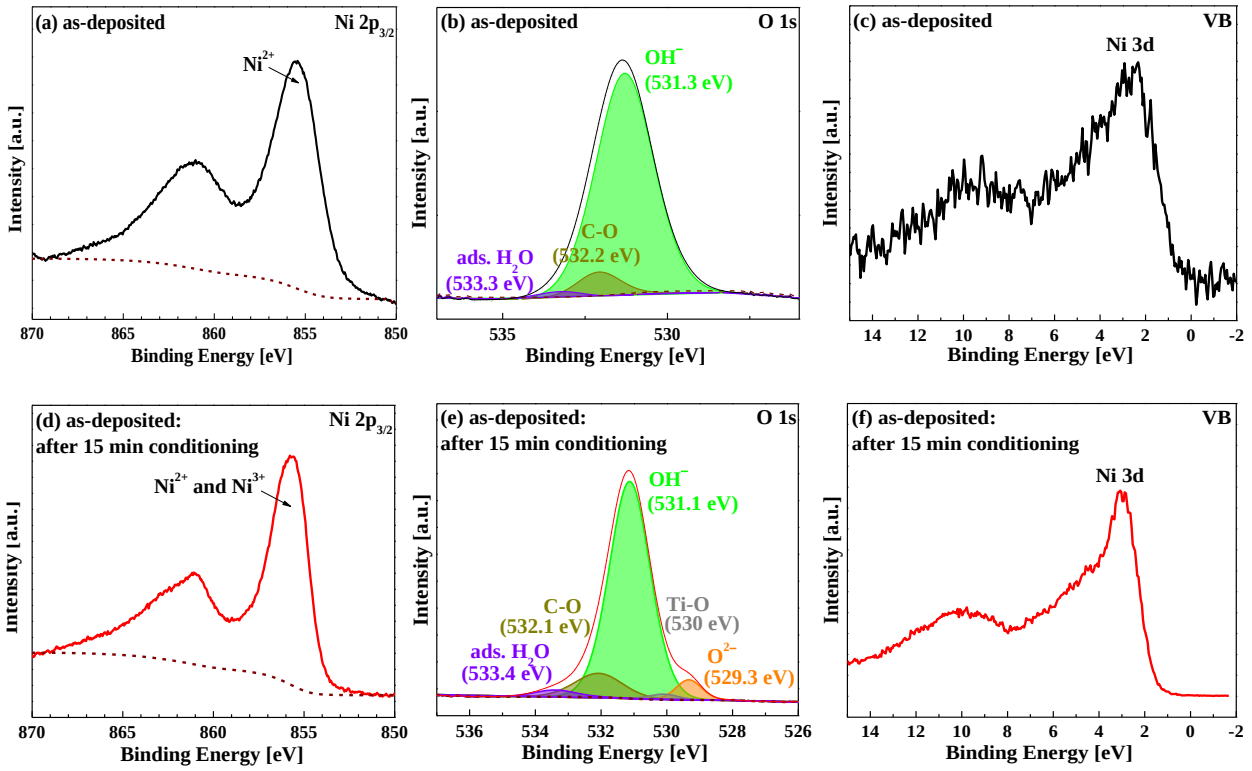

Figure 5.22 XPS Ni $2p_{3/2}$, O 1s and VB detail spectra of the as-deposited $Ni(OH)_2$ sample and the sample after 15 min electrochemical conditioning.

5.3.6 Stability test

In addition to catalytic efficiency, stability is another major concern, particularly for the OER catalysts, because of the relatively high overpotential involved. **Figure 5.23a** illustrates the stability performance of the annealed $Ni(OH)_2$ films electrodeposited with 3 cycles (S3) tested by chronopotentiometry measurement at 10 mA cm^{-2} for 26 h. It can be observed that the potential is gradually decreasing during the first 2 h indicating the catalyst activation. The overpotential at the lowest point is around 292 mV. After this process, the catalyst exhibits outstanding electrochemical stability with negligible potential increase till the end of the measurement. The CV scans of the films before and after the chronoamperometry (**Figure 5.23b**) show an improved activity with the η_{10} of 318 mV and a Tafel slope of 46.8 mV dec^{-1} after the long-time stability test. **Figure 5.24** displays the SEM images of the annealed films before and after the stability measurement, showing that there are some cracked layers formed during the reaction, but they are sticking

well to the substrate.

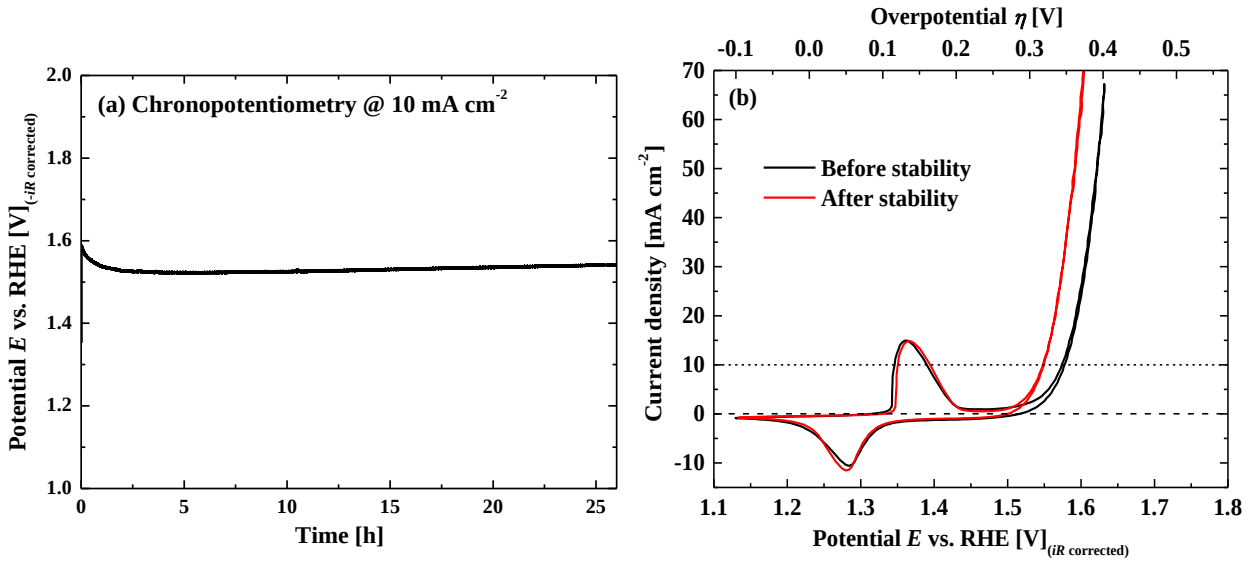

Figure 5.23 (a) Chronopotentiometry measurement of the annealed $Ni(OH)_2$ films under a constant current density of 10 mA cm^{-2} for 26 h in 1.0 M KOH. (b) CVs of the annealed $Ni(OH)_2$ films before and after chronoamperometry at a scan rate of 10 mV s^{-1}.

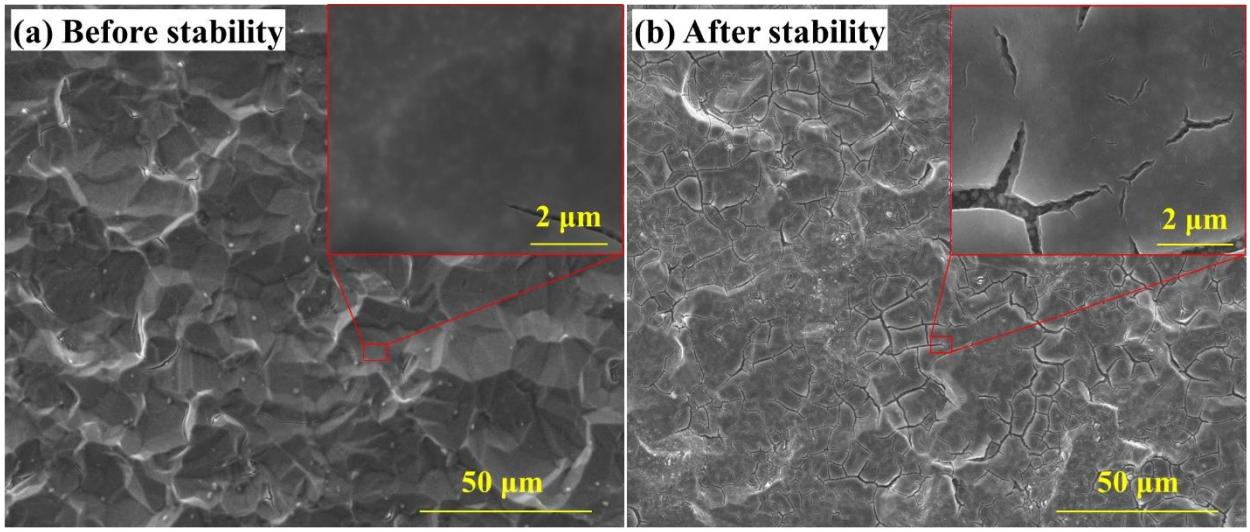

Figure 5.24 SEM images of the annealed $Ni(OH)_2$ films before and after the stability measurement. Insets in right-upper corners show the high-resolution images of the marked areas.

Figure 5.25 presents the XPS of the annealed $Ni(OH)_2$ films after the stability measurement. The survey spectrum in **Figure 5.25a** shows the presence of Ti signals collected from the substrate, which can be interpreted by the cracking of the original films during the electrochemical measurement. Compared to the data shown in **Figure 5.21g and h**, the high-resolution Ni $2p_{3/2}$ and O 1s spectra after stability (**Figure 5.25b and c**) clearly explain the outstanding stability of the annealed films in terms of the very stable chemical composition.

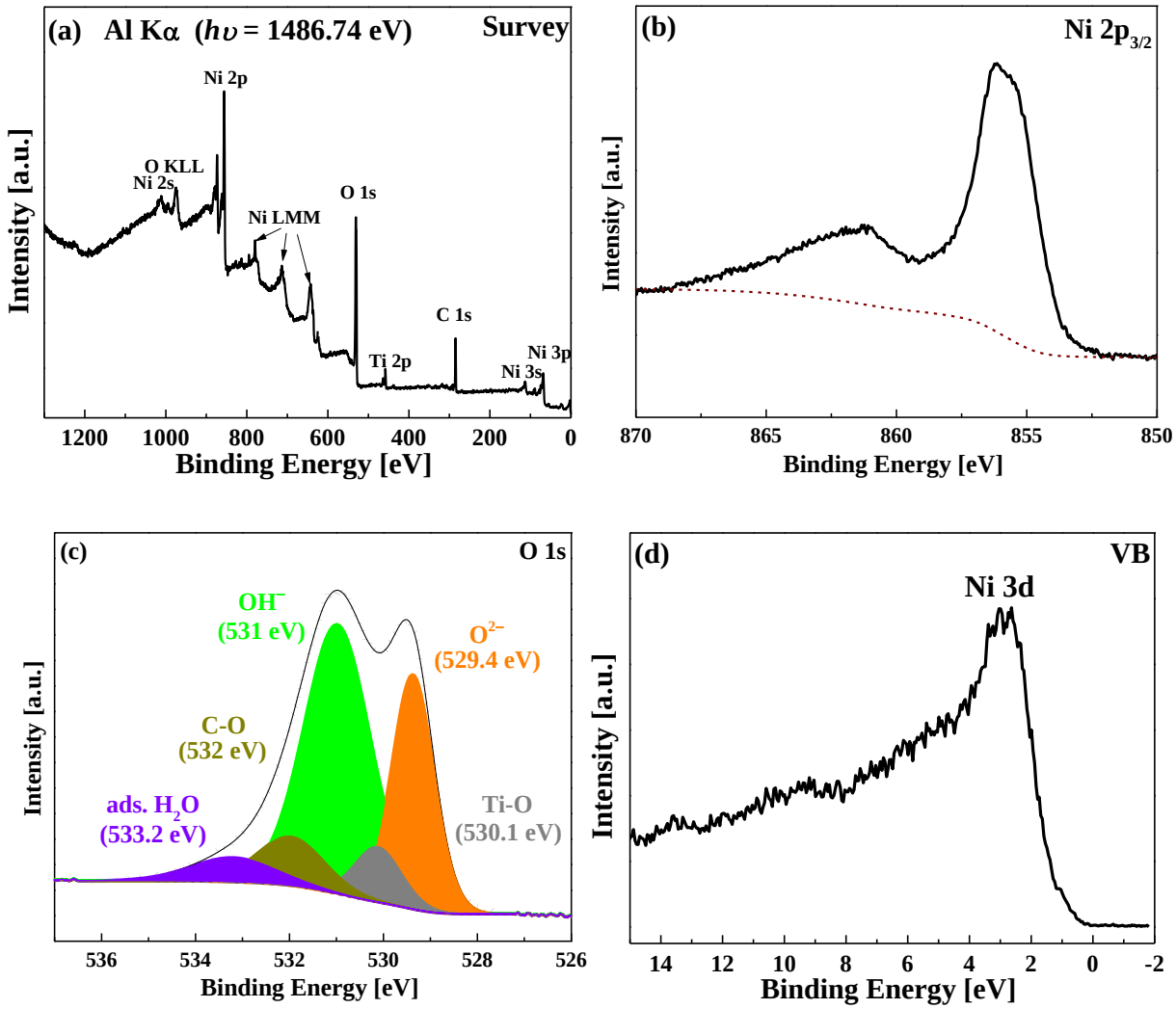

Figure 5.25 XPS survey, Ni $2p_{3/2}$, O 1s and VB detail spectra of the annealed $Ni(OH)_2$ films after the stability measurement.

5.4 Summary

Transparent $Ni(OH)_2$ films have been electrodeposited onto the Ti surface using cyclic voltammetry. In addition, some Ni composite NPs can be found under the $Ni(OH)_2$ films, forming a unique NPs-film structure. The catalytic OER activities of the $Ni(OH)_2$ films are remarkably improved by a simple thermal annealing treatment in air atmosphere. The optimal treatment condition towards maximized OER is determined at a moderate temperature of 150 °C for 1 h. XPS and SEM investigations show, that the annealing treatment does not significantly change the chemical composition and surface morphology of the $Ni(OH)_2$ catalysts. XPS and voltammetry analysis reveal, that annealing (mainly a dehydration process) caused conductivity improvement and an increase in the active site are the essential factors to the highly enhanced OER activity. Moreover, the OER catalytic activity of the annealed $Ni(OH)_2$ films can be further improved by electrochemical galvanostatic conditioning. The annealed $Ni(OH)_2$ catalyst (electrodeposited for 3 cycles) after conditioning exhibit a small overpotential of 310 mV at an anodic current density of 10 mA cm^{-2} with a small Tafel slope of 42.6 mV dec^{-1} in 1.0 M KOH. These films show a better OER activity than a commercial RuO_2 electrode (η_{10}: 356 mV; Tafel slope: 80 mV dec^{-1}). Stability measurements for up to 26 h exhibit an excellent electrochemical stability. XPS investigations performed before and after the electrocatalytic OER indicate that the pre-treatment of the nickel compound by annealing accelerates the formation of a large amount of the catalytically active NiOOH species on the surface during the electrochemical reaction, and the further improved OER activity is correlated with the increased amount of NiOOH formed during the activation process.

It is further interesting to identify the phase transformation of the $Ni(OH)_2$ films before and after annealing as well as electrochemical OER test by X-ray diffraction characterization to clarify the most active phase. Data obtained by in-situ techniques, such as Raman spectroscopy and X-ray absorption spectroscopy, will be necessary to compare with the present XPS data to gain a full understanding of the elementary reaction steps.

6. Electrodeposition of Porous Nickel-Molybdenum Films as Bifunctional Electrocatalysts for the Water Splitting Reaction

6.1 Introduction

Up till now, many transition metal compounds e.g. phosphides, sulfides, carbides and nitrides for the HER, and oxides, nitrides and (oxy)hydroxides for the OER, have been reported. Although there exciting progress has been made,[21, 127, 193, 251, 257-258] the catalytic activities of these electrocatalysts need to be further improved towards both the HER and the OER in the same electrolyte. Such bifunctional electrocatalysts are highly attractive because different equipment and processes used to produce different electrocatalysts can be avoided, thus decreasing the overall cost.[88, 259]

Bimetal-based compounds have been reported to exhibit enhanced catalytic activity compared to their corresponding single-metal counterparts. Typically, previous work has shown, that alloying of nickel and of molybdenum can render a greatly enhanced HER activity.[260] Meanwhile, oxidized high-valence Ni and Mo species were also identified to be the active centers for the OER.[260-261] Therefore, Ni-Mo alloys directly subjected to anodic conditions are also expected to provide promising OER activity, suggesting the possible construction of a symmetric electrochemical system for overall water splitting using both Ni-Mo active materials for the HER and the OER.

Here, a 3-D porous Ni-Mo film catalyst is presented, which is synthesized via a simple one-step electrodeposition method by applying a large cathodic current density. A highly porous structure is obtained due to the concurrent evolution of hydrogen during the deposition of the mixed Ni-Mo compound. SEM characterization was carried out on the Ni-Mo films deposited with different time windows to witness the fabrication process of the porous structure. The electrocatalytic activities of the Ni-Mo films towards the HER in acidic and alkaline solutions and the OER in alkaline solution were evaluated. The oxidation state and the chemical composition of the Ni-Mo films before and after the electrochemical reactions were obtained by XPS and are discussed in correlation to the electrocatalytic activity to identify the real active sites.

6.2 Experimental section

6.2.1 Electrocatalysts preparation

Information on the electrodeposition setup has been given in chapter 3.

Preparation of Ni-Mo films

Ni-Mo films were electrodeposited from an electrolytic solution containing 0.3 M nickel (II) sulfate hexahydrate ($NiSO_4 \cdot 6H_2O$, 99.97%, Alfa Aesar), 0.2 M sodium molybdate dihydrate ($Na_2MoO_4 \cdot 2H_2O$,

99.97%, Alfa Aesar) and 0.3 M trisodium citrate dihydrate ($Na_3C_6H_5O_7 \cdot 2H_2O$, 99%, Alfa Aesar), with pH 10.5 adjusted by the addition of 25% ammonia solution (Ph.Eur., Carl Roth GmbH + Co. KG). The deposition electrolyte was prepared according to the data published by McCrory, et al.[262] Prior to electrodeposition, the cleaned Ti foils were chemically etched in 6 N HCl (volumetric standard solution, Carl Roth GmbH + Co. KG) at room temperature to remove the native oxides (TiO_x) and to form a homogenized as well as a rough surface. **Figure 6.1** presents the SEM images of the cleaned Ti foil (without etching) and the Ti foils etched in 6 N HCl for 1, 5 and 7 days. It shows, that the Ti surface with higher roughness is obtained after etching in HCl solution, and the homogeneity and roughness of the HCl treated Ti surface can be varied by changing the etching time.

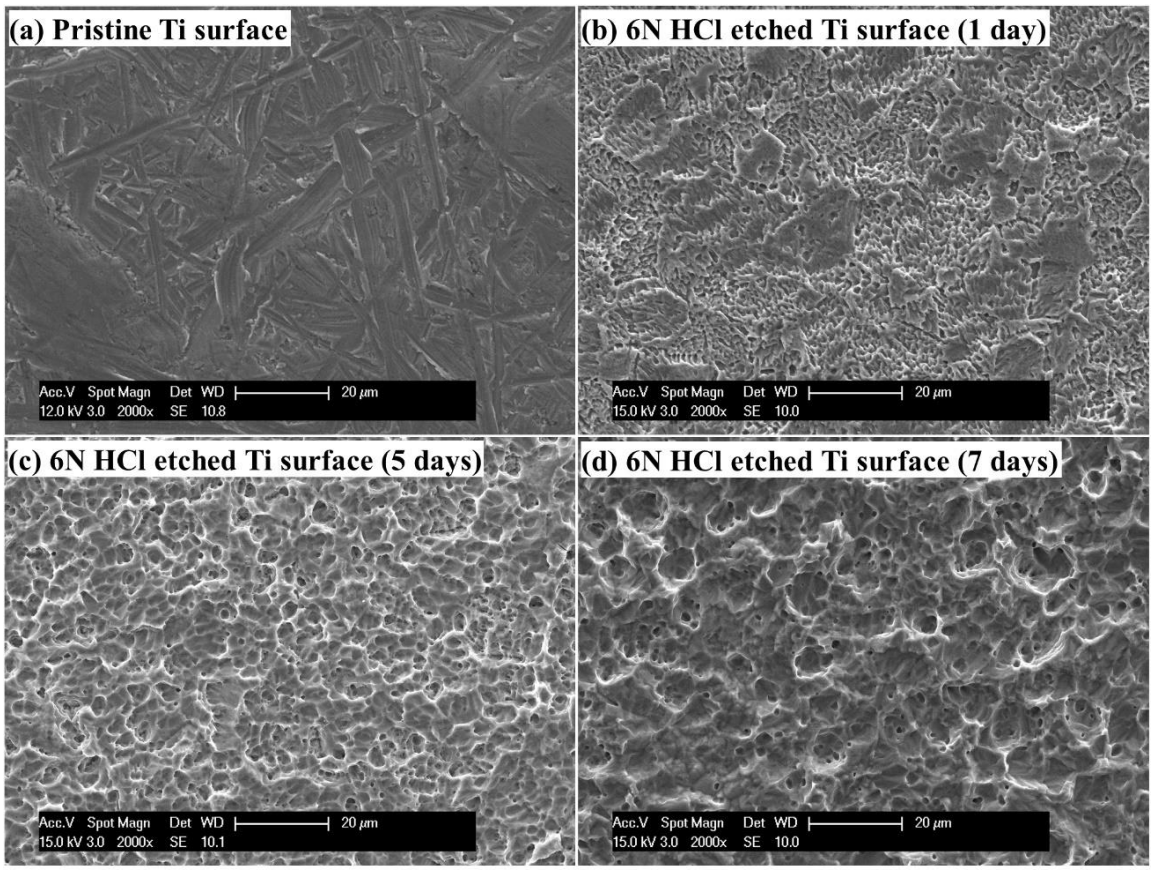

Figure 6.1 SEM images of (a) the pristine (cleaned) Ti surface and (b-d) the Ti surfaces after etching in 6 N HCl for 1, 5 and 7 days.

Determination of the optimal etching time was performed by investigating the HER catalytic activity of the Ni-Mo films deposited on the Ti surfaces etched with different periods (**Figure 6.2**). The Ni-Mo films were electrodeposited under an identical condition with a cathodic current density of 160 mA cm^{-2} for 20 min. Ni-Mo films deposited on the pristine Ti substrate show a very bad adhesion, while the opposite was observed for the HCl etched Ti surfaces. The LSV curves in **Figure 6.2** indicate, that the surface morphology of the Ti substrate shows only a minor effect on the Ni-Mo films towards the HER in acidic solution (0.5 M H_2SO_4), while an apparent effect can be observed in alkaline solution (1.0 M KOH). It can

be seen, that the Ni-Mo films deposited on the Ti substrate etched for 5 days show the best performce both in 0.5 M H_2SO_4 and in 1.0 M KOH. Thus, the Ti foil etched in 6 N HCl for 5 days was utilized as the substrate for the following studies.

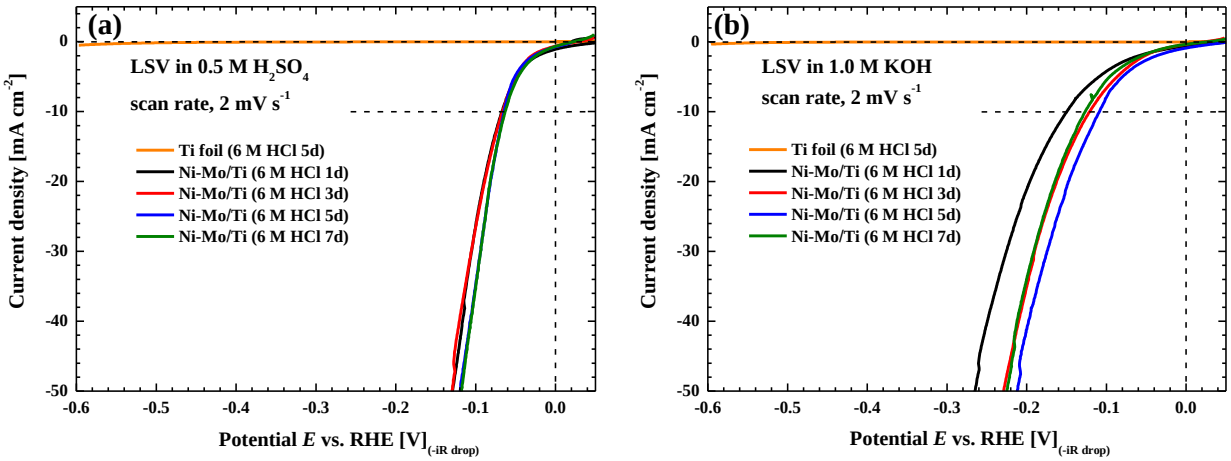

Figure 6.2 HER catalytic performance of the Ni-Mo films deposited on Ti substrates after etching in 6 N HCl for different time periods: (a) Linear sweep voltammetry (LSV) curves in 0.5 M H_2SO_4; (b) LSV curves in 1.0 M KOH. Scan rate: 2 mV s^{-1}.

In this work, different Ni-Mo films were galvanostatically deposited onto the HCl etched Ti foil substrates by applying a high cathodic current density of 160 mA cm^{-2} with the deposition time from 1 to 20 min. **Figure 6.3** shows the current density and the potential vs. RHE as a function of deposition time. The potential required to drive the deposition at cathodic current density of 160 mA cm^{-2} did slightly increase from -1.8 V to -1.7 V with reaction time up to 20 min. After each electrodeposition, the prepared Ni-Mo films were rinsed in Millipore water and dried under a nitrogen gas flow for further characterization.

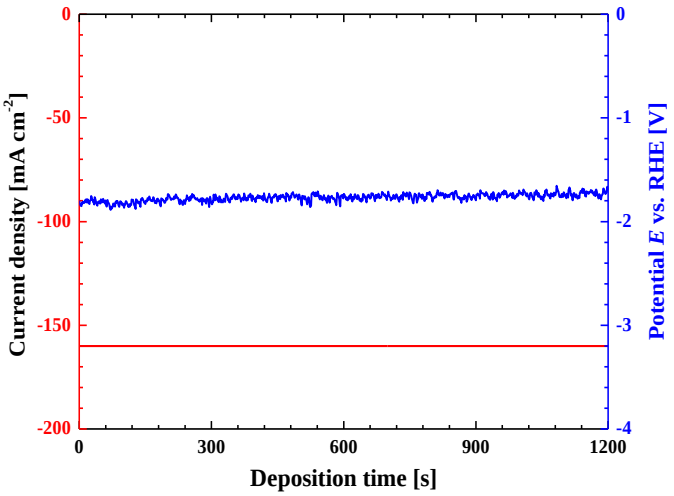

Figure 6.3 Current density (red curve) and potential vs. RHE (blue curve) as a function of the deposition time for the galvanostatic electrodeposition of Ni-Mo films at a cathodic current density of 160 mA cm^{-2}.

Preparation of Ni NPs

Ni NPs were electrodeposited onto the HF etched Ti substrate by cyclic voltammetry according to the optimal data shown in chapter 4.

Preparation of Pt-decorated Ni NPs

The Pt-decorated Ni NPs were prepared by electrodeposition of Pt on the Ni NPs/Ti electrode via cathodic electrolysis of a 0.5 mM H_2PtCl_6 (Sigma-Aldrich, ≥ 99.9% trace metals basis) in 0.1 M H_2SO_4 aqueous solution (volumetric standard solution, Carl Roth GmbH + Co. KG) at a current density of -5 mA cm^{-2} (with potential around -1.2 V vs. RHE) for 2 min. After electrodeposition, the prepared Pt-decorated Ni NPs were rinsed in Millipore water and dried under a nitrogen gas flow for further characterization.

Preparation of Ni films

Ni films were electrodeposited onto the HF etched Ti substrate by cyclic voltammetry for three cycles according to the data shown in chapter 5.

Preparation of RuO_2/Ti electrode

The preparation of RuO_2/Ti electrode can be seen in experimental section in chapter 5.

6.2.2 Structural characterization

Surface morphologies of the prepared Ni-Mo samples were observed using SEM, coupled with EDX to examine the elemental composition. Chemical composition and oxidation state of the Ni-Mo samples before and after electrochemical measurements were investigated by means of XPS. Wide scan and high-resolution spectra (for C 1s, O 1s, Ni 2p and Mo 3d peaks) were recorded. Assignment of peaks to particular nickel species was made according to the criteria established by Biesinger et al.,[190] while the association of peaks with particular molybdenum species was done in accordance with previous estimates of binding energies for Mo(0), Mo_2O_3, MoO_2, Mo_2O_5, Na_2MoO_4 and MoO_3 as shown in **Table 6.1**.[226, 263-266]

Table 6.1 Binding energies of Mo 3d obtained from literature,[263-266] and binding energies of peaks used to assign species from the present measurements.

Oxidation state	Binding energy (eV) (lit.)		Binding energy (eV) (meas.)	
	Mo $3d_{5/2}$	Mo $3d_{3/2}$	Mo $3d_{5/2}$	Mo $3d_{3/2}$
Mo (0)	227.7 ~ 228.0	231.0 ~ 231.2	227.6 ~ 228.0	230.8 ~ 231.0
Mo (III) – Mo_2O_3	228.4	231.6	228.4 ~ 228.6	231.6 ~ 231.7
Mo (IV) – MoO_2	230.2	233.4	230.1 ~ 230.2	233.4 ~ 233.7
Mo (V) – Mo_2O_5	230.8 ~ 231.6	234.0 ~ 234.8	–	–
Mo (VI) – Na_2MoO_4/MoO_3	232.1 ~ 232.8	235.5 ~ 235.9	232.1 ~ 232.6	235.2 ~ 235.7

Further information on the SEM and XPS setups and parameters has been given in chapter 3. Phase composition of the Ni-Mo films was identified by X-ray diffraction (XRD). For the XRD analysis, the dried Ni-Mo films were peeled off from the Ti substrates using transparent tape. XRD patterns of the Ni-Mo films were recorded using a STADI P powder diffractometer (STOE & Cie GmbH, Darmstadt, Germany) with a molybdenum Kα1 radiation source (λ = 0.709300 Å).

6.2.3 Electrochemical measurements

Electrochemical measurements were performed in a standard three-electrode system as illustrated in chapter 3. The catalyst decorated Ti substrates and a Pt coil were used as the working electrodes and the counter electrode, respectively. An Ag/AgCl (3 M KCl) reference electrode was used for the measurements in 0.5 M H_2SO_4, and a Hg/HgO (1 M NaOH) reference electrode was used for the measurements in 1.0 M KOH. HER activity was determined by LSV in 0.5 M H_2SO_4 and 1.0 M KOH electrolyte solutions at a scan rate of 2 mV s^{-1}. OER activity was evaluated using CV in 1.0 M KOH at a scan rate of 10 mV s^{-1}. EIS measurements were carried out in the frequency range from 1 Hz to 100 KHz with a modulated signal amplitude of 10 mV near the OCP to obtain the uncompensated series resistance. Potentials measured against the reference electrodes ($E_{\text{vs. ref.}}$) in 0.5 M H_2SO_4 and 1.0 M KOH were converted into the potentials versus the RHE ($E_{\text{vs. RHE}}$) according to equation **(3.1)**. The values were further corrected for uncompensated resistance on the basis of the EIS data.

6.3 Results and Discussion

6.3.1 Surface morphology

The SEM images in **Figure 6.4** witness the changes in morphology of the Ni-Mo coatings with increasing deposition time from 1 to 20 min. After electrodeposition for 1 min **(Figure 6.4a)** the Ni-Mo film shows a relatively flat surface without a porous structure produced. After 5 min, the Ni-Mo film has a considerably rougher surface with micrometer-sized spherical shaped crystals observed **(Figure 6.4b)**. The SEM images of the Ni-Mo catalyst electrodeposited with 10 min show, that the resulting layer contains micron-scale holes, which are constructed by the randomly and loosely stacked spherical crystals **(Figure 6.4c)**. With deposition time extending to 20 min, deeper and homogeneously distributed pores were formed **(Figure 6.4d)**. At the cathodic deposition current density of 160 mA cm^{-2} used in this work, we can observe bubbles evolving on the electrode surface, indicating a concurrent evolution of hydrogen and deposition of Ni-Mo. The porous structure is formed by the hydrogen bubbles blocking the surface from access to the plating solution.[22, 226, 267] The SEM images with higher magnification (the right-most column) show, that the micrometer-sized spherical shaped crystals were agglomerated by smaller spherical particles with an average diameter of 300 nm. The porous three-dimensional structure indicates a high surface area available for the water splitting reaction. The insets show the results from the EDX analyses for each sample: Ni and Mo signals can be observed on all these samples, indicating, that the surface is composed primarily of the Ni and Mo elements.

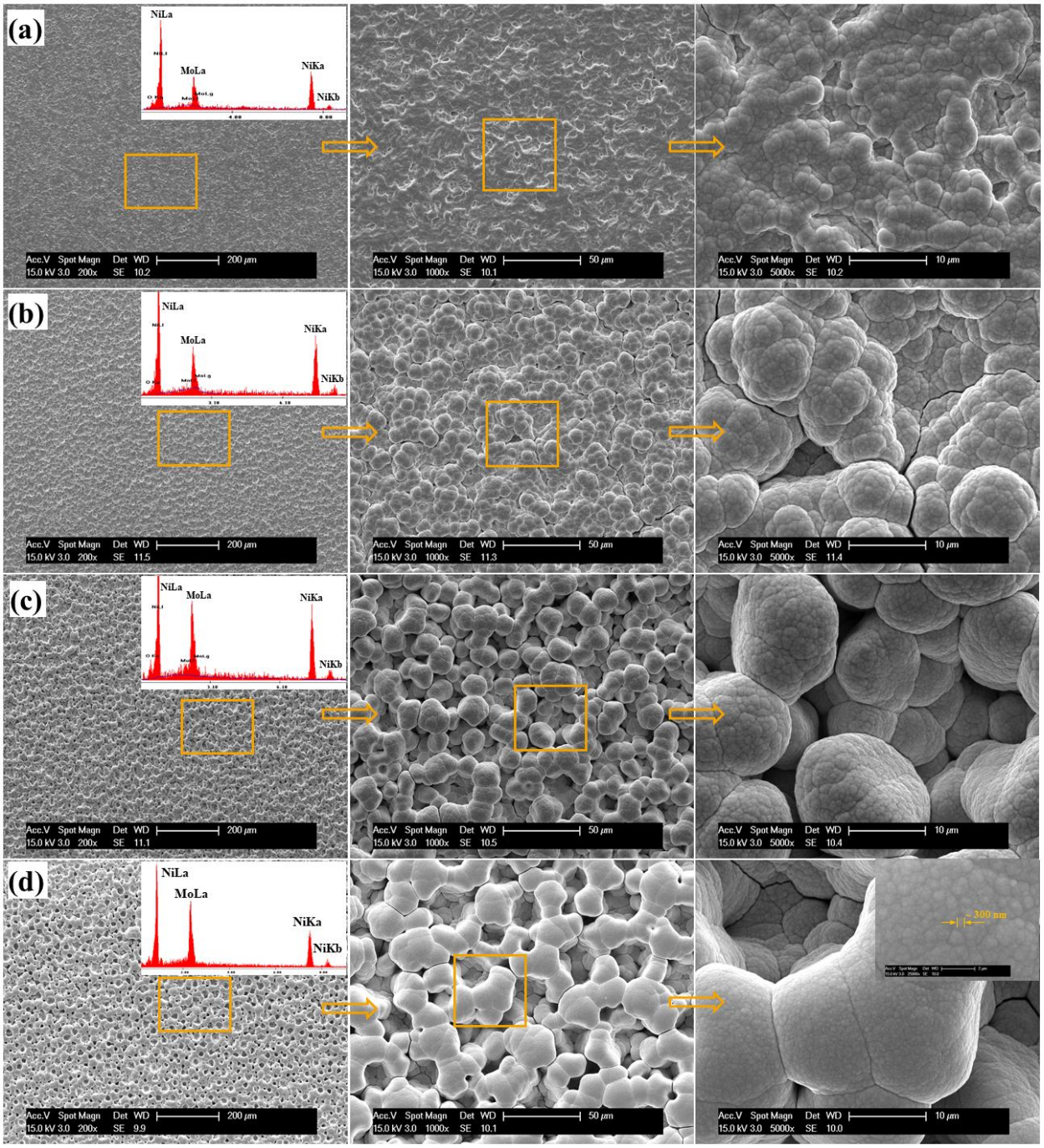

Figure 6.4 SEM images of the Ni-Mo catalysts electrodeposited at a current density of -160 mA cm^{-2} with different deposition time: (a) 1 min, (b) 5 min, (c) 10 min, and (d) 20 min. Insets are the EDX spectra.

Figure 6.5a displays the SEM image of the Pt-decorated Ni NPs on Ti substrate. Compared with the SEM image of the Ni NPs shown in chapter 4 (**Figure 4.14**), no obvious change can be observed after the decoration of Pt. While, the EDX analysis (**Figure 6.5b)** validates the presence of Pt, besides the elements of Ni, O, and Ti.

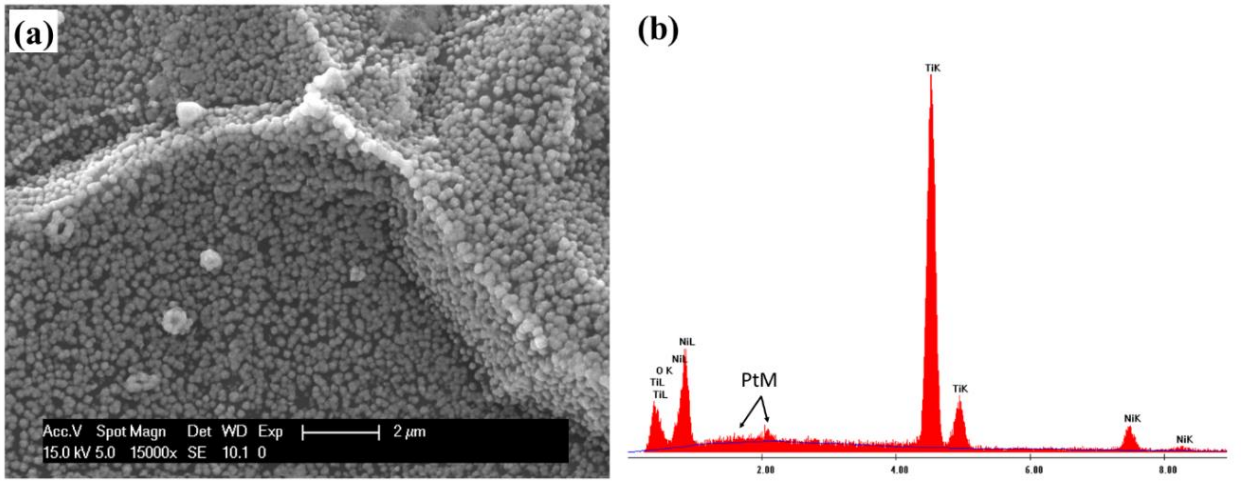

Figure 6.5 (a) SEM image of the Pt-decorated Ni NPs on Ti substrate. (b) EDX spectrum.

6.3.2 Phase composition

XRD patterns of the electrodeposited Ni-Mo films are shown in **Figure 6.6**. The reflection peaks attributed to NiMo alloys can be clearly observed. Compared with the reflection peaks of standard Ni (the red lines on **Figure 6.6a**), the peaks of the electrodeposited NiMo alloys are observed with a shift towards low 2θ values due to the presence of Mo atoms within the lattice of Ni crystals. The Full-Profile Rietveld patterns of the NiMo alloys are shown in **Figure 6.6b**. The peak shapes were modeled using the Thompson-Cox-Hastings pseudo-Voigt function for average grain size and the pseudo-Voigt function for lattice parameters, respectively.[268-269] The grain size and lattice parameters of the NiMo alloys obtained by Full-Profile Rietveld refinement of the XRD patterns are 1.6 nm and 3.6128(6) Å, respectively.

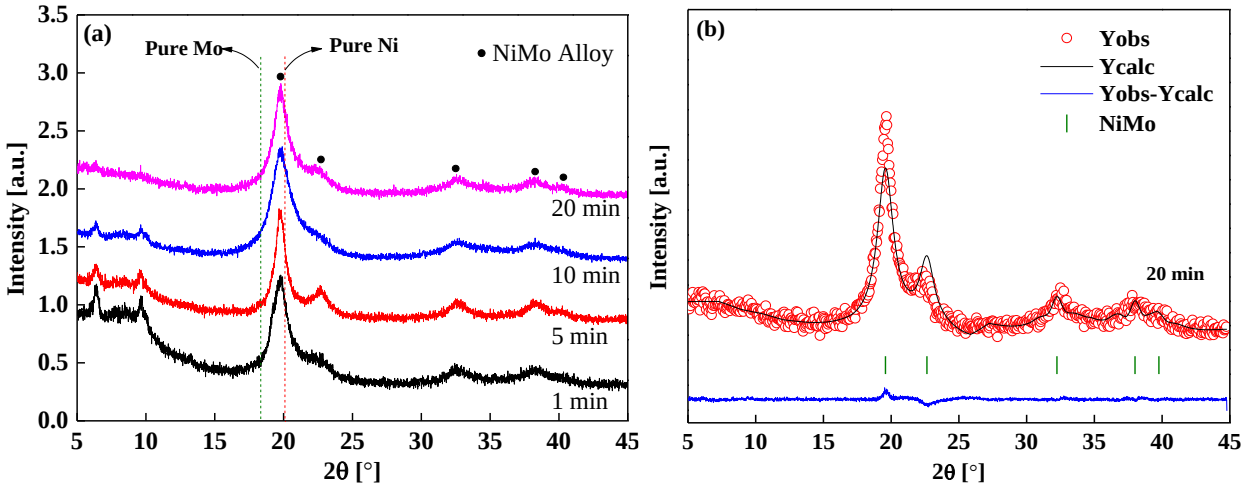

Figure 6.6 (a) XRD patterns of the electrodeposited Ni-Mo films with different deposition time. (b) Full-Profile Rietveld patterns. In (b), Y_{obs} and Y_{calc} represent the observed and calculated profiles, respectively; Green lines are Bragg peak positions of related phase; Blue line at the bottom denotes the difference intensities between the observed and calculated profiles.

6.3.3 Surface chemical composition

X-ray photoelectron spectroscopy (XPS) characterization was conducted on the as-deposited Ni-Mo catalysts to investigate their chemical composition and electronic properties. **Figure 6.7** shows the XPS survey spectra of the Ni-Mo samples prepared with deposition times of 5, 10 and 20 min at a cathodic current density of 160 mA cm^{-2} (denoted as Ni-Mo-5, Ni-Mo-10 and Ni-Mo-20, respectively). As expected, the wide-scan spectra reveal the presence of Ni and Mo elements. In addition, peaks corresponding to O and C elements are also observable. The sources of carbon have been discussed in Chapter 4. Signals attributed to the Ti element are absent on the samples, indicating that Ni-Mo films with thickness higher than 10 nm are formed on the substrate surface. Unexpectedly, very strong peaks assigned to the Na element are observed on the sample deposited for 20 min. The impurity of Na is presumably adsorbed from the deposition solution, considering the high concentration of Na^+ (0.4 M) in the electrolyte and the relatively long electrodeposition time. Except of Na, no other metal impurities have been detected.

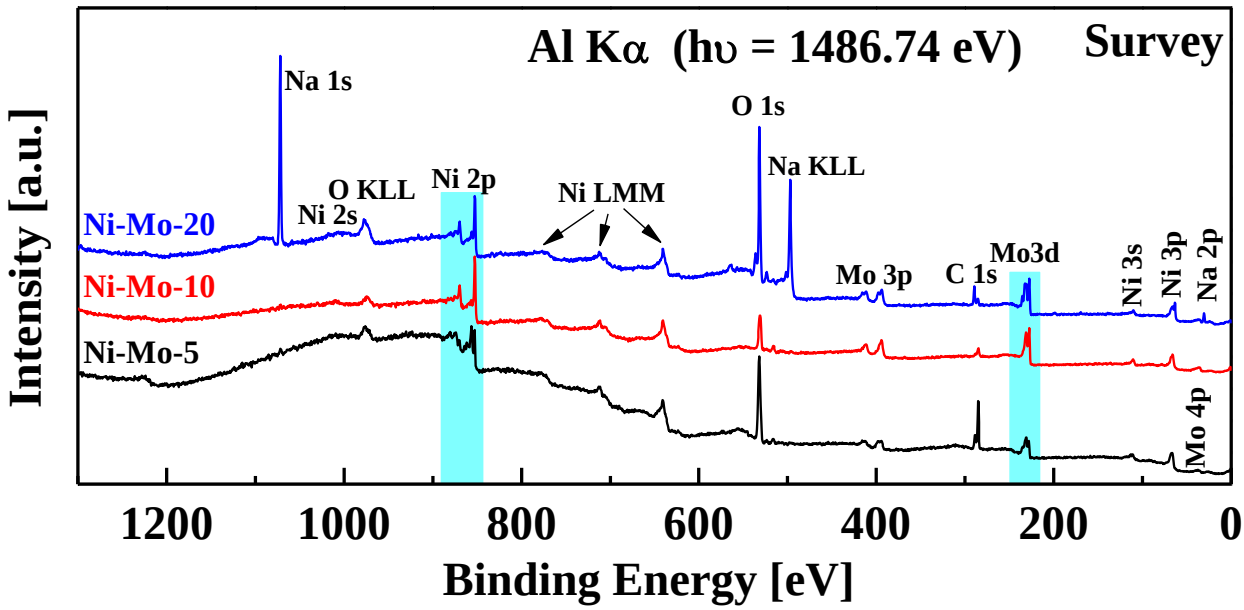

Figure 6.7 XPS survey spectra of the Ni-Mo catalysts electrodeposited at a cathodic current density of 160 mA cm^{-2} for 5, 10 and 20 min (denoted as Ni-Mo-5, Ni-Mo-10 and Ni-Mo-20, respectively).

Figure 6.8 displays the high-resolution Ni 2p and Mo 3d detail X-ray photoelectron spectra of the as-deposited Ni-Mo samples. Quantitative XPS analysis shows an atomic ratio of ≈ 2:1 for total Ni (Ni_{Total}) with respect to total Mo (Mo_{Total}) on the sample deposited for 5 min, revealing that nickel is primarily deposited at the initial stage of the electrodeposition process. After deposition for 10 min, the ratio decreases to ≈ 1:1 and the same relationship is observed on the sample deposited for 20 min. It was reported, that the deposition of molybdenum can be accelerated by the nickel species, which are capable of catalyzing the reduction of molybdenum to form a Ni-Mo intermediate, either through the adsorbed intermediate (Ni^+_{ads}) or directly with solution-based Ni species.[270-272]

Fitting and deconvolution of the Ni $2p_{3/2}$ spectra according to the criteria established by Biesinger et al. (**Figure 6.8a**) [190] indicates the presence of Ni metal (≈ 852.6 eV), NiO (≈ 854.1 eV) and $Ni(OH)_2$ (≈ 856.0 eV) on these Ni-Mo samples.[21] Features corresponding to Ni metal and $Ni(OH)_2$ are significantly observed on Ni-Mo-5. Interestingly, with the deposition time increasing to 10 (Ni-Mo-10) and 20 min (Ni-Mo-5), the peak intensity related to $Ni(OH)_2$ is highly reduced with mainly pure Ni present on the surface. Very weak signals assigned to NiO are observed on these three Ni-Mo samples.

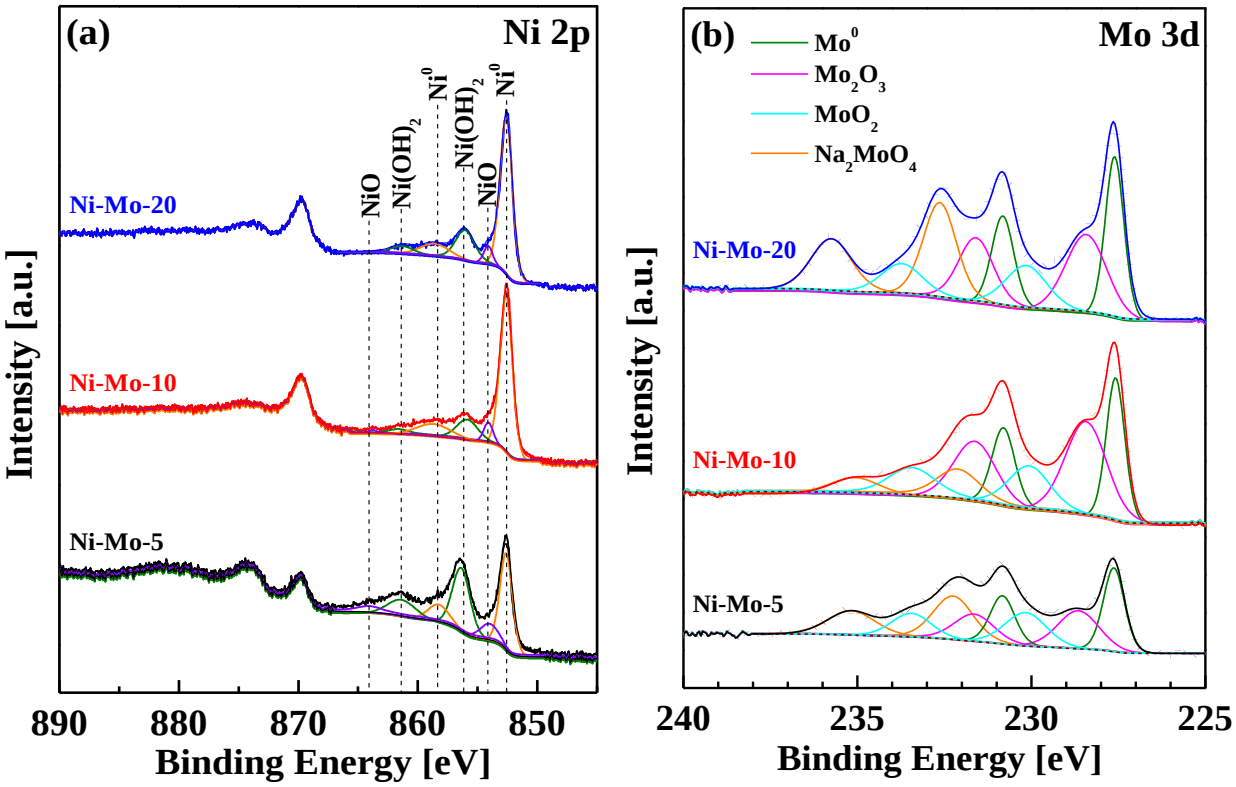

Figure 6.8 XPS Ni 2p (a) and Mo 3d (b) spectra of the Ni-Mo catalysts electrodeposited at a current density of -160 mA cm^{-2} for 5, 10 and 20 min (denoted as Ni-Mo-5, Ni-Mo-10 and Ni-Mo-20, respectively).

High-resolution Mo 3d signals were fitted using similar full width at half maximum (FWHM) for the metallic molybdenum and for the oxidized molybdenum species. An area ratio of 2:3 has been used for the $3d_{3/2}$ and $3d_{5/2}$ components of the Mo 3d peak, as shown in **Figure 6.8b**. The resulting features show a spin-orbit split doublet for the metallic Mo (≈ 227.6 eV and ≈ 230.8 eV) and three spin-orbit split doublets for oxidized Mo species associated with Mo_2O_3 (≈ 228.5 eV and ≈ 231.7 eV), MoO_2 (≈ 230.2 eV and ≈ 233.4 eV) and Na_2MoO_4 (≈ 232.2 eV and ≈ 235.4 eV), which are well consistent with data reported in previous studies.[99, 263-264, 273] The fitted Ni 2p and Mo 3d XPS spectra are additionally used to determine the surface chemical composition of the Ni-Mo catalysts by calculating the atomic concentrations of Ni and Mo related oxidation states. The quantitative analysis results are summarized in **Table 6.2**.

Table 6.2 Surface chemical composition of the Ni-Mo films determined by the quantitative analysis of the Ni 2p and Mo 3d XPS peaks.

Sample	Ni_{Total} : Mo_{Total}[a]	Surface chemical composition (%)						
		Ni_xMo_y alloy		$Ni(OH)_2$	NiO	Mo_2O_3	MoO_2	Na_2MoO_4
Ni-Mo-5	64.8% : 35.2%	$Ni_{2.9}Mo$	38.4	28.7	6.9	8.8	7.7	9.5
Ni-Mo-10	53.3% : 46.7%	$Ni_{2.9}Mo$	52.6	10.2	3.0	19.5	8.9	5.8
Ni-Mo-20	50.3% : 49.7%	$Ni_{2.4}Mo$	48.8	10.8	2.5	15.3	8.3	14.3

[a] The Ni_{Total} : Mo_{Total} ratio refers to atomic ratio. [b] The atomic concentration of Ni species was calculated using the atomic sensitivity factor (RSF) of Ni $2p_{3/2}$ with the value of 14.6. [c] The atomic concentration of Mo species was calculated using the atomic sensitivity factor (RSF) of Mo 3d with the value of 9.5.

The co-electrodeposition of Ni-Mo can be described by following reaction equations according to a previously proposed mechanism:[22]

$$MoO_4^{2-} + 4H^+ + 2e^- \rightarrow MoO_2 + 2H_2O \quad \textbf{(6.1)}$$

$$Ni^{2+} + MoO_2 + 2e^- \rightarrow Ni\text{-}MoO_2 \quad \textbf{(6.2)}$$

$$2H^+ + 2e^- \rightarrow H_2 \quad \textbf{(6.3)}$$

$$2H_2 + Ni\text{-}MoO_2 \rightarrow Ni\text{-}Mo + 2H_2O \quad \textbf{(6.4)}$$

Thus, simultaneous HER during deposition plays an important role in forming the porous NiMo alloys containing layers. On one hand, the produced hydrogen involves in the electrochemical reactions by reducing the intermediate Ni-Mo mixed oxide to a neutral alloy; On the other hand, bubbles evolved on the electrode act as dynamic templates that Ni-Mo deposits around.

Figure 6.9 shows the XP spectra of the Pt-decorated Ni NPs on Ti substrate. The Pt 4f spectrum exhibits typical peaks located at binding energies of 71.2 eV and 74.5 eV, which are attributed to Pt $4f_{7/2}$ and Pt $4f_{5/2}$ for metallic Pt (Pt^0), respectively.[182, 209] The Ni 2p and O 1s spectra show the deposited Ni species include Ni^0, NiO and $Ni(OH)_2$.[21] According to the quantitative XPS analysis, the atomic ratio of Ni:Pt was observed to be 4:1 on the surface.

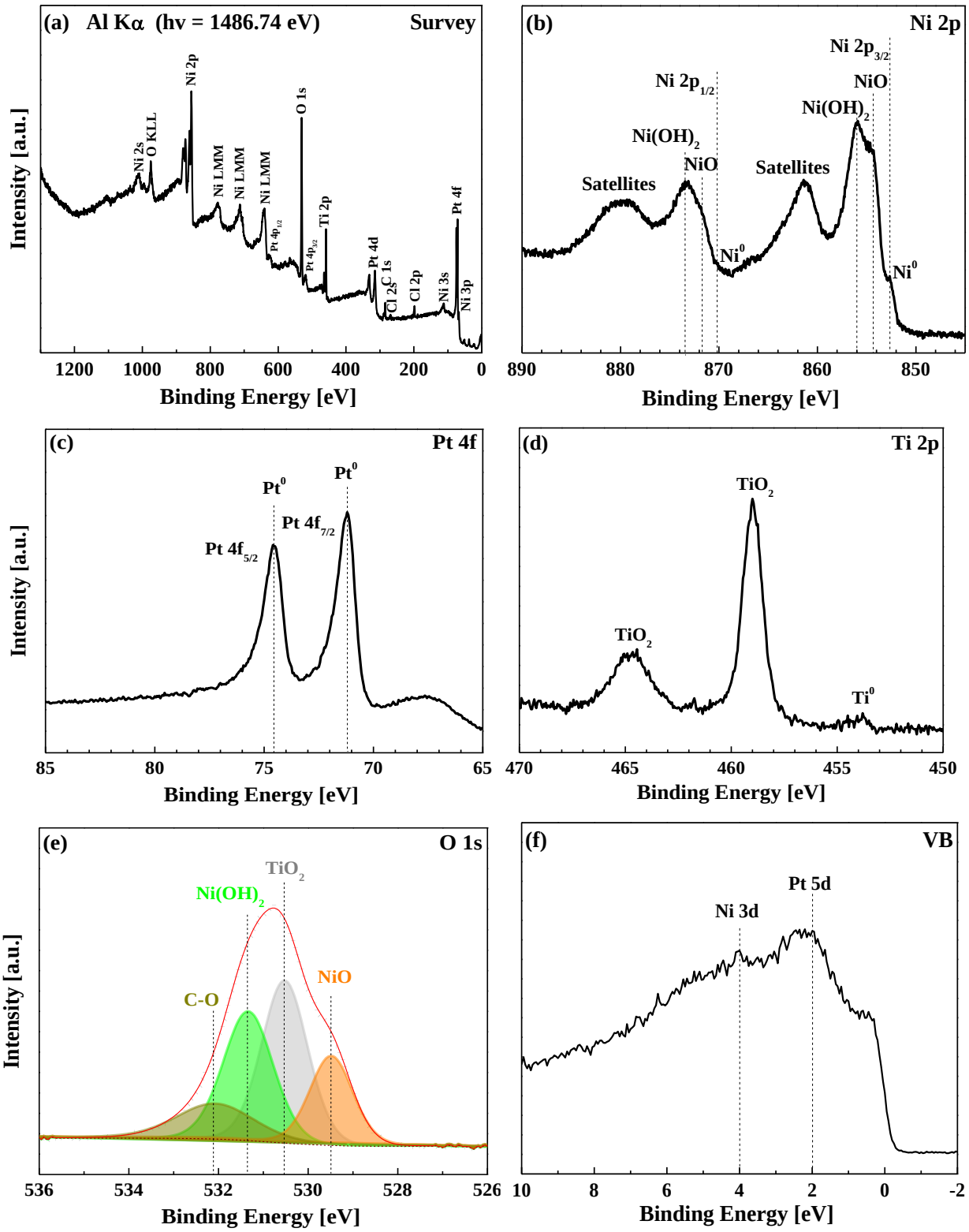

Figure 6.9 XP spectra of Pt-decorated Ni NPs on Ti substrate: (a) survey, (b) Ni 2p, (c) Pt 4f, (d) Ti 2p, (e) O 1s and (f) valence band (VB).

6.3.4 HER catalytic activity

The series of Ni-Mo electrocatalysts were investigated for the HER catalysis both under acidic (0.5 M H_2SO_4) and alkaline (1.0 M KOH) conditions in a standard three-electrode electrochemical cell.

6.3.4.1 HER catalytic activity in acidic solution

Figure 6.10a shows the LSV curves of the as-deposited Ni-Mo catalysts, along with an HER-inactive Ti substrate and highly active Pt foil as an HER benchmark electrode. Both the overpotentials and the current densities at the given potentials of the Ni-Mo catalysts were influenced by the electrodeposition time. The acidic HER activity increases with the deposition time increasing from 1 to 10 min. The better HER electrocatalytic performance probably results from more chemically reactive NiMo alloys deposited on the Ti substrate with longer time. Additionally, evolution of the porous structure can be another reasonable explanation, which will lead to a high surface area and correspondingly will provide many active sites exposed for the HER. However, the HER activity decreases with deposition time extending to 20 min. This might be caused by the adsorption of residual Na_2MoO_4 on the surface (see **Figure 6.7**), thereby blocking the active sites for the HER. Thus, Ni-Mo-10 shows the highest HER activity with an overpotential of 66 mV required to produce a cathodic current density of 10 mA cm^{-2} (η_{10} = 66 mV), a benchmark current density relevant to operating photoelectrochemical devices. The observed low overpotential at 10 mA cm^{-2} indicates a highly active HER catalyst, which approaches that of the Pt foil benchmark (η_{10} = 46 mV).

Correlated with the XPS investigation (**Figure 6.8** and **Table 6.2**), the higher HER activity of Ni-Mo-10 can be attributed to the higher amount of Ni+Mo+MoO_2 (61.5%) compared to that of the Ni-Mo-5 (46.1%) and Ni-Mo-20 (57.5%). This observation is consistent with data reported by P. Soriaga et. al.,[274] showing that the post-HER formed Ni-Mo-MoO_2 composite is an active electrocatalyst for the HER in acidic solution. In addition, MoO_2 was reported to have excellent performance for H_2 generation.[275] According to the literature data,[275-276] MoO_2 is a metallic transition metal oxide with a distorted rutile crystal structure. The bonding is complex and involves some delocalized Mo electrons in the conduction band, which account for the metallic conductivity.[275-276]

The catalytic activity of the Ni-Mo catalysts was also studied after a certain time of HER conditioning. **Figure 6.10b** shows the LSV curves collected after the initial LSV scan and the followed 15 min galvanostatic scan at a cathodic current density of 10 mA cm^{-2}. By comparison of the overpotentials at -10 mA cm^{-2} for the Ni-Mo catalysts before and after the galvanostatic scans (see **Figure 6.10c**), one can observe that all these Ni-Mo catalysts show decreased overpotentials after the galvanostatic scan, indicating that the operando modification of the catalysts during the HER process does happen. After the galvanostatic conditioning, Ni-Mo-10 still exhibits the smallest overpotential at the current density of 10 mA cm^{-2} (η_{10} = 63 mV).

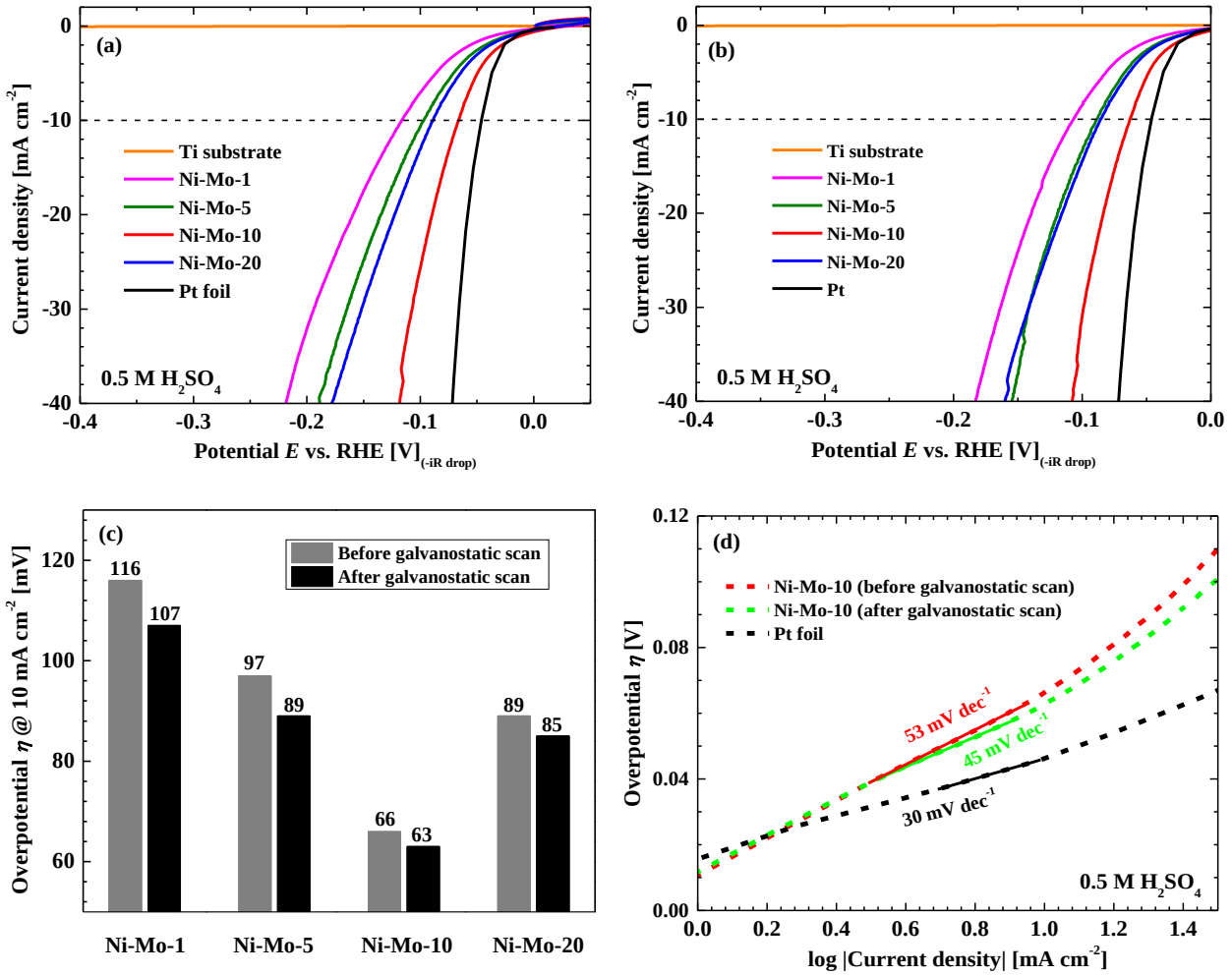

Figure 6.10 (a) LSV curves of the as-deposited Ni-Mo catalysts in 0.5 M H_2SO_4. HCl etched Ti foil substrate and Pt foil electrodes, tested under identical conditions, are shown for comparison. (b) LSV curves of the Ni-Mo films after 15 min cathodic galvanostatic conditioning at -10 mA cm^{-2}. (c) Comparison of the overpotentials at -10 mA cm^{-2} for the Ni-Mo catalysts before and after the galvanostatic scans. (d) Tafel plots of Ni-Mo-10 and Pt foil obtained from the LSV curves in (b). Scan rate, 2 mV s^{-1}.

Figure 6.10d displays the Tafel plots [η vs. log $|j|$] for Ni-Mo-10 and Pt foil. The Tafel slope (b) is an inherent property of a electrocatalyst, and a low Tafel slope means the HER rate increases rapidly with increasing overpotential.[277] Additionally, the exchange current density (j_0) calculated from Tafel curves using an extrapolation method is another reasonable measure of the catalytic efficiency for the HER. In the linear region, the Pt foil electrode exhibits a Tafel slope of 30 mV dec^{-1} and an exchange current density of 3.0×10^{-4} A cm^{-2}. Both parameters are consistent with previous reported values.[199, 277-278] The initial Ni-Mo-10 before the galvanostatic scan shows a Tafel slope of 53 mV dec^{-1} and a higher exchange current density of 5.7×10^{-4} A cm^{-2} than that of Pt. After the galvanostatic scan, a decreased Tafel slope of 45 mV dec^{-1} and an exchange current density of 4.4×10^{-4} A cm^{-2} are obtained. The HER process in acidic solution can be described by either the Volmer-Heyrovsky mechanism or the Volmer-Tafel mechanism,[99] as depicted in

equations **(6.5)** to **(6.7)**:

Volmer reaction: $(M + H^+ + e^- \leftrightarrow M\text{-}H_{ads})$ **(6.5)**

Heyrovsky reaction: $(M\text{-}H_{ads} + H^+ + e^- \leftrightarrow H_2 + M)$ **(6.6)**

or Tafel reaction: $(2\ M\text{-}H_{ads} \leftrightarrow H_2 + 2\ M)$ **(6.7)**

Under standard conditions, the Tafel slopes of the Volmer, Heyrovsky, and Tafel reactions are calculated to be 118 mV dec^{-1}, 39 mV dec^{-1}, and 29 mV dec^{-1}, respectively.[198-199, 223] The observed Tafel slope of 30 mV dec^{-1} for the HER on Pt foil indicates the Volmer-Tafel mechanism with the Tafel reaction as the rate-determining step, while the observed Tafel slope of 45 mV dec^{-1} for Ni-Mo-10 after galvanostatic scan suggests that the Volmer-Heyrovsky mechanism with the Heyrovsky reaction as the rate-determining step is operative in this Ni-Mo catalyzed HER, which does well agree with previous studies.[103]

6.3.4.2 HER catalytic activity in alkaline solution

The HER performance of the Ni-Mo catalysts was also evaluated in 1.0 M KOH alkaline solution. **Figure 6.11a** shows the LSV curves of the Ni-Mo films prepared with deposition time from 1 to 20 min. Data for the bare Ti substrate, electrodeposited Ni NPs (discussed in Chapter 4) and Pt-decorated Ni (Pt-Ni) NPs are shown for comparison. As expected, the Ti substrate exhibits no activity. The catalytic activity of the electrodeposited Ni NPs can be highly improved by decorating small amount of Pt on their surface, with the overpotential required to sustain a cathodic current density of 10 mA cm^{-2} (η_{10}) decreasing from 195 to 60 mV. The LSV curves of the Ni-Mo films exhibit that the η_{10} decreases from 211 to 109 mV with increasing deposition time from 1 to 20 min. The Ni NPs show a higher activity than the Ni-Mo films prepared for 1 and 5 min, but the activity was surpassed by the Ni-Mo films deposited for 10 and 20 min. The worse activity of Ni-Mo-1 and Ni-Mo-5 than that of the Ni NPs is probably due to the low surface areas. Ni-Mo-10 and Ni-Mo-20 providing relatively higher activity than Ni NPs likely results from a combination of the afore-mentioned substantially enhanced surface area and the synergistic effect between Ni and Mo on the HER.

The HER activity of the Ni-Mo catalysts after operando modification by galvanostatic scan was also studied. **Figure 6.11b** shows the LSV curves collected after the initial LSV scan and the followed galvanostatic scan at a cathodic current density of 10 mA cm^{-2} for 15 min. As can be seen, Ni-Mo-1 and Ni-Mo-5 exhibit similar HER activities with overpotentials at -10 mA cm^{-2} still lower than that of Ni NPs after galvanostatic scan. Meanwhile, similar activities were also observed on Ni-Mo-10 and Ni-Mo-20 with both better performances. The comparison of the overpotentials at -10 mA cm^{-2} for the Ni-Mo catalysts before and after the galvanostatic scans in 1.0 M KOH is presented in **Figure 6.11c**. Interestingly, remarkably reduced overpotentials are observed on these Ni-Mo samples especially for Ni-Mo-10 with η_{10} decreased by 46 mV (38%), indicating a significantly increased electrocatalytic activity. After the galvanostatic conditioning, Ni-Mo-10 exhibits the smallest overpotential required to produce a cathodic current density of 10 mA cm^{-2} (i.e. $\eta_{10} = 74$ mV).

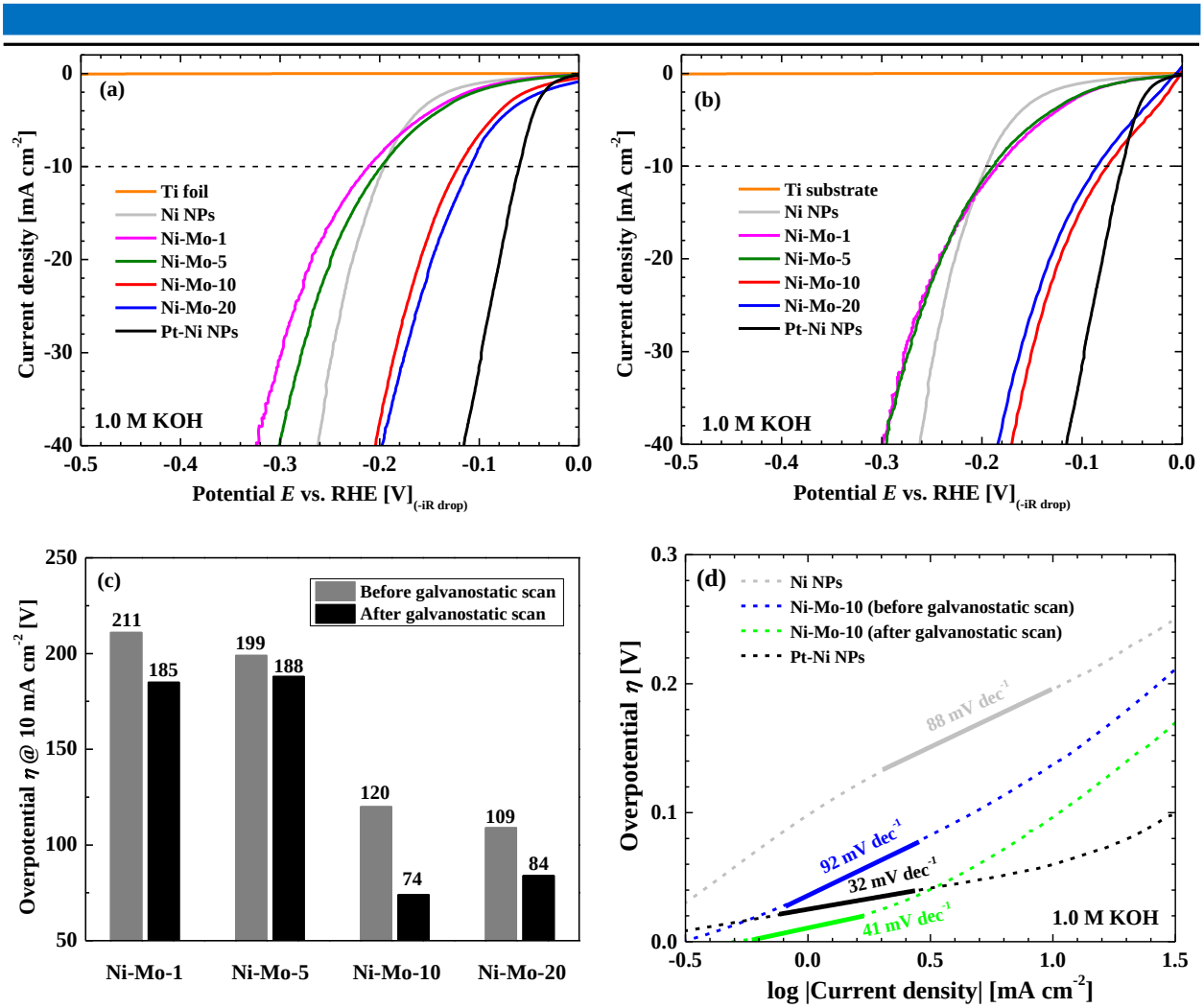

Figure 6.11 (a) LSV curves of the as-deposited Ni-Mo catalysts in 1.0 M KOH. HCl etched Ti foil, Ni NPs, and Pt-decorated Ni (Pt-Ni) NPs, tested under identical conditions, are shown for comparison. (b) LSV curves of the Ni-Mo catalysts after 15 min cathodic galvanostatic conditioning at -10 mA cm^{-2}. (c) Comparison of the overpotential at -10 mA cm^{-2} for the Ni-Mo catalysts before and after the galvanostatic scans. (d) Tafel plots of Ni NPs, Ni-Mo-10 and Pt-decorated Ni NPs derived from the LSV curves in (b). Scan rate, 2 mV s^{-1}.

Figure 6.11d shows the Tafel plots of the Ni NPs, Ni-Mo-10 and Pt-decorated Ni NPs in 1.0 M KOH. In the linear region, the Pt-decorated Ni NPs display a Tafel slope of 32 mV dec^{-1} and an exchange current density of 1.7×10^{-4} A cm^{-2}. As discussed in Chapter 4, the Tafel slope of the Ni NPs was determined to be 88 mV dec^{-1} with an exchange current density of 5.7×10^{-5} mA cm^{-2}. Ni-Mo-10 before the galvanostatic scan shows a Tafel slope of 92 mV dec^{-1} and an exchange current density of 4.1×10^{-4} A cm^{-2}. After the galvanostatic scan, the Tafel slope decreases to 41 mV dec^{-1} and the exchange current density rises to 5.5×10^{-4} A cm^{-2}, showing an increased intrinsic catalytic activity of the Ni-Mo film due to the galvanostatic conditioning. In alkaline solution, the HER in water electrolysis process generally proceeds by following steps:

Volmer step: ($H_2O + e^- \leftrightarrow H_{ads} + OH^-$). **(6.8)**

This is then followed either by a second electron transfer through the

Heyrovsky step: ($H_{ads} + H_2O + e^- \leftrightarrow H_2 + OH^-$), **(6.9)**

or by the

Tafel step: ($H_{ads} + H_{ads} \leftrightarrow H_2$). **(6.10)**

The Tafel slope of 32 mV dec^{-1} for the Pt-decorated Ni NPs indicates the Volmer-Tafel mechanism with the Tafel reaction as the rate-determining step. For Ni-Mo-10, the Tafel slopes of 92 mV dec^{-1} and 41 mV dec^{-1} before and after the galvanostatic conditioning, respectively, reveal the HER proceeds with the Volmer-Heyrovsky mechanism, but the rate-determining step is changed from the Volmer reaction to the Heyrovsky reaction due to the conditioning.

6.3.5.3 Post-HER XPS characterization

Motivated by the observed operando improved catalytic activity during the HER both in acidic and alkaline media, XPS was used to obtain a chemical description of the Ni-Mo catalysts after catalyzing the HER so as to identify the real active sites for the acidic and alkaline HER. Here, the Ni-Mo-10 film was selected as an example. **Figure 6.12** shows the survey spectra and high-resolution Ni 2p, Mo 3d and O 1s detail spectra of Ni-Mo-10 as-deposited and after electrochemical HER measurements in 0.5 M H_2SO_4 and 1.0 M KOH.

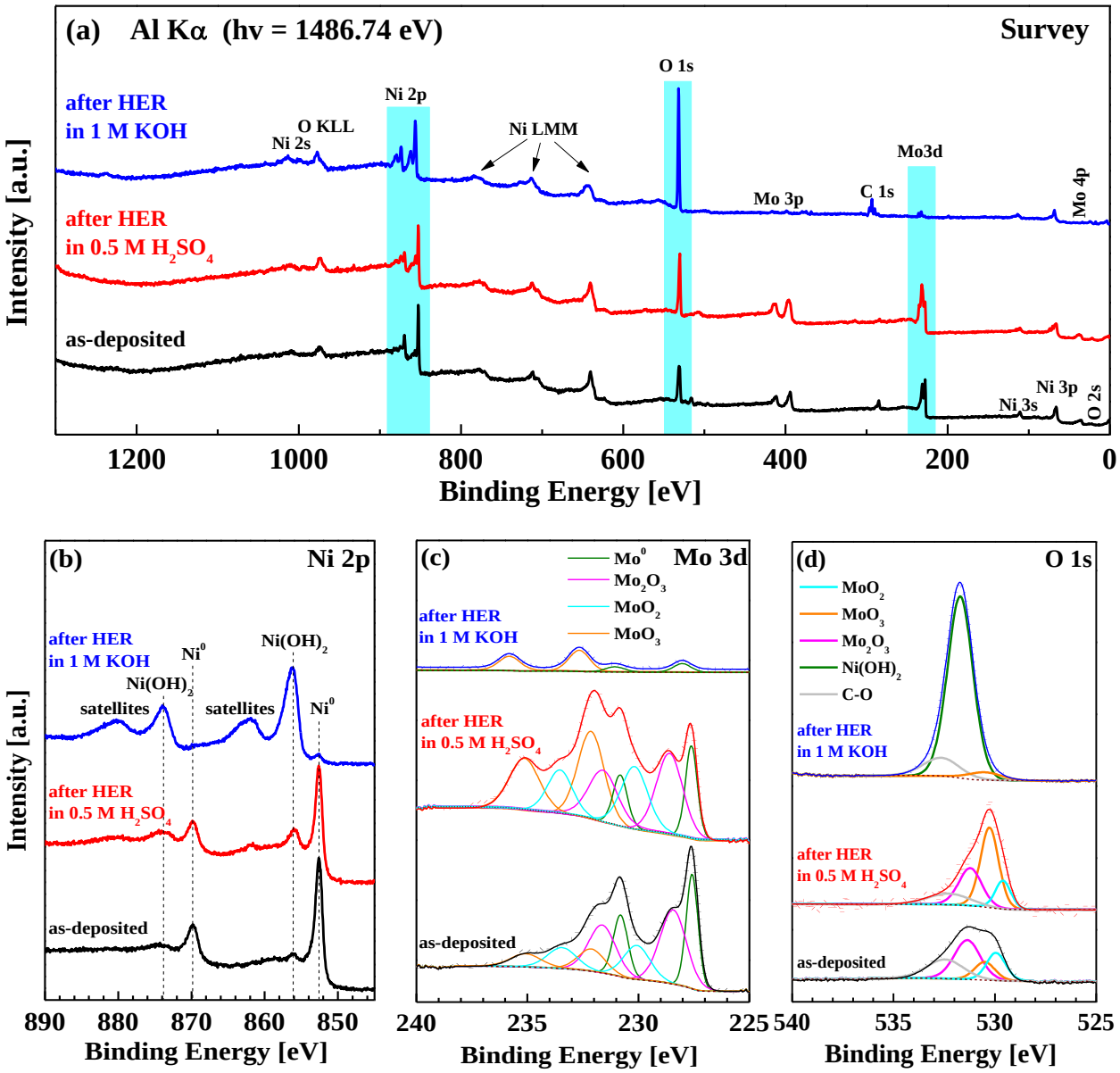

Figure 6.12 XP spectra of Ni-Mo-10 as-deposited and after electrochemical HER measurements in 0.5 M H_2SO_4 and 1.0 M KOH: (a) survey (a) Ni 2p, (b) Mo 3d and (c) O 1s.

The quantitative analysis of the high-resolution Ni 2p and Mo 3d XPS peaks of Ni-Mo-10 after the HER in 0.5 M H_2SO_4 reveals that the atomic ratio of Ni_{Total} : Mo_{Total} (≈ 1:1) has not changed compared with the value for the as-deposited sample. Meanwhile, the Ni 2p spectrum shares similar features with the as-deposited sample (**Figure 6.12b**). The peak intensity corresponding to the metallic Ni is slightly decreased with a small increase of the peak intensity associated with $Ni(OH)_2$. After fitting and deconvolution of the high-resolution Mo 3d spectrum after acidic HER (**Figure 6.12c**), the resulting features with a spin-orbit split doublet for the metallic Mo (≈ 227.6 eV and ≈ 230.8 eV) and three spin-orbit split doublets for oxidized molybdenum species associated with Mo_2O_3 (≈ 228.6 eV and ≈ 231.7 eV), MoO_2 (≈ 230.2 eV and ≈ 233.5 eV) and MoO_3 (≈ 232.2 eV and ≈ 235.4 eV) are still obtained as before the test. But, the contents of Mo species with lower valence states, including Mo^0 and Mo_2O_3, are decreased during the acidic HER operation,

while the contents of MoO_2 and MoO_3 species are increased. The analysis of Ni 2p and Mo 3d spectra can be further verified by the O 1s spectrum (**Figure 6.12d**). The surface chemical composition of the post-acidic HER Ni-Mo catalyst is listed in **Table 6.3**.

Table 6.3 Surface chemical composition of Ni-Mo-10 as-deposited and after electrochemical HER measurements in 0.5 M H_2SO_4 and 1.0 M KOH derived from the quantitative analysis of Ni 2p and Mo 3d XPS peaks.

Sample	**Ni_{Total} : Mo_{Total}[a]**	**Surface chemical composition (%)**						
		Ni_xMo_y alloy		$Ni(OH)_2$	NiO	Mo_2O_3	MoO_2	Na_2MoO_4/MoO_3
as-deposited	53.3% : 46.7%	$Ni_{2.9}Mo$	52.6	10.2	3.0	19.5	8.9	5.8
after HER in 0.5 M H_2SO_4	46.9% : 53.1%	$Ni_{3.7}Mo$	38.7	13.2	2.2	16.1	12.2	17.2
after HER in 1.0 M KOH	92.9% : 7.1%	$Ni_{1.7}Mo$	5.3	88.9	-	-	-	5.8
after HER in 1.0 M KOH **(Ni-Mo-20)**	88.8% : 11.2%	$Ni_{1.1}Mo$	8.7	83.1	-	-	-	8.2

[a] The Ni_{Total} : Mo_{Total} ratio refers to atomic ratio.

Significant changes are observed in the surface chemical composition of the post-alkaline HER Ni-Mo catalyst. The Ni 2p and Mo 3d XPS data reveal a highly increased Ni_{Total} : Mo_{Total} atomic ratio of about 9:1, indicating Ni-rich surface obtained after the alkaline HER. The degradation of Mo species can be related to the Pourbaix diagram of Molybdenum.[279-280] At a current density of -10 mA cm^{-2} in 1.0 M KOH (pH = 14), the potential is around -0.9 V vs. SHE (**Figure 6.11a** and **b**). Under this condition, highly soluble MoO_4^{2-} is the favored compound. The high-resolution Ni 2p spectrum shows, that the peak intensity related to the metallic Ni is remarkably reduced after the alkaline HER, and at the same time the peak intensity assigned to $Ni(OH)_2$ is highly increased. This observation is well consistent with the results shown in Chapter 4, which is indicative of a transformation of the Ni^0 to $Ni(OH)_2$. Moreover, the peak intensities of the Mo 3d spectrum are significantly decreased after the HER in 1 M KOH. Fitting and deconvolution of the Mo 3d spectrum, only the spin-orbit split doublets for the metallic Mo (≈ 227.6 eV and ≈ 230.8 eV) and MoO_3 (≈ 232.6 eV and ≈ 235.8 eV) can be detected. The corresponding fitted O 1s spectrum shows a strong peak located at binding energy of 531.7 eV associated with $Ni(OH)_2$. Additionally, a very small shoulder centered at lower binding energy of 530.5 eV can be assigned to MoO_3. The feature situated at higher binding energy is attributed to carbon-oxygen species. Basically, the same results are obtained for the Ni-Mo-20 after HER in 1.0 M KOH. The surface chemical composition of the Ni-Mo catalyst after HER in 1.0 M KOH is also summarized in **Table 6.3**. Related to the highly improved activity during the EC operation in alkaline solution, the XPS spectra reveal, that $Ni(OH)_2$ is the active species on the electrode surface. It was suggested previously, that $Ni(OH)_2$ is able to promote the water dissociation by lowering the energy barrier, hence improving the HER in alkaline solution.[104] This is also well consistent with the above Tafel analysis, which shows the rate-determining step of the alkaline HER on the Ni-Mo film is

changed from the Volmer reaction to the Heyrovsky reaction after the 15 min galvanostatic scan.

6.3.5 OER catalytic activity

The electrochemical OER activities of the electrodeposited Ni-Mo films, electrodeposited Ni films commercial RuO_2 and a 6 N HCl treated Ti substrate were evaluated in 1.0 M KOH solution.

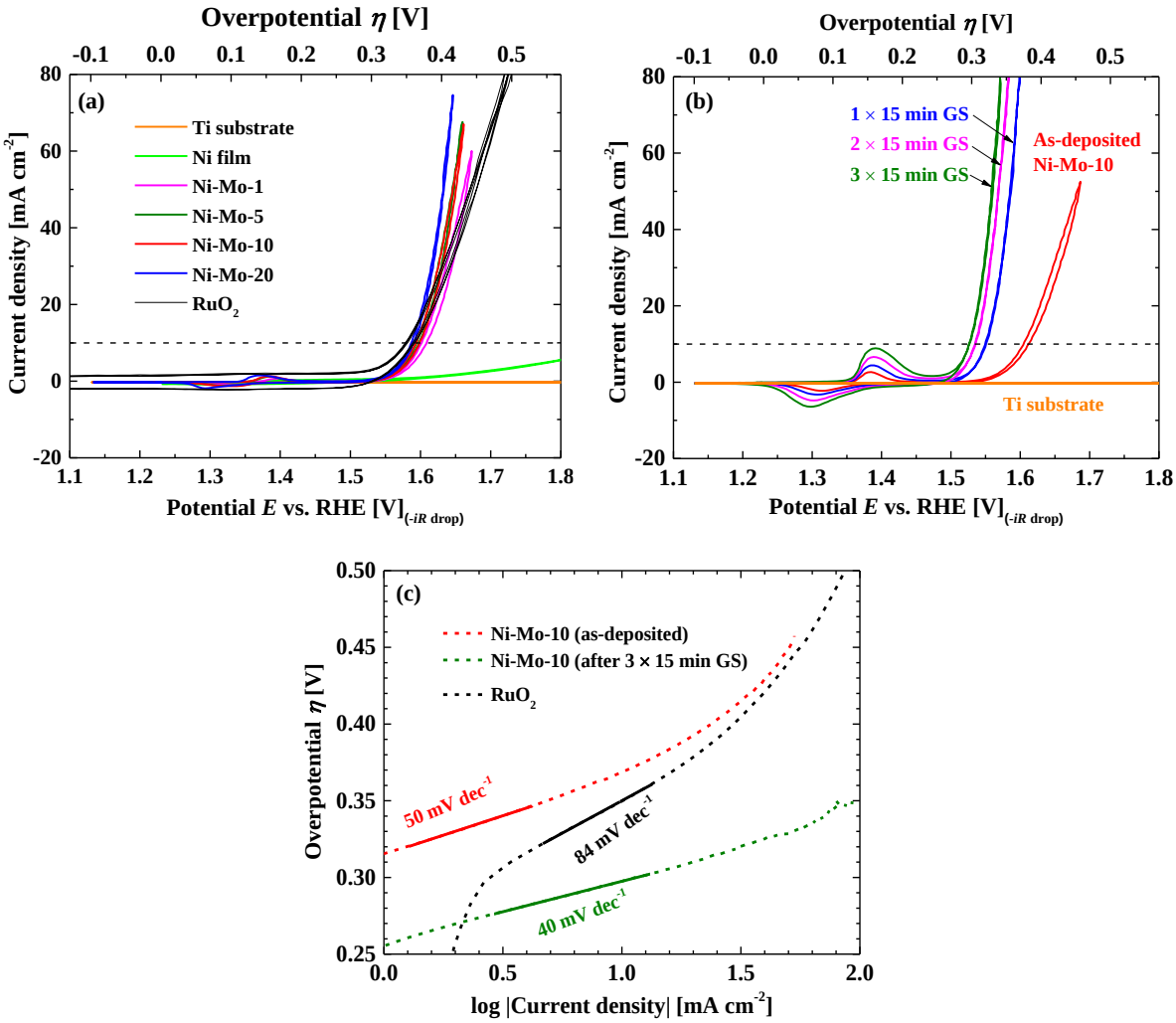

Figure 6.13 (a) CVs of electrodeposited Ni-Mo films, electrodeposited Ni films, commercial RuO_2 and Ti foil substrate. (b) CVs of Ni-Mo-10 after galvanostatic scans (GS) at -10 mA cm^{-2}. (c) Tafel plots of Ni-Mo-10 and the commercial RuO_2 catalyst.

Figure 6.13a shows that, the OER catalytic activity of the Ni-Mo films is just slightly improved by increasing of the deposition time from 1 to 20 min, with the η_{10} decreasing from 374 mV to 358 mV. Notably, the Ni-Mo films show a comparable activity to that of the commercial RuO_2 catalyst (η_{10} = 356) and a much higher activity than that of the electrodeposited Ni films. Interestingly, it is observed that the OER activity of the Ni-Mo films can be further enhanced by a cathodic treatment. As shown in **Figure 6.13b** (see the blue curve), after 15 min galvanostatic scans (GS) at -10 mA cm^{-2}, the η_{10} for the Ni-Mo-10 decreases from 366 mV to 320 mV, and it can be further reduced to 296 mV after 3 × 15 min GS (see the

green curve). Meanwhile, the Tafel analysis (**Figure 6.13c**) exhibits a reduced Tafel slope from 50 to 40 mV dec^{-1} for the Ni-Mo-10 after 3 × 15 min GS. Actually, the GS can be considered as a HER process at -10 mA cm^{-2}. Therefore, by correlating with the XPS analysis on the Ni-Mo-10 after the HER in alkaline solution (**Figure 6.12 and Table 6.3**) and the increasing redox peak in the CV curves (**Figure 6.13b**), the highly improved activity is obtained due to the increase of the $Ni(OH)_2$ active sites which are caused by the Ni^0-to-$Ni(OH)_2$ transformation and the selective corrosion of Mo.

6.4 Summary

Porous Ni-Mo films were prepared by a simple one-step electrodeposition onto the HCl etched Ti surface. Simultaneous hydrogen evolution during deposition plays an important role in forming the porous NiMo alloys contained layers. The Ni-Mo films were investigated as bifunctional electrocatalysts for the overall water splitting reaction, i.e. the HER in acidic and alkaline solutions and OER in alkaline solution. The higher HER and OER catalytic activities of the Ni-Mo catalyst compared to those of the Ni catalysts are resulted from a combination of the large surface area and the synergistic effect between Ni and Mo. Improved activities can be observed after cathodic galvanostatic scans, especially for the HER and the OER in 1.0 M KOH. XPS studies show, that the operando improvement of the HER in acidic solution is related to the higher amount of MoO_2 and MoO_3, while the operando improved HER and the OER activities in alkaline environment is attributed to increase of the $Ni(OH)_2$ active sites which are caused by two factors: (1) Ni^0-to-$Ni(OH)_2$ transformation; (2) selective corrosion of Mo. The optimal HER Ni-Mo sample shows an overpotential of 63 mV at a cathodic current density of 10 mA cm^2 (η_{10} = 63 mV) in 0.5 M H_2SO_4 and an overpotential of 74 mV (η_{10} = 74 mV) in 1.0 M KOH, which are comparable to that of the commercial Pt (η_{10} = 46 mV in 0.5 M H_2SO_4) and electrodeposited Pt-Ni NPs (η_{10} = 60 mV in 1.0 M KOH). Tafel analysis shows a low Tafel slope of 45 mV dec^{-1} in 0.5 M H_2SO_4 and 41 mV dec^{-1} in 1.0 M KOH, indicating the HER proceeds on the Ni-Mo catalyst through the Volmer-Heyrovsky route with the Heyrovsky reaction as the rate-determining step in both solutions. For the OER, the Ni-Mo film presents an overpotential of 296 mV at an anodic current density of 10 mA cm^{-2} and a Tafel slope of 40 mV dec^{-1} in 1.0 M KOH, showing a better OER activity than that of commercial RuO_2 (η_{10}: 356 mV; Tafel slop: 80 mV dec^{-1}).

Future experiments will focus on the elucidation of the detailed chemical composition and redox states of the Ni-Mo films before during and after the electrochemical reactions, especially for the OER, in order to gain a full understanding of the synergistic effect between the Ni and Mo species on activity, stability and Faradaic efficiency under water splitting conditions. It is also interesting to study the electrochemical performance of an overall water splitting system assembled with the porous Ni-Mo films as both the anode and cathode.

7. Conclusions and Outlook

Within the scope of the here presented work, Ni composite NPs, $Ni(OH)_2$ films, and porous Ni-Mo films have been successfully prepared by electrochemical deposition for the electrocatalytic HER, OER and overall water splitting, respectively. This final chapter will give a conclusion of the results which were obtained and end with an outlook for further experiments that could be conducted.

7.1 Conclusions

Part I: Electrodeposition of Ni NPs for the HER

- Ni composite NPs with a mixture of Ni^0, NiO and $Ni(OH)_2$ were electrodeposited onto Ti substrates by using the cyclic voltammetry technique. The average particle size and the amount of Ni^0, NiO and $Ni(OH)_2$ in the composite NPs could be tuned by varying the deposition parameters like potential range and scan rate.
- The electrocatalytic activity for the HER was evaluated for each prepared catalyst in alkaline solutions (0.1 M and 1.0 M KOH). The optimized catalyst achieves an onset potential of ~ 0 V and an overpotential of 197 mV at a cathodic current density of 10 mA cm^{-2} as well as a small Tafel slope of 88 mV dec^{-1} in 1.0 M KOH, values that are comparable to those of the Pt foil measured under the same conditions.
- Stability measurements for up to 30 h show the slow conversion of the Ni/NiO/$Ni(OH)_2$ NPs to $Ni(OH)_2$ NPs, which requires then the double overpotential to keep the cathodic current density at 10 mA cm^{-2}. The conversion is finished after a period of about 12 h, from where on the potential and the surface composition stay constant as measured by chronopotentiometry and XPS, respectively.
- By correlating the activity and stability to the chemical composition obtained by XPS, the higher activity of the Ni/NiO/$Ni(OH)_2$ composite NPs is observed to be strongly related to the larger amount of NiO. However, the pure NiO on its own shows only a reduced activity, and the same has been observed for the pure Ni^0 and pure $Ni(OH)_2$ NPs. Therefore, the right combination of materials providing the active sites for the reaction steps of the HER gives the highest activity. These NPs consist of approximately 25% Ni and $Ni(OH)_2$ each, as well as approximately 50% NiO. This implies that to obtain a successful HER electrocatalyst, active sites with differing compositions have to be close to each other to promote the different reaction steps.

Part II: Electrodeposition of $Ni(OH)_2$ films for the OER

- Transparent $Ni(OH)_2$ films have been electrodeposited onto the Ti surface using cyclic voltammetry. In addition, some Ni composite NPs can be found under the $Ni(OH)_2$ films, forming a unique NPs-film structure. The electrodeposited films and NPs are sticking strongly to the substrate after annealing and

also the long-term stability measurements.

- The catalytic OER activity of the electrodeposited $Ni(OH)_2$ films in alkaline solution is remarkably improved by a simple thermal annealing treatment in air atmosphere. The optimal treatment condition is determined at a moderate temperature of 150 °C for 1 h. XPS and voltammetry analyses reveal, that the annealing (mainly a dehydration process) caused an improvement of the conductivity and an increase in the catalytically active site are the essential factors to the highly enhanced OER activity. In addition, XPS investigations performed before and after the electrocatalytic OER indicate, that the pre-treatment of the electrodeposited $Ni(OH)_2$ by annealing accelerates the formation of a large amount of the catalytically active NiOOH species during the electrochemical reaction.
- The catalytic activity of the annealed $Ni(OH)_2$ films can be further improved by the electrochemically conditioning, which is contributed by the increased amount of NiOOH formed during the activation process. The conditioned $Ni(OH)_2$ films exhibit a small overpotential (η_{10}) of 310 mV at an anodic current density of 10 mA cm^{-2} and a low Tafel slope (b) of around 43 mV dec^{-1} in 1.0 M KOH. These values are much lower than those of the commercial RuO_2 catalyst measured under the same conditions (η_{10} = 356 mV and b = 80 mV dec^{-1}).
- Stability measurements for up to 26 h indicate an activation in the first 2 h showing a decrease of the overpotential, which is associated with the formation of the catalytically active NiOOH species. After the activation, the catalyst exhibits excellent electrochemical stability in the following 24 h.

Part III: Electrodeposition of porous Ni-Mo films as bifunctional electrocatalysts for the water splitting reaction

- Porous Ni-Mo films were prepared by a simple one-step electrodeposition onto the HCl etched Ti substrates. Simultaneous hydrogen evolution during the deposition plays an important role in formation of the porous structure.
- The Ni-Mo films were investigated as bifunctional electrocatalysts for the HER and OER. The high HER and OER catalytic activities of the Ni-Mo catalysts result from a combination of the large surface area and the synergistic effects between Ni and Mo.
- The HER catalytic behavior of the Ni-Mo films in acidic & alkaline solutions can be improved by cathodic galvanostatic scans, especially in 1.0 M KOH. XPS studies show that the operando improvement of the HER in acidic solution is related to the higher amount of MoO_2 and MoO_3, while the operando improved HER activity in alkaline environment is attributed to the increase of the $Ni(OH)_2$ on the surface.
- The OER catalytic activity of the Ni-Mo films was evaluated in alkaline solution. The experimental results show, that Ni-Mo films with different surface areas show a similar activity. A highly improved activity is also obtained after the cathodic galvanostatic scans due to the increase of the $Ni(OH)_2$ active

sites which are caused by two factors: (1) Ni^0-to-$Ni(OH)_2$ transformation; (2) selective corrosion of Mo.

- The optimal Ni-Mo catalyst for the HER shows the η_{10} of 63 mV in 0.5 M H_2SO_4 and the η_{10} of 74 mV in 1.0 M KOH, which are comparable to that of the Pt foil (η_{10} = 46 mV in 0.5 M H_2SO_4) and the electrodeposited Pt-Ni NPs (η_{10} = 60 mV in 1.0 M KOH), respectively. Tafel analyses present low Tafel slopes of 45 mV dec^{-1} in 0.5 M H_2SO_4 and 41 mV dec^{-1} in 1.0 M KOH. For the OER, the Ni-Mo film presents the η_{10} of 296 mV and a Tafel slope of 40 mV dec^{-1} in 1.0 M KOH, showing a better OER activity than that of the commercial RuO_2.

In summary, with the aim of replacing precious-metal materials as HER and OER catalysts, a series of Ni-based catalysts were synthesized and investigated for their electrocatalytic activity towards the partial and overall water splitting reactions. They were formed by electrochemical deposition and surface engineering to maximize the catalytically active sites and to modify the physical and chemical properties by tailoring the oxide/hydroxide-metal interfaces. Additionally, alloys were fabricated to increase the intrinsic activity of each active site. The HER activity of the Ni/NiO/$Ni(OH)_2$ NPs is comparable to that of the Pt foil. The thermally annealed $Ni(OH)_2$ films exhibit an OER activity better than that of the commercial RuO_2 and maintain the high efficiency over a long-time scale. The bifunctional Ni-Mo catalyst achieves HER activities comparable to that of the Pt foil in acidic solution or the Pt-Ni NPs in alkaline solution and also shows a higher OER activity than that of the commercial RuO_2. By comparison with the data obtained from XPS and SEM characterization, the catalytic activity and stability of the Ni-based catalysts are unambiguously demonstrated to be strongly dependent on their chemical composition, electronic structure and surface morphology, which are heavily influenced by the chosen preparation process.

For use in a water splitting device, a good HER or OER catalyst must satisfy two basic requirements: First, the catalyst must be highly active for the selected chemical reaction; Second, the effective catalyst must be robust enough to maintain its efficiency over long time scales. The high catalytic activity and very good stability make the $Ni(OH)_2$ NPs-films a great choice for the OER. The Ni NPs catalyst is a good candidate for the HER. The Ni-Mo film is a promising material to be used as a bifunctional catalyst for an overall water splitting system.

7.2 Outlook

With the important information obtained in this work, some challenging investigations can be conducted in the future:

- Improving the stability of the Ni NPs catalyst using an optimized substrate or to try to recover the catalyst to the original condition with a higher activity. In-situ techniques will be necessary to gain an even deeper understanding of the ongoing processes at the active sites.
- Identifying the changes of the phase composition for the $Ni(OH)_2$ films before and after annealing as well as electrochemical OER test by gracing incident x-ray photoelectron spectroscopy to clarify

the effect of phase composition. Data obtained by in-situ techniques, such as Raman spectroscopy and X-ray absorption spectroscopy, will be necessary to compare with the present XPS data to gain a full understanding of the elementary reaction steps and the formation of the broad variety of Ni, NiO_x, $Ni(OH)_2$ and $NiO_x(OH)_y$ phases.

- Elucidation of the detailed chemical composition and redox states of the Ni-Mo film before during and after the electrochemical reactions, especially for the OER, in order to gain a deeper understanding of the synergistic effect between the Ni and Mo species on the activity, stability and Faradaic efficiency under water splitting conditions. It would be also very interesting, to study the electrochemical performance and stability of an overall water splitting system assembled with the porous Ni-Mo films as both the anode and cathode, even in combination with a photovoltaic device or on a semiconductor surface.
- Control over the particle size and film thickness without sacrifice of the catalytic efficiency and stability, which is especially important when solar irradiation is to be used to drive the water splitting: (ultra)thin-film and (ultra)small-particle catalysts ensure that the amount of light reaching the underlying photo-active substrate is not significantly attenuated by scattering or absorption in the catalyst layer.

The here presented results further underscore the importance of recognizing and accounting for the effects of surface treatment and surface composition on the performance of heterogeneous electrocatalysts. A rigorous investigation of the particles, films and interfaces by surface science methods as e.g. XPS and SEM in parallel to the use of electrochemical techniques is necessary and able to deliver essential information, which is of great importance for comparison with theoretical predictions, and ultimately to derive a complete understanding of the origins of the high activity in Ni-based HER and OER electrocatalysts. Last but not least the here obtained results are of great relevance to enable the formation of practical water splitting devices.

8. References

1. Crabtree, G. W.; Dresselhaus, M. S.; Buchanan, M. V., The hydrogen economy. *Physics Today* **2004,** *57* (12), 39-44.
2. Sapountzi, F. M.; Gracia, J. M.; Fredriksson, H. O.; Niemantsverdriet, J. H., Electrocatalysts for the generation of hydrogen, oxygen and synthesis gas. *Progress in Energy and Combustion Science* **2017,** *58*, 1-35.
3. Sawin, J. L.; Rutovitz, J.; Sverrisson, F.; Aberg, E.; Adib, R.; Appavou, F.; Brown, A.; Dwyer, S.; Epp, B.; Guerra, F., Renewables 2018 Global Status Report. **2018**.
4. Gür, T. M., Review of electrical energy storage technologies, materials and systems: challenges and prospects for large-scale grid storage. *Energy & Environmental Science* **2018,** *11* (10), 2696-2767.
5. Lewis, N. S.; Nocera, D. G., Powering the planet: Chemical challenges in solar energy utilization. *Proceedings of the National Academy of Sciences* **2006,** *103* (43), 15729-15735.
6. Akinyele, D.; Rayudu, R., Review of energy storage technologies for sustainable power networks. *Sustainable Energy Technologies and Assessments* **2014,** *8*, 74-91.
7. Hadjipaschalis, I.; Poullikkas, A.; Efthimiou, V., Overview of current and future energy storage technologies for electric power applications. *Renewable and sustainable energy reviews* **2009,** *13* (6-7), 1513-1522.
8. Berseneff, B.; Perrin, M.; Tran-Quoc, T.; Brault, P.; Mermilliod, N.; Hadjsaid, N.; Delaplagne, T.; Martin, N.; Crouzevialle, B., The significance of energy storage for renewable energy generation and the role of instrumentation and measurement. *IEEE Instrumentation and Measurement Magazine* **2014,** *17*, 34-40.
9. Turner, J. A., A realizable renewable energy future. *Science* **1999,** *285* (5428), 687-689.
10. Balat, M.; Balat, M., Political, economic and environmental impacts of biomass-based hydrogen. *International journal of hydrogen energy* **2009,** *34* (9), 3589-3603.
11. Cipriani, G.; Di Dio, V.; Genduso, F.; La Cascia, D.; Liga, R.; Miceli, R.; Galluzzo, G. R., Perspective on hydrogen energy carrier and its automotive applications. *International Journal of Hydrogen Energy* **2014,** *39* (16), 8482-8494.
12. Walter, M. G.; Warren, E. L.; McKone, J. R.; Boettcher, S. W.; Mi, Q.; Santori, E. A.; Lewis, N. S., Solar water splitting cells. *Chemical reviews* **2010,** *110* (11), 6446-6473.
13. Jiao, Y.; Zheng, Y.; Jaroniec, M.; Qiao, S. Z., Design of electrocatalysts for oxygen-and hydrogen-involving energy conversion reactions. *Chemical Society Reviews* **2015,** *44* (8), 2060-2086.
14. Seh, Z. W.; Kibsgaard, J.; Dickens, C. F.; Chorkendorff, I.; Nørskov, J. K.; Jaramillo, T. F., Combining theory and experiment in electrocatalysis: Insights into materials design. *Science* **2017,** *355* (6321), eaad4998.
15. Veziroglu, A.; Macario, R., Fuel cell vehicles: State of the art with economic and environmental concerns. *International Journal of Hydrogen Energy* **2011,** *36* (1), 25-43.
16. Kato, T.; Kubota, M.; Kobayashi, N.; Suzuoki, Y., Effective utilization of by-product oxygen from electrolysis hydrogen production. *Energy* **2005,** *30* (14), 2580-2595.
17. Vij, V.; Sultan, S.; Harzandi, A. M.; Meena, A.; Tiwari, J. N.; Lee, W.-G.; Yoon, T.; Kim, K. S., Nickel-based electrocatalysts for energy-related applications: oxygen reduction, oxygen evolution, and hydrogen evolution reactions. *ACS Catalysis* **2017,** *7* (10), 7196-7225.
18. Gottlieb, E.; Kopeć, M.; Banerjee, M.; Mohin, J.; Yaron, D.; Matyjaszewski, K.; Kowalewski, T., In-situ platinum deposition on nitrogen-doped carbon films as a source of catalytic activity in a hydrogen evolution reaction. *ACS applied materials & interfaces* **2016,** *8* (33), 21531-21538.
19. Pfeifer, V.; Jones, T. E.; Vélez, J. J. V.; Arrigo, R.; Piccinin, S.; Hävecker, M.; Knop-Gericke, A.; Schlögl, R., In situ observation of reactive oxygen species forming on oxygen-evolving iridium surfaces. *Chemical science* **2017,** *8* (3), 2143-2149.
20. Ji, L.; Lv, C.; Chen, Z.; Huang, Z., Nickel-based (photo) electrocatalysts for hydrogen production. *Advanced Materials* **2018,** *30* (17), 1705653.
21. Tao, S.; Yang, F.; Schuch, J.; Jaegermann, W.; Kaiser, B., Electrodeposition of nickel nanoparticles for the alkaline hydrogen evolution reaction: Correlating electrocatalytic behavior and chemical composition. *ChemSusChem* **2018,** *11* (5), 948-958.
22. McKone, J. R.; Warren, E. L.; Bierman, M. J.; Boettcher, S. W.; Brunschwig, B. S.; Lewis, N. S.; Gray, H. B., Evaluation of Pt, Ni, and Ni-Mo electrocatalysts for hydrogen evolution on crystalline Si electrodes. *Energy & Environmental Science* **2011,** *4* (9), 3573-3583.
23. Zhou, H.; Wang, Y.; He, R.; Yu, F.; Sun, J.; Wang, F.; Lan, Y.; Ren, Z.; Chen, S., One-step synthesis of self-supported porous $NiSe_2$/Ni hybrid foam: an efficient 3D electrode for hydrogen evolution reaction. *Nano Energy* **2016,** *20*, 29-36.
24. Zhu, W.; Yue, X.; Zhang, W.; Yu, S.; Zhang, Y.; Wang, J.; Wang, J., Nickel sulfide microsphere film on Ni foam as an efficient bifunctional electrocatalyst for overall water splitting. *Chemical Communications* **2016,** *52* (7), 1486-1489.

25. Chen, G. F.; Ma, T. Y.; Liu, Z. Q.; Li, N.; Su, Y. Z.; Davey, K.; Qiao, S. Z., Efficient and stable bifunctional electrocatalysts Ni/Ni_xM_y (M = P, S) for overall water splitting. *Advanced Functional Materials* **2016,** *26* (19), 3314-3323.
26. Duan, J.; Chen, S.; Zhao, C., Ultrathin metal-organic framework array for efficient electrocatalytic water splitting. *Nature communications* **2017,** *8*, 15341.
27. Roger, I.; Symes, M. D., First row transition metal catalysts for solar-driven water oxidation produced by electrodeposition. *Journal of Materials Chemistry A* **2016,** *4* (18), 6724-6741.
28. Lu, X.; Zhao, C., Electrodeposition of hierarchically structured three-dimensional nickel-iron electrodes for efficient oxygen evolution at high current densities. *Nature communications* **2015,** *6*, 6616.
29. Fan, C.; Piron, D., Electrodeposition as a means of producing large-surface electrodes required in water electrolysis. *Surface and Coatings Technology* **1995,** *73* (1-2), 91-97.
30. Therese, G. H. A.; Kamath, P. V., Electrochemical synthesis of metal oxides and hydroxides. *Chemistry of materials* **2000,** *12* (5), 1195-1204.
31. Choi, K.-S.; Jang, H. S.; McShane, C. M.; Read, C. G.; Seabold, J. A., Electrochemical synthesis of inorganic polycrystalline electrodes with controlled architectures. *MRS bulletin* **2010,** *35* (10), 753-760.
32. Shinagawa, T.; Takanabe, K., Towards versatile and sustainable hydrogen production through electrocatalytic water splitting: electrolyte engineering. *ChemSusChem* **2017,** *10* (7), 1318-1336.
33. GRIMES, C.; VARGHESE, O.; RANJAN, S., *Light, water, hydrogen: the solar generation of hydrogen by water photoelectrolysis*. Springer Science & Business Media: 2007.
34. You, B.; Sun, Y., Innovative strategies for electrocatalytic water splitting. *Accounts of chemical research* **2018**.
35. Hamann, C. H.; Hamnett, A.; Vielstich, W., Electrochemistry. Second, completely revised and updated edition. *Wiley-VCH* **2007**.
36. Bard, A. J.; Faulkner, L. R., Fundamentals and applications. *Electrochemical Methods* **2001,** *2*, 482.
37. Lefrou, C.; Fabry, P.; Poignet, J.-C., *Electrochemistry: the basics, with examples*. Springer Science & Business Media: 2012.
38. Eyring, H., The activated complex in chemical reactions. *The Journal of Chemical Physics* **1935,** *3* (2), 107-115.
39. Peter Atkins, J. d. P., Physical Chemistry. *W. H. Freeman* **2009**.
40. Holewinski, A.; Linic, S., Elementary mechanisms in electrocatalysis: revisiting the ORR Tafel slope. *Journal of The Electrochemical Society* **2012,** *159* (11), H864-H870.
41. Doyle, R. L.; Godwin, I. J.; Brandon, M. P.; Lyons, M. E., Redox and electrochemical water splitting catalytic properties of hydrated metal oxide modified electrodes. *Physical Chemistry Chemical Physics* **2013,** *15* (33), 13737-13783.
42. Fang, Y.-H.; Liu, Z.-P., Tafel kinetics of electrocatalytic reactions: From experiment to first-principles. *ACS Catalysis* **2014,** *4* (12), 4364-4376.
43. Suen, N.-T.; Hung, S.-F.; Quan, Q.; Zhang, N.; Xu, Y.-J.; Chen, H. M., Electrocatalysis for the oxygen evolution reaction: recent development and future perspectives. *Chemical Society Reviews* **2017,** *46* (2), 337-365.
44. Bockris, J. O. M.; Reddy, A. K., *Modern electrochemistry: an introduction to an interdisciplinary area [by] John O'M. Bockris and Amulya KN Reddy*. Plenum Publishing Corporation: 1970; Vol. 2.
45. Bard, A. J.; Faulkner, L. R., Electrochemical methods: fundamentals and applications. John Wiley & Sons, Inc.: 2001.
46. Burke, M. S.; Kast, M. G.; Trotochaud, L.; Smith, A. M.; Boettcher, S. W., Cobalt-iron (oxy) hydroxide oxygen evolution electrocatalysts: the role of structure and composition on activity, stability, and mechanism. *Journal of the American Chemical Society* **2015,** *137* (10), 3638-3648.
47. Marković, N.; Grgur, B.; Ross, P. N., Temperature-dependent hydrogen electrochemistry on platinum low-index single-crystal surfaces in acid solutions. *The Journal of Physical Chemistry B* **1997,** *101* (27), 5405-5413.
48. Gomez, R.; Fernandez-Vega, A.; Feliu, J.; Aldaz, A., Hydrogen evolution on platinum single crystal surfaces: effects of irreversibly adsorbed bismuth and antimony on hydrogen adsorption and evolution on platinum (100). *The Journal of Physical Chemistry* **1993,** *97* (18), 4769-4776.
49. Castelli, P.; Trasatti, S.; Pollak, F. H.; O'Grady, W. E., Single crystals as model electrocatalysts: oxygen evolution on RuO_2 (110). *Journal of electroanalytical chemistry and interfacial electrochemistry* **1986,** *210* (1), 189-194.
50. Lasia, A., Hydrogen evolution reaction. *Handbook of fuel cells* **2010,** *2*.
51. Conway, B.; Tilak, B., Interfacial processes involving electrocatalytic evolution and oxidation of H_2, and the role of chemisorbed H. *Electrochimica Acta* **2002,** *47* (22-23), 3571-3594.
52. Anantharaj, S.; Ede, S. R.; Sakthikumar, K.; Karthick, K.; Mishra, S.; Kundu, S., Recent trends and perspectives in electrochemical water splitting with an emphasis on sulfide, selenide, and phosphide catalysts of Fe, Co, and Ni: a review. *ACS Catalysis* **2016,** *6* (12), 8069-8097.
53. Shi, Y.; Zhang, B., Recent advances in transition metal phosphide nanomaterials: synthesis and applications

in hydrogen evolution reaction. *Chemical Society Reviews* **2016,** *45* (6), 1529-1541.
54. Vesborg, P. C.; Seger, B.; Chorkendorff, I., Recent development in hydrogen evolution reaction catalysts and their practical implementation. *The journal of physical chemistry letters* **2015,** *6* (6), 951-957.
55. Mahmood, N.; Yao, Y.; Zhang, J. W.; Pan, L.; Zhang, X.; Zou, J. J., Electrocatalysts for hydrogen evolution in alkaline electrolytes: Mechanisms, challenges, and prospective solutions. *Advanced Science* **2018,** *5* (2), 1700464.
56. Wang, J.; Xu, F.; Jin, H.; Chen, Y.; Wang, Y., Non-noble metal-based carbon composites in hydrogen evolution reaction: Fundamentals to applications. *Advanced materials* **2017,** *29* (14), 1605838.
57. Zheng, Y.; Jiao, Y.; Vasileff, A.; Qiao, S. Z., The hydrogen evolution reaction in alkaline solution: From theory, single crystal models, to practical electrocatalysts. *Angewandte Chemie International Edition* **2018,** *57* (26), 7568-7579.
58. Jaramillo, T. F.; Jørgensen, K. P.; Bonde, J.; Nielsen, J. H.; Horch, S.; Chorkendorff, I., Identification of active edge sites for electrochemical H_2 evolution from MoS_2 nanocatalysts. *science* **2007,** *317* (5834), 100-102.
59. Zheng, Y.; Jiao, Y.; Zhu, Y.; Li, L. H.; Han, Y.; Chen, Y.; Du, A.; Jaroniec, M.; Qiao, S. Z., Hydrogen evolution by a metal-free electrocatalyst. *Nature communications* **2014,** *5*, 3783.
60. Parsons, R., The rate of electrolytic hydrogen evolution and the heat of adsorption of hydrogen. *Transactions of the Faraday Society* **1958,** *54*, 1053-1063.
61. Nørskov, J. K.; Bligaard, T.; Logadottir, A.; Kitchin, J.; Chen, J. G.; Pandelov, S.; Stimming, U., Trends in the exchange current for hydrogen evolution. *Journal of the Electrochemical Society* **2005,** *152* (3), J23-J26.
62. Greeley, J.; Jaramillo, T. F.; Bonde, J.; Chorkendorff, I.; Nørskov, J. K., Computational high-throughput screening of electrocatalytic materials for hydrogen evolution. *Nature Materials* **2006,** *5*, 909.
63. Skúlason, E.; Tripkovic, V.; Björketun, M. E.; Gudmundsdóttir, S. d.; Karlberg, G.; Rossmeisl, J.; Bligaard, T.; Jónsson, H.; Nørskov, J. K., Modeling the electrochemical hydrogen oxidation and evolution reactions on the basis of density functional theory calculations. *The Journal of Physical Chemistry C* **2010,** *114* (42), 18182-18197.
64. Greeley, J.; Mavrikakis, M., Alloy catalysts designed from first principles. *Nature materials* **2004,** *3* (11), 810.
65. Sheng, W.; Myint, M.; Chen, J. G.; Yan, Y., Correlating the hydrogen evolution reaction activity in alkaline electrolytes with the hydrogen binding energy on monometallic surfaces. *Energy & Environmental Science* **2013,** *6* (5), 1509-1512.
66. Danilovic, N.; Subbaraman, R.; Strmcnik, D.; Chang, K. C.; Paulikas, A.; Stamenkovic, V.; Markovic, N. M., Enhancing the alkaline hydrogen evolution reaction activity through the bifunctionality of $Ni(OH)_2$/metal catalysts. *Angewandte Chemie* **2012,** *124* (50), 12663-12666.
67. Quaino, P.; Juarez, F.; Santos, E.; Schmickler, W., Volcano plots in hydrogen electrocatalysis-uses and abuses. *Beilstein journal of nanotechnology* **2014,** *5*, 846.
68. Sheng, W.; Zhuang, Z.; Gao, M.; Zheng, J.; Chen, J. G.; Yan, Y., Correlating hydrogen oxidation and evolution activity on platinum at different pH with measured hydrogen binding energy. *Nature communications* **2015,** *6*, 5848.
69. Zheng, Y.; Jiao, Y.; Zhu, Y.; Li, L. H.; Han, Y.; Chen, Y.; Jaroniec, M.; Qiao, S.-Z., High electrocatalytic hydrogen evolution activity of an anomalous ruthenium catalyst. *Journal of the American Chemical Society* **2016,** *138* (49), 16174-16181.
70. Fajín, J. L.; DS Cordeiro, M. N. l.; Gomes, J. R., Density functional theory study of the water dissociation on platinum surfaces: general trends. *The Journal of Physical Chemistry A* **2014,** *118* (31), 5832-5840.
71. Abbas, S. A.; Iqbal, M. I.; Kim, S.-H.; Jung, K.-D., Catalytic activity of urchin-like Ni nanoparticles prepared by solvothermal method for hydrogen evolution reaction in alkaline solution. *Electrochimica Acta* **2017,** *227*, 382-390.
72. Sun, T.; Zhang, C.; Chen, J.; Yan, Y.; Zakhidov, A. A.; Baughman, R. H.; Xu, L., Three-dimensionally ordered macro-/mesoporous Ni as a highly efficient electrocatalyst for the hydrogen evolution reaction. *Journal of Materials Chemistry A* **2015,** *3* (21), 11367-11375.
73. Ahn, S. H.; Hwang, S. J.; Yoo, S. J.; Choi, I.; Kim, H.-J.; Jang, J. H.; Nam, S. W.; Lim, T.-H.; Lim, T.; Kim, S.-K., Electrodeposited Ni dendrites with high activity and durability for hydrogen evolution reaction in alkaline water electrolysis. *Journal of Materials Chemistry* **2012,** *22* (30), 15153-15159.
74. McKone, J. R.; Sadtler, B. F.; Werlang, C. A.; Lewis, N. S.; Gray, H. B., Ni-Mo nanopowders for efficient electrochemical hydrogen evolution. *ACS catalysis* **2013,** *3* (2), 166-169.
75. Zhang, J.; Wang, T.; Liu, P.; Liao, Z.; Liu, S.; Zhuang, X.; Chen, M.; Zschech, E.; Feng, X., Efficient hydrogen production on $MoNi_4$ electrocatalysts with fast water dissociation kinetics. *Nature communications* **2017,** *8*, 15437.
76. Jia, Y.; Zhang, L.; Gao, G.; Chen, H.; Wang, B.; Zhou, J.; Soo, M. T.; Hong, M.; Yan, X.; Qian, G., A heterostructure coupling of exfoliated Ni-Fe hydroxide nanosheet and defective graphene as a bifunctional electrocatalyst for overall water splitting. *Advanced Materials* **2017,** *29* (17), 1700017.
77. Wang, L.; Lin, C.; Huang, D.; Chen, J.; Jiang, L.; Wang, M.; Chi, L.; Shi, L.; Jin, J., Optimizing the Volmer step by single-layer nickel hydroxide nanosheets in hydrogen evolution reaction of platinum. *ACS Catalysis* **2015,** *5* (6), 3801-3806.
78. Xie, L.; Ren, X.; Liu, Q.; Cui, G.; Ge, R.; Asiri, A. M.; Sun, X.; Zhang, Q.; Chen, L., A $Ni(OH)_2$-PtO_2 hybrid

nanosheet array with ultralow Pt loading toward efficient and durable alkaline hydrogen evolution. *Journal of Materials Chemistry A* **2018,** *6* (5), 1967-1970.
79. Li, X.; Liu, P. F.; Zhang, L.; Zu, M. Y.; Yang, Y. X.; Yang, H. G., Enhancing alkaline hydrogen evolution reaction activity through Ni-Mn_3O_4 nanocomposites. *Chemical Communications* **2016,** *52* (69), 10566-10569.
80. Yan, X.; Tian, L.; Chen, X., Crystalline/amorphous Ni/NiO core/shell nanosheets as highly active electrocatalysts for hydrogen evolution reaction. *Journal of Power Sources* **2015,** *300*, 336-343.
81. Gong, M.; Zhou, W.; Tsai, M.-C.; Zhou, J.; Guan, M.; Lin, M.-C.; Zhang, B.; Hu, Y.; Wang, D.-Y.; Yang, J., Nanoscale nickel oxide/nickel heterostructures for active hydrogen evolution electrocatalysis. *Nature communications* **2014,** *5*, 4695.
82. Gong, M.; Zhou, W.; Kenney, M. J.; Kapusta, R.; Cowley, S.; Wu, Y.; Lu, B.; Lin, M. C.; Wang, D. Y.; Yang, J., Blending Cr_2O_3 into a NiO-Ni electrocatalyst for sustained water splitting. *Angewandte Chemie International Edition* **2015,** *54* (41), 11989-11993.
83. Fan, L.; Liu, P. F.; Yan, X.; Gu, L.; Yang, Z. Z.; Yang, H. G.; Qiu, S.; Yao, X., Atomically isolated nickel species anchored on graphitized carbon for efficient hydrogen evolution electrocatalysis. *Nature communications* **2016,** *7*, 10667.
84. Xing, Z.; Li, Q.; Wang, D.; Yang, X.; Sun, X., Self-supported nickel nitride as an efficient high-performance three-dimensional cathode for the alkaline hydrogen evolution reaction. *Electrochimica Acta* **2016,** *191*, 841-845.
85. Chen, W. F.; Sasaki, K.; Ma, C.; Frenkel, A. I.; Marinkovic, N.; Muckerman, J. T.; Zhu, Y.; Adzic, R. R., Hydrogen-evolution catalysts based on non-noble metal nickel-molybdenum nitride nanosheets. *Angewandte Chemie International Edition* **2012,** *51* (25), 6131-6135.
86. Xing, Z.; Yang, X.; Asiri, A. M.; Sun, X., Three-dimensional structures of MoS_2@Ni core/shell nanosheets array toward synergetic electrocatalytic water splitting. *ACS applied materials & interfaces* **2016,** *8* (23), 14521-14526.
87. Ledendecker, M.; Krick Calderón, S.; Papp, C.; Steinrück, H. P.; Antonietti, M.; Shalom, M., The synthesis of nanostructured Ni_5P_4 films and their use as a non-noble bifunctional electrocatalyst for full water splitting. *Angewandte Chemie International Edition* **2015,** *54* (42), 12361-12365.
88. Tang, C.; Cheng, N.; Pu, Z.; Xing, W.; Sun, X., NiSe nanowire film supported on nickel foam: an efficient and stable 3D bifunctional electrode for full water splitting. *Angewandte Chemie* **2015,** *127* (32), 9483-9487.
89. Li, Y.; Wang, H.; Xie, L.; Liang, Y.; Hong, G.; Dai, H., MoS_2 nanoparticles grown on graphene: an advanced catalyst for the hydrogen evolution reaction. *Journal of the American Chemical Society* **2011,** *133* (19), 7296-7299.
90. Gong, M.; Dai, H., A mini review of NiFe-based materials as highly active oxygen evolution reaction electrocatalysts. *Nano Research* **2015,** *8* (1), 23-39.
91. Gong, M.; Wang, D.-Y.; Chen, C.-C.; Hwang, B.-J.; Dai, H., A mini review on nickel-based electrocatalysts for alkaline hydrogen evolution reaction. *Nano Research* **2016,** *9* (1), 28-46.
92. Xiao, P.; Chen, W.; Wang, X., A review of phosphide-based materials for electrocatalytic hydrogen evolution. *Advanced Energy Materials* **2015,** *5* (24), 1500985.
93. Ghosh Chaudhuri, R.; Paria, S., Core/shell nanoparticles: classes, properties, synthesis mechanisms, characterization, and applications. *Chemical reviews* **2011,** *112* (4), 2373-2433.
94. Grzelczak, M.; Pérez-Juste, J.; Mulvaney, P.; Liz-Marzán, L. M., Shape control in gold nanoparticle synthesis. *Chemical Society Reviews* **2008,** *37* (9), 1783-1791.
95. Raveendran, P.; Fu, J.; Wallen, S. L., Completely "green" synthesis and stabilization of metal nanoparticles. *Journal of the American Chemical Society* **2003,** *125* (46), 13940-13941.
96. Brown, D.; Mahmood, M.; Man, M.; Turner, A., Preparation and characterization of low overvoltage transition metal alloy electrocatalysts for hydrogen evolution in alkaline solutions. *Electrochimica Acta* **1984,** *29* (11), 1551-1556.
97. Raj, I. A.; Vasu, K., Transition metal-based hydrogen electrodes in alkaline solution—electrocatalysis on nickel based binary alloy coatings. *Journal of applied electrochemistry* **1990,** *20* (1), 32-38.
98. Raj, I. A.; Vasu, K., Transition metal-based cathodes for hydrogen evolution in alkaline solution: electrocatalysis on nickel-based ternary electrolytic codeposits. *Journal of applied electrochemistry* **1992,** *22* (5), 471-477.
99. Wang, X.; Su, R.; Aslan, H.; Kibsgaard, J.; Wendt, S.; Meng, L.; Dong, M.; Huang, Y.; Besenbacher, F., Tweaking the composition of NiMoZn alloy electrocatalyst for enhanced hydrogen evolution reaction performance. *Nano Energy* **2015,** *12*, 9-18.
100. Lupi, C.; Dell'Era, A.; Pasquali, M., Nickel-cobalt electrodeposited alloys for hydrogen evolution in alkaline media. *international journal of hydrogen energy* **2009,** *34* (5), 2101-2106.
101. Angelo, A.; Lasia, A., Surface effects in the hydrogen evolution reaction on Ni-Zn alloy electrodes in alkaline solutions. *Journal of The Electrochemical Society* **1995,** *142* (10), 3313-3319.
102. Greeley, J.; Nørskov, J. K.; Mavrikakis, M., Electronic structure and catalysis on metal surfaces. *Annual review of physical chemistry* **2002,** *53* (1), 319-348.

103. Highfield, J.; Claude, E.; Oguro, K., Electrocatalytic synergism in Ni/Mo cathodes for hydrogen evolution in acid medium: a new model. *Electrochimica acta* **1999,** *44* (16), 2805-2814.
104. Subbaraman, R.; Tripkovic, D.; Strmcnik, D.; Chang, K.-C.; Uchimura, M.; Paulikas, A. P.; Stamenkovic, V.; Markovic, N. M., Enhancing hydrogen evolution activity in water splitting by tailoring Li+-Ni(OH)$_2$-Pt interfaces. *Science* **2011,** *334* (6060), 1256-1260.
105. Subbaraman, R.; Tripkovic, D.; Chang, K.-C.; Strmcnik, D.; Paulikas, A. P.; Hirunsit, P.; Chan, M.; Greeley, J.; Stamenkovic, V.; Markovic, N. M., Trends in activity for the water electrolyser reactions on 3d M (Ni, Co, Fe, Mn) hydr (oxy) oxide catalysts. *Nature materials* **2012,** *11* (6), 550.
106. Zeng, Z.; Chang, K.-C.; Kubal, J.; Markovic, N. M.; Greeley, J., Stabilization of ultrathin (hydroxy) oxide films on transition metal substrates for electrochemical energy conversion. *Nature Energy* **2017,** *2* (6), 17070.
107. LeRoy, R.; Janjua, M.; Renaud, R.; Leuenberger, U., Analysis of time-variation effects in water electrolyzers. *Journal of The Electrochemical Society* **1979,** *126* (10), 1674-1682.
108. Nidola, A.; Schira, R., Poisoning mechanisms and structural analyses on metallic contaminated cathode catalysts in chlor-alkali membrane cell technology. *Journal of the Electrochemical Society* **1986,** *133* (8), 1653-1656.
109. Divisek, J.; Mergel, J.; Schmitz, H., Improvements of water electrolysis in alkaline media at intermediate temperatures. *International Journal of Hydrogen Energy* **1982,** *7* (9), 695-701.
110. Huot, J. Y., Hydrogen Evolution and Interface Phenomena on a Nickel Cathode in 30 w/o KOH I. Kinetics Parameters and Electrode Impedance Between 303 and 363 K. *Journal of The Electrochemical Society* **1989,** *136* (7), 1933-1939.
111. Bockris, J. O. M., Kinetics of activation controlled consecutive electrochemical reactions: anodic evolution of oxygen. *The Journal of Chemical Physics* **1956,** *24* (4), 817-827.
112. Dau, H.; Limberg, C.; Reier, T.; Risch, M.; Roggan, S.; Strasser, P., The mechanism of water oxidation: from electrolysis via homogeneous to biological catalysis. *ChemCatChem* **2010,** *2* (7), 724-761.
113. Reier, T.; Nong, H. N.; Teschner, D.; Schlögl, R.; Strasser, P., Electrocatalytic oxygen evolution reaction in acidic environments-reaction mechanisms and catalysts. *Advanced Energy Materials* **2017,** *7* (1), 1601275.
114. Jin, H.; Guo, C.; Liu, X.; Liu, J.; Vasileff, A.; Jiao, Y.; Zheng, Y.; Qiao, S.-Z., Emerging two-dimensional nanomaterials for electrocatalysis. *Chemical reviews* **2018**.
115. Surendranath, Y.; Kanan, M. W.; Nocera, D. G., Mechanistic studies of the oxygen evolution reaction by a cobalt-phosphate catalyst at neutral pH. *Journal of the American Chemical Society* **2010,** *132* (46), 16501-16509.
116. Rossmeisl, J.; Logadottir, A.; Nørskov, J. K., Electrolysis of water on (oxidized) metal surfaces. *Chemical physics* **2005,** *319* (1-3), 178-184.
117. Fabbri, E.; Habereder, A.; Waltar, K.; Kötz, R.; Schmidt, T. J., Developments and perspectives of oxide-based catalysts for the oxygen evolution reaction. *Catalysis Science & Technology* **2014,** *4* (11), 3800-3821.
118. Man, I. C.; Su, H. Y.; Calle-Vallejo, F.; Hansen, H. A.; Martínez, J. I.; Inoglu, N. G.; Kitchin, J.; Jaramillo, T. F.; Nørskov, J. K.; Rossmeisl, J., Universality in oxygen evolution electrocatalysis on oxide surfaces. *ChemCatChem* **2011,** *3* (7), 1159-1165.
119. Rossmeisl, J.; Qu, Z.-W.; Zhu, H.; Kroes, G.-J.; Nørskov, J. K., Electrolysis of water on oxide surfaces. *Journal of Electroanalytical Chemistry* **2007,** *607* (1-2), 83-89.
120. Hansen, H. A.; Man, I. C.; Studt, F.; Abild-Pedersen, F.; Bligaard, T.; Rossmeisl, J., Electrochemical chlorine evolution at rutile oxide (110) surfaces. *Physical Chemistry Chemical Physics* **2010,** *12* (1), 283-290.
121. Song, F.; Bai, L.; Moysiadou, A.; Lee, S.; Hu, C.; Liardet, L.; Hu, X., Transition metal oxides as electrocatalysts for the oxygen evolution reaction in alkaline solutions: an application-inspired renaissance. *Journal of the American Chemical Society* **2018,** *140* (25), 7748-7759.
122. Bockris, J. O. M.; Otagawa, T., The electrocatalysis of oxygen evolution on perovskites. *Journal of The Electrochemical Society* **1984,** *131* (2), 290-302.
123. Matsumoto, Y.; Sato, E., Electrocatalytic properties of transition metal oxides for oxygen evolution reaction. *Materials chemistry and physics* **1986,** *14* (5), 397-426.
124. Risch, M.; Ringleb, F.; Kohlhoff, M.; Bogdanoff, P.; Chernev, P.; Zaharieva, I.; Dau, H., Water oxidation by amorphous cobalt-based oxides: in situ tracking of redox transitions and mode of catalysis. *Energy & Environmental Science* **2015,** *8* (2), 661-674.
125. Zhang, M.; De Respinis, M.; Frei, H., Time-resolved observations of water oxidation intermediates on a cobalt oxide nanoparticle catalyst. *Nature chemistry* **2014,** *6* (4), 362.
126. Yang, J.; Cooper, J. K.; Toma, F. M.; Walczak, K. A.; Favaro, M.; Beeman, J. W.; Hess, L. H.; Wang, C.; Zhu, C.; Gul, S., A multifunctional biphasic water splitting catalyst tailored for integration with high-performance semiconductor photoanodes. *Nature materials* **2017,** *16* (3), 335.
127. Trotochaud, L.; Ranney, J. K.; Williams, K. N.; Boettcher, S. W., Solution-cast metal oxide thin film electrocatalysts for oxygen evolution. *Journal of the American Chemical Society* **2012,** *134* (41), 17253-17261.
128. Zou, X.; Zhang, Y., Noble metal-free hydrogen evolution catalysts for water splitting. *Chemical Society*

Reviews **2015,** *44* (15), 5148-5180.
129. Tahir, M.; Pan, L.; Idrees, F.; Zhang, X.; Wang, L.; Zou, J.-J.; Wang, Z. L., Electrocatalytic oxygen evolution reaction for energy conversion and storage: A comprehensive review. *Nano Energy* **2017,** *37*, 136-157.
130. Fominykh, K.; Feckl, J. M.; Sicklinger, J.; Döblinger, M.; Böcklein, S.; Ziegler, J.; Peter, L.; Rathousky, J.; Scheidt, E. W.; Bein, T., Ultrasmall dispersible crystalline nickel oxide nanoparticles as high-performance catalysts for electrochemical water splitting. *Advanced Functional Materials* **2014,** *24* (21), 3123-3129.
131. Zhao, Y.; Jia, X.; Chen, G.; Shang, L.; Waterhouse, G. I.; Wu, L.-Z.; Tung, C.-H.; O'Hare, D.; Zhang, T., Ultrafine NiO nanosheets stabilized by TiO_2 from monolayer NiTi-LDH precursors: an active water oxidation electrocatalyst. *Journal of the American Chemical Society* **2016,** *138* (20), 6517-6524.
132. Long, X.; Ma, Z.; Yu, H.; Gao, X.; Pan, X.; Chen, X.; Yang, S.; Yi, Z., Porous FeNi oxide nanosheets as advanced electrochemical catalysts for sustained water oxidation. *Journal of Materials Chemistry A* **2016,** *4* (39), 14939-14943.
133. Qiu, Y.; Xin, L.; Li, W., Electrocatalytic oxygen evolution over supported small amorphous Ni-Fe nanoparticles in alkaline electrolyte. *Langmuir* **2014,** *30* (26), 7893-7901.
134. Xiao, Y.; Feng, L.; Hu, C.; Fateev, V.; Liu, C.; Xing, W., $NiCo_2O_4$ 3 dimensional nanosheet as effective and robust catalyst for oxygen evolution reaction. *RSC Advances* **2015,** *5* (76), 61900-61905.
135. Yang, Y.; Fei, H.; Ruan, G.; Xiang, C.; Tour, J. M., Efficient electrocatalytic oxygen evolution on amorphous nickel-cobalt binary oxide nanoporous layers. *ACS nano* **2014,** *8* (9), 9518-9523.
136. Gao, M.; Sheng, W.; Zhuang, Z.; Fang, Q.; Gu, S.; Jiang, J.; Yan, Y., Efficient water oxidation using nanostructured α-nickel-hydroxide as an electrocatalyst. *Journal of the American Chemical Society* **2014,** *136* (19), 7077-7084.
137. Luan, C.; Liu, G.; Liu, Y.; Yu, L.; Wang, Y.; Xiao, Y.; Qiao, H.; Dai, X.; Zhang, X., Structure effects of 2D materials on α-nickel hydroxide for oxygen evolution reaction. *ACS nano* **2018,** *12* (4), 3875-3885.
138. Zhou, X.; Xia, Z.; Zhang, Z.; Ma, Y.; Qu, Y., One-step synthesis of multi-walled carbon nanotubes/ultra-thin $Ni(OH)_2$ nanoplate composite as efficient catalysts for water oxidation. *Journal of Materials Chemistry A* **2014,** *2* (30), 11799-11806.
139. Xiong, D.; Li, W.; Liu, L., Vertically aligned porous nickel(II) hydroxide nanosheets supported on carbon paper with long-term oxygen evolution performance. *Chemistry – An Asian Journal* **2017,** *12* (5), 543-551.
140. Zhang, Q.; Zhang, C.; Liang, J.; Yin, P.; Tian, Y., Orthorhombic α-NiOOH nanosheet arrays: phase conversion and efficient bifunctional electrocatalysts for full water splitting. *ACS Sustainable Chemistry & Engineering* **2017,** *5* (5), 3808-3818.
141. Zhang, W.; Wu, Y.; Qi, J.; Chen, M.; Cao, R., A thin NiFe hydroxide film formed by stepwise electrodeposition strategy with significantly improved catalytic water oxidation efficiency. *Advanced Energy Materials* **2017,** *7* (9), 1602547.
142. Louie, M. W.; Bell, A. T., An investigation of thin-film Ni-Fe oxide catalysts for the electrochemical evolution of oxygen. *Journal of the American Chemical Society* **2013,** *135* (33), 12329-12337.
143. Song, F.; Hu, X., Exfoliation of layered double hydroxides for enhanced oxygen evolution catalysis. *Nature communications* **2014,** *5*, 4477.
144. Fan, K.; Chen, H.; Ji, Y.; Huang, H.; Claesson, P. M.; Daniel, Q.; Philippe, B.; Rensmo, H.; Li, F.; Luo, Y., Nickel-vanadium monolayer double hydroxide for efficient electrochemical water oxidation. *Nature communications* **2016,** *7*, 11981.
145. Long, X.; Xiao, S.; Wang, Z.; Zheng, X.; Yang, S., Co intake mediated formation of ultrathin nanosheets of transition metal LDH—an advanced electrocatalyst for oxygen evolution reaction. *Chemical Communications* **2015,** *51* (6), 1120-1123.
146. Chen, S.; Kang, Z.; Hu, X.; Zhang, X.; Wang, H.; Xie, J.; Zheng, X.; Yan, W.; Pan, B.; Xie, Y., Delocalized spin states in 2D atomic layers realizing enhanced electrocatalytic oxygen evolution. *Advanced Materials* **2017,** *29* (30), 1701687.
147. Xu, K.; Chen, P.; Li, X.; Tong, Y.; Ding, H.; Wu, X.; Chu, W.; Peng, Z.; Wu, C.; Xie, Y., Metallic nickel nitride nanosheets realizing enhanced electrochemical water oxidation. *Journal of the American Chemical Society* **2015,** *137* (12), 4119-4125.
148. Stern, L.-A.; Feng, L.; Song, F.; Hu, X., Ni_2P as a Janus catalyst for water splitting: the oxygen evolution activity of Ni_2P nanoparticles. *Energy & Environmental Science* **2015,** *8* (8), 2347-2351.
149. Masa, J.; Sinev, I.; Mistry, H.; Ventosa, E.; de la Mata, M.; Arbiol, J.; Muhler, M.; Roldan Cuenya, B.; Schuhmann, W., Ultrathin high surface area nickel boride (Ni_xB) nanosheets as highly efficient electrocatalyst for oxygen evolution. *Advanced Energy Materials* **2017,** *7* (17), 1700381.
150. Zhang, J.; Zhang, D.; Zhang, R.; Zhang, N.; Cui, C.; Zhang, J.; Jiang, B.; Yuan, B.; Wang, T.; Xie, H., Facile synthesis of mesoporous and thin-walled Ni-Co sulfide nanotubes as efficient electrocatalysts for oxygen evolution reaction. *ACS Applied Energy Materials* **2018,** *1* (2), 495-502.
151. Ren, J.; Antonietti, M.; Fellinger, T. P., Efficient water splitting using a simple Ni/N/C paper electrocatalyst.

Advanced Energy Materials **2015,** *5* (6), 1401660.
152. Lee, Y.; Suntivich, J.; May, K. J.; Perry, E. E.; Shao-Horn, Y., Synthesis and activities of rutile IrO_2 and RuO_2 nanoparticles for oxygen evolution in acid and alkaline solutions. *The journal of physical chemistry letters* **2012,** *3* (3), 399-404.
153. Han, L.; Dong, S.; Wang, E., Transition-metal (Co, Ni, and Fe)-based electrocatalysts for the water oxidation reaction. *Advanced Materials* **2016,** *28* (42), 9266-9291.
154. Feng, L.-L.; Yu, G.; Wu, Y.; Li, G.-D.; Li, H.; Sun, Y.; Asefa, T.; Chen, W.; Zou, X., High-index faceted Ni_3S_2 nanosheet arrays as highly active and ultrastable electrocatalysts for water splitting. *Journal of the American Chemical Society* **2015,** *137* (44), 14023-14026.
155. Su, D.; Ford, M.; Wang, G., Mesoporous NiO crystals with dominantly exposed {110} reactive facets for ultrafast lithium storage. *Scientific reports* **2012,** *2*, 924.
156. Dhavale, V. M.; Gaikwad, S. S.; George, L.; Devi, R. N.; Kurungot, S., Nitrogen-doped graphene interpenetrated 3D Ni-nanocages: efficient and stable water-to-dioxygen electrocatalysts. *Nanoscale* **2014,** *6* (21), 13179-13187.
157. Yu, X.; Hua, T.; Liu, X.; Yan, Z.; Xu, P.; Du, P., Nickel-based thin film on multiwalled carbon nanotubes as an efficient bifunctional electrocatalyst for water splitting. *ACS applied materials & interfaces* **2014,** *6* (17), 15395-15402.
158. Chen, S.; Duan, J.; Ran, J.; Jaroniec, M.; Qiao, S. Z., N-doped graphene film-confined nickel nanoparticles as a highly efficient three-dimensional oxygen evolution electrocatalyst. *Energy & Environmental Science* **2013,** *6* (12), 3693-3699.
159. Landon, J.; Demeter, E.; İnoğlu, N.; Keturakis, C.; Wachs, I. E.; Vasić, R.; Frenkel, A. I.; Kitchin, J. R., Spectroscopic characterization of mixed Fe-Ni oxide electrocatalysts for the oxygen evolution reaction in alkaline electrolytes. *Acs Catalysis* **2012,** *2* (8), 1793-1801.
160. Singh, A.; Chang, S. L.; Hocking, R. K.; Bach, U.; Spiccia, L., Highly active nickel oxide water oxidation catalysts deposited from molecular complexes. *Energy & Environmental Science* **2013,** *6* (2), 579-586.
161. Bediako, D. K.; Surendranath, Y.; Nocera, D. G., Mechanistic studies of the oxygen evolution reaction mediated by a nickel-borate thin film electrocatalyst. *Journal of the American Chemical Society* **2013,** *135* (9), 3662-3674.
162. Dincă, M.; Surendranath, Y.; Nocera, D. G., Nickel-borate oxygen-evolving catalyst that functions under benign conditions. *Proceedings of the National Academy of Sciences* **2010,** *107* (23), 10337-10341.
163. Gerken, J. B.; Shaner, S. E.; Massé, R. C.; Porubsky, N. J.; Stahl, S. S., A survey of diverse earth abundant oxygen evolution electrocatalysts showing enhanced activity from Ni-Fe oxides containing a third metal. *Energy & Environmental Science* **2014,** *7* (7), 2376-2382.
164. Smith, R. D.; Prévot, M. S.; Fagan, R. D.; Trudel, S.; Berlinguette, C. P., Water oxidation catalysis: electrocatalytic response to metal stoichiometry in amorphous metal oxide films containing iron, cobalt, and nickel. *Journal of the American Chemical Society* **2013,** *135* (31), 11580-11586.
165. McCrory, C. C.; Jung, S.; Peters, J. C.; Jaramillo, T. F., Benchmarking heterogeneous electrocatalysts for the oxygen evolution reaction. *Journal of the American Chemical Society* **2013,** *135* (45), 16977-16987.
166. Mellsop, S. R.; Gardiner, A.; Johannessen, B.; Marshall, A. T., Structure and transformation of oxy-hydroxide films on Ni anodes below and above the oxygen evolution potential in alkaline electrolytes. *Electrochimica Acta* **2015,** *168*, 356-364.
167. Bode, H.; Dehmelt, K.; Witte, J., Zur kenntnis der nickelhydroxidelektrode—I. Über das nickel (II)-hydroxidhydrat. *Electrochimica Acta* **1966,** *11* (8), 1079-IN1.
168. Bediako, D. K.; Lassalle-Kaiser, B.; Surendranath, Y.; Yano, J.; Yachandra, V. K.; Nocera, D. G., Structure-activity correlations in a nickel-borate oxygen evolution catalyst. *Journal of the American Chemical Society* **2012,** *134* (15), 6801-6809.
169. Falk, S. U.; Salkind, A. J., Alkaline storage batteries. **1969**.
170. Tichenor, R. L., Nickel oxides-relation between electrochemical and foreign ion content. *Industrial & Engineering Chemistry* **1952,** *44* (5), 973-977.
171. Hickling, A.; Hill, S., Oxygen overvoltage. Part I. The influence of electrode material, current density, and time in aqueous solution. *Discussions of the Faraday Society* **1947,** *1*, 236-246.
172. Munshi, M.; Tseung, A.; Parker, J., The dissolution of iron from the negative material in pocket plate nickel-cadmium batteries. *Journal of applied electrochemistry* **1985,** *15* (5), 711-717.
173. Corrigan, D. A., The catalysis of the oxygen evolution reaction by iron impurities in thin film nickel oxide electrodes. *Journal of The Electrochemical Society* **1987,** *134* (2), 377-384.
174. Koza, J. A.; Hull, C. M.; Liu, Y.-C.; Switzer, J. A., Deposition of β-$Co(OH)_2$ films by electrochemical reduction of tris (ethylenediamine) cobalt (III) in alkaline solution. *Chemistry of Materials* **2013,** *25* (9), 1922-1926.
175. Cai, Z.; Bu, X.; Wang, P.; Ho, J. C.; Yang, J.; Wang, X., Recent advances in layered double hydroxide electrocatalysts for the oxygen evolution reaction. *Journal of Materials Chemistry A* **2019**.

176. Tengeler, S. Cubic silicon carbide for direct photoelectrochemical water splitting. PhD Thesis, Technische Universität Darmstadt, 2017.
177. Klein, A.; Mayer, T.; Thissen, A.; Jaegermann, W., Photoelectron spectroscopy in materials science and physical chemistry. *Bunsen-Magazin* **2008,** *10* (4), 124-139.
178. Hüfner, S., *Photoelectron spectroscopy: principles and applications*. 3rd ed.; Springer Science & Business Media: 2013.
179. Hertz, H., Ueber einen Einfluss des ultravioletten Lichtes auf die electrische Entladung. *Annalen der Physik* **1887,** *267* (8), 983-1000.
180. Einstein, A., Über einen die Erzeugung und Verwandlung des Lichtes betreffenden heuristischen Gesichtspunkt. *Annalen der physik* **1905,** *322* (6), 132-148.
181. Siegbahn, K. M. G., A discussion on photoelectron spectroscopy-electron spectroscopy for chemical analysis (esca). *Philosophical Transactions of the Royal Society of London. Series A, Mathematical and Physical Sciences* **1970,** *268* (1184), 33-57.
182. Moulder, J. F.; Chastain, J.; King, R. C., *Handbook of X-ray photoelectron spectroscopy: a reference book of standard spectra for identification and interpretation of XPS data*. Physical Electronics Eden Prairie, MN: 1995.
183. Weidler, N. Plasma-enhanced chemical vapor deposition of cobalt-based catalysts for the oxygen evolution reaction. PhD thesis, Technische Universität Darmstadt, 2017.
184. Metson, J. B., Charge compensation and binding energy referencing in XPS analysis. *Surface and Interface Analysis* **1999,** *27* (12), 1069-1072.
185. Cros, A., Charging effects in X-ray photoelectron spectroscopy. *Journal of Electron Spectroscopy and Related Phenomena* **1992,** *59* (1), 1-14.
186. Watts, J. F.; Wolstenholme, J., An introduction to surface analysis by XPS and AES. *Wiley-VCH* **2003**.
187. Niemantsverdriet, J. W., *Spectroscopy in catalysis: an introduction*. Third, completely revised and enlarged ed.; WILEY-VCH: 2007.
188. Fairley, N., *CasaXPS Manual 2.3.15*. Casa Software Ltd.: 2009.
189. Seah, M., Quantification of AES and XPS. *Practical surface analysis* **1990,** *1*.
190. Biesinger, M. C.; Payne, B. P.; Lau, L. W.; Gerson, A.; Smart, R. S. C., X-ray photoelectron spectroscopic chemical state quantification of mixed nickel metal, oxide and hydroxide systems. *Surface and Interface Analysis* **2009,** *41* (4), 324-332.
191. West, A. R., *Solid state chemistry and its applications*. John Wiley & Sons: 2014.
192. Stevens, M. B.; Enman, L. J.; Batchellor, A. S.; Cosby, M. R.; Vise, A. E.; Trang, C. D.; Boettcher, S. W., Measurement techniques for the study of thin film heterogeneous water oxidation electrocatalysts. *Chemistry of Materials* **2016,** *29* (1), 120-140.
193. Luo, J.; Im, J.-H.; Mayer, M. T.; Schreier, M.; Nazeeruddin, M. K.; Park, N.-G.; Tilley, S. D.; Fan, H. J.; Grätzel, M., Water photolysis at 12.3% efficiency via perovskite photovoltaics and earth-abundant catalysts. *Science* **2014,** *345* (6204), 1593-1596.
194. Trasatti, S., Work function, electronegativity, and electrochemical behaviour of metals: III. Electrolytic hydrogen evolution in acid solutions. *Journal of Electroanalytical Chemistry and Interfacial Electrochemistry* **1972,** *39* (1), 163-184.
195. Greeley, J.; Jaramillo, T. F.; Bonde, J.; Chorkendorff, I.; Nørskov, J. K., Computational high-throughput screening of electrocatalytic materials for hydrogen evolution. *Nature materials* **2006,** *5* (11), 909-913.
196. Safizadeh, F.; Ghali, E.; Houlachi, G., Electrocatalysis developments for hydrogen evolution reaction in alkaline solutions–a review. *international journal of hydrogen energy* **2015,** *40* (1), 256-274.
197. Subbaraman, R.; Tripkovic, D.; Chang, K.-C.; Strmcnik, D.; Paulikas, A. P.; Hirunsit, P.; Chan, M.; Greeley, J.; Stamenkovic, V.; Markovic, N. M., Trends in activity for the water electrolyser reactions on 3d M (Ni, Co, Fe, Mn) hydr (oxy) oxide catalysts. *Nature materials* **2012,** *11* (6), 550-557.
198. Gong, M.; Zhou, W.; Tsai, M.-C.; Zhou, J.; Guan, M.; Lin, M.-C.; Zhang, B.; Hu, Y.; Wang, D.-Y.; Yang, J., Nanoscale nickel oxide/nickel heterostructures for active hydrogen evolution electrocatalysis. *Nature communications* **2014,** *5*.
199. Xu, Y. F.; Gao, M. R.; Zheng, Y. R.; Jiang, J.; Yu, S. H., Nickel/nickel (II) oxide nanoparticles anchored onto cobalt (IV) diselenide nanobelts for the electrochemical production of hydrogen. *Angewandte Chemie International Edition* **2013,** *52* (33), 8546-8550.
200. Bates, M. K.; Jia, Q.; Ramaswamy, N.; Allen, R. J.; Mukerjee, S., Composite Ni/NiO-Cr_2O_3 catalyst for alkaline hydrogen evolution reaction. *The Journal of Physical Chemistry C* **2015,** *119* (10), 5467-5477.
201. Yan, X.; Tian, L.; He, M.; Chen, X., Three-dimensional crystalline/amorphous Co/Co_3O_4 core/shell nanosheets as efficient electrocatalysts for the hydrogen evolution reaction. *Nano letters* **2015,** *15* (9), 6015-6021.
202. Stern, L.-A.; Hu, X., Enhanced oxygen evolution activity by NiO_x and $Ni(OH)_2$ nanoparticles. *Faraday discussions* **2015,** *176*, 363-379.

203. Di Bari, G. A., Electrodeposition of nickel. *Modern Electroplating* **2000,** *5*, 79-114.
204. Hutton, L. A.; Vidotti, M.; Patel, A. N.; Newton, M. E.; Unwin, P. R.; Macpherson, J. V., Electrodeposition of nickel hydroxide nanoparticles on boron-doped diamond electrodes for oxidative electrocatalysis. *The Journal of Physical Chemistry C* **2010,** *115* (5), 1649-1658.
205. Sonavane, A.; Inamdar, A.; Shinde, P.; Deshmukh, H.; Patil, R.; Patil, P., Efficient electrochromic nickel oxide thin films by electrodeposition. *Journal of Alloys and Compounds* **2010,** *489* (2), 667-673.
206. Yuan, H.; Lunt, R. R.; Thompson, J. I.; Ofoli, R. Y., Electrodeposition of Ni/$Ni(OH)_2$ catalytic films for the hydrogen evolution reaction produced by using cyclic voltammetry. *ChemElectroChem* **2016**.
207. https://nano-measurer.software.informer.com/.
208. Xue, Z.; Yin, B.; Li, M.; Rao, H.; Wang, H.; Zhou, X.; Liu, X.; Lu, X., Direct electrodeposition of well dispersed electrochemical reduction graphene oxide assembled with nickel oxide nanocomposite and its improved electrocatalytic activity toward 2, 4, 6-Trinitrophenol. *Electrochimica Acta* **2016,** *192*, 512-520.
209. Crist, B. V., *Handbook of monochromatic XPS spectra Volume 1: The elements and native oxides*. XPS-International: Ames, 1999; Vol. 1.
210. Yan, J.; Fan, Z.; Sun, W.; Ning, G.; Wei, T.; Zhang, Q.; Zhang, R.; Zhi, L.; Wei, F., Advanced asymmetric supercapacitors based on $Ni(OH)_2$/graphene and porous graphene electrodes with high energy density. *Advanced Functional Materials* **2012,** *22* (12), 2632-2641.
211. Yin, H.; Zhao, S.; Zhao, K.; Muqsit, A.; Tang, H.; Chang, L.; Zhao, H.; Gao, Y.; Tang, Z., Ultrathin platinum nanowires grown on single-layered nickel hydroxide with high hydrogen evolution activity. *Nature communications* **2015,** *6*.
212. Weidler, N.; Schuch, J.; Knaus, F.; Stenner, P.; Hoch, S.; Maljusch, A.; Schäfer, R.; Kaiser, B.; Jaegermann, W., X-ray photoelectron spectroscopic investigation of plasma-enhanced chemical vapor deposited NiO_x, $NiO_x(OH)_y$, and $CoNiO_x(OH)_y$: Influence of the chemical composition on the catalytic activity for the oxygen evolution reaction. *The Journal of Physical Chemistry C* **2017,** *121* (12), 6455-6463.
213. Luo, P. F.; Kuwana, T.; Paul, D. K.; Sherwood, P. M., Electrochemical and XPS study of the nickel-titanium electrode surface. *Analytical chemistry* **1996,** *68* (19), 3330-3337.
214. Ratcliff, E. L.; Meyer, J.; Steirer, K. X.; Garcia, A.; Berry, J. J.; Ginley, D. S.; Olson, D. C.; Kahn, A.; Armstrong, N. R., Evidence for near-surface NiOOH species in solution-processed NiO_x selective interlayer materials: impact on energetics and the performance of polymer bulk heterojunction photovoltaics. *Chemistry of Materials* **2011,** *23* (22), 4988-5000.
215. Crist, B. V., Handbook of monochromatic XPS spectra Volume 2: Commercially pure binary oxides. *XPS International LLC* **2005**.
216. Weidler, N.; Paulus, S.; Schuch, J.; Klett, J.; Hoch, S.; Stenner, P.; Maljusch, A.; Brötz, J.; Wittich, C.; Kaiser, B., CoO_x thin film deposited by CVD as efficient water oxidation catalyst: change of oxidation state in XPS and its correlation to electrochemical activity. *Physical Chemistry Chemical Physics* **2016**.
217. Epelboin, I.; Joussellin, M.; Wiart, R., Impedance measurements for nickel deposition in sulfate and chloride electrolytes. *Journal of Electroanalytical Chemistry and Interfacial Electrochemistry* **1981,** *119* (1), 61-71.
218. Zach, M. P.; Penner, R. M., Nanocrystalline nickel nanoparticles. *Advanced Materials* **2000,** *12* (12), 878-883.
219. Oriňáková, R.; Turoňová, A.; Kladeková, D.; Gálová, M.; Smith, R. M., Recent developments in the electrodeposition of nickel and some nickel-based alloys. *Journal of Applied Electrochemistry* **2006,** *36* (9), 957-972.
220. Jiang, N.; Tang, Q.; Sheng, M.; You, B.; Jiang, D.-e.; Sun, Y., Nickel sulfides for electrocatalytic hydrogen evolution under alkaline conditions: a case study of crystalline NiS, NiS_2, and Ni_3S_2 nanoparticles. *Catalysis Science & Technology* **2016,** *6* (4), 1077-1084.
221. Xu, R.; Wu, R.; Shi, Y.; Zhang, J.; Zhang, B., Ni_3Se_2 nanoforest/Ni foam as a hydrophilic, metallic, and self-supported bifunctional electrocatalyst for both H_2 and O_2 generations. *Nano Energy* **2016,** *24*, 103-110.
222. He, X.-D.; Xu, F.; Li, F.; Liu, L.; Wang, Y.; Deng, N.; Zhu, Y.-W.; He, J.-B., Composition-performance relationship of Ni x Cu y nanoalloys as hydrogen evolution electrocatalyst. *Journal of Electroanalytical Chemistry* **2017**.
223. Popczun, E. J.; McKone, J. R.; Read, C. G.; Biacchi, A. J.; Wiltrout, A. M.; Lewis, N. S.; Schaak, R. E., Nanostructured nickel phosphide as an electrocatalyst for the hydrogen evolution reaction. *Journal of the American Chemical Society* **2013,** *135* (25), 9267-9270.
224. Tian, J.; Liu, Q.; Asiri, A. M.; Sun, X., Self-supported nanoporous cobalt phosphide nanowire arrays: an efficient 3D hydrogen-evolving cathode over the wide range of pH 0–14. *Journal of the American Chemical Society* **2014,** *136* (21), 7587-7590.
225. Zhao, S.; Huang, J.; Liu, Y.; Shen, J.; Wang, H.; Yang, X.; Zhu, Y.; Li, C., Multimetallic Ni–Mo/Cu nanowires as nonprecious and efficient full water splitting catalyst. *Journal of Materials Chemistry A* **2017,** *5* (8), 4207-4214.
226. Crist, B. V., *Handbook of monochromatic XPS spectra Volume 1: The elements and native oxides*. XPS-International: Ames, 1999.
227. Robinson, D. M.; Go, Y. B.; Greenblatt, M.; Dismukes, G. C., Water oxidation by λ-MnO_2: catalysis by the

cubical Mn_4O_4 subcluster obtained by delithiation of spinel $LiMn_2O_4$. *Journal of the American Chemical Society* **2010,** *132* (33), 11467-11469.
228. Indra, A.; Menezes, P. W.; Zaharieva, I.; Baktash, E.; Pfrommer, J.; Schwarze, M.; Dau, H.; Driess, M., Active mixed‐valent MnO_x water oxidation catalysts through partial oxidation (corrosion) of nanostructured MnO particles. *Angewandte Chemie International Edition* **2013,** *52* (50), 13206-13210.
229. Zaharieva, I.; Chernev, P.; Risch, M.; Klingan, K.; Kohlhoff, M.; Fischer, A.; Dau, H., Electrosynthesis, functional, and structural characterization of a water-oxidizing manganese oxide. *Energy & Environmental Science* **2012,** *5* (5), 7081-7089.
230. Chen, M.; Wu, Y.; Han, Y.; Lin, X.; Sun, J.; Zhang, W.; Cao, R., An iron-based film for highly efficient electrocatalytic oxygen evolution from neutral aqueous solution. *ACS applied materials & interfaces* **2015,** *7* (39), 21852-21859.
231. Wu, Y.; Chen, M.; Han, Y.; Luo, H.; Su, X.; Zhang, M. T.; Lin, X.; Sun, J.; Wang, L.; Deng, L., Fast and simple preparation of iron‐based thin films as highly efficient water‐oxidation catalysts in neutral aqueous solution. *Angewandte Chemie International Edition* **2015,** *54* (16), 4870-4875.
232. Liang, Y.; Li, Y.; Wang, H.; Zhou, J.; Wang, J.; Regier, T.; Dai, H., Co_3O_4 nanocrystals on graphene as a synergistic catalyst for oxygen reduction reaction. *Nature materials* **2011,** *10* (10), 780.
233. Yeo, B. S.; Bell, A. T., Enhanced activity of gold-supported cobalt oxide for the electrochemical evolution of oxygen. *Journal of the American Chemical Society* **2011,** *133* (14), 5587-5593.
234. Kanan, M. W.; Nocera, D. G., In situ formation of an oxygen-evolving catalyst in neutral water containing phosphate and Co^{2+}. *Science* **2008,** *321* (5892), 1072-1075.
235. Du, J.; Chen, Z.; Ye, S.; Wiley, B. J.; Meyer, T. J., Copper as a robust and transparent electrocatalyst for water oxidation. *Angewandte Chemie International Edition* **2015,** *54* (7), 2073-2078.
236. Chen, Z.; Rathmell, A. R.; Ye, S.; Wilson, A. R.; Wiley, B. J., Optically transparent water oxidation catalysts based on copper nanowires. *Angewandte Chemie* **2013,** *125* (51), 13953-13956.
237. Motori, A.; Sandrolini, F.; Davolio, G., Electrical properties of nickel hydroxide for alkaline cell systems. *Journal of power sources* **1994,** *48* (3), 361-370.
238. Bergman, S. L.; Sahasrabudhe, G. S.; Ji, H.; Cava, R. J.; Bernasek, S. L., Useful x-ray photoelectron spectroscopy-based chemical tool: Differential charging studies of complex composite materials. *Chemistry of Materials* **2017,** *29* (10), 4162-4166.
239. Grosvenor, A. P.; Biesinger, M. C.; Smart, R. S. C.; McIntyre, N. S., New interpretations of XPS spectra of nickel metal and oxides. *Surface Science* **2006,** *600* (9), 1771-1779.
240. Gorham, J. M.; Osborn, W. A.; Woodcock, J. W.; Scott, K. C.; Heddleston, J. M.; Walker, A. R. H.; Gilman, J. W., Detecting carbon in carbon: Exploiting differential charging to obtain information on the chemical identity and spatial location of carbon nanotube aggregates in composites by imaging X-ray photoelectron spectroscopy. *Carbon* **2016,** *96*, 1208-1216.
241. Suzer, S., Differential charging in X-ray photoelectron spectroscopy: A nuisance or a useful tool? *Analytical chemistry* **2003,** *75* (24), 7026-7029.
242. Payne, B. P.; Biesinger, M. C.; McIntyre, N. S., The study of polycrystalline nickel metal oxidation by water vapour. *Journal of Electron Spectroscopy and Related Phenomena* **2009,** *175* (1), 55-65.
243. Zhou, F.; Izgorodin, A.; Hocking, R. K.; Armel, V.; Spiccia, L.; MacFarlane, D. R., Improvement of catalytic water oxidation on MnO_x films by heat treatment. *ChemSusChem* **2013,** *6* (4), 643-651.
244. Khan, M.; Xiao, J.; Zhou, F.; Yablonskikh, M.; MacFarlane, D. R.; Spiccia, L.; Aziz, E. F., On the origin of the improvement of electrodeposited MnO_x films in water oxidation catalysis induced by heat treatment. *ChemSusChem* **2015,** *8* (11), 1980-1985.
245. Mani, B.; de Neufville, J., Dehydration of chemically and electrochemically impregnated (CI and EI) nickel hydroxide electrodes. *Journal of The Electrochemical Society* **1988,** *135* (4), 800-803.
246. Hall, D. S.; Lockwood, D. J.; Bock, C.; MacDougall, B. R. In *Nickel hydroxides and related materials: a review of their structures, synthesis and properties*, Proc. R. Soc. A, The Royal Society: 2015; p 20140792.
247. Zhao, D.; Zhou, W.; Li, H., Effects of deposition potential and anneal temperature on the hexagonal nanoporous nickel hydroxide films. *Chemistry of materials* **2007,** *19* (16), 3882-3891.
248. Burke, M. S.; Enman, L. J.; Batchellor, A. S.; Zou, S.; Boettcher, S. W., Oxygen evolution reaction electrocatalysis on transition metal oxides and (oxy)hydroxides: activity trends and design principles. *Chemistry of Materials* **2015,** *27* (22), 7549-7558.
249. Wang, L.; Chen, H.; Daniel, Q.; Duan, L.; Philippe, B.; Yang, Y.; Rensmo, H.; Sun, L., Promoting the water oxidation catalysis by synergistic interactions between $Ni(OH)_2$ and carbon nanotubes. *Advanced Energy Materials* **2016,** *6* (15), 1600516-n/a.
250. Hoang, T. T. H.; Gewirth, A. A., High activity oxygen evolution reaction catalysts from additive-controlled

electrodeposited Ni and NiFe Films. *ACS Catalysis* **2016,** *6* (2), 1159-1164.
251. Fominykh, K.; Feckl, J. M.; Sicklinger, J.; Döblinger, M.; Böcklein, S.; Ziegler, J.; Peter, L.; Rathousky, J.; Scheidt, E.-W.; Bein, T.; Fattakhova-Rohlfing, D., Ultrasmall dispersible crystalline nickel oxide nanoparticles as high-performance catalysts for electrochemical water splitting. *Advanced Functional Materials* **2014,** *24* (21), 3123-3129.
252. Fabregat-Santiago, F.; Garcia-Belmonte, G.; Bisquert, J.; Zaban, A.; Salvador, P., Decoupling of transport, charge storage, and interfacial charge transfer in the nanocrystalline TiO_2/electrolyte system by impedance methods. *The Journal of Physical Chemistry B* **2002,** *106* (2), 334-339.
253. EC-Lab Software User's Manual, Version 10.1x. BioLogic Science Instruments: 2011.
254. Batchellor, A. S.; Boettcher, S. W., Pulse-electrodeposited Ni-Fe (oxy)hydroxide oxygen evolution electrocatalysts with high geometric and intrinsic activities at large mass loadings. *ACS Catalysis* **2015,** *5* (11), 6680-6689.
255. Payne, B.; Biesinger, M.; McIntyre, N., The study of polycrystalline nickel metal oxidation by water vapour. *Journal of Electron Spectroscopy and Related Phenomena* **2009,** *175* (1-3), 55-65.
256. Payne, B.; Biesinger, M.; McIntyre, N., Use of oxygen/nickel ratios in the XPS characterisation of oxide phases on nickel metal and nickel alloy surfaces. *Journal of Electron Spectroscopy and Related Phenomena* **2012,** *185* (5-7), 159-166.
257. Wang, D.-Y.; Gong, M.; Chou, H.-L.; Pan, C.-J.; Chen, H.-A.; Wu, Y.; Lin, M.-C.; Guan, M.; Yang, J.; Chen, C.-W., Highly active and stable hybrid catalyst of cobalt-doped FeS_2 nanosheets-carbon nanotubes for hydrogen evolution reaction. *Journal of the American Chemical Society* **2015,** *137* (4), 1587-1592.
258. Voiry, D.; Yamaguchi, H.; Li, J.; Silva, R.; Alves, D. C.; Fujita, T.; Chen, M.; Asefa, T.; Shenoy, V. B.; Eda, G., Enhanced catalytic activity in strained chemically exfoliated WS_2 nanosheets for hydrogen evolution. *Nature materials* **2013,** *12* (9), 850.
259. Jin, Y.; Wang, H.; Li, J.; Yue, X.; Han, Y.; Shen, P. K.; Cui, Y., Porous MoO_2 nanosheets as non-noble bifunctional electrocatalysts for overall water splitting. *Advanced Materials* **2016,** *28* (19), 3785-3790.
260. McKone, J. R.; Marinescu, S. C.; Brunschwig, B. S.; Winkler, J. R.; Gray, H. B., Earth-abundant hydrogen evolution electrocatalysts. *Chemical Science* **2014,** *5* (3), 865-878.
261. Wang, H. Y.; Hsu, Y. Y.; Chen, R.; Chan, T. S.; Chen, H. M.; Liu, B., Ni^{3+} - induced formation of active NiOOH on the spinel Ni-Co oxide surface for efficient oxygen evolution reaction. *Advanced Energy Materials* **2015,** *5* (10), 1500091.
262. McCrory, C. C.; Jung, S.; Ferrer, I. M.; Chatman, S. M.; Peters, J. C.; Jaramillo, T. F., Benchmarking hydrogen evolving reaction and oxygen evolving reaction electrocatalysts for solar water splitting devices. *Journal of the American Chemical Society* **2015,** *137* (13), 4347-4357.
263. Brox, B.; Olefjord, I., ESCA studies of MoO_2 and MoO_3. *Surface and interface analysis* **1988,** *13* (1), 3-6.
264. Okonkwo, I.; Doff, J.; Baron-Wiecheć, A.; Jones, G.; Koroleva, E.; Skeldon, P.; Thompson, G., Oxidation states of molybdenum in oxide films formed in sulphuric acid and sodium hydroxide. *Thin Solid Films* **2012,** *520* (19), 6318-6327.
265. Clayton, C.; Lu, Y., Electrochemical and XPS evidence of the aqueous formation of Mo_2O_5. *Surface and Interface Analysis* **1989,** *14* (1-2), 66-70.
266. Lu, Y.; Clayton, C., An XPS study of the passive and transpassive behavior of molybdenum in deaerated 0.1 M HCl. *Corrosion science* **1989,** *29* (8), 927-937.
267. Oh, S.; Kim, H.; Kwon, Y.; Kim, M.; Cho, E.; Kwon, H., Porous Co-P foam as an efficient bifunctional electrocatalyst for hydrogen and oxygen evolution reactions. *Journal of Materials Chemistry A* **2016,** *4* (47), 18272-18277.
268. Li, W.; Li, D.; Gao, X.; Gurlo, A.; Zander, S.; Jones, P.; Navrotsky, A.; Shen, Z.; Riedel, R.; Ionescu, E., A study on the thermal conversion of scheelite-type ABO_4 into perovskite-type $AB(O, N)_3$. *Dalton Transactions* **2015,** *44* (17), 8238-8246.
269. Wen, Q.; Yu, Z.; Xu, Y.; Lu, Y.; Fasel, C.; Morita, K.; Guillon, O.; Buntkowsky, G.; Ionescu, E.; Riedel, R., $SiC/Hf_yTa_{1-y}C_xN_{1-x}$/C ceramic nanocomposites with $Hf_yTa_{1-y}C_xN_{1-x}$-carbon core-shell nanostructure and the influence of the carbon-shell thickness on electrical properties. *Journal of Materials Chemistry C* **2018,** *6* (4), 855-864.
270. Kang, D.; Kim, T. W.; Kubota, S. R.; Cardiel, A. C.; Cha, H. G.; Choi, K.-S., Electrochemical synthesis of photoelectrodes and catalysts for use in solar water splitting. *Chemical reviews* **2015,** *115* (23), 12839-12887.
271. Podlaha, E.; Landolt, D., Induced codeposition III. Molybdenum alloys with nickel, cobalt, and iron. *Journal of the Electrochemical Society* **1997,** *144* (5), 1672-1680.
272. Podlaha, E.; Landolt, D., Induced codeposition I. An experimental investigation of Ni - Mo alloys. *Journal of the Electrochemical Society* **1996,** *143* (3), 885-892.
273. Gruenert, W.; Stakheev, A. Y.; Feldhaus, R.; Anders, K.; Shpiro, E.; Minachev, K. M., Analysis of molybdenum (3d) XPS spectra of supported molybdenum catalysts: an alternative approach. *The Journal of Physical Chemistry*

1991, *95* (3), 1323-1328.
274. Soriaga, M. P.; Baricuatro, J. H.; Cummins, K. D.; Kim, Y.-G.; Saadi, F. H.; Sun, G.; McCrory, C. C.; McKone, J. R.; Velazquez, J. M.; Ferrer, I. M., Electrochemical surface science twenty years later: Expeditions into the electrocatalysis of reactions at the core of artificial photosynthesis. *Surface Science* **2015,** *631*, 285-294.
275. Jin, Y.; Shen, P. K., Nanoflower-like metallic conductive MoO_2 as a high-performance non-precious metal electrocatalyst for the hydrogen evolution reaction. *Journal of Materials Chemistry A* **2015,** *3* (40), 20080-20085.
276. Eyert, V.; Horny, R.; Höck, K.; Horn, S., Embedded Peierls instability and the electronic structure of MoO_2. *Journal of Physics: Condensed Matter* **2000,** *12* (23), 4923.
277. Mahmood, J.; Li, F.; Jung, S.-M.; Okyay, M. S.; Ahmad, I.; Kim, S.-J.; Park, N.; Jeong, H. Y.; Baek, J.-B., An efficient and pH-universal ruthenium-based catalyst for the hydrogen evolution reaction. *Nature nanotechnology* **2017,** *12* (5), 441.
278. Tang, Y. J.; Gao, M. R.; Liu, C. H.; Li, S. L.; Jiang, H. L.; Lan, Y. Q.; Han, M.; Yu, S. H., Porous molybdenum‐based hybrid catalysts for highly efficient hydrogen evolution. *Angewandte Chemie International Edition* **2015,** *54* (44), 12928-12932.
279. Chen, P. C.; Hsieh, S. J.; Chen, C. C.; Zou, J., The microstructure and capacitance characterizations of anodic titanium based alloy oxide nanotube. *Journal of Nanomaterials* **2013,** *2013*, 73.
280. Pourbaix, M., Atlas of electrochemical equilibria in aqueous solution. *NACE* **1974,** *307*.

Acknowledgements

Finally, it comes to acknowledgements, the indispensable part of a Ph.D. thesis. In spite it is impossible to completely express my appreciation to the people who supported me during my Ph.D. period by saying some nice words, I still want to say:

I would like to express the deepest appreciation and respect to Prof. Dr. Wolfram Jaegermann, who gave me a golden opportunity to work in his group and learn new scientific skills. Many thanks for his constant support and nice suggestions during my Ph.D. study. I also would like to express my heartfelt gratitude for his financial support that gives me enough time to finish my thesis.

I would like to sincerely thank PD. Dr. Bernhard Kaiser who introduced me into the field of water splitting. Warm thanks for his kind supervision and important contributions to my work, including productive discussions and careful revision of my manuscripts and Ph.D. dissertation.

I also would like to deeply acknowledge Water Splitting members for the productive discussions during our meetings and for being considerate in terms of the language medium. Special thanks to: Florent Yang, for all the technical and theoretical supports you gave to me, including introduction to apparatus in DAISY-FUN and in Electrochemistry Lab, discussion of the results and revision of my manuscripts; Joachim Klett, for the introduction to XPS measurements; Jona Schuch, for the introduction to CasaXPS and discussion; Thorsten Cottre, for the introduction to Gamry; Sven Tengeler, for the shared technical knowledge, lab-wise and thesis-wise; and Jürgen Ziegler, Natascha Weidler, Andreas Hajduk and Paula Connor for general laboratory and theoretical support.

I also would like to thank Surface Science group members, who kindly supported my work in different ways. Special mention to: Marga Lang and Leslie Frotscher, for taking care of the paperwork and helping me manage my way through living in Darmstadt; and Gennady Cherkashinin for the theoretical supports.

I really appreciate all my friends in Darmstadt and the time we spend together. We are the best friends forever. “Auld acquaintance will never be forgot and will always be brought to mind.”

Particularly, I would like to deeply thank my dear parents, Mr. Changjiu Tao (陶长久) and Mrs. Shuwan Liu (刘淑完), and all other family members who always love me, trust me and encourage me in my life. I wish you all the best. I’m looking forward to coming back home soon.

Special thanks to my beloved husband, Dr.-Ing. Qingbo Wen, who loves me, cares about me, bears with me, supports me, trusts me, understands me and encourages me. I appreciate every minute we live together. I’m very happy to marry you.

Importantly, I would like to greatly acknowledge the Chinese Scholarship Council (CSC), Technische Universität Darmstadt and the Deutsche Forschungsgemeinschaft (DFG) for financial supports on my Ph.D. study in Germany. I’m proud of this experience forever.

Curriculum vitae

Name: Shasha Tao

Nationality: Chinese

Gender: Female

E-mail: stao@surface.tu-darmstadt.de or taoshasha0905@gmail.com

Address: Nieder-Ramstädter Str. 11, 64283 Darmstadt, Germany

Education

- **Ph.D. Candidate of Material Science (Aug. 2014 ~ present)**, Department of Materials and Earth Sciences, Technische Universität Darmstadt, Germany.
- **Research assistant of Global Ecology (Oct. 2013 ~ Jul. 2014),** Centre for Ecological Research and Forestry Applications (CREAF), Universitat Autònoma de Barcelona (UAB), Spain.
- **Master of Environmental Engineering (Sep. 2010 ~ Jun. 2013)**, Department of Environmental Science and Engineering, Hunan University.
- **Bachelor of Environmental Engineering (Sep. 2006 ~ Jun. 2010)**, Department of Bioengineering and Environmental Science, Changsha University.

Research Experience

- **08/2014 ~ present, Supervisor:** Prof. Dr. Wolfram Jaegermann and PD Dr. Bernhard Kaiser
  - ✧ **Topic:** Electrodeposition of nickel-based non-noble transition metal compounds for electrocatalytic water splitting.
- **10/2013 ~ 07/2014, Supervisor**: Prof. Dr. Josep Peñuelas
  - ✧ **Topic:** Metabolomic analyses of BVOCs emission from vegetation and the formation of secondary organic aerosols.
- **09/2010 ~ 06/2013, Supervisor**: Prof. Dr. Caiting Li
  - ✧ **Topic:** Experimental investigation of cerium chloride impregnated activated coke for simultaneous removal of SO_2, NO and Hg^0 from coal-fired flue gas.
- **09/2009 ~ 06/2010, Supervisor:** Prof. Dr. Xingsheng Liao
  - ✧ **Topic:** Investigation of refinery sewage disposal and the re-use by reverse osmosis method.

Conferences

- **Shasha Tao**, Florent Yang, Bernhard Kaiser, Wolfram Jaegermann. Electrodeposition of Nickel Nanoparticles as Catalysts for Hydrogen and Oxygen Evolution Reactions under Alkaline Condition. The 115th General Assembly of the German Bunsen Society for Physical Chemistry (2016), *Rostock*, *Germany*. **(Poster)**
- Summer school of priority program of the DFG SPP 1613, 2016, *Berlin*, *Germany*.
- Annual project meeting of priority program of the DFG SPP 1613, 2016, *Berlin*, *Germany*.

Honors and Awards

- Doctoral scholarship supported by Technische Universität Darmstadt
- Chinese scholarship for 3 years of Ph.D. study in Germany (2014 ~ 2017)
- National Scholarship for Excellent Master Students (the highest prize for Master students in China)
- Outstanding Master Student of Hunan University
- "The Yangtze river environment scholarship" for Excellent Master Students
- Outstanding Award of "Sang-De" Excellent Research Paper Prize
- National Inspirational Scholarship for Bachelor Students (I won twice)
- Excellent Student Prize in Undergraduate School

Publications

1) **Shasha Tao**, Florent Yang, Jona Schuch, Wolfram Jaegermann, Bernhard Kaiser. Electrodeposition of nickel nanoparticles for the alkaline hydrogen evolution reaction: correlating electrocatalytic behavior and chemical composition. *ChemSusChem* **2018**, *11* (5), 948-958.

2) Yao Feng, Zhaoju Yu, Jona Schuch, **Shasha Tao**, Leonore Wiehl, Claudia Fasel, Wolfram Jaegermann, Ralf Riedel. Ternary nowotny phase $Mo_{4.8}Si_3C_{0.6}$ dispersed in a porous SiC/C nanocomposite matrix: a novel catalyst for Hydrogen Evolution Reaction. *Journal of American Ceramic Society*. In major revision.

3) **Shasha Tao**, Caiting Li, Xiaopeng Fan, Guangming Zeng, Pei Lu, Xing Zhang, Qingbo Wen, Weiwei Zhao, Diqiang Luo, Chunzhen Fan. Activated coke impregnated with cerium chloride used for elemental mercury removal from simulated flue gas. *Chemical engineering journal* **2012**, *210*, 547-556.

4) Yine Xie, Caiting Li, Lingkui Zhao, Jie Zhang, Guangming Zeng, Xunan Zhang, Wei Zhang, **Shasha Tao**. Experimental study on Hg^0 removal from flue gas over columnar MnO_x-CeO_2/activated coke. *Applied Surface Science* **2015**, *333*, 59-67.

5) Fuman Zhan, Caiting Li, Guangming Zeng, **Shasha Tao**, Yujun Xiao, Xing Zhang, Lingkui Zhao, Jie Zhang, Jinfeng Ma. Experimental study on oxidation of elemental mercury by UV/Fenton system. *Chemical engineering journal* **2013**, *232*, 81-88.

6) Weiwei Zhao, Caiting Li, Pei Lu, Qingbo Wen, Yapei Zhao, Xing Zhang, Chunzhen Fan, **Shasha Tao**. Iron, lanthanum and manganese oxides loaded on γ-Al_2O_3 for selective catalytic reduction of NO with NH_3 at low temperature. *Environmental technology* **2013**, *34* (1), 81-90.

7) Xiaopeng Fan, Caiting Li, Guangming Zeng, Xing Zhang, **Shasha Tao**, Pei Lu, Ya Tan, Diqiang Luo. Hg^0 removal from simulated flue gas over CeO_2/HZSM-5. *Energy & Fuels* **2012**, *26* (4), 2082-2089.

8) Xiaopeng Fan, Caiting Li, Guangming Zeng, Xing Zhang, **Shasha Tao**, Pei Lu, Shanhong Li, Yapei Zhao. The effects of Cu/HZSM-5 on combined removal of Hg^0 and NO from flue gas. *Fuel processing technology* **2012**, *104*, 325-331.

9) Xing Zhang, Caiting Li, Xiaopeng Fan, Pei Lu, **Shasha Tao**, Weiwei Zhao, Chunzhen Fan, Qianru Zhao. Experimental research of removing elemental mercury from simulated flue gas by $CeCl_3$-loaded activated carbon fiber. *China Environmental Science* **2012**, *32* (5), 816-821.

10) Chunzhen Fan, Caiting Li, Pei Lu, Xing Zhang, Weiwei Zhao, **Shasha Tao**. Experimental research of purification NO-containing gas by aqueous oxidation with Fenton-like agent. *China Environmental Science* **2012**, *32* (6), 988-993.